Numerical Simulations of Steel Frames Equipped with Friction-Damped Diagonal-Bracing Devices

Juan David Morales

A Thesis

in

The Department

of

Building, Civil & Environmental Engineering

Presented in Partial Fulfillment of the Requirements

for the Degree of Master of Applied Science (Civil Engineering) at

Concordia University

Montreal, Quebec, Canada

November 2011

CONCORDIA UNIVERSITY

School of Graduate Studies

This is to certify that the thesis prepared

By: Juan David Morales

Entitled: Numerical Simulation of Steel Frames Equipped with Friction-Damped Diagonal-Bracing Devices

and submitted in partial fulfillment of the requirement for the degree of

Master of Applied Science (Civil Engineering)

complies with the regulations of the University and meets the accepted standards with respect to originality and quality

Signed by the final examining committee:

Dr. Oscar A. Pekau   Chair

Dr. Ramin Sedaghati   Examiner

Dr. Lan Lin   Examiner

Dr. Lucia Tirca   Supervisor

Approved by   Dr. Maria Elektorowicz
                Chair of Department or Graduate Program Director

                Dean of Faculty

Date

ABSTRACT

Numerical Simulation of Steel Frames Equipped with Friction-Damped Diagonal-Bracing Devices

Juan David Morales

Among passive energy dissipation devices, friction dampers are used worldwide as means of increasing damping into structural building systems with the aim to reduce the seismic response. These devices, added either in-line with diagonal braces, or at the intersection zone of X- and chevron-bracing and installed in moment frame buildings, can reduce the demand of the primary frame system, the interstorey drift, and control the damage of non-structural components as building envelope. Regarding to their mechanical behavior, friction dampers dissipate energy through the relative sliding of plates clamped with post-tensioned bolts, while slipping occurs along the length of the slotted hole. This device reveals a rigid-plastic behavior defined by three phases such as: "stick-slip" before sliding occurs, "slipping", and the "slip-lock" when the force in the device increases due to the bearing of the post-tensioned bolts.

Thus, the first part of this study is focused on establishing a computer model able to simulate the three-phase behavior of the friction damper installed in diagonal bracing by using OpenSees software framework. In light of this, the Bouc-Wen material characterized by smooth transition from elastic to plastic was calibrated through parametric study and employed to characterize the first two behavioural phases mainly controlled by the slip-force and available slip-distance. In addition, earlier experimental studies conducted by Pall (1979) were used to control the calibration. To simulate the

slip-lock phase exhibited due to bearing of post-tensioned bolts, gap-elements were added in parallel to the Bouc-Wen model. In addition, to complete the friction-damped brace model, the action in series of the elastic brace and the friction damper model is considered.

The second part of this study illustrates the behavior of the 4, 8 and 12-storey building designed as moderately ductile (MD) moment resisting frame structure accordingly to NBCC 2010 and CSA/S16-2009. The studied buildings are located in Montreal and are subjected to 15 simulated and historical ground motions scaled to match the uniform hazard spectrum. Herein, beams and columns were defined as nonlinear force-based beam column element with fiber section and Steel02 material. From analyses, the mean values of the following parameters: maximum interstorey drift, maximum drift angle and maximum beam rotation are computed.

The third part is designated to analyze the seismic response of MD-MRF structures equipped with friction-damped brace devices through numerical simulations of 4-, 8- and 12-storey building, using OpenSees. It is showed that the proposed hysteresis model for friction-damped brace responds well under dynamic loading and it is able to tune the response within the prescribed limits. Driving devices into bearing shows transitional changes consisted of decreasing damping and increasing stiffness. When this phase is encountered, the MD-MRF might respond as a back-up system and as a re-centering system. It is revealed that the three-phase hysteresis model of friction damper developed in this study must be calibrated against experimental test results conducted under cyclic loading until failure is reached. Due to lack of experimental test results several assumptions were made.

ACKNOWLEDGEMENTS

Para mi madre Carmen, mi hermana Lina y mi sobrina Sara, a

quienes les debo todo…..

TABLE OF CONTENTS

LIST OF FIGURES

xi

xv

LIST OF TABLES

CHAPTER 1

Introduction

1.1 GENERAL

The damage caused by seismic events has driven structural engineers to figure out cost-efficient solutions with the aim to reduce the demand triggered in structural members of buildings. In this regard, by adding supplemental damping to a structural system, the damage energy is reduced and the inelastic response of earthquake resistant members is controlled. In general, damping can be added by incorporating passive or/and active energy dissipaters. When passive dampers are selected, for instance friction dampers, they are able to use the seismic demand translated in term of displacement induced into the structural system in order to activate the friction mechanism.

In light of this, Pall friction dampers have been widely used in North America either in new or retrofit design projects of steel or reinforced concrete structure (e.g. A. Pall et al. 1987; Soli et al, 1996; Sadek et al.1996; Vail et al. 2004; Pasquin et al. 2004 and others). These devices dissipate energy through the relative sliding of plates clamped by post-tensioned bolts. The experimental studies conducted by Pall (1979) identified clearly that sliding along the available slip distance is controlled by the length of slotted hole and the behaviour is similar to that of an elastic-perfectly plastic system. However, under a large seismic input, the post-tensioned bolts belonging to the friction damper

device may undergo an additional phase following sliding, characterised by bearing of bolts or adjacent plates. Thus, in this stage, a sudden increment in storey shear force accompanied by decreasing of supplemental damping is encountered. Therefore, the behaviour of friction damper can be divided in three phases as follows: "stick-slip" before sliding occurs, "slipping", and the "slip-lock" when the force in the device is increased due to the bearing of the bolts. Nevertheless, in literature, there are no reported test results concerning the failure of Pall friction damper due to bearing or shearing of post-tensioned bolts, although this phenomena has been anticipated (Pall 1979). Later on, Roik et al. (1988) and Lukkunaprasit et al. (2004) performed cyclic tests where they showed that a possible "bolt-impact" occurred if the demand has lead the sliding plates to enter in contact with the post-tensioned bolts. Lukkunaprasit et al. (2004) evidenced that this jump in force resistant at bearing is limited by failure of friction device. In addition, degradation in the hysteresis capacity of device was observed after the bolt impacted the slotted hole and a sudden loss of post-tension force in the bolts occurred. When the bearing phase is considered, an increment in the base shear was noticed.

Previous studies have used mainly elastic-plastic models which considered only the rectangular hysteresis shape characterised by the dry Coulomb friction, while the bearing phase has been ignored. Other researchers have developed multi-linear models to incorporate the bearing phase, but Lukkunaprasit et al. (2004), have pointed out that previous studies did not take into account the nonlinear behaviour neither the decoupling of the device from structure when failure was encountered.

The current provisions of NBCC 2010 do not provide guidelines regarding earthquake resistant structures equipped with friction damper devices nor suggestions

referring at adding damping into a structural system in order to reduce the seismic demand. Although FEMA 356 (2000) contains information regarding friction devices and some design recommendations such as "all energy dissipation devices shall be capable of sustaining displacements equal to 130% of the maximum calculated displacement in the device" when subjected to ground motions defined for 2% in 50 years probability of exceedance, it does not stipulate complete design provisions.

1.2 OBJECTIVES AND SCOPE

The scope of this research is to develop a numerical model able to simulate the seismic response of a moment resisting frame structure equipped with friction-damped diagonal-bracing devices and to emphasise the behaviour of the 4-, 8- and 12-storey building located in Montreal when a minimum of four dampers per floor have been installed as follows: i) at each floor; ii) at alternative floors; and ii) staggered at reduced number of floors. Herein, the identified engineering demand parameters are reported based on their mean and the 84th percentile and are obtained from time-history analyses of the aforementioned buildings subjected to 15 simulated and historical ground motions. In addition, until today, there is not an accurate computer model reported in literature able to capture the complexity of the real friction damper behaviour and the response of earthquake resistant structure with friction dampers incorporated.

Thus, the objectives of this study are:

- To develop a computer model of friction damper device able to integrate the three phases pointed out by Lukkunaprasit et al. (2004): stick-slip; slipping or sliding; and the slip-lock by using the finite element library of the OpenSees software.

- To develop a design method in order to compute the number of devices per floor, the slip force and the required slip distance.

- To analyse the performance of the 4-, 8-, and 12- storey buildings equipped with energy dissipative devices such as friction-damped diagonal-bracing system.

The seismic response is discussed based on three scenarios of dampers' locations and by considering two simulated models: with and without slip-lock phase incorporated. Based on numerical results, the effect of bearing phase on the adjacent structural members is emphasised. It is assumed that no degradation of the hysteresis loop occurred during the friction damper response and the diagonal-bracing system is designed to behave elastically.

1.3 DESCRIPTION OF METHODOLOGY

To simulate in OpenSees software framework the first two behavioural phases of Pall friction dampers: stick-slip and slipping, the Bouc-Wen material characterized by smooth transition from elastic to plastic was employed. The main parameters required to define the Bouc-Wen material are: the slip-force and the available slip-distance which was calibrated through parametric studies. In addition, earlier experimental tests conducted by Pall (1979) were used to control the calibration. The slip-lock phase occurred due to bearing of post-tensioned bolts and is simulated by adding Elastic-

Perfectly plastic Gap material object in parallel to the Bouc-Wen material. For decoupling the device from the system at failure, when bearing force equates the bearing strength, the MinMax material object was assigned to the ensemble of Bouc-Wen and the Elastic Perfect plastic Gap material. In order to complete the modelling of friction-damped diagonal-bracing device, the action in series of the elastic brace and the defined friction damper is considered.

The design technique proposed herein to define the number of dampers per floor and the assigned slip-load is based on minimizing the damage energy absorbed into the bare frame system such that the moment resisting frame members to behave elastically. In this context, the MRF is considered to be simultaneously a backup system and a re-centering system.

The proposed hysteresis model, able to simulate the behaviour of friction-damped diagonal-bracing system, is incorporated into the OpenSees framework of 4-, 8-, and 12-storey MRF buildings. Herein, force-base nonlinear beam-column elements (beam with hinges) were selected to simulate the behaviour of MRF's members and Steel02 material (known as uniaxial Giuffre- Menegotto-Pinto steel material) was assigned. Time-history nonlinear analyses were conducted for each case study located in Montreal and subjected to 15 simulated and historical records, scaled to fit the uniform hazard spectrum (UHS) of 2% in 50 years probability of exceedance. For each case study, three different scenarios of dampers location along the building height were considered, while the device model was defined with and without slip distance limitation.

1.4 THESIS ORGANISATION

The first chapter summarises the scope of this research, the objectives and the applied methodology.

In Chapter 2 a detailed literature review regarding friction damper devises is illustrated in addition to the presentation of Bouc-Wen hysteresis model through mathematical equations.

The Chapter 3 focuses on establishing a computer model able to simulate the three-phase behavior of the friction damper installed in diagonal-bracing system by using OpenSees software framework (open system for seismic simulation). In light of this, the Bouc-Wen material characterized by smooth transition from elastic to plastic was calibrated through parametric study in order to characterize the first two behavioural phases mainly controlled by the slip-force and available slip-distance. The slip-lock phase due to bearing exhibited when the post-tensioned bolts impact the edge of the slotted hole is simulated by adding in parallel to the Bouc-Wen material the uniaxial Elastic Perfectly plastic Gap material. At the end of the chapter, a brace with friction device was numerically simulated in OpenSees and studied under quasi-static displacement loading.

Chapter 4 illustrates the behavior of the 4, 8 and 12-storey building designed as moderately ductile (MD) moment resisting frame structure accordingly to NBCC 2010 and CSA/S16-2009. Herein, the MD-MRF system was selected versus conventional MRF due to its cost-efficiency and capability to behave elastically when friction damper devices are installed. In addition, the purpose of considering moment frame structure as a

bare frame for dampers installation is to have a backup system during the time when dampers are activated. In this study, the MD-MRF structure are analysed for comparison purpose and are subjected to 15 simulated and historical ground motions scaled to match the uniform hazard spectrum. In this study, the following parameters were selected to capture the seismic response: interstorey drift, drift angle and maximum rotation demand after plastic hinges were formed in beams.

In Chapter 5 the seismic response of MD-MRF structures equipped with friction-damped diagonal-bracing system devices is analyzed through numerical simulations. First, the design technique consisting of defining the number of dampers per floor and the assigned slip-load is carried out based on minimizing the damage energy in the bare frame system. Three different scenarios of friction-damped diagonal-bracing devices location and the available slip-distance parameter are considered herein. Numerical analyses are conducted under the 15 selected records and results are expressed based on a statistical distribution.

Finally, Chapter 6 provides conclusions and future work recommendations resulted from this research work.

CHAPTER 2

Literature Review

2.1 PASSIVE ENERGY DISSIPATION DEVICES

A continued increase of human population and its concentration in urban areas have triggered the development of infrastructure and building constructions.

In general, the total input energy (E_I) induced by a seismic event into a structural system can be expressed as a summation of kinetic energy, E_k, cumulative strain energy, E_S, inherent damping, E_D and the hysteretic damping or the post-yield hysteretic damping of the seismic force resistant system (SFRS), E_h which in this case is the damping induced by friction devices (Foliente 1993; Filiatrault 1997). The energy balance equation is:

$$E_I = E_K + E_D + E_S + E_h \tag{2.1}$$

The kinetic and cumulative strain energy are accumulated by the primary structural system and are related to the structural damage (Akiyama 2000; Tirca et al. 2010), while both E_D and E_h are amplitude-dependent and able to damp the SFRS. In general, the contribution of E_D and E_h is related to the amount of post-yielding response.

Rearranging terms of Equation (2.1) gives:

$$E_K + E_S = E_I - (E_h + E_D) \qquad\qquad (2.2)$$

The left side of Equation (2.2) accounts for the elastic vibration energy, E_V (Akiyama 2000) which in turn becomes the potential damage energy, while the right side accounts for the effective energy level dissipated by the system during an earthquake. Thus, as shown in Figure 2.1, by increasing the damping in the system, the damage energy as percentage of the input energy is reduced as per Equation (2.2). Therefore, by adding damping into the structural system, the elastic vibration energy is reduced, while structural members are protected from damage associated to permanent deformations.
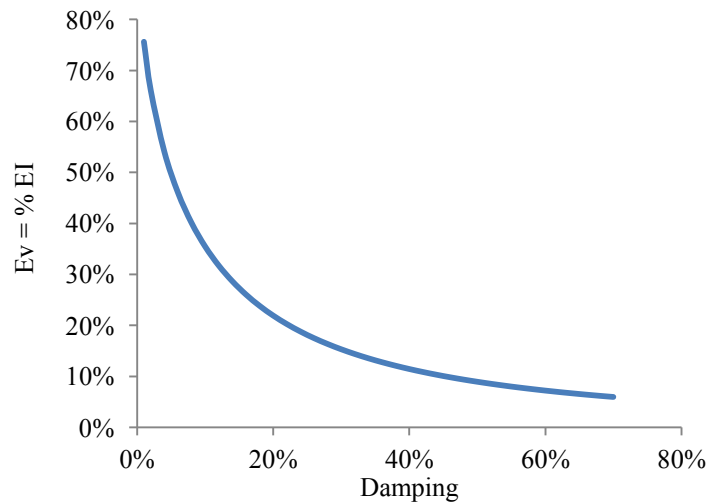
Figure 2.1 Variation of structural damage energy with the equivalent damping ratio
(According to Akiyama 2000)

By incorporating passive energy dissipation devices (PEDD) into a structural system, it means adding damping to that system. Furthermore, based on the energy dissipation mechanism criterion, PEDDs may be classified as: friction dampers; metallic dampers;

viscoelastic dampers; viscous fluid dampers; and tuned mass dampers (Soong and Dargush 1997).

Friction dampers dissipate energy through friction developed by the relative sliding within two surfaces in contact. If an adequate surface treatment and lining material is applied, their behaviour is characterized by a rectangular stable hysteresis loop similar to that of Columb friction (A. Pall 1979).Thus, the following dampers are designed to dissipate energy by friction: slotted bolted connections (Grigorian et al. 1992); Pall friction devices (Pall 1979); Sumitomo damper devices (Aiken et al. 1990 and 1993) and energy dissipating restraint damper (EDR) developed by Flour Daniel Inc. (Nims et al.1993). A description of each type of friction dampers is given below.

2.2 FRICTION DAMPERS

2.2.1 Limited Slip Bolted Joint and Pall Friction Dampers:

Based on the concept of energy dissipation throughout the relative sliding within two surfaces in contact, A. Pall (1979) developed a dissipative joint for connecting two adjacent concrete panels. This type of dissipative connection, labelled limited slip bolted joint (LSB) is shown in Figure 2.2a and was developed with the purpose to reduce the seismic demand. Herein, the slip length (distance) is defined by the slotted hole dimension and the friction force is computed as being the product between the friction coefficient and the normal force arising from the clamping action of the post-tensioned bolts which are "sandwiching" the surfaces in contact. The hysteretic behaviour follows a

smooth rectangular shape which is characteristic to Coulomb friction law. However, the real hysteresis shape may be largely influenced by the fluctuation of the friction coefficient during the slipping process. These variations might be originated by diverse factors such as temperature, wear effects, loss of the pretension load, and others (Pall 1979; Bondonet and Filiatrault 1997; Sextro 2002). In light of this, Pall has carried out several experimental tests under monotonic and quasi-static cyclic loading in order to select the type of surface treatment and lining material that are able to provide a stable friction coefficient. The hysteresis behaviour of six case studies such as: mill scale, sand blasted, inorganic zinc-rich paint, metalized, brake lining pads and polyethylene coating are shown in Figure 2.2b In conclusion, Pall has reported that the most stable behavior under the static and dynamic tests was obtained when brake lining pads in contact with mill scale surface on plates was chosen. During the performed quasi-static cyclic tests, the corresponding hysteretic behaviour did not show appreciable degradation. However, a minor difference between the static and slip (dynamic) coefficient of friction remained and is shown in Table 2.1.

Table 2.1 Degradation of hysteretic behavior (after Pall 1979)

Surface finish	Degradation factor (ratio between the average energy per cycle after 20 cycles and the energy dissipated in the 1st cycle)
Mill scale	0.88
Sand blasted	0.98
Zinc-rich paint	0.66
Metalized	1.27
Brake lining pads over mill scale surface	0.98
Brake lining pads over sand blasted surface	0.82
Brake lining pads over galvanized surface	0.78
P.V.C coating on sand blasted surface	1.8
Polyethylene coating over sand blasted surface	1.08

b)

a)
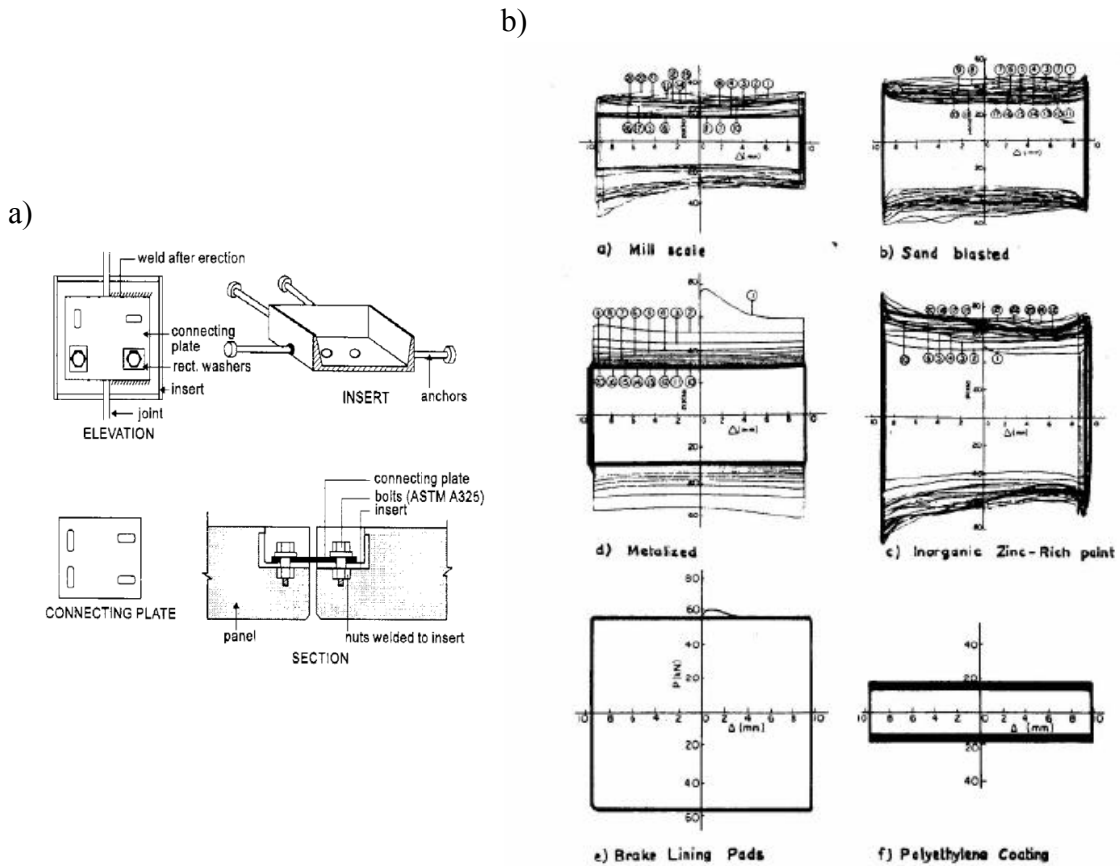
Figure 2.2 The LSB joint and its behaviour: a) Wall-to-wall joint and b) Hysteresis behaviour under cyclic test of six case studies (after Pall 1979).
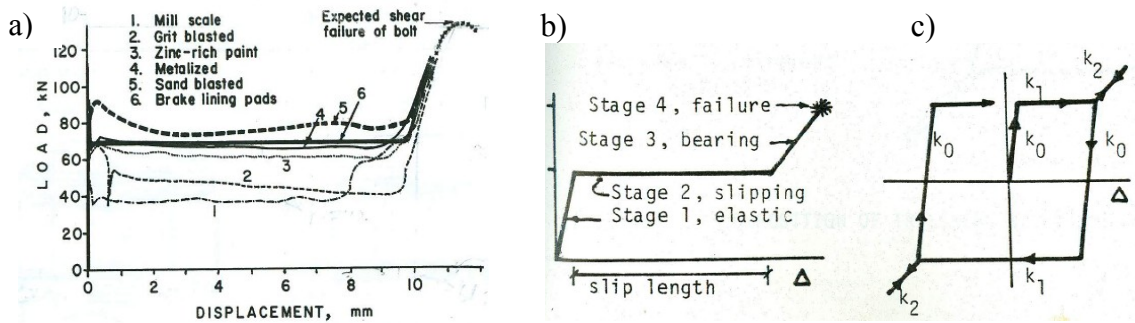
Figure 2.3 Response of the LSB joint: a) monotonic test; b) back-bone curve; c) hysteretic behavior (after Pall 1979)

12

Based on the force – displacement (slip distance) relationship resulted from monotonic test showed in Figure 2.3a, the behaviour of the joint follows four possible phases: elastic, slipping, bearing and failure of bolts, while the back-bone curve is illustrated in Figure 2.3b. The slipping phase, simulated by the plateau, occurs due to the relative sliding within the surfaces in contact. The bearing phase corresponds to the bearing phase corresponds to the bearing of bolts and/or plates which occurs when the demand is larger than the available slip distance provided by the length of slotted holes. Thus, the failure of the joint may occur either in bearing or in shear (bolt shear failure). However, the cyclic behaviour of joint in bearing was not detailed by Pall during his earlier case studies. Changes between adjacent phases were simulated without transition zones and the nonlinearity observed during the phase previous to failure was not considered. These shortcomings were documented later in studies conducted by Roik et al. (1988) and Lukkunaprasit et al. (2004) and discussed in the further subsections.

The experience gained during the development of the LSB joint was enhanced and a group of friction dampers were developed by A. Pall later on.

In this regard, depending on the installed support, Pall friction dampers can be classified as follows: friction damper incorporated in X-type braces (Figure 2.4), friction damper installed in-line with diagonal bracing (Figure 2.5a), and friction dampers incorporated in chevron bracing (Figure 2.5b). Their basic functioning mechanism is similar to that of the LSB joint and it refers to the relative sliding within surfaces in contact while the resulted friction force depends on the specific treatment applied to the surfaces in contact and the brake lining pad clamped together by the post-tensioned high strength bolts. For example, the in-line Pall friction damper with diagonal braces and

13

dampers in X-type bracing were used to retrofit the Boeing Assembly Plant, Everett, U. S. (Vail et al. 2004), while friction dampers in chevron bracing were chosen for the seismic upgrade of the Sharp Memorial Hospital, San Diego, U. S. (Soli et al. 2004).

Therefore, as reported by researchers and professional engineers, Pall friction dampers have been used widely in North America as additional means for seismic protection of existing and new structural systems.

To evaluate the performance of passive energy dissipation devices, seven different types of dampers were tested at the Earthquake Research Center, Berkeley, California between 1986 and 1991 (Aiken et al. 1993)). Among them, Pall friction dampers in X-bracing configuration were incorporated in the middle bay of a 9-storey existing moment resisting frame (MRF) built at ¼ scale and tested on a shaking table measuring 6.1m x 6.1m. To accommodate the X-bracing connections into the MRF, the structure was modified in order to provide suitable beam-column connections. The studied 3 bays frame (28 ft high and 18ft wide) was subjected to several horizontal records simulated through one horizontal and possible one vertical component. For low level of excitations during which the frame behaved elastically, the amount of damping was found to be 5.6% while for the MRF 2.4% (Aiken et al. 1988). Once the devise experienced slipping at higher level of excitation, the damping of the system was significantly increased. Thus, depending on the amplification level of excitations, damping was observed to increase in the range of 8.5% to 37.6%, while stiffness of the system has diminished. For example, under the El-Centro record scaled at 0.17g, the test yielded the following results: 22.4% damping and 47.2 kips/inch stiffness. When the same record was scaled at a peak ground acceleration of 0.838g, damping was increased

14

to 32.2% and stiffness was diminished at 29.9 kips/inch. In order to keep the frame undamaged for other tests, the maximum interstorey drift reported was 1%h_s where h_s is the storey height. However, the aforementioned test was not conducted to emphasise the failure phase and there are not other experimental test data referring to the behaviour at failure or when the interstorey drift reaches 2.5%h_s.

Therefore, the computer models used up to this point are not considering the limitation of slip distance and nor the bearing stage because the additional phases evidenced by Roik et al. (1988) and Lukkunaprasit et al. (2004) are not included

a)   b)

Figure 2.4 Pall friction dampers in X-type bracing: a) Concordia library building, Montreal, Canada (after Pall et al. 1987) and b) Boeing Assembly Plant, US,(after Vail et al. 2004)

a)   b)

Figure 2.5 Pall friction dampers in diagonal and chevron-bracing a) Boeing Assembly Plant, US, (after Vail et al. 2004) and b) Sharp Memorial Hospital, San Diego, US (after Soli et al. 2004)

2.2.2 Fiction Grip Connections:

Based on the work done by A. Pall and employing the mechanism of friction within two solid surfaces, Roik et al. (1988) proposed a three-stage friction-grip connection able to be designed for serviceability, life-safety and collapse prevention limit state under seismic loads. Experimental tests were conducted on steel-steel and steel-concrete friction-grip joints in order to provide a mechanism of energy dissipation (Figure 2.6). Based on tests, they concluded that coupling in parallel the displacement of three structural elements as shown in Figure 2.7a it smoothes the transition phase from elastic behaviour to the slipping stage and avoids the induction of possible vibrations. The force deformation relation of an element is shown in Figure 2.7b, while the predicted performance of a three-stage stiffening element is illustrated in Figure 2.7c.

It was revealed that stiffness and the nonlinear behavior are depended on the pretension force applied to the clamping bolts even if no considerable damage occurred in the joint. When implemented in a building, the mechanical properties of the bolts and the geometrical limit of slotted holes influence largely the lateral stiffness of each story, the activation of the slip force and the amount of energy dissipated per cycle.

Therefore, by combining a set of these joints as braking system into a 7-storey CBF building subjected to seismic actions, an enhancement of the response during a ground motion event was achieved; meanwhile the slip distance was not exceeded by the developed interstory drift throughout the duration of excitation during the test.

.
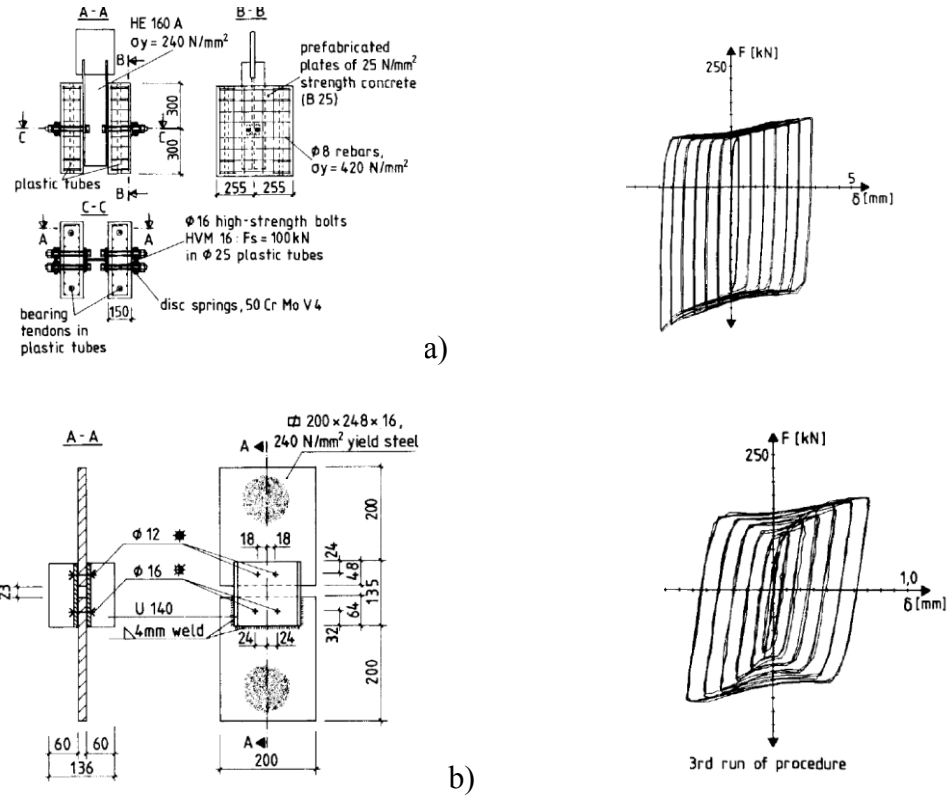
Figure 2.6 Friction grip connections (after Roik et al. 1988): a) Steel-concrete-friction-grip and its hysteresis response; b) Steel-steel-friction-grip and its hysteresis response.

a) Three stage implementation

b) Behavior of one component i.
C_i: stiffness, γ_i: frictional displacement,
T_i: level of friction.

c) Predicted performance of a typical story
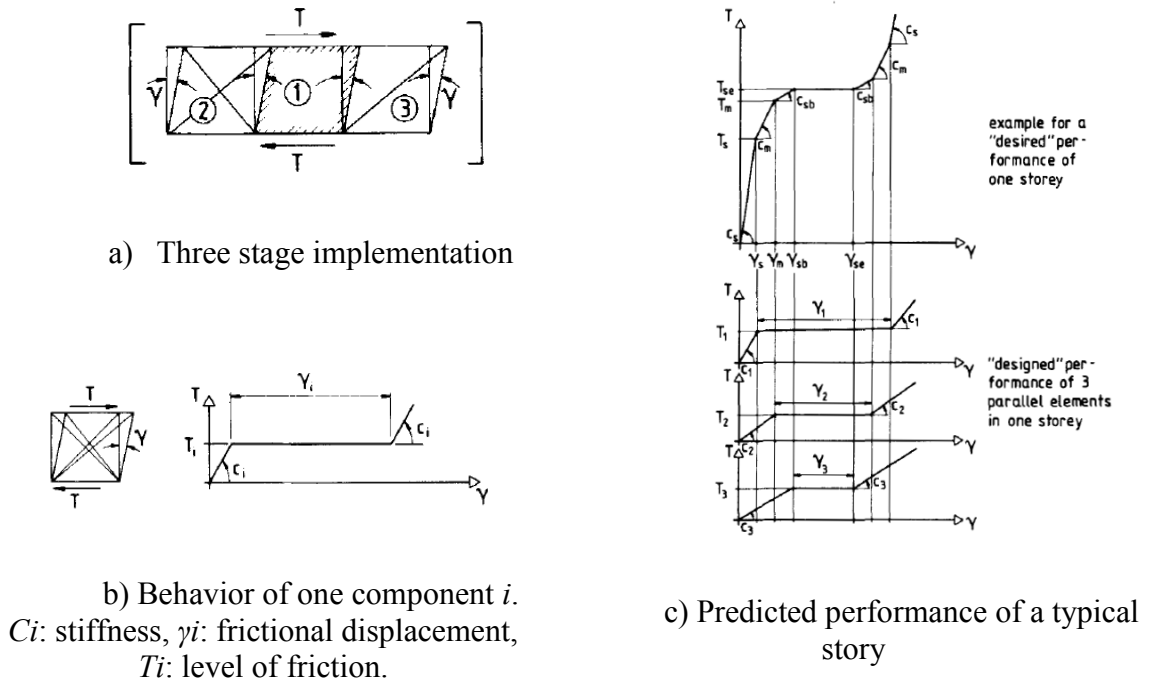
Figure 2.7 SFRS with three stiffening elements acting in parallel (after Roik et al.1988)

17
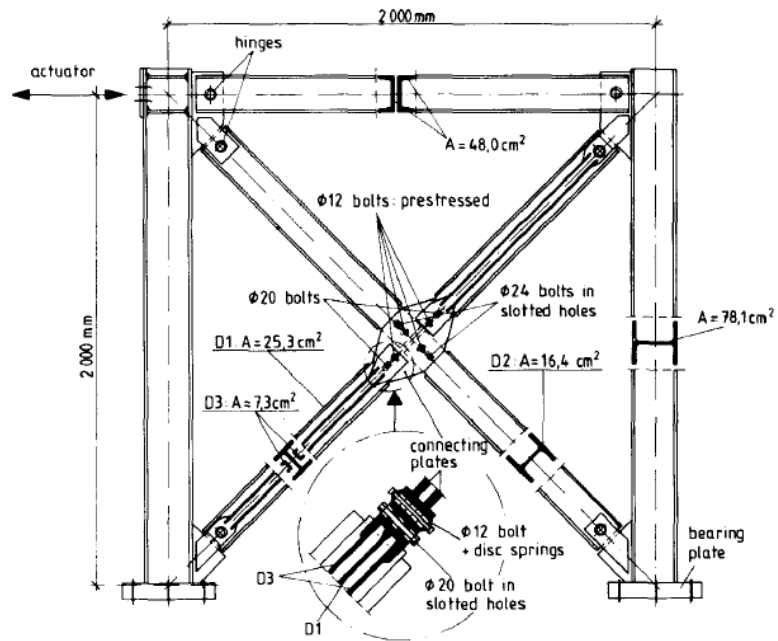
a)
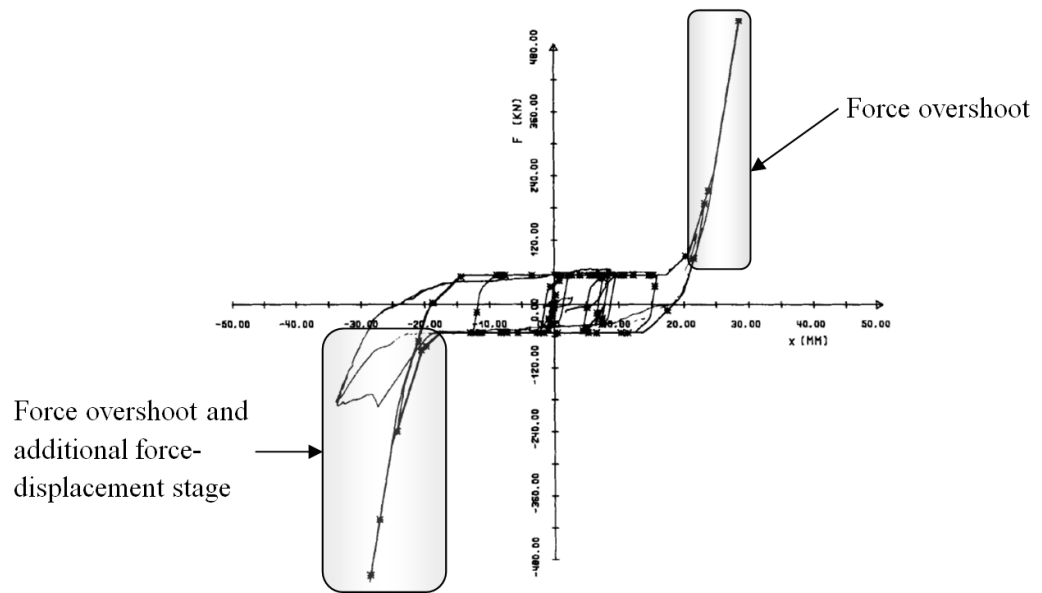
b)

Figure 2.8 Set-up and behaviour of a three stage truss system: a) Specimen set-up, b) Measured and calculated (star symbol) hysteresis response (after Roik et al. 1988).

Despite of underlined improvements, the bearing stage due to the bolt impact arose as a consequence of limited slip distance imposed by the length of slotted hole and the post-tensioned force of high strength bolts. This behaviour shown in Figure 2.8a was identified in analytical and experimental test conducted on a CBF system by modelling a three-stage truss system. The hysteresis loop of the specimen tested under the N-S component of El Centro record provides an insight of the force overshoot due to the bolt impact that is shown in Figure 2.8b. It is evident that the additional force-displacement stage encountered was not emphasised in previous tests. As consequence, the model proposed was unable to capture this further feature.

2.2.3 Slotted Bolted Connections:

Grigorian et al. (1992) studied a typical slotted bolted connection (SBC), which dissipates energy by friction developed within two steel splice plates pressed against a steel gusset plate by the action of pre-stressed high strength A325 bolts, as shown in Figure 2.9. In this case study, the clamped plates were made of clean mill-scale A36 steel. These devices were tested at the University of California at Berkley using an MTS loading frame. According to their initial results and by considering the research reported by A. Pall (1979), the hysteresis shapes obtained have showed a rather non-stable trend due to the fluctuations on the friction coefficient and abrasive wear effects among other. After analysing several specimens, they proposed to add 1/8 inches (3.175mm) shims between the gusset and the clamped plates, whereas shims were made of half-hard cartridge brass USN-260 as depicted in Figure 2.9. The energy dissipated by friction between mill-scale steel and brass surfaces has showed a more stable hysteretic loop than

the former one, which was maintained throughout the entire duration of quasi-static displacement loading and is showed in Figure 2.10c.
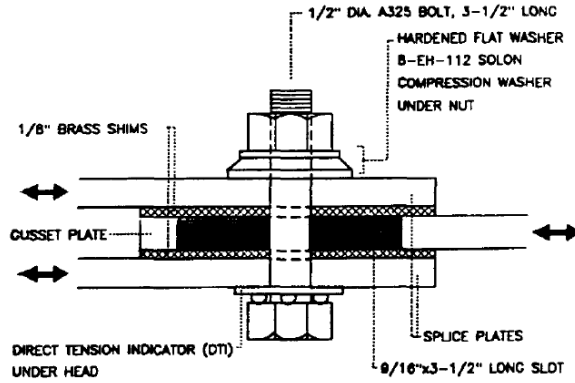
Figure 2.9 Detail of a typical SBC (after Grigorian et al. 1992).

a)

b)

c)
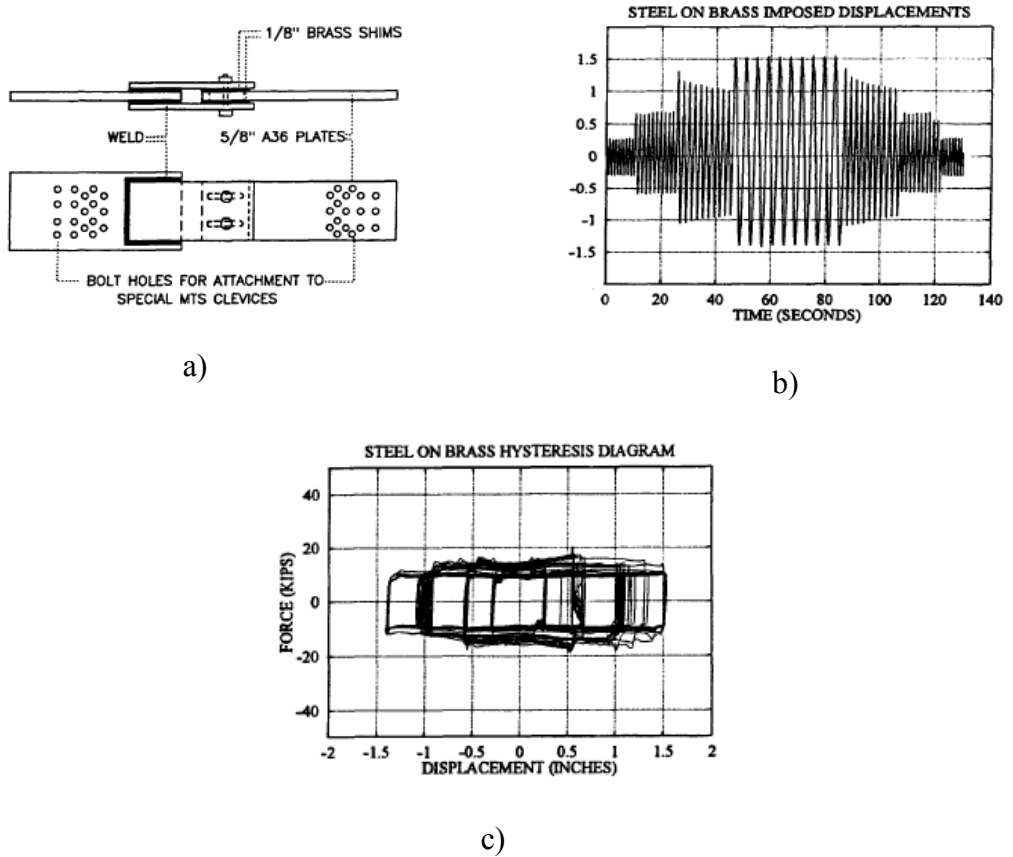
Figure 2.10 The response of SBC : a) Specimen tested, b) Displacement loading protocol and c) Hysteretic behaviour :(after Grigorian et al. 1992).

20

Although the trend of the hysteresis cycles followed a rectangular shape as per Coulomb friction law, there are fluctuations within the loop when the sliding surfaces are exhibited the stick-slip stage due to variation of friction coefficient from static to the dynamic value. This change may induce additional vibration into the structure which depends on the variation rate of friction coefficient.

The potential effectiveness in energy dissipation and the consistency of the hysteresis loop of SBCs was emphasised by Popov et al. (1995) through experimental tests. Thus, two braced frames of 3-storey, equipped with SBCs installed at the upper part of each brace were tested on a shake table under the Llolleo earthquake, Chile, 1985.. The response of the SBCs were measured at each floor level of the frame and it was shown that a significant part of input energy was dissipated by friction devices rather than by means of the inherent damping of the system or inelastic deformation of structural members, as shown in Figure 2.11 b. Nonetheless, the recorded hysteretic behaviour shows clearly in Figure 2.11a that the experimental test ended before the entire slip distance was reached. Thus the behaviour of the connection after the slip distance was reached is not reported in spite of the earlier work conducted by Roik et al.(1988).

Later on, Tremblay (1993) conducted an extensive experimental program for analyzing the behaviour of concentrically braced frames in seismic areas. In his study, the behaviour of braces in-line with SBC devices was analysed through several dynamic tests comprising displacement quasi-static loading and historical records. It was considered that the mechanism of energy dissipation occurs in the SBC devices due to the relative movement within the connected components. Thus, it was showed that by incorporating SBCs into a structural system might be a practical and economic alternative, since the

elaboration of such connections following proper guidelines would consist mainly of steel plates with a defined finishing surface clamped against determined filler plates by pre-tensioned bolts (Figure 2.12). In contrast, the need of further studies referring to filler material and surface finishing was suggested in order to smooth the friction coefficient variation and reduce the deterioration process due to the wear effect.

Additionally, it was underlined the importance of studying the behaviour of multi-bolt friction connections from the stage when the slip travel exceeds the available length of slotted holes upon the failure was reached in bearing or/and bolt shear.

a)   b)
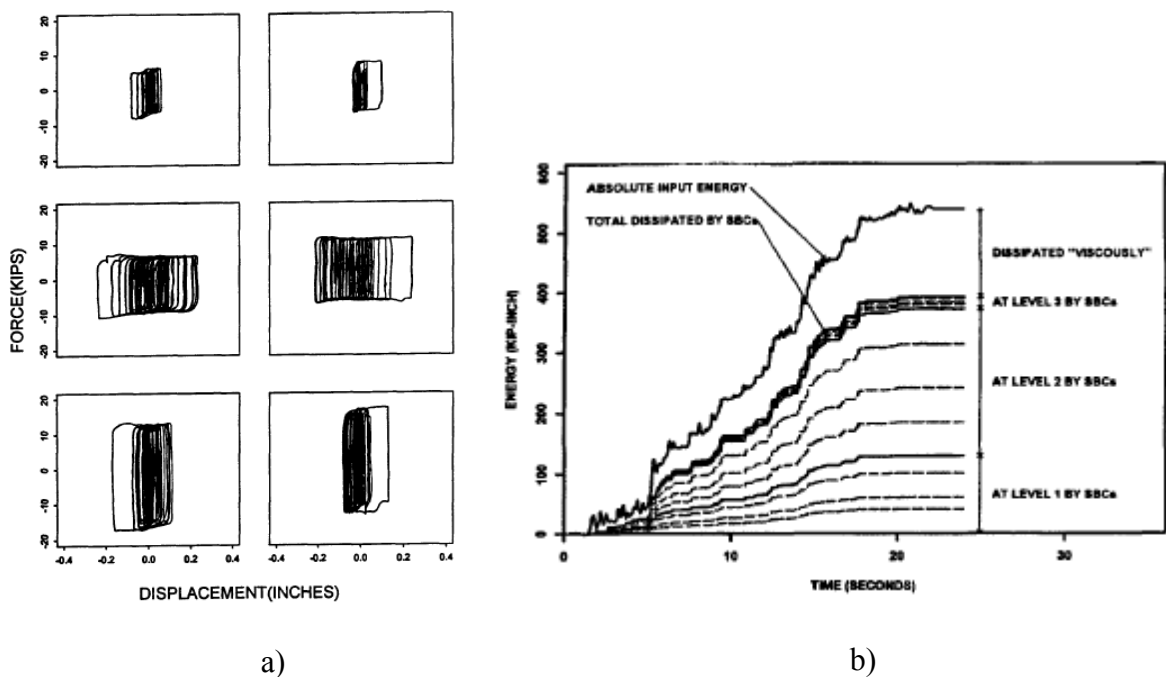
Figure 2.11 Braced frame response equipped with SBC devices under Llolleo event,
Chile '85: a)Hysteresis response of SBC and b) Energy history (after Popov et al.1995).

22
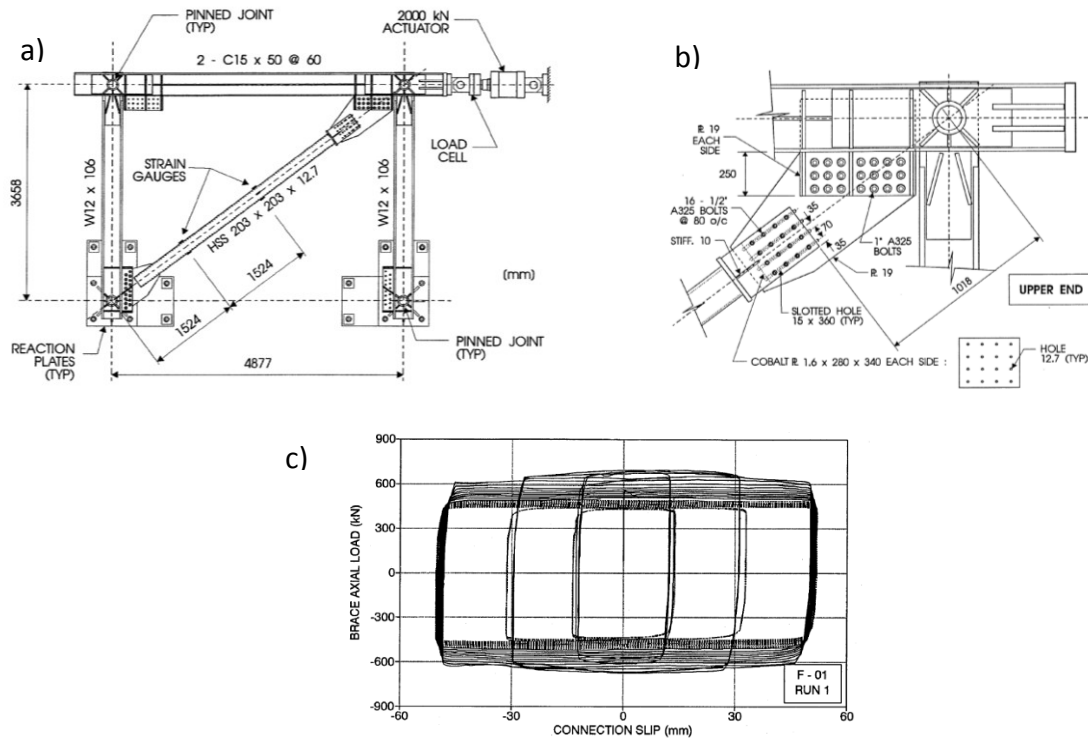
Figure 2.12 CBF with SBCs: a) Test set-up; b) detail of the SBC and. c) Hysteretic behavior under displacement controlled cyclic test (after Tremblay 1993).

In 2004, Lukkunaprasit et al. investigated the behaviour of SBCs subjected to cyclic loading, before and after the available slip length was reached. The results showed that the bolt impact comprises a nonlinear additional stage added to the customary rectangular hysteretic characteristic due to the loss of post-tension force when the clamping bolts have acted in bearing. As a consequence, the capacity of energy dissipation was diminished, while the hysteresis shape was reduced due to a repeating exceedance of the slip length limit throughout cycles (Figure 2.13a). In order to control this effect, Lukkunaprasit et al. proposed to use restrainers in his model and choose to employ the concept implemented in friction-grip connection devices by Roik et al.

(1988). Thus, in the developed model, it can be accounted on the bearing force when the available slip distance was reached and on the action of restrainers after a predefined force threshold is recorded. This hysteresis model is shown in Figure 2.13b where F_s is the slip load, Δ_g is the provided slip distance and F_{max} is the restraining force limited at a threshold value. The maximum force F_{max} depends on the brace buckling capacity, rather than the capacity of the high strength bolts used in the device or the bearing force of adjacent plates. Thus, the restraining stiffness of the device, K_f is equal to the axial stiffness of the attached brace. However, the magnitude of the restraining force can be controlled by design.

a)   b)
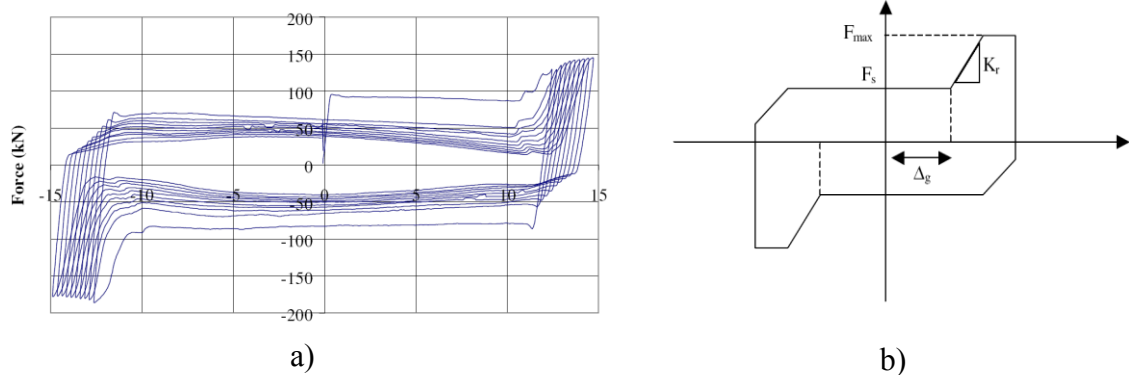
Figure 2.13 Hysteretic behavior of SBC with and without restrainers:. a) Hysteresis cycles under cyclic loads considering the effect of the bolt impact, b) Hysteresis model of friction-grip connectors with restrainers (after Lukkunaprasit et al. 2004)

By using this approach an additional segment related to bearing force action was included in the hysteretic behaviour of connection. Nevertheless, the aforementioned hysteresis models do not account on the velocity developed during the lateral movement of the building which further implies the travel of the SBC's bolts along the slotted hole. Regarding this, the dependency of the dry Coulomb friction law with velocity was not accounted, neither the possibility of providing a soft transitions between the stick-slip-

24

stage to the slipping stage nor the option of a gradual nonlinear transition from slipping to bearing or slip-lock stage when the post-tensioned bolts are pushed beyond the elastic behavior as is shown on Figure 2.13a. Since the response of a structural system depends on the frequency content of ground motions, it is required that the hysteresis model of friction devices to incorporate the following features: stick-slip changes, the relative velocity dependency, the simulation of bearing stage and the gradual nonlinear transition. Furthermore, a gradual change in the neighbouring zones of transition points such as stick-slip and slip-lock is desired in order to reduce the overshoot in forces due to the high nonlinearity occurred during the dynamic response (Gear 1971, Casarotti 2004; Bathe 2006; and Strang 2007).

2.2.4 Sumitomo Devices:

This type of friction damper was developed by Sumitomo Metal Industries, Ltd. of Japan with traditional application in railway cars as a mean of shock absorber. The energy dissipation of the Sumitomo damper is due to the friction generated throughout the sliding of the friction pad made of cooper and the outer cylinder as shown on Figure 2.14a. The former is impregnated with graphite in such a way that the hysteretic behavior exhibits stable cycles by reducing the variation of the friction coefficient (Sadek et al.1996).The movement of the pads and the normal force are originated by the set of internal and external wedges and transmitted by the cut springs. In Japan, the use of this device was extended to structures with the aim of reducing the damage caused by seismic events. The study of Sumitomo device was included into the experimental program about passive energy dissipators which was carried out at Earthquake Research Center,

Berkeley (Aiken et al. 1990; 1993). The tests related to the Sumitomo friction damper installed in-line with braces were done in a ¼ scale 9-story MRF specimen, shown schematically in Figure 2.14b. It was concluded that Sumitomo dampers incorporated in a frame system are able to reduce the frame displacements, to increase damping in the system and to dissipate a significant amount of input energy by friction following the rectangular hysteresis pattern (Figure 2.14c).

a) Sumitomo friction damper

b) ¼ scale 9-story friction damped MRF specimen

c) Typical hysteretic behavior of one friction damper
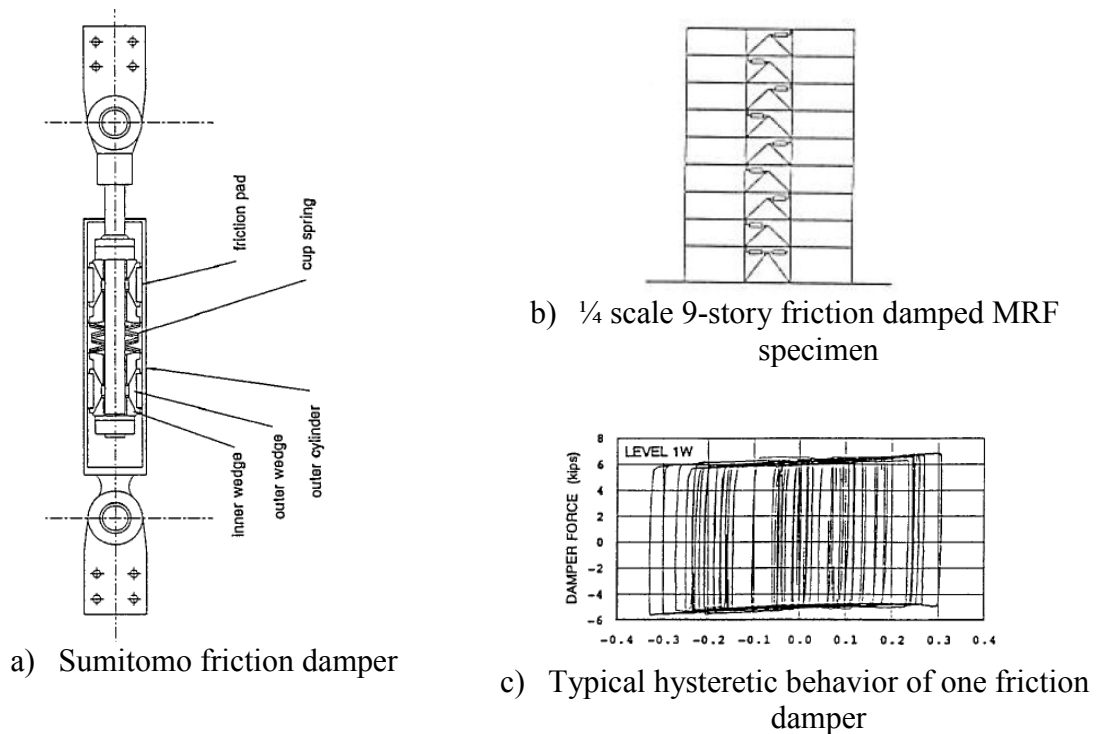
Figure 2.14 Sumitomo friction damper (after Aiken et al. 1990))

2.2.5 Energy Dissipating Restraint Device:

The energy dissipating restraint devices (EDR) were manufactured by Fluor Daniel, Inc. and their main components are depicted in Figure 2.15. Initially, the EDR device was developed to protect the support structures of piping system in nuclear plant

against seismic loads. The EDE device is similar to the Sumitomo device in term of components: internal spring, wedges, pads, external cylinder. Their mechanism and functioning might appear to be alike (Nims et al.1993) but some behaviour aspects are different. In this light, Soong and Dargush (1997) and Zhou and Peng. (2009) concluded:

i) The friction force depends on the axial force of the spring that is transformed into a normal pressure acting outwards against the cylinder wall by the wedges. on the other hand, the elastic action of the internal spring and the triangular basic hysteresis characteristic, are making the EDR self centering when the external load is reduced to zero without residual deformation. Furthermore, the internal stops allow tension and compression gaps that might be adjusted as required.

ii) For different adjustments of the device such as the variation of the pre-compressive force applied to the spring and the distance between the nuts and the stops yields to different hysteresis shapes as shown in Figure 2.15b, c and d. (Nims et al.1993).

The EDR device induces stiffness and damping into the system. Nevertheless, the work done by Nims et al. (1993) evidenced that the EDR friction force is very low for practical structural systems and its functioning depends largely on the internal spring which is able to carry a limited force without losing its deformability.

Zhou and Peng (2009) proposed a new friction variable damper based on the EDR device where the spring and wedges were replaced by a sliding shaft and a friction ring, while in the internal walls of the external cylinder two zones with high and low friction coefficient have been defined (Figure 2.16). In contrast with the Sumitomo and EDR devices, the friction force developed in this FVD device is due radial stress resulting from

27

the contact within the friction ring and the inner surface of the cylinder. The friction force increases as the sliding shaft travels upon reaching the maximum length value, while the hysteresis behaviour follows a characteristic butterfly shape as shown in Figure 2.17

a) EDR damper

b) Hysteresis rule

c) Double flag shape

d) Rectangular shape
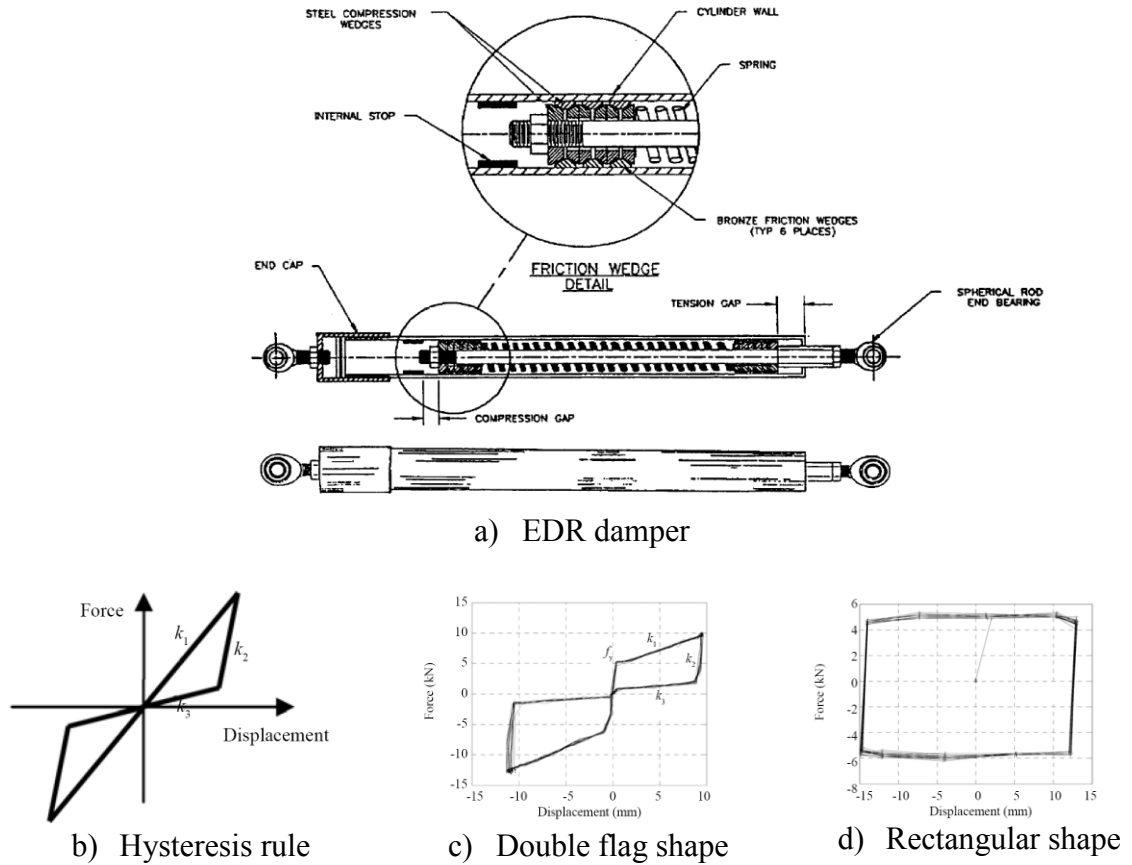
Figure 2.15 The EDR device and different hysteresis behaviour: a) sample; b) hysteresis rule; c) double flag shape and d) rectangular shape (after Nims et al. 1993)

a) Configuration

(b) Sectional drawing 1-1

(c) Detail of friction surface
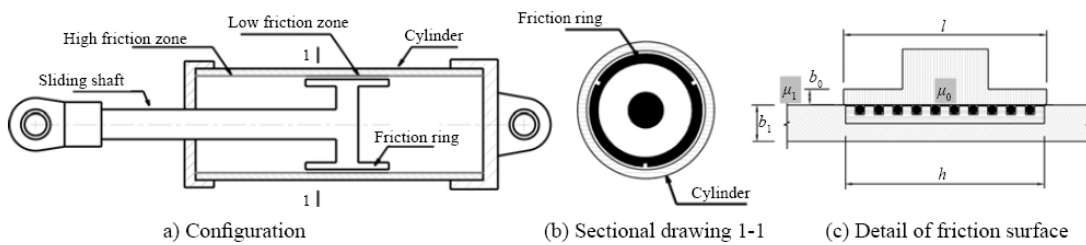
Figure 2.16 Friction variable damper, FVD (after Zhou and Peng 2009)

In order to evaluate numerically the effectiveness of this device in dissipating energy, a numerical simulation of a 7-story building equipped with FVD devices were carried out under several ground motion excitations (Zhou and Peng 2009). From numerical simulation it was found that up to 61% of the cumulative nonlinear energy was dissipated by devices. Despite these results, since there is not an exhaustive experimental test program carried out the advantages shown by the numerical simulation are still preliminary.
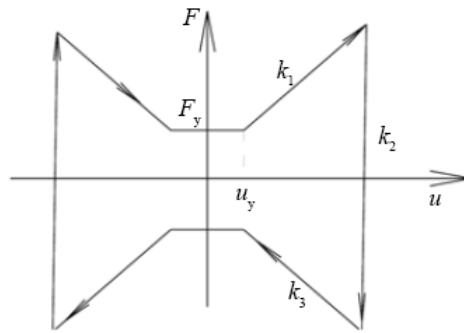
Figure 2.17 Butterfly shape hysteretic loop of FVD device (after Zhou and Peng 2009)

a) 7-story building used in numerical simulations

b) Hysteretic behavior of dampers at the first and last story
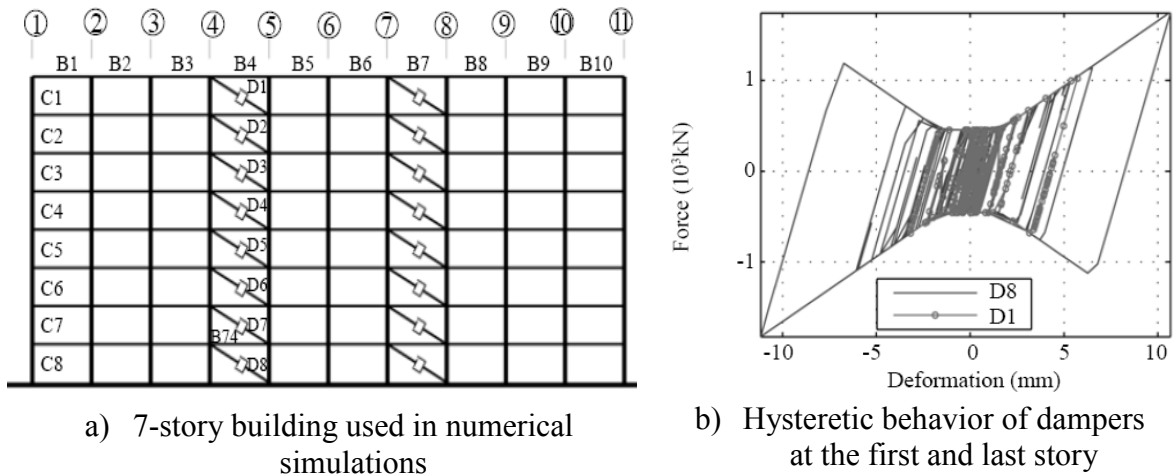
Figure 2.18 Numerical simulation of a 7-storey building: a) frame elevation; b) hysteresis behaviour of dampers located at the 1st floor (after Zhou and Peng 2009)

2.3 MODELING OF FRICTION DEVICES

2.3.1 Coulomb Friction:

It is well known that the relative sliding between two surfaces in contact produces energy dissipation through friction, which involves mechanisms rather complex than the simplification shown for the single degree of freedom (SDOF) system in Figure 2.19. Such complexity is derived from the sliding mechanism itself which depends on the following parameters: the surface finishing, relative velocity, temperature, confinement pressure and loading history (Constantineau et al. 1990; Bondonet and Filiatrault 1997; Sextro 2002).

In this section, the discussion is focused on the case of sliding block shown in Figure 2.19a, by narrowing the occurrence of the stick-slip phase at instants when the relative velocity |du/dt| approaches to zero and the dependency of friction coefficient on sliding velocity is considered. As consequence, wear effects and temperature dependency are neglected herein and the behavioural model proposed for friction device in Chapter 3 does not intent to be as general as to include such variables in its capabilities.

For evaluating the effect of different parameters on the friction model in a simplified way, the single degree of freedom vibratory system with mass *m* and a specified inherent damping shown in Figure 2.19c, is analysed under an applied external force P(t). The free body diagram is shown in Figure 2.19d and the equation of motion is:

$$m\ddot{u} + FD + Ff = P(t) \qquad (2.3)$$

Herein, the FD represents the force due to the inherent viscous damping and Ff is the friction force represented by a slider equivalent to a non-linear spring. In this case, the Coulomb friction model was used to compute the dry friction force governed by the equation Ff ≤ μN, where μ is the coefficient of friction and N the normal force to the sliding surface (Figure 2.19e). Thus, Ff is a force with the same sign as the relative velocity. In the simplest case, the coefficient of friction varies within two values depending if the relative motion within the sliding surfaces is initiated or is not.

Before the movement starts, the system is in the stick stage due to the action of the friction force opposite to the direction of movement. At the verge of relative movement, the friction coefficient reaches a maximum value called the static coefficient of friction (μS) and yields to the maximum friction force. When the block is in relative movement (|du/dt| > 0), the coefficient of friction reaches a stable value called the kinetic coefficient of friction (μK). Therefore, a more realistic but yet simplified relationship between Ff and relative sliding velocity should reflect the jump from the static to the kinetic (dynamic) value as shown on Figure 2.20. This jump and the transition between stick-slipping stages characterized by an infinite stiffness ko, make the Coulomb's friction model a highly nonlinear mechanism, while is evident that Ff is not defined at the point of zero velocity (Roberts and Spanos 1990). Hence, after the relative motion has started, the friction force may be expressed in a simplified fashion as follows:

$$Ff = \begin{cases} \mu_k N & ; \dot{u} > 0 \\ -\mu_k N & ; \dot{u} < 0 \end{cases} \qquad (2.4)$$

This in turn can be rewritten in terms of the signum function:

$$Ff = \mu_k N sgn(\dot{u}) \qquad (2.5)$$

31
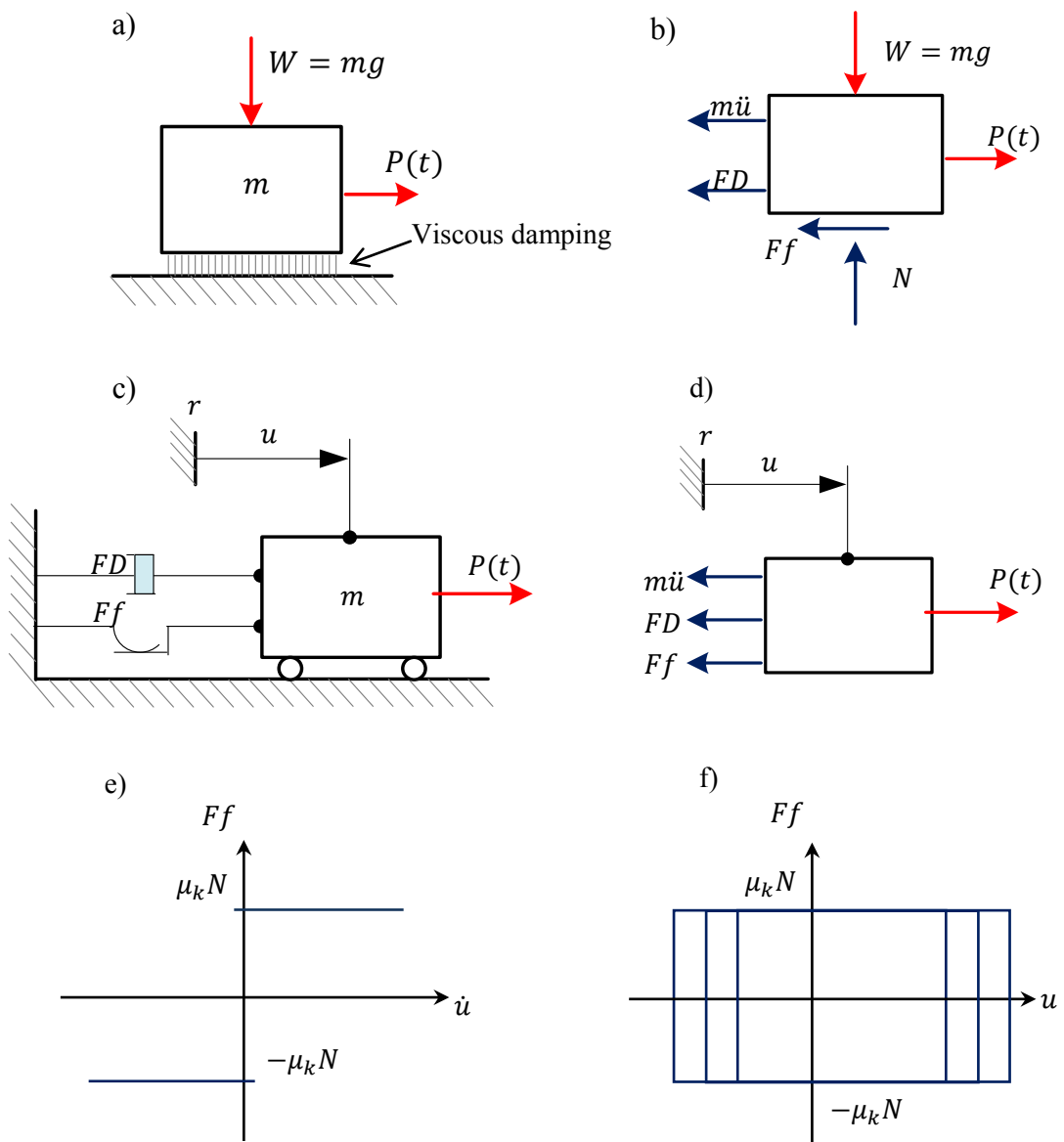
Figure 2.19 Sliding block behaviour: a) Actual system: b) Restoring and external forces; c) Equivalent SDOF system; d) FBD of the Equivalent system (components along u only); e) Coulomb's dry friction model; f) Typical Coulomb's friction hysteresis loops.

As mentioned before, the friction force developed within the surfaces in contact after the relative motion is initiated $(\pm\mu_K N)$ has a reduced magnitude than that on the verge of sliding $(\pm\mu_s N)$. Although this difference doesn't produce an additional discontinuity, experimental results reported by Bondonet and Filiatrault (1997), Sextro (2002), (Lukkunaprasit et al. (2004) have shown that this change from μ_s to μ_K follows a transition curve, sharper when the relative velocity approaches to zero, and then smoother when $|du/dt|$ increases, as illustrated in Figure 2.13a. In general, the measured friction force developed on the sliding segment (namely kinetic friction force) shows fluctuations which depend on the material, finishing, temperature, etc. However, as showed by A. Pall (1979) and Bondonet and Filiatrault (1997) the kinetic friction coefficient might attain a stable value for specific materials.
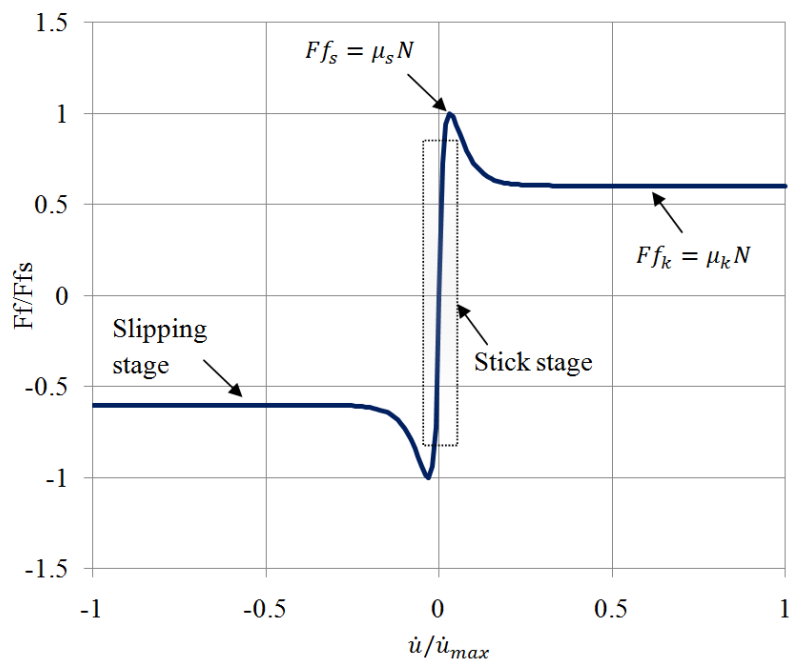
Figure 2.20 The stick-slip phase of a friction model (according to Roberts & Spanos 1990)

Accordingly, a more realistic friction model might be defined by a smooth function able to approximate the transition between the stick-slip stages shown in Figure 2.20.

An alternative is to replace the signum function in Equation (2.5) by other, whose derivatives are specially defined at the point of zero relative velocity in order to account for the stick-slip transition stage. For instance, Figure 2.21 shows the models proposed by Sextro (2002) and Makkar et al. (2005), where they used the *(2/π)arctan(.)* and the *tanh(.)* functions to smooth the transition between stick-slip and slip stages. For considering the decay from the static to kinetic coefficient of friction, the *exp(.)* and the *tanh(.)* functions are introduced by Sextro (2002) in Equation (2.6) and Makkar et al. (2005) in Equation (2.7) as shown below:

$$Ff = \left[\mu_k + (\mu_s - \mu_k)e^{-\lambda_e|\dot{u}|}\right]\left[\frac{2}{\pi}\right]arctan(k_S\,\dot{u}) \tag{2.6}$$

where λ_e controls the decay of the difference between μ_S and μ_K, while k_S defines the sharpness of the slope for fitting the signum function.

$$Ff = \gamma_1[tanh(\gamma_2\dot{u}) - tanh(\gamma_3\dot{u})] + \gamma_4 tanh(\gamma_5\dot{u}) \tag{2.7}$$

Accordingly to Makkar et al. proposal, the first part of Eq. (2.7) controls the transition between μ_S and μ_K, while the second part (last term) defines the behavior during the slipping stage after the first part vanished, hence $\mu_K \approx \gamma_4$. Parameters γ_2, γ_3 and γ_5 define the slope of the hyperbolic function.
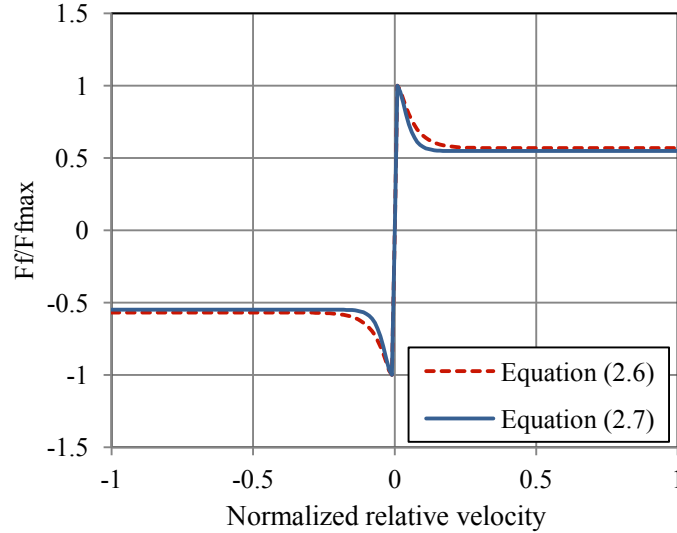
Figure 2.21 Models with smooth transitions within μ_S and μ_K (according to Sextro 2002 and Makkar et al. 2005)

It is clear that the transition between stages produces peak values in the friction force which strongly depend on the change of velocity sign. For some devices using friction as mean of energy dissipation might introduce additional vibrations due to the finishing process of their surfaces and lining pad material (Christopoullos and Filiatrault 2006). However, A. Pall (1979) showed that using brake lining pads (heavy-duty) in contact with mill scale surface on plates, the jump in the measured friction force is reduced and a smooth transition from static to kinematic followed by a stable value of friction force at slipping was observed, which is in agreement with Equation 2.5. Hence, if the slip distance is not exceeded, the principal source of nonlinearity remains the smooth stick-slip transition stage governed by Equation (2.5), while neglecting the transition introduced by Eqns. (2.6) and (2.7). Thus, the smooth hysteresis Bouc-Wen model improved by Baber and Noori is used hereinafter...

2.3.2 Smooth Hysteresis Representation: Bouc-Wen-Baber-Noori (BWBN) Model:

As discussed in the previous sections, the highly nonlinear behavior involved in the cyclic response of friction devices, requires the use of hysteresis models able to simulate smoothly the sharp and sudden changes within stages. Therefore, models with continuous variation of stiffness are suitable alternatives for describing the hysteresis cycles (Sivaselvan and Reinhorn 2000). The smooth hysteresis model (SHM) described herein is based on the modified version proposed by Wen (1980) of the strong-nonlinear oscillator model developed by Bouc (1967), in order to consider the nonlinear hysteretic behaviour exerted by structural members. A detailed survey about the use and modifications of this SHM was conducted by Ismail et al. (2009); Ikhouane et al. (2007).
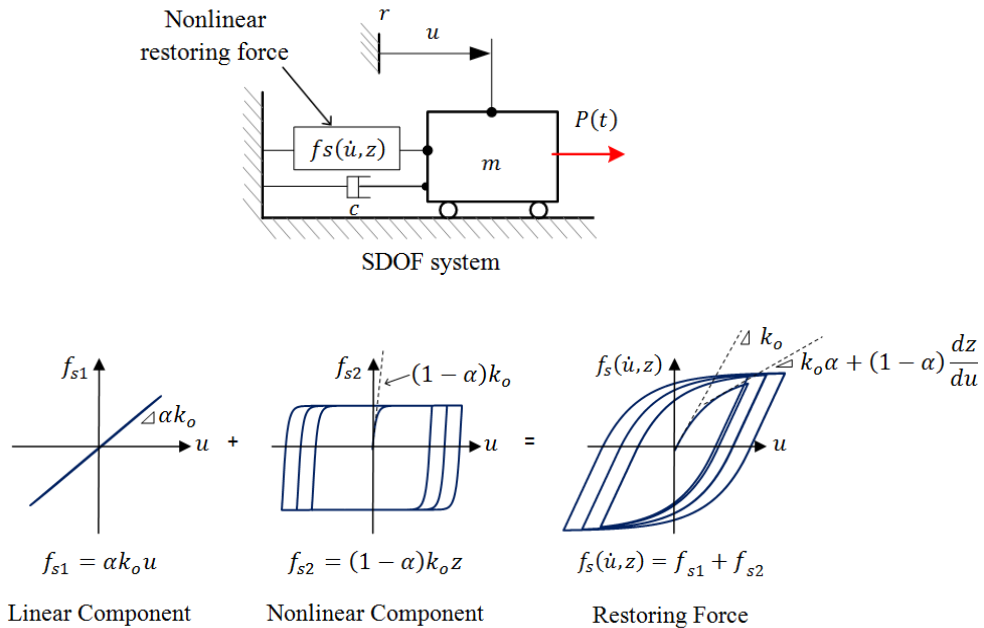
Figure 2.22 Components of nonlinear restoring force represented by the BWBN model.

The SHM has its roots in the endochronic theory and evolves according to the differential formulation of the hysteresis influenced by the evolutionary variable z with memory of the past cycles. The model has the ability to represent different hysteresis shapes according to the values of the parameters involved. In order to extend its modeling capabilities to more complex, but realistic, hysteretic systems, in 1981, Baber introduced the effect of degradation in strength and stiffness and in 1985 Baber and Noori added the pinching function. Later on, Foliente (1993) and Heine (2001) changed the pinching function for including an initial slack observed in some wood connections. Meanwhile Dobson et al. (1997) and Song and Der Kiureghian (2006) proposed major modifications in the differential formulation of the hysteresis variable to account for asymmetric shapes of the hysteresis cycles. Since the desired shape of the Coulomb dry friction law is symmetric, the model proposed by Bouc and Wen (1980) is employed hereafter and is referred as BWBN model although the variable added by Baber and Noori are not used in this study.

In general terms, the BWBN can be assimilated to a single degree of freedom (SDOF) oscillator of mass m, inherent damping ξ_o, circular frequency of vibration ω_o and a nonlinear restoring force f_s as shown in Figure 2.22, from where the equation of motion under the external loading $P(t)$ may be described as follows:

$$\ddot{u} + 2\xi_o\omega_o\dot{u} + (1/m)fs(\dot{u}, z) = (1/m)P(t) \qquad (2.8)$$

where $\dot{u}$ and $\ddot{u}$ account for the first and second derivative with respect to time.

The nonlinear restoring force *fs* defines the hysteretic behavior of the SDOF system and has two components: the first one is the linear part representing the participation level of the initial stiffness into the inelastic response of the oscillator, whereas the later accounts on the nonlinear hysteretic characteristic with memory of previous loading cycles by means of the evolutionary variable z. Hence, the restoring force *fs* can be written as:

$$fs(\dot{u}, z) = \alpha k_o u + (1 - \alpha) k_o z \tag{2.9}$$

where α is the participation ratio of the initial stiffness in the nonlinear response, k_o is the initial stiffness of the system, u is the displacement of the SDOF system and z is the hysteresis variable, evolving according to the nonlinear ordinary differential equation:

$$\dot{z} = h(z) \left[\frac{A\dot{u} - v(\beta|\dot{u}||z|^{n-1}z + \gamma\dot{u}|z|^n)}{\eta} \right] \tag{2.10}$$

Thus, in equation (2.10), γ and β are parameters controlling the shape of the hysteresis cycle and the exponent n influences the sharpness of the model in the transition zones. Meanwhile *h(z)* is a function controlling the pinching (if required) of the hysteresis loops and the remaining parameters *A, v* and η control the degradation process in stiffness and strength. Depending upon the memory of past cycles, i.e. the hysteretic energy accumulated up to the actual time, the degradation process is introduced into the hysteretic response by the following expressions:

$$A = A_o - \delta_A \varepsilon(t) \tag{2.11}$$

$$v = 1 + \delta_v \varepsilon(t) \tag{2.12}$$

$$\eta = 1 + \delta_\eta \varepsilon(t) \tag{2.13}$$

Therefore equation (2.11) induces both strength and stiffness degradation whilst equation (2.12) influences the strength and equation (2.13) the stiffness degradation process. The term $\varepsilon(t)$ is the hysteretic energy up to the specified time tf, defined by (Foliente 1993):

$$\varepsilon(t) = \int_{uo}^{uf} fs(\dot{u}, z)du = (1 - \alpha)(k_o/m) \int_{to}^{tf} z\dot{u}dt \tag{2.14}$$

If $\varepsilon(t)$ is written in rate form it becomes:

$$\dot{\varepsilon}(t) = z\dot{u} \tag{2.15}$$

On the other hand, the pinching process is controlled by function given in Equation (2.16) where ζ_1 and ζ_2 are parameters dependent on the energy dissipated and the desired drop in the slope. A detailed explanation may be found in literature (Foliente 1993).

$$h(z) = 1 - \zeta_1 exp[-(z/\zeta_2)^2] \tag{2.16}$$

The case of no pinching effects, neither stiffness nor strength degradation in the hysteretic behavior is defined by setting up the terms δ_A, δ_v, δ_η, and ζ_1 equal to zero. Thus, equations (2.11) to (2.13) and equation (2.16) are simplified as follows:

$$A = A_o \tag{2.17}$$

$$v = 1 \tag{2.18}$$

$$\eta = 1 \tag{2.19}$$

$$h(z) = 1 \qquad\qquad (2.20)$$

Based on experimental data reported for friction devices, in this work it is assumed that no degradation or pinching effects are presented during the slipping stage. Although Lukkunaprasit et al. (2004) has shown that in case of bolt impact there is a reduction in the slip load for the following cycles, this issue is outside the scope of this thesis.

Therefore, the friction force is simulated by the BWBN model defined by the set of Equations (2.9), (2.10) and (2.17) to (2.20). Through the survey made in this chapter concerning the practical application and behaviour of friction dampers incorporated in building structures (the EDR device is excepted), it is concluded that an accurate non-linear behavior of these devices could be simulated when all stages encountered during the cyclic loading (stick-slip, slipping and slip-lock) are considered.

CHAPTER 3

Behaviour and Simulation of Friction Devices

The objective of this chapter is to propose a hysteresis model able to simulate the behaviour of friction device during cyclic loading, by means of considering the gradual transition at the vicinity of sharp changes in slope within different phases of the behaviour. The computer model developed herein, doesn't account degradation during sliding, if any, since there are not experimental test results reported to calibrate the model. However, employing earlier experimental studies reported by Pall in literature, a comparison is made with the backbone curve representing the friction damper behaviour. The stick-slip phase mentioned by previous researchers is embedded in this model by assigning a set of material objects acting in parallel and playing the role of nonlinear lateral restrainers able to simulate the plastic behaviour during the bearing stage.

3.1 PRAMETRIC STUDY OF THE BOUC-WEN MODEL (A, n, β, γ)

The parameters involved in the Bouc-Wen model influence the shape of the hysteresis response. Thus, tuning the hysteresis response parameters in accordance with the frame system behaviour, is an important issue addressed by several researchers (Baber and Noori 1985, Foliente 1993, Haukaas and Der Kiureghian 2004, Song and Der Kiureghian 2006). However to simulate the inelastic behaviour of friction dampers based on the Bouc-Wen (BW) model a parameter study regarding the hysteresis shape is

required to be conducted. In this regard, the main findings of Foliente (1993) and Song and and Der Kiureghian (2006) about the influence of parameters embodied into the BW model without pinching of slope in the *z-u* and *dz/du-z/z$_u$* planes are used herein. In addition, the smooth hysteresis model (SHM) is mostly restrained to the initial Bouc-Wen model because pinching as well as degradation of strength and stiffness are not considered Thus, in this work, the function controlling pinching is set *h(z) = 1,* as well as the parameters controlling degradation $\nu = \eta = 1$. Because the available uniaxial material available in OpenSees library is labelled BWBN, in the following text we will refers as Bouc-Wen material.The BWBN hysteresis model is defined by the nonlinear restoring force with hysteresis as per Equations (2.9) and (2.10). Multiplying the right hand side of Equation (2.10) by $\dot{u}/\dot{u}$, using the properties of the abs(.) function and replacing Equation (2.20), the differential equation may be re-written as

$$\dot{z} = \dot{u}\left[\frac{A - |z|^n(\gamma + \beta sgn(\dot{u}z))\nu}{\eta}\right] \qquad (3.1)$$

The expression between brackets represents the inelastic behaviour and is a function of velocity, $\dot{u}$ and the variable *z*. This expression, given in Equation (3.2) is labelled the shape control function. Then, Equation (3.3) results by replacing (3.2) in Equation (3.1):

$$\psi(\dot{u}, z) = \gamma + \beta sgn(\dot{u}z) \qquad (3.2)$$

$$\dot{z} = \dot{u}\left[\frac{A - |z|^n\psi(\dot{u}, z)\nu}{\eta}\right] \qquad (3.3)$$

Multiplying both sides of Equation (3.3) by dt/du, recalling that $\dot{z} = dz/dt$ and $\dot{u} = du/dt$, the slope in the *z-u* is given below:

42

$$\frac{dz}{du} = \frac{A - |z|^n \psi(\dot{u}, z)v}{\eta} \tag{3.4}$$

Since the relationship between the response in the f_s–u plane (nonlinear restoring force - displacement) and z-u plane (hysteresis variable - displacement) is provided by Equation (2.9), the current tangent of the loading-displacement curve namely k_n^t can be calculated by the derivative of the former function given in (Eq. 2.9) with respect to u.

$$k_n^t = \frac{\partial fs(\dot{u}, z)}{\partial u} = \alpha k_o + (1 - \alpha)k_o \frac{\partial z}{\partial u} \tag{3.5}$$

Thus at the beginning of the motion (t = 0.0 s) the initial stiffness is

$$k_{n=0}^t = \alpha k_o + (1 - \alpha)k_o A_o \tag{3.6}$$

Note that by choosing $A_o = 1$, the tangent stiffness becomes equal to the initial stiffness of the system $k_{n=0}^t = k_o$. On the other hand, the shape of hysteresis cycles depends on the sign of z and $\dot{u}$ due to the action of function $\psi(\dot{u}, z)$ at each state such as loading (both $\dot{u}$ and z have equal signs), or unloading ($\dot{u}$ and z have opposite signs). As discussed in section 2.3.2, the decreasing rate of stiffness and strength dependents on parameters v, η and the response history. In this regard, Figure 3.1 and Table 3.1 show a breakdown of the shape-control functions which affect the hysteresis response given on the z-u plane for possible values of velocity and the memory variable z during each stage. By considering the shape of the full hysteresis cycle to pass through the points a, b, c and d, is observed that the hysteresis loop is defined by four distinguee phases controlled by the sign of $\dot{u}$ and z. In addition, parameters γ and β given in Equation (3.2) control the shape of the hysteresis loop and are shown in Figure 3.1. Thus, between a-b and c-d the value of the shape-control function is *(γ+β)*, while between b-c and d-a is *(γ-β)*.

Additionally, mathematical expressions defining the tangent stiffness in the z-u plane are provided. All these information can be transformed to the actual restoring force-displacement (f_s–u) scenario by using the mapping functions defined by the Equations (2.9) and (3.4). For friction force simulation is important to bind the response, for example to connect the evolutionary variable z to a threshold value defined by the slip load. In this aim, the maximum value of z (z_u), is derived from Equation (3.4) knowing that the variable attains its maximum value when $dz/du=0$. At this point, the sign of the evolutionary variable z and the velocity of the system have the same sign, which implies that z_u occurs during the loading stage which yields to:

$$|z_u|^n(\gamma + \beta)v = A \rightarrow z_u{}^n sgn(z_u)^n(\gamma + \beta)v = A \rightarrow z_u = \pm\left[\frac{A}{v(\gamma + \beta)}\right]^{1/n} \qquad (3.7)$$

This Equation (3.7) is used later to set up the activation force of the friction device (slip load). Thus the maximum value of the variable z depends also on the A parameter which can be negative, zero or positive, respectively. In addition, parameters A and n control the scale and sharpness of the hysteresis loop.
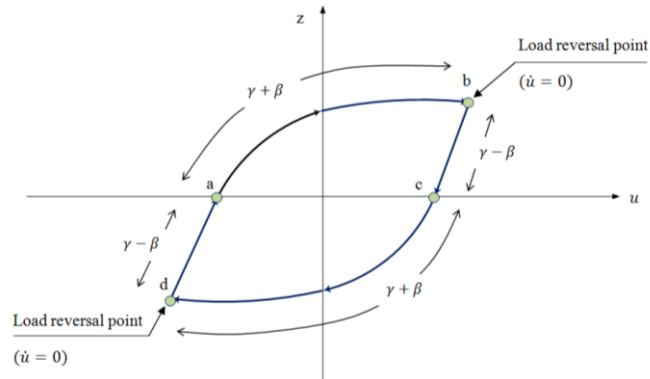
Figure 3.1 Plane z-u: behaviour of the shape control functions $\psi(\dot{u}, z)$ (according to Song and Der Kiureghian 2006)

Accordingly to Foliente (1993), Haukaas and Der Kiureghian (2004), and Song and Der Kiureghian (2006) a summary of shape- control functions $\psi(\dot{u},z)$ and tangent stiffness (dz/du) in the z-u plane is given in Table 3.1.

Table 3.1 Summary of shape control functions $\psi(\dot{u},z)$ and tangent stiffness (dz/du) in the z-u plane

Stage	Description	$sgn(\dot{u})$	$sgn(z)$	$\psi(\dot{u},z)$	dz/du
a-b	Loading in tension	+1	+1	$\gamma + \beta$	$\dfrac{A - |z|^n(\gamma + \beta)v}{\eta}$
b-c	Unloading	-1	+1	$\gamma - \beta$	$\dfrac{A - |z|^n(\gamma - \beta)v}{\eta}$
c-d	Loading in compression	-1	-1	$\gamma + \beta$	$\dfrac{A - |z|^n(\gamma + \beta)v}{\eta}$
d-a	Unloading	+1	-1	$\gamma - \beta$	$\dfrac{A - |z|^n(\gamma - \beta)v}{\eta}$

As mentioned before, the SHM may simulate cyclic responses with different signatures such as softening, hardening or linear behavior in the loading-unloading stages according to the value of parameters involved, resulting in completely different hysteretic behaviours for the same system. For instance, Figure 3.2 shows two different hysteresis shapes (without consideration of degradation) as potential responses of an SDOF system. In this case, the nonlinear restoring force is characterized by the SHM defining by Equations (2.9) and (3.3). For both cases, the mechanical properties (mass, stiffness) and external loading were kept the same and only parameters γ, β and n were changed from 1.5 to 1 for the ratio of β/γ and from 1 to 1.2 for n. As it can be seen from the normalized hysteresis responses, the variation in force and displacement is not considerable but the shape of hysteresis cycles is largely affected.
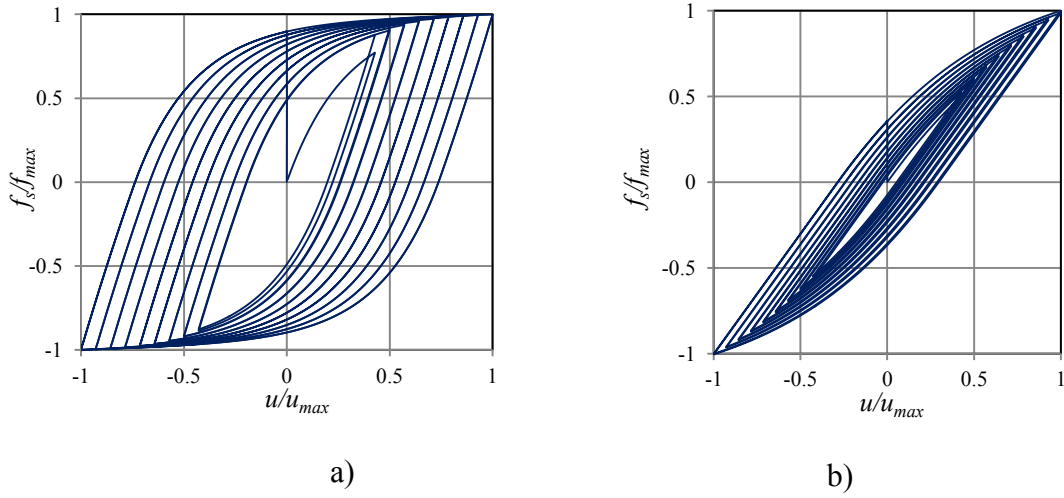
Figure 3.2 Hysteretic response of a SDOF system simulated with the BWBN model. ($Ao = 1$, $\delta_A = \delta_v = \delta_\eta = 0$. a) $\beta/\gamma=1.5$, $n=1$, $v=1$, $\eta=1$ and b) $\beta/\gamma=1$, $n=1.2$, $v=1$, $\eta=1$)

Since the shape of each cycle is related to the tangent at each point, (Baber and Noori 1985) has established the dependency of the tangent stiffness on the hysteresis cycles through the shape control function $\psi(\dot{u}, z)$ equal to $(\gamma+\beta)$ for the loading phase and to $(\gamma-\beta)$ for the unloading phase. In this regard by considering data provided in Table 3.1 and given numerical values to the $\psi(\dot{u}, z)$ function a better insight of the slope variation dz/du in the z-u plane is emphasised in Figure 3.3 To capture the trend of the tangent stiffness, the "flow" of dz/du is shown in the plane z-u by normalising the z and u variables with respect to their maximum values z_u and $umax$. If in the Equation (3.4) the parameters v and η are equal to 1 and at the limit $z = u = 0$, the slope $dz/du = A$. Thus it means that the parameter $A = Ao$ sets the initial tangent stiffness.

Regarding to the general behaviour which is divided in four phases (2 loading and 2 unloading), the following conclusions are noted:

- Loading phase where $\dot{u}$ and z have the same sign:

  When $\psi(\dot{u}, z) > 0$: the slope dz/du is reduced gradually from A_o at a rate of $\psi(\dot{u}, z) = \gamma + \beta$. It leads to a softening effect (see Figure 3.3a).

  When $\psi(\dot{u}, z) = 0$: the slope dz/du is constant to A_o, being equal to 45° for A_o=1. The response is linear (see Figure 3.3b).

  When $\psi(\dot{u}, z) < 0$: the slope dz/du is increased gradually from A_o at a rate of $\psi(\dot{u}, z) = \gamma + \beta$. It leads to a hardening effect (see Figure 3.3c).

- Unloading stages where $\dot{u}$ and z have opposite sign:

  When $\psi(\dot{u}, z) > 0$: the slope dz/du is reduced gradually, starting at the load reversal point at a rate of $\psi(\dot{u}, z) = \gamma - \beta$. It leads to a softening effect (see Figure 3.3f).

  When $\psi(\dot{u}, z) = 0$: the slope dz/du is constant. It leads to a linear response (see Figure 3.3e).

  When $\psi(\dot{u}, z) < 0$: the slope dz/du is increased gradually, starting at the load reversal point at a rate of $\psi(\dot{u}, z) = \gamma - \beta$. It leads to a hardening effect (see Figure 3.3d).

Loading Stages	Unloading Stages
$dz/du = A_o - |z|^n(\gamma + \beta)$	$dz/du = A_o - |z|^n(\gamma - \beta)$
(it is considered $n = 1$)	(it is considered $n = 1$)

a) $\gamma + \beta > 0$

d) $\gamma - \beta < 0$

b) $\gamma + \beta = 0$

e) $\gamma - \beta = 0$

c) $\gamma + \beta < 0$

f) $\gamma - \beta > 0$
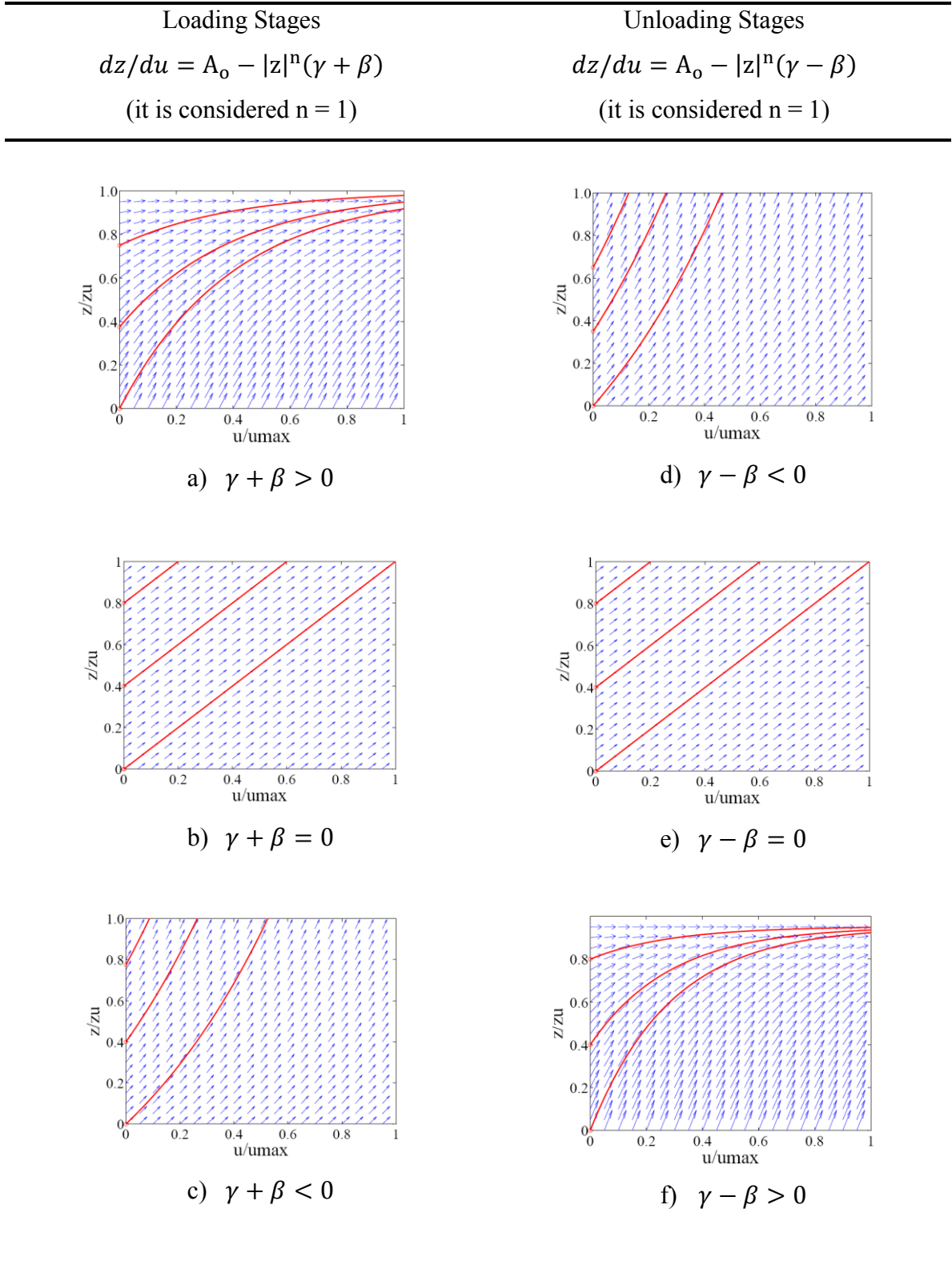
Figure 3.3 Direction fields showing the tendency of the tangent stiffness dz/du for a non-degrading and non-pinching BWBN model in the particular case when $A_o = 1$ and $n = 1$

The effect of the parameter "exponent n" on the hysteresis response is illustrated in Figure 3.4. Thus, as n increases, a smooth model is obtained which approaches to the elasto-plastic behaviour and better approximates the sharp transition zone.

However, for approximating the bounded value of the variable z in the z-u plane as per Equation (3.7) without degradation, beside increasing parameter n it is necessary to set parameters γ and β which are sensitive to the units. Regarding this, Figure 3.4 shows one quarter of the hysteresis loop plotted for $n = 0.5, 1, 3, 5, 10$ and 15; A = 1 and $\beta = \gamma$ as per Equation (3.12) from where it is clear that when using meters (m) as the basic unit for distance, γ and β increases dramatically since for the systems of interest, i.e. braces with in-line friction dampers the slipping distance u is usually below 100mm, while 1mm $<< u_y <<$ 1m and as consequence, for these parameters the order of magnitude is increased by 10^3. In contrast, when the unit used is millimetre (mm) γ and β shall be decreased with slower variation as n grows than in the previous case. In light of this, Heine (2001) recommended the use of millimetre (mm) and (kN) as the basic units for displacement and force in order to reduce computational time and numerical problems. For the braces with in-line friction dampers, the slip forces used are lower than 500kN and the total displacements are below 100mm before the capacity considered is reached as shown in Chapter 5, therefore these units are used herein for the SHM.

On the other hand, Figure 3.4 shows that a value of n in the interval 5 to 10 provides a good approximation without resorting to higher values.
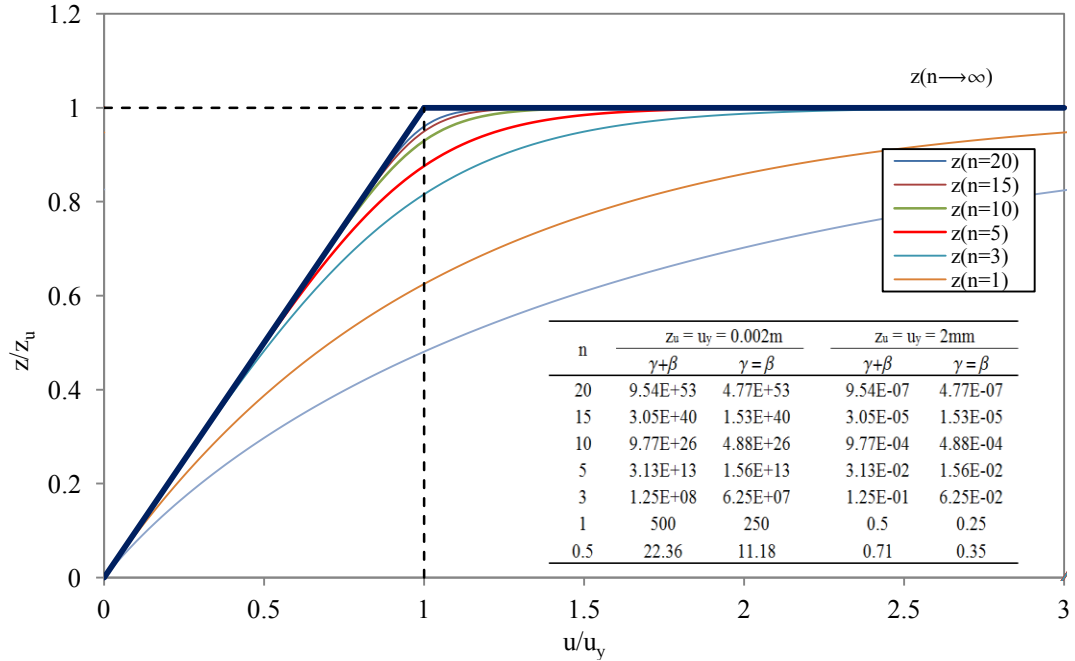
Figure 3.4 Variation of exponent n (loading stage) in the z-u plane to define a smooth curve instead of the bilinear curve (bold line)

The results of Baber and Noori (1985) and Foliente (1993) related to the approximate yielding point are adapted here for defining the thresholds forces for a given friction damper. Consider the case of a SDOF system shown in Figure 3.5. This system is characterized by a restoring force $fs(\dot{u}, z)$ as defined in Equations (2.9) and (3.3) which has a linear and a non-linear component. For non-degrading conditions the control parameters are: $\eta = \nu = 1$ and $A = A_o$. Knowing that the evolutionary variable z is bounded by the Equation (3.7) and the initial stiffness in the z-u plane can be derived from Equation (3.6), the displacement u_y at which the maximum value of z (z_u) intersects the tangent of the response (initial stiffness) as shown in Figure 3.5 is expressed as:

$$u_y = \frac{z_u}{A_o} \rightarrow u_y = \frac{1}{A_o}\left[\frac{A_o}{\gamma + \beta}\right]^{1/n} \tag{3.8}$$
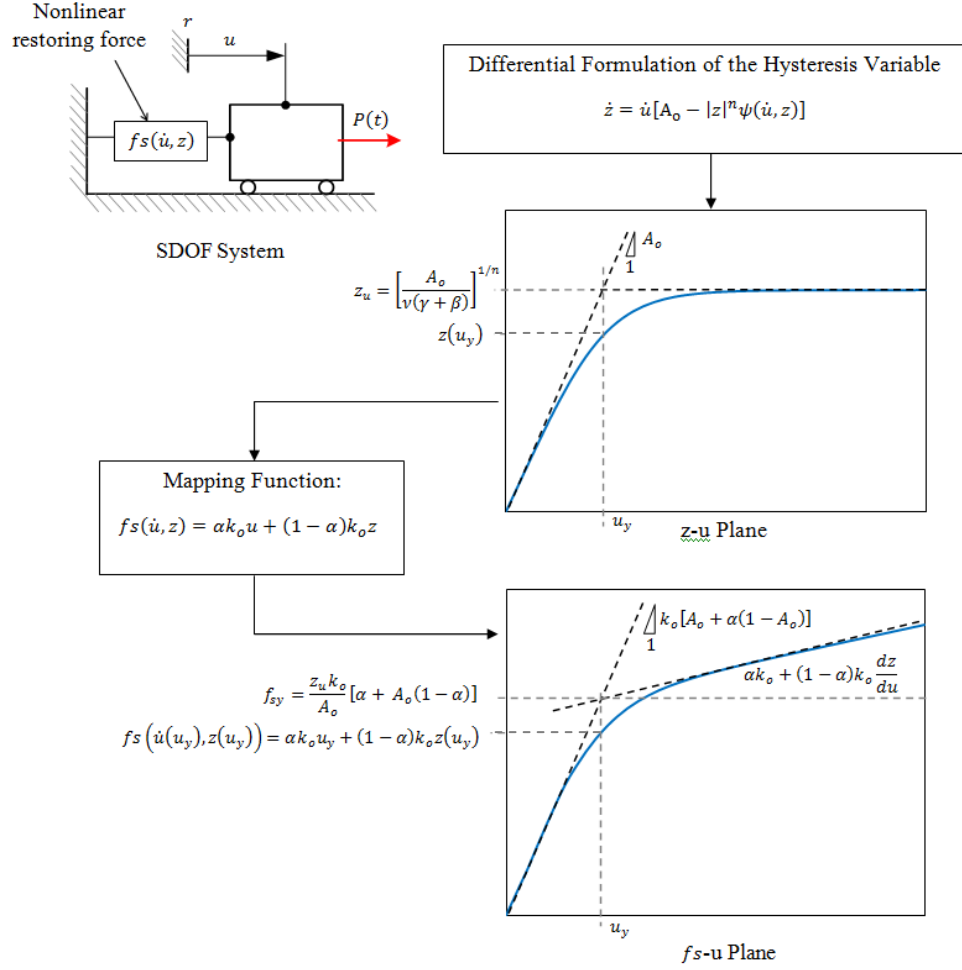
Figure 3.5 Correspondence between *z-u* and f_s-*u* planes (according to Foliente 1993)

In Equation (3.8) for a non-degrading system $v = 1$. Hence, for the mapping function given by Equation (2.9), the restoring force at the level of yielding displacement (u_y) obtained from the *z-u* plane ($u_y = z_u/A_o$) is:

$$f_{sy} = \frac{z_u k_o}{A_o}[\alpha + A_o(1 - \alpha)] \tag{3.9}$$

Replacing *u* by u_y in Equation (2.9) yields to

$$f_s\left(\dot{u}(u_y), z(u_y)\right) = \alpha k_o u_y + (1 - \alpha)k_o z(u_y) \tag{3.10}$$

51

Therefore, when comparing the two Equations (3.9) and (3.10) it is evident that Equation (3.9) overestimates the yielding force by an amount depending on the difference between the SHM curve and the bilinear curve (backbone curve).

Herein, the displacement at yield, u_y, is defined as being the location where the horizontal line of force, f_{sy}, crosses the intersection of the two tangents plotted at the load displacement curve (initial segment and non-linear segment) as shown in Figure 3.5. The tangent for the non-linear segment is defined by Equation (3.4) (i.e. $|u| > u_y$) and for the initial segment (initial stiffness) by Equation (3.6). Thus for a given initial stiffness and set of parameters, Equations (3.8) and (3.9) retrieve the yielding displacement and yielding force accordingly to the backbone curve. The yielding force of the SHM which initiates the displacement at yield is given by Equation (3.10). This force leads to an approximation shifted by an amount equal to the difference between the values obtained from Equations (3.9) and (3.10). Nevertheless, it is more convenient for the application purposes to give the mechanical properties of a system and then to retrieve the set of characteristic parameters, since the later are the unknown values usually. Solving Equation (3.8) for $\gamma + \beta$ yields to:

$$\gamma + \beta = A_o \left[\frac{1}{u_y A_o} \right]^n \tag{3.11}$$

where the yielding displacement can be determined by using the actual yielding force of the system ($f_{sy}{}^*$) and Equation (3.9). Choosing $A_o = 1$ for the case when the initial stiffness of the hysteresis cycle is equal to the stiffness of the system in the elastic range, the previous equations are reduced to:

$$\gamma + \beta = \frac{1}{u_y{}^n} \tag{3.12}$$

$$u_y = \frac{f_{sy}{}^*}{k_o} \tag{3.13}$$

From Equations (3.12) and (3.13), parameters γ and β may be adjusted in accordance with the physical properties of the system ($f_{sy}{}^*$ and k_o), the smoothness level at transition zones (n), and the tendency of the tangent stiffness during the loading and unloading stages as depicted in Figure 3.3.

Two arbitrary SDOF systems labelled specimens A and B are characterized by the following yielding points and initial stiffness as: specimens 1-A & 1-B: (u_y=1.5mm, f_{sy}=100kN) and f_{sy}/u_y=66.7kN/mm and specimens 2-A & 2-B: (u_y=2.5mm, f_{sy}=200kN) and f_{sy}/u_y=80kN/mm. For specimens A the participation ratio is $\alpha = 0.1$ and for specimens B, $\alpha = 0.001$ as shown in Table 3.2. Herein, α is the ratio of the initial stiffness. The hysteresis shapes are built by varying the parameters γ and β according to the previous procedure. Thus, in this study, SDOF systems with nonlinear restoring forces which are represented by the BWBN model are used. Furthermore, only the loading case with softening effect ($\gamma + \beta > 0$) and the unloading case with linear behavior ($\gamma + \beta = 0$) were taken into account, since the main purpose of using the BWBN model is to reproduce the high nonlinearities of the Coulomb's dry friction law applied to friction dampers (Chapter 2, part 2.3.1).

A quasi-static displacement loading pattern composed of five incremented amplitudes proportional to the target yielding displacement (u_y) such as: *0.5, 0.75, 1.0, 1.5* and *$2u_y$* is shown in Figure 3.6 and was defined with the aim to analyse the response

of the 4 SDOF specimens (1-A; 2-A; 1-B and 2-B) before, near and after the specified yielding condition. For solving each case study, a program in MATLAB was implemented following the procedure developed by Haukaas (2004) with the aim to incorporate the BWBN model without pinching effects into OpenSees framework (open system for earthquake engineering simulation). The algorithm uses an implicit Euler step to solve the incremental form of the hysteresis variable, z, and then applies the iterations of Newton's method in order to approximate the solution of the non-linear equation resulting from the implicit method.
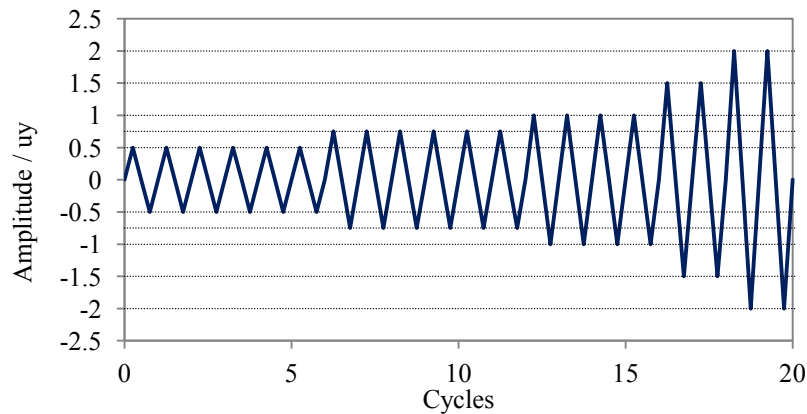
Figure 3.6 Quasi-static displacement loading pattern

Table 3.2 Characteristics of SDOF systems: 1-A; 1-B; 2-A; and 2-B

System	α	f_{sy} [kN]	u_y [mm]	n	System	α	f_{sy} [kN]	u_y [mm]	n
	0.1	100	1.5	1		0.1	200	2.5	1
1-A	0.1	100	1.5	5	2-A	0.1	200	2.5	5
	0.1	100	1.5	10		0.1	200	2.5	10
	0.1	100	1.5	20		0.1	200	2.5	20
	0.001	100	1.5	1		0.001	200	2.5	1
1-B	0.001	100	1.5	5	2-B	0.001	200	2.5	5
	0.001	100	1.5	10		0.001	200	2.5	10
	0.001	100	1.5	20		0.001	200	2.5	20

Table 3.3 summarizes the values of $\gamma + \beta$ used in accordance with the given yielding point illustrated in Table 3.2 and Equations (3.12) and (3.13) and Figure 3.7 shows the hysteresis loops of case 1-B. The hysteresis loops of the remained cases are shown in Appendix A. In addition to the response under the quasi-static displacement loading excitation, each graph has a backbone curve as a bilinear reference system with a hardening ratio equal to α, and passing through the points $\left(-u_y, -f_{sy}\right)$ and $\left(u_y, f_{sy}\right)$ in order to assess the level of approximation achieved with the SHM within the stick-slip stages.

Table 3.3 $\gamma + \beta$ values for different yielding points (u_y, f_{sy})

System	f_{sy} [kN]	u_y [mm]	$\gamma + \beta$			
			n=1	n=5	n=10	n=20
1-A, 1-B	100	1.5	0.6667	0.1317	0.0173	3.01E-4
2-A, 2-B	200	2.5	0.4	0.0102	1.05E-4	1.10E-8
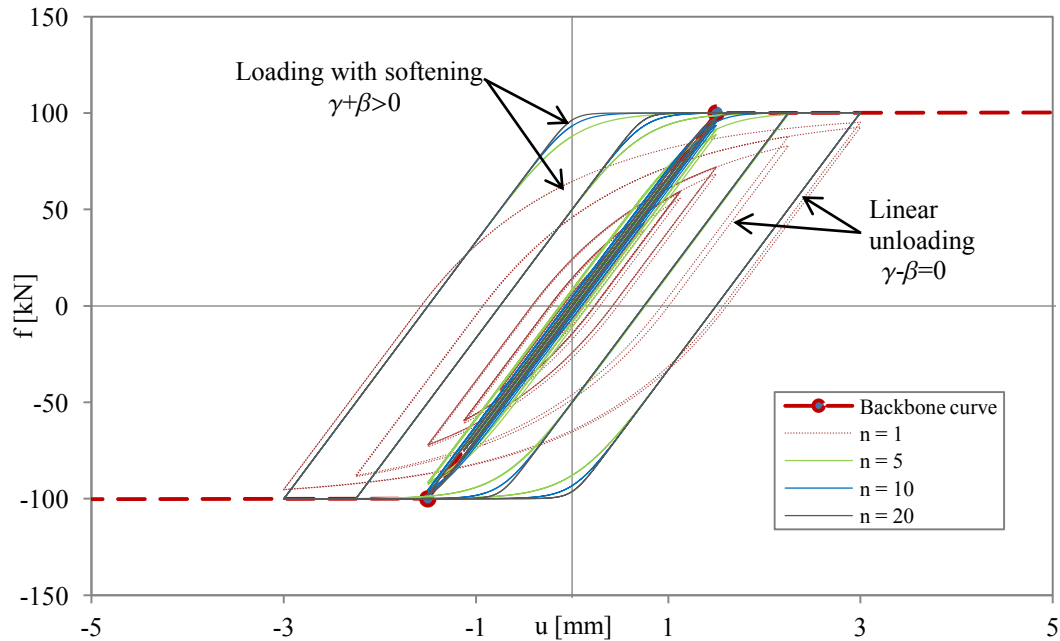
Figure 3.7 Response of SDOF system, case 1-B under the cyclic displacement loading

The absolute value of the relative difference between the hysteresis model and the two tangents defined at the target yielding point $\left(\pm u_y , \pm f_{sy}{}^* \right)$ and shown in Figure 3.5, is calculated as:

$$\% RelDiff = \left| \frac{f_s - f_s{}^o}{f_s{}^o} \right| \tag{3.14}$$

where:

f_s: is the nonlinear restoring force defined by Equations (2.9) and (3.3)

$f_s{}^o$: is the force of the backbone curve given by the following equation:

$$f_s{}^o = \begin{cases} k_o u & ; -u_y \leq u \leq u_y \\ f_{sy}{}^* + \alpha k_o \left(u - u_y \right) & ; u > u_y \\ -f_{sy}{}^* + \alpha k_o \left(u + u_y \right) & ; u < -u_y \end{cases} \tag{3.15}$$

As it can be seen in Table 3.3, $\gamma + \beta$ grows as the parameter n increases and when parameter u_y decreases. This growth is also evidenced in Figure 3.4. The loading and unloading stages (see Figure 3.7) summarize important findings with respect of tuning the BWBN parameters without pinching or degradation. The hysteresis behavior shows that during the loading stages, the nonlinear response follows, with a smooth curve, the tendency given by the bilinear representation when the parameters $\gamma \ and \ \beta$ are defined for a softening behavior in accordance with Equation (3.12) and when $\gamma + \beta$ is positive. In contrast, after the load reversal point, either in tension or compression, is evident that the unloading branch corresponds to a linear behavior if provided that β was chosen equal to γ in order that the condition $\gamma - \beta = 0$ to be satisfied as shown on Figure 3.3.

On the other hand, among the different values of *n* parameter tested in the SDOF systems, the closer response to the backbone curve was given by the higher value *of n = 20*, fitting with a smooth curve the transition zones between the elastic and inelastic response as shown on Figure 3.7. Furthermore, when *n* increases, the relative difference between the response curve and the backbone curve is being reduced largely after the prescribed yielding point was reached (see Figure 3.8). For instance, when *n = 5* the difference drops from *11.7% to 2.5%*, meanwhile for *n = 10, goes from 6.9% to 0.6%* as it can be seen in Figure 3.8a for the quasi-static displacement loading pattern. The approximation level is computed as the difference (*1- the relative difference)* and is

a)

	0.75uy	uy	1.25uy
n = 1	25.7%	31.9%	22.0%
n = 5	3.6%	11.7%	2.9%
n = 10	0.5%	6.9%	0.6%
n = 20	0.02%	4.0%	0.04%

b)
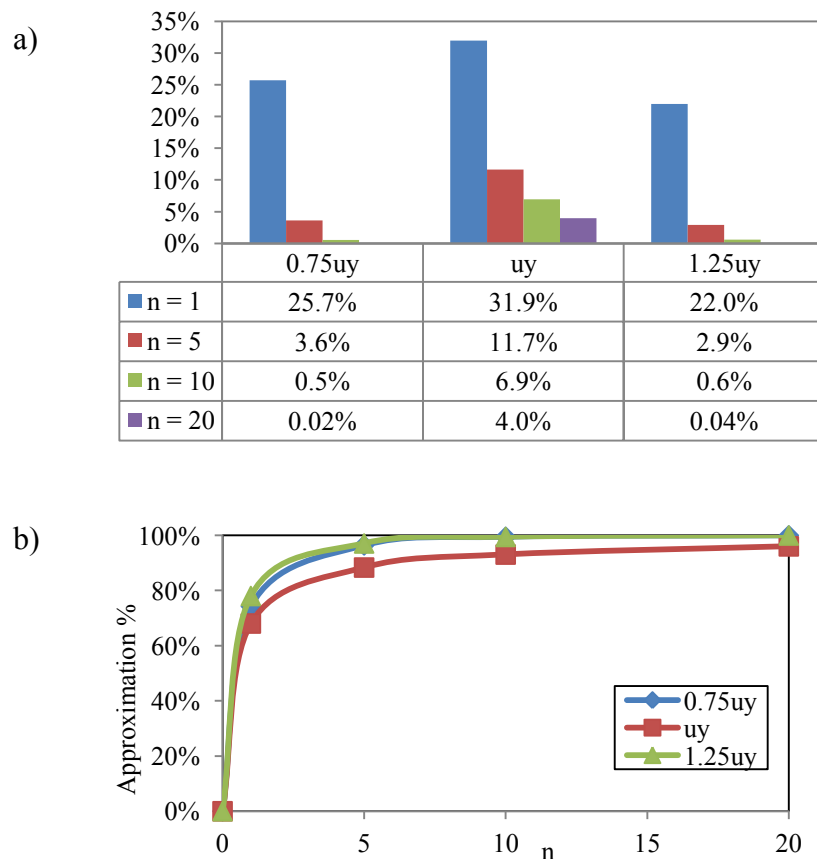
Figure 3.8 Relative difference between the backbone curve and the response of 1-B: a) bar chart; b) curves based on level of approximation

shown for different *n* values in Figure 3.8b. The larger difference in terms of the restoring force happens at the target yielding point. This is a natural consequence of the smooth variable *z* used for the nonlinear response, since this hysteresis model approximates the tangents before and after the transition and estimates the singularity of the derivative at that zone by a smooth function, rather than the specific yielding point.

Among the different values of *n*, the case of *n* = 1 tends to underestimate the restoring force and produce larger displacement when compared with *n* = 5, *n* = 10 and *n* = 20 for the same SDOF system. Hence, using *n*=1 might yield to a flexible behavior, enlarging the period of vibration and reducing the inertial forces, when using the hysteresis model to simulate friction dampers installed in a building structure. This behavior was consequent throughout the 4 case studies analysed (see appendix A).

To reduce the difference between the two curves at the point $u = u_y$ it required an increasing of variable *n* which for MDOF systems might become computationally expensive, because the transient analysis requires the evaluation of $\dot{z}$ at each step for a single element, that in general involves a nonlinear iterative solver (such as Newton's method and its variants). Nevertheless, for using the BWBN model without pinching or degradation, in order to approximate high nonlinearities such as Coulomb's friction law, the value of *n* = *10* gives an acceptable level of prediction because the difference is reduced rapidly throughout the evolution of the post yielding stage.

3.2 HYSTERESIS MODEL WITH SLIP-LOCK EFFECTS

When an applied load is still acting after the friction device has consumed the slipping distance, the postensioned bolts are acting as restrains and may evolve from an initial elastic behavior (bolt impact) to an inelastic stage due to the plastification of slotted holes in bearing or yielding of bolts in shear. As discussed in sections 2.2.1 to 2.2.3, there are not experimental tests conducted for friction devices such as Pall dampers and slotted bolted connections with the aim to investigate the behaviour of the device after the slip limit have been exceeded. However, results based on monotonic tests of limited slip bolted joints reported by Pall (1979) and the cyclic tests performed by Lukkunaprasit et al. (2004), revealed an additional bearing stage of the backbone curve as discussed in Chapter 2.

Since the scope of this work is not to develop a degradation model of the slip force but to provide a hysteresis model able to consider the bearing stage, a set of gap-hook elements without degradation is used to create the slip-lock stage with the aim to represent the transition zone gradually from the bolt impact to failure in bearing or shear. For analysis, a simplified model of friction damper is depicted in Figure 3.9. When no relative motion exists within the two ends of the device, the force in the brace to which the device is attached, F_{br} is:

$$Fbr = 2 \times \left(\frac{Rj}{2}\right) = Rj \qquad (3.16)$$

In words, the axial force transferred from the brace to the device is equal to the reaction of the friction damper support inside the structure. Also is clear that this relation holds if shear, torsional and bending actions are neglected at both ends. It is assumed that

loads are axially transferred throughout the device from the brace to the structure (or vice versa) and there is no appreciable axial deformations in the stationary body of the device (clamping elements), nor deformation due to the contact of the bolts with the inner faces

a)

b)

Section A-A

c)
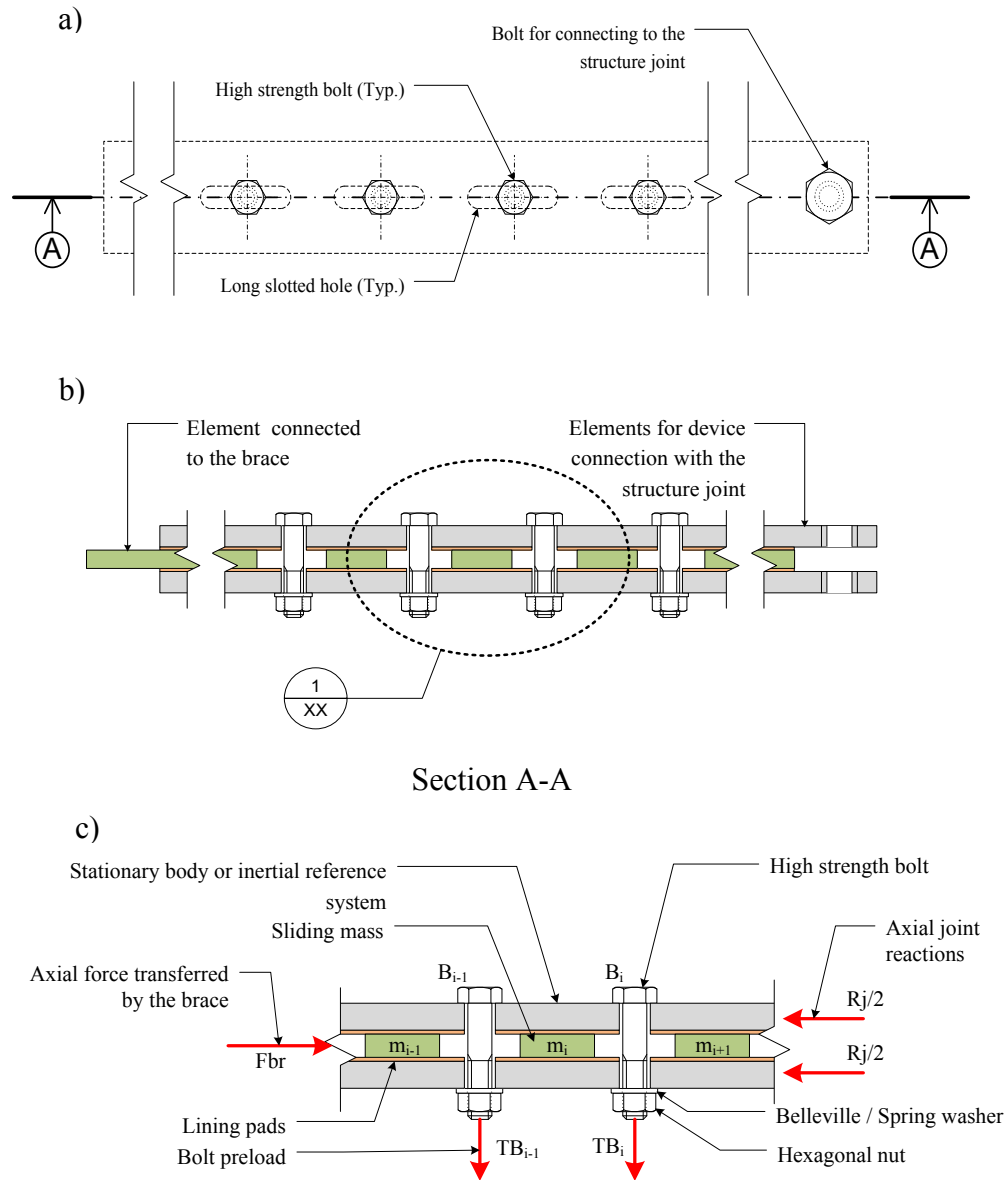
Detail 1

Figure 3.9 Friction device. Schematic arrangement of one row of high strength bolts: a) plan view, b) transversal section of bolts and connected plates c) Detail of the main elements considered in the sliding process

60

along slotted holes. The action of axial load produces interface damping due to the Coulomb dry friction between the sliding mass and the stationary body considered as reference system (Roberts and Spanos 1990). Additionally, temperature dependent effects are neglected. These assumptions allow the main portion of the energy dissipated by the device to be attributed to friction of the sliding mass and to bearing due to the inelastic action of the bolts, when the slip limitation has been reached. Thus, forces developed in a friction device (FD) during the sliding stage are shown in Figure 3.10.
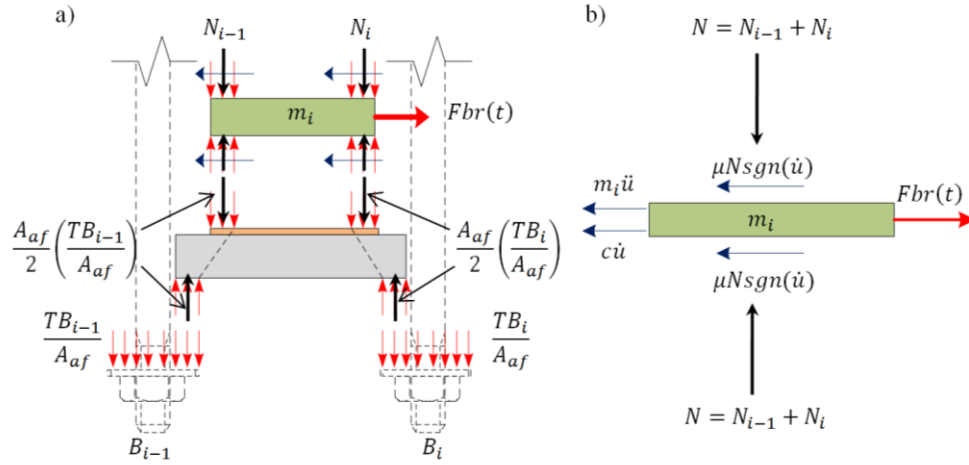
Figure 3.10 Mechanism of sliding mass. a) Forces transferred by the clamping elements, b) FBD of the sliding mass

From the equilibrium of forces shown in Figure 3.10b, and recalling Equation (2.5), the friction force opposing the relative motion of the mass m_i (Ff_i) which is developed on the two sliding planes, can be defined as

$$Ff_i = 2\mu N sgn(\dot{u}) \tag{3.17}$$

By definition, the normal force N, corresponds to the load applied perpendicular to the sliding plane. By assuming that the clamped force transferred by each bolt is equal, i.e. $TB_{i-1} = TB_i = TB$, $N_{i-1} = N_i$, then, Equation (3.17) yields to

$$Ff_i = 2\mu \left[A_{af} \left(\frac{TB_{i-1}}{2A_{af}} \right) + A_{af} \left(\frac{TB_i}{2A_{af}} \right) \right] sgn(\dot{u})$$

$$\rightarrow Ff_i = \mu(TB_{i-1} + TB_i)sgn(\dot{u}) \tag{3.18}$$

$$\rightarrow Ff_i = 2\mu TB sgn(\dot{u})$$

To create the interface between the Equation (3.18) and the BWBN model, used herein to approximate the nonlinearity of the Coulomb's friction the aforementioned equation can be re-written as:

$$Ff_i(\dot{u}, z) = \alpha k_o u + (1 - \alpha)k_o z \tag{3.19}$$

$$u_f = \frac{2\mu TB}{k_o[A_o + \alpha(1 - A_o)]} \tag{3.20}$$

In the above equation, z is the variable evolving from Equation (3.3), u_f is the displacement corresponding to the activation load of the device and coefficient 2 means the number of slip lanes considered. If the velocity is close to zero, then the coefficient of friction, μ, appearing in Equation (3.20) is equal to the static coefficient of friction μ_s. If the motion has already started, then the coefficient of friction attains a stable value $\mu = \mu_k$ as mentioned in section 2.3.1.

After the relative velocity exceeds the critical value and the sliding process has initiated the equation of motion of the sliding mass m_i is given in Equation (3.21) which is in agreement with Figure 3.10b:

$$m_i\ddot{u} + c\dot{u} + Ff_i(\dot{u}, z) = Fbr(t) \tag{3.21}$$

If we consider the total sliding mass $m = \sum m_i$ and the total friction force $Ff\ (\dot{u},z) = \sum Ff_i(\dot{u},z)$ that is developed due to the clamped action produced by the bolts under the assumption of rigid sliding, then Equation (3.21) might be written as:

$$m\ddot{u} + c\dot{u} + Ff(\dot{u},z) + Fsl = Fbr(t) \qquad (3.22)$$

where Fsl is the term to account for the bearing stage and $Ff(\dot{u},z)$ is defined as per Equations (3.19) and (3.20), but using the following variables:

$$Ps = rQ\mu TB \qquad (3.23)$$

Herein, Ps is defined as being the activation load or the slip load of the device, TB is the clamped force transferred by one bolt, while the terms r and Q are the number of slip planes and bolts in the device accordingly. For this given case, r takes the value of 2. Thus, from Equation (3.20), the displacement corresponding to the slip load is:

$$u_f = \frac{Ps}{k_o[A_o + \alpha(1 - A_o)]} \qquad (3.24)$$

Hence, the set of Equations (3.3), (3.19), (3.22), (3.24) and the mechanical system shown in Figure 3.11 (SDOF) are used to simulate he inelastic behaviour of the friction device.
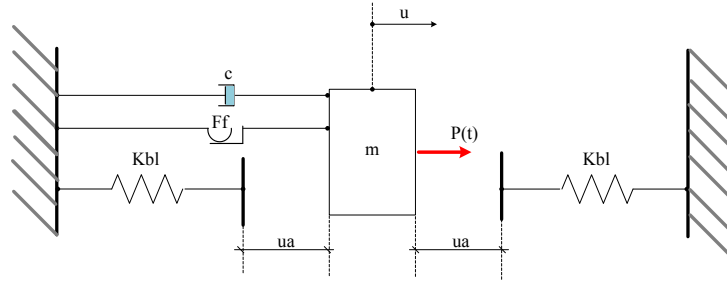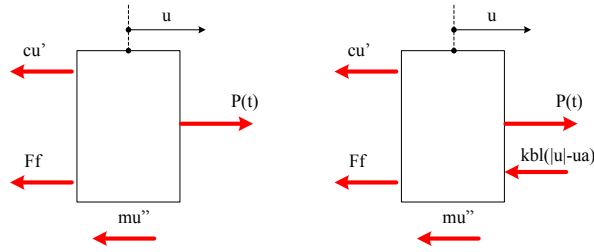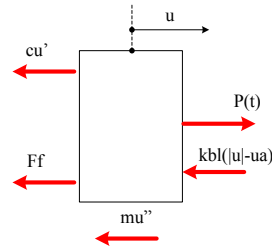
Figure 3.11 Simplified SDOF system with slip-lock simulation: a) SDOF system; b) FD in slipping stage (before the slip distance was reached); c) FD in bearing stage (after reaching the slip distance) (according to Heine 2001).

Thus, for $|u| - ua < 0$:

$$m\ddot{u} + c\dot{u} + Ff(\dot{u}, z) = Fbr(t) \tag{3.25}$$

for $|u| - ua > 0$:

$$m\ddot{u} + c\dot{u} + Ff(\dot{u}, z) + kbl(|u| - ua) = Fbr(t) \tag{3.26}$$

Both cases can be summarized as:

$$m\ddot{u} + c\dot{u} + fs(\dot{u}, z) = Fbr(t) \tag{3.27}$$

where $fs(\dot{u}, z)$ is the nonlinear restoring force defined as:

$$fs(\dot{u}, z) = \begin{cases} Ff(\dot{u}, z) & ; |u| - ua < 0 \\ Ff(\dot{u}, z) + kbl(|u| - ua) & ; |u| - ua > 0 \end{cases} \qquad (3.28)$$

The Equation (3.28) may be regarded as reproducing the action of two nonlinear springs acting in parallel: the first one is active throughout the entire process since simulates the friction law, while the second one is activated during the bearing stage and simulate the slip-lock phase. Both springs are deemed to approximate the backbone curve shown in Figure 3.12.

As stated before, the slip-lock transition phase can be simulated by a set of elements able to provide gradual transition from a point to the other belonging to a curve with sharp changes in the slope during the nonlinear response of the system. Other wards, this set of points is followed when the sliding mass makes contact with the bolt, i.e. the case of $u = u_a$ shown in Figure 3.12. Herein, a transition is considered from $u = u_b$ to $u = u_d$ and accounts on the nonlinear behavior during the bearing stage after the first yielding of the bolt due to bearing was initiated at $u = u_b$.

Consequently, the bearing stage exhibited by the device beyond the slip limit u_a can be characterized by a multi-linear curve shown in Figure 3.12. Thus, in order to build this behavioural curve, the investigator should know the point at which the available slip distance is reached *(u = u_a)*; the yielding point where the behavior changes from elastic to inelastic due to bearing (u_b, f_b), an intermediate point within the plastification process (u_c, f_c) and the threshold point reached before a drop in the force occurred while the displacement is increased (u_d, f_d). These values required to build the load-displacement curve might be recommended from static experimental test conducted upon failure.

In this regard, a set of 6 gap-hook elements was used to approximate the bearing stage when the slip limit is exceeded. Among them, one subset of 3 elements acts only in tension and the other 3 in compression. By splitting the length of the transition zone δu measured after the first yielding point was reached, for springs 1, 2, and 3, the activation displacements for the subset in tension can be defined as: $u_1 = u_2 - \delta u/3$, $u_2 = u_a$ and $u_3 = u_2 + \delta u/3$. The yielding force of these elements is determined from the work in parallel of each subset of springs. Thus, knowing the displacement in the transition zone after yielding due to bearing occurred u_b, u_c, u_d, and the corresponding forces f_b, f_c, f_d, the elastic stiffness can be computed for each bilinear component in the tension side. The post-yielding stiffness ratio (η_i) may be considered as zero or a negative value to account for the drop in the force when the threshold point is reached. The properties for the subset in compression can be defined similarly by assuming a symmetric shape. Thus, in Table 3.4 are summarised the parameters used in the slip-lock model for each one of the six gap-hook elements considered as being perfectly plastic elements.

Since in this research no experimental studies were performed, results from the static test conducted by A. Pall (1979) are adapted here. Thus, for the comparison purpose, the slip-lock model showed in Figure 3.13 is employed. The results reported by Pall and simulated herein correspond to a specimen with two slip planes, one bolt 12.7mm ASTM A325 which clamps two outer plates against a central plate. The central plate has a slotted hole of 14x32mm and the slip distance in each side of the bolt is computed to be 10mm, while the activation force was normalised to 70kN (see Figure 2.3a). The maximum force reported during the experiment was 100kN and the capacity of bolt in shear exceeded 100kN (A. Pall 1979).
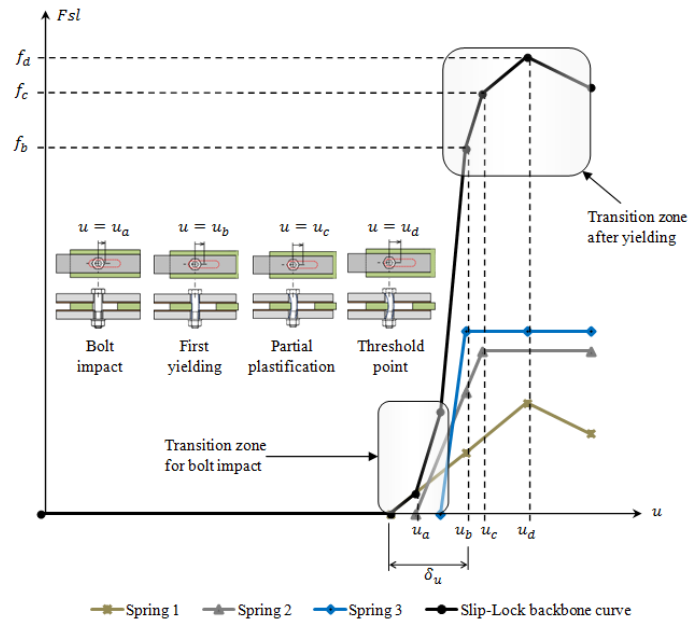
Figure 3.12 Bearing stage in tension, including bolt impact effect and nonlinear behavior after the first yielding of bolts occurred

Table 3.4 Parameters of the slip-lock model Fsl

Element	u_i	k_i	f_i	η_i
1	$u_2 - \delta u/3$	$\dfrac{f_d - f_c}{u_d - u_c}$	$k_1(u_d - u_1)$	$-\eta_o$
2	u_a	$\dfrac{f_d - f_b - k_1(u_d - u_b)}{u_c - u_b}$	$k_2(u_c - u_2)$	0
3	$u_2 + \delta u/3$	$\dfrac{f_d - k_1(u_d - u_1) - k_2(u_c - u_2)}{u_b - u_3}$	$k_3(u_b - u_3)$	0
4	$-(u_2 - \delta u/3)$	$\dfrac{f_d - f_c}{u_d - u_c}$	$-k_1(u_d - u_1)$	$-\eta_o$
5	$-u_a$	$\dfrac{f_d - f_b - k_1(u_d - u_b)}{u_c - u_b}$	$-k_2(u_c - u_2)$	0
6	$-(u_2 + \delta u/3)$	$\dfrac{f_d - k_1(u_d - u_1) - k_2(u_c - u_2)}{u_b - u_3}$	$-k_3(u_b - u_3)$	0

Thus, with the difference between these values, the elastic-plastic curve shown in Figure 3.13 was defined. Computations were done in Excel spreadsheet.
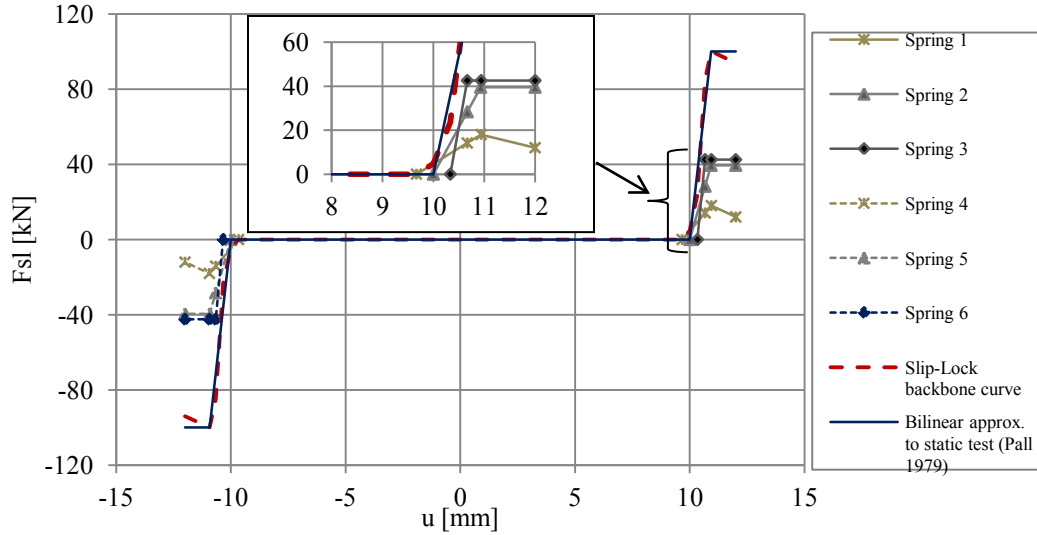
Figure 3.13 Complete slip-lock model. Zoomed portion corresponds to the bolt impact transition at the side in tension. The continuous bold lines are approximating the tendency shown on the static test performed by Pall (1979)

Therefore, the nonlinear restoring force $fs(\dot{u}, z)$ given in Equation (3.27) is defined as a combination composed of the BWBN model $Ff(\dot{u}, z)$ and the slip-lock model Fsl added in parallel. The BWBN model is given by Equations (3.3), (3.19) and (3.24) whereas the slip-lock model is given by the parameters of bilinear gap springs defined in Table 3.4. Thus, for simulating the computer model of a friction device, both components such as the Bouc-Wen model in paralel with the bilinear gap spring model are assigned.

The procedure developed by Roberts and Spanos (1990) to emphasise the hysteresis behaviour of friction devices attached to a structural member is adapted here with the aim to include the stick-slip transition due to the bearing stages. The brace element is assumed to behave elastically even the device may experience excursions into the bearing stage. For example, Figure 3.14a shows a typical system composed of a brace equipped with friction damper installed in a bare frame. Thus, the brace is designed to

68

remain in the elastic range, while the energy is dissipated by the device due to the relative slipping within the sliding plates. In order to slip, the system needs an input load able to overcome the resisting friction force developed in the device due to the clamping action of the high strength bolts. This load is labelled slip force and is the minimum input required to activate the device. The mechanical model of the damped brace is shown in Figure 3.14b where the Bouc-Wen model (elastic component and non-linear spring) is defined in parallel with the slip-lock model. At the beginning of the motion, when the transferred load is lesser than the activation load *Ps*, the device is not slipping (Figure 3.14 c). According to the plane *fs-u* shown in Figure 3.5, the force in spring 2 is equal to $(1 - \alpha)k_o u_e$ where u_e is the excursion of the device before sliding occurred (an infinitesimally value for illustrative purposes). Meanwhile, the force in springs 1 is $\alpha k_o u$ and the force in brace (spring 4) is $(u - u_e)k_{br}$. It should be noted that springs 1 and 4 remain elastic throughout the motion, while spring 3 remains inactive. At this stage, the equivalent stiffness of the system brace equipped with friction device is:

$$k_s = \frac{k_o k_{br}}{k_o + k_{br}} \tag{3.29}$$

As mentioned in section 2.3.1, the elastic stiffness of friction damper k_o has to have a larger value in order to fit the signum function. For a perfect match, it is obvious that $k_o \to \infty$. Therefore at the limit, the numerator and denominator of Equation (3.29), trend to infinity. For this indeterminate form (∞/∞), l'Hopital's rule may be applied which yields to:

$$\lim_{k_o \to \infty} (k_s) = \frac{k_{br}}{1} = k_{br} \to k_s = k_{br} \tag{3.30}$$

69
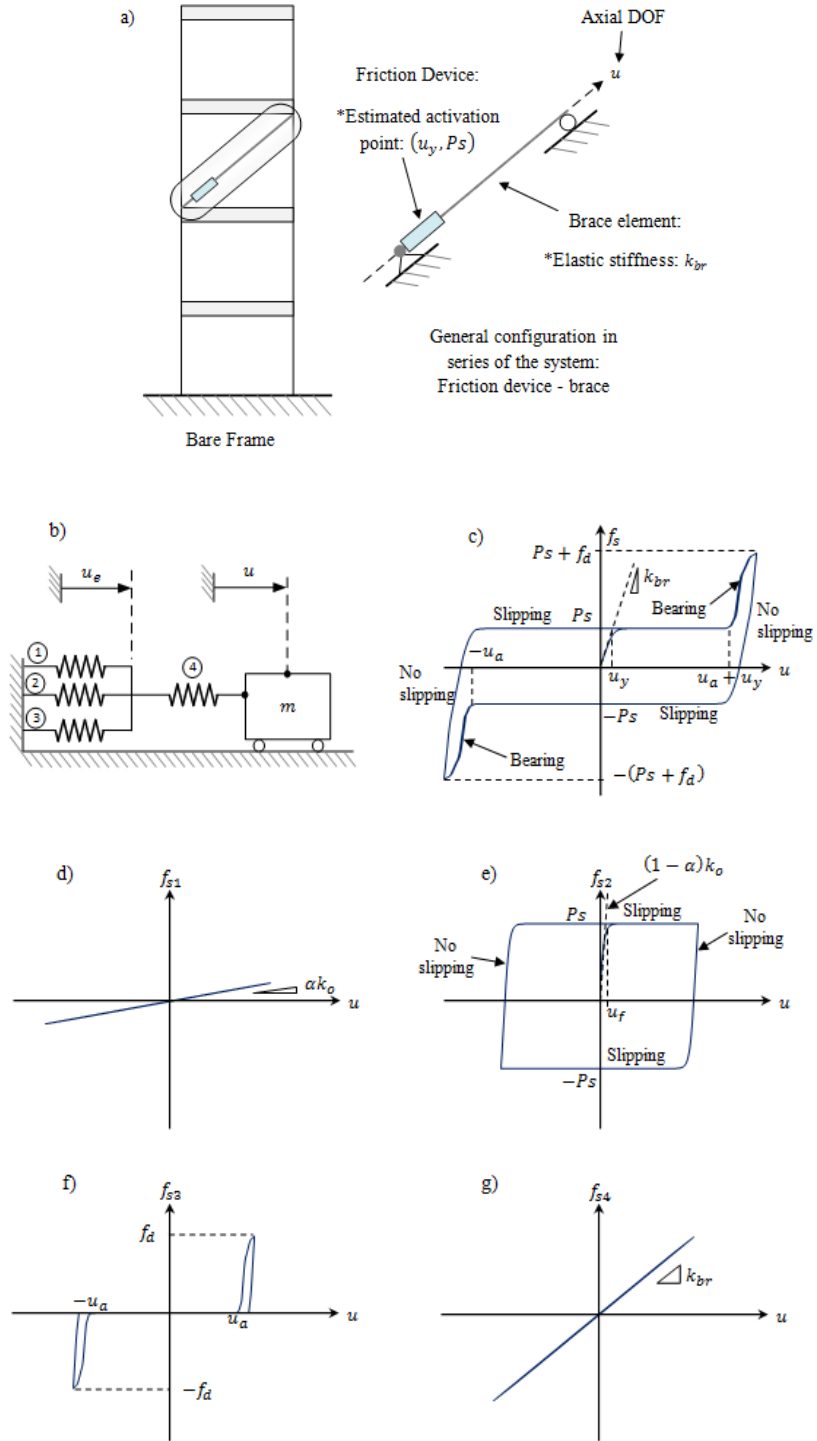
Figure 3.14 Schematic model of friction-damped diagonal-bracing device: a) Typical case; b) SDOF system (mechanical model); c) Hysteresis model; d) Spring 1: linear component BWBN model; e) Spring 2: nonlinear component BWBN model; f) Srping 3: slip-lock system; g) Spring 4: brace in elastic range

70

Thus the equivalent stiffness of the friction damper, k_s, is equal to the stiffness of the brace, k_{br}. When the load is bigger than the activation force, the device is slipping with an almost constant force Ps since α value is very small. The force in the brace is equal to the slip load while springs 1and 2 are activated in parallel and act in series with spring 4 which simulates the brace. Thus, $f_{s4} = Ps$ and the deformation is equal to $u_{yb} = Ps/k_{br}$.

When the activation force is reached in the device, the excursion is small and the displacement is much lesser than u_{yb}. Hence at the activation force, the total axial displacement of the system is given by the deformation of the brace P_S/k_{br} and the deformation of the device $P_S./k_0$. The total slipping displacement is:

$$u_y = \frac{Ps}{k_o} + \frac{Ps}{k_{br}}; \; k_o \gg k_{br} \rightarrow u_y \approx \frac{Ps}{k_{br}} \tag{3.31}$$

If the load is reversed (i.e. a change in the sign of the velocity), the device stops the slipping process and starts the unloading phase with a tangent parallel to the elastic stiffness (recall that $\gamma - \beta = 0$) until the force is zero. Since the system is acting in series, the equivalent stiffness during the unloading phase is also equal to k_{br}. When the applied load is increased in compression, the equivalent stiffness is equal to k_{br}, while the device experiences the slipping stage. Then, after the unloading stage,) the hysteresis cycle is completed. The friction device develops a hysteresis cycle with a symmetric shape. If, during the slipping in tension, the applied load is still acting after the slipping distance was consumed, the spring 3 which models the slip-lock stage is activated. The force experienced by the device is increased with the amount of f_{s3}. Hence, the force in the brace becomes $Ps + f_{s3}$ and the corresponding deformation changes from Ps/k_{br} to

$(Ps + f_{s3})/k_{br}$ at a rate defined by the bearing force f_{s3}. At this point, if the threshold value of the device f_d exceeds the compressive capacity of the brace, buckling may occur (provisions regarding to avoid this undesirable phenomena are given in Chapter 5). The stiffness of the device during this bearing stage is still bigger than the stiffness of the brace, but lower than that k_o defined during the stick-slip transition phase (see Figure 3.14e). For practical applications, Pall (1979) defined the bearing stiffness of the device equal to the half of the initial stiffness ($k_o/2$), even if his tests were not performed until failure of the device was reached. Hence, by considering Pall remark, the bearing stiffness of the system is:

$$k_{sb} = \frac{k_o k_{br}}{k_o + 2k_{br}} \quad \rightarrow \quad \lim_{k_o \to \infty} (k_{sb}) = k_{br} \tag{3.32}$$

Nevertheless, using the slip-lock model, Equation (3.32) yields to

$$k_{sb} = \frac{k_{sl} k_{br}}{k_{sl} + k_{br}} \tag{3.33}$$

where k_{sl} is the stiffness of the slip-lock model varying according to the elements depicted in Table 3.4. Thus, by considering the effective stiffness of a brace equipped with friction as summarised in Table 3.5, the backbone curve of the hysteresis model with the stick-slip phase incorporated is shown in Figure 3.15. It is noted that during the unloading stage, the stiffness is equal to the initial stiffness and spring 3 becomes inactive when the force is reduced below the slip load. This is not true if degradation in the post-tensioned bolts occur and some reduction in the activation load (slip force) is recorded (see Figure 2.13). This type of uncertainty is not considered in this study. Thus, using the BWBN model in parallel with the proposed slip-lock model enable the possibility of modeling a softer transition zones and bounds the developed device's force to $\pm f_d$ as per

Figure 3.15. The former is of particular interest for the performance based design and nonlinear time history analysis, since allows the distribution of the lateral force among the device and the bare frame members when an unbalanced force computed as $(f_{demand} - f_d)$ has to be redistributed.

Table 3.5 Effective axial stiffness k_s of the system brace-friction device (tension side)

Stage	Stiffness[(*)]
Before slipping	k_{br}
Slipping	k_n^t (See eq. 3.4)
Bearing – zone 1 (k_{s1})	$k_1 k_{br}/(k_1 + k_{br})$
Bearing – zone 2 (k_{s2})	$(k_1 + k_2)k_{br}/(k_1 + k_2 + k_{br})$
Bearing – zone 3 (k_{s3})	$(k_1 + k_2 + k_3)k_{br}/(k_1 + k_2 + k_3 + k_{br})$
Bearing – zone 4 (k_{s4})	$(k_1 + k_2)k_{br}/(k_1 + k_2 + k_{br})$
Bearing – zone 5 (k_{s5})	$k_1 k_{br}/(k_1 + k_{br})$
Bearing – zone 6 (k_{s6})	$\eta k_1 k_{br}/(\eta k_1 + k_{br}), \ \eta < 0$

(*) for k_1, k_2 and k_3 see Table 3.4.

Other advantage of the proposed model is the expression of sliding force in terms of the force transferred by the pretensioned high strength bolts, the coefficient of friction and the number of sliding planes, beside a stable value of the dynamic friction force. To account for the brace stiffness which acts in series with the friction damper model, parameters given in Table 3.4 (force, displacement and stiffness) were modified accordingly and are illustrated in Table 3.6.

Table 3.6 Modified components of the slip-lock model Fsl

i	u_{SLi}	k_{SLi}	f_{SLi}	η_{SLi}
1	u_1	k_{s1}	$k_{SL1}(u_d + f_d/k_{br} - u_{SL1})$	$-\eta_o$
2	$u_2 + k_1(u_a - u_1)/k_{br}$	$k_{s2} - k_{SL1}$	$k_{SL2}(u_c + f_c/k_{br} - u_{SL2})$	0
3	$u_3 + [k_1(u_3 - u_1) + k_2(u_3 - u_2)]/k_{br}$	$k_{s3} - (k_{SL1} + k_{SL2})$	$k_{SL3}(u_b + f_b/k_{br} - u_{SL3})$	0
4	$-u_1$	k_{s1}	$-k_{SL1}(u_d + f_d/k_{br} - u_{SL1})$	$-\eta_o$
5	$-u_2 - k_1(u_a - u_1)/k_{br}$	$k_{s2} - k_{SL1}$	$-k_{SL2}(u_c + f_c/k_{br} - u_{SL2})$	0
6	$-u_3 - [k_1(u_3 - u_1) + k_2(u_3 - u_2)]/k_{br}$	$k_{s3} - (k_{SL1} + k_{SL2})$	$-k_{SL3}(u_b + f_b/k_{br} - u_{SL3})$	0
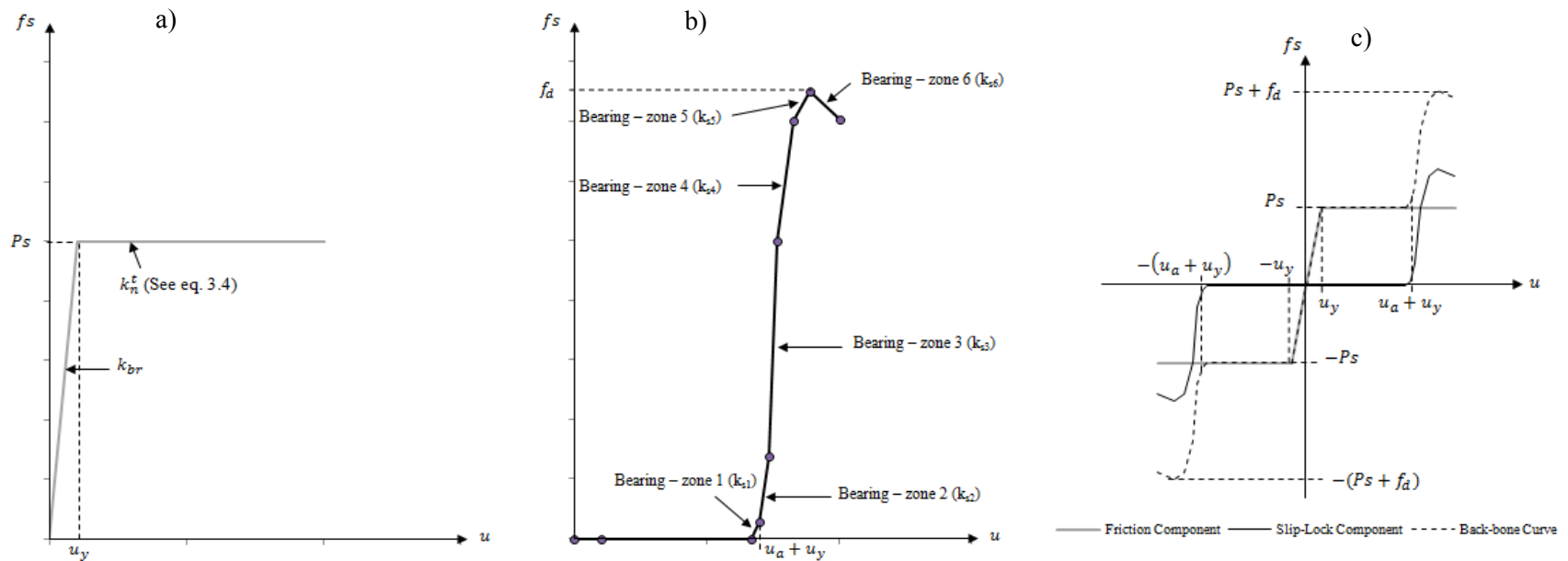
Figure 3.15 Backbone curve of the proposed hysteresis model: a) Friction component (bilinear behaviour); b) slip-lock component (non-linear behaviour) as per Table 3.5 (b), both in series with the elastic brace (tension side), c) complete back-bone curve (friction and slip-lock component working in parallel)

3.3 NUMERICAL EXAMPLE OF A BRACE EQUIPPED WITH FRICTION DEVICE USING OPENSEES

The following numerical example shows an application of the hysteresis model proposed using the FE software OpenSees (some generalities about OpenSees and the modeling process are given in chapters 4 and 5).

Thus, for modelling the stick-slip and slipping phases of friction devices, a SHM must be chosen such as the uniaxial BoucWen materials, which is available in the OpenSees library. The BoucWen material was implemented in OpenSees by Haukaas and Der Kiureghian (2004) and the stress (σ) of the material is expressed in terms of strain (ε) and variable z as per Equation (3.34), where z evolves according to the ordinary differential Equation (3.35).

$$\sigma = \alpha k_o \varepsilon + (1 - \alpha)k_o z \qquad (3.34)$$

$$\dot{z} = \frac{A - |z|^n \{\beta sgn(\dot{\varepsilon}z) + \gamma\}\nu}{\eta} \dot{\varepsilon} \qquad (3.35)$$

In Figure 3.16 it is shown the breakdown of the in-line brace- friction damper in term of stress strain curves as modelled in Opensees. The Element #1 represents the SHM component of the friction device without degradation $(\delta_A = \delta_\nu = \delta_\eta = 0)$ tuned in such a way that the device is activated when the stress related to the slip force is $\sigma_s = P_s/A_{br}$ and the strain related to the deformation of the brace-damper system acting in series is defined by $\varepsilon_y = \sigma_s/E^*$, where P_s is the slip force, A_{br} is the area of the brace cross section and $E^* = k_{br}L_{br}/A_{br}$. Elements #2 and #3 are acting in parallel with the BoucWen material component and in series with the brace and are able to model the locking of the system. They are made of 3 bilinear gap springs arranged in parallel and characterised by the

Elastic-Perfectly Plastic Gap Material defined in OpenSees. Element #2 is working in tension in such a way that when the imposed displacement in the system (in-line brace-friction damper) exceeds the distance $(u_y + u_a)$, it becomes active. Once activated, element #2 is able to limit the displacement and to increase the force experienced by the in-line brace friction damper system. Element #3 is similar to element #2, but is activated in compression when the travel distance $(u_y + u_a)$ is exceeded. The threshold force for these gap elements is related with the maximum force that the device is able to withstand. Furthermore, if the damper is pushed beyond the point at which the axial force drops, then the failure is expected, whether by bearing of bolts and/or sliding plates or by shearing of bolts, where the later should be avoided (brittle failure).

For this work, since no laboratory tests regarding Pall friction dampers are available in the literature, it is assumed that after the bearing capacity was consumed, the axial force drops and the in-line brace friction damper system reached failure. Therefore, after failure occurs the bare frame is working alone. For such purpose, let $\lambda_o u_d$ be the displacement measured from the original position at which a drop in the axial force was encountered after the device was pushed into the bearing stage beyond the threshold point u_d was reached, where $u_d > (u_y+u_a)$. Herein u_y is the elastic displacement of the brace at the slip load and u_a is the available slip distance which is defined herein as the maximum displacement recorded by the friction device alone throughout the analysis. If this distance u_a is labelled u_{smax} as shown in Figure 3.17, it defines the available travel distance experienced by the device in one direction. Then, after loads were reversed, the available slip distance is established as $2u_{max}$ which covers the sliding distance of the device without hitting the clamping bolts. Thus, if the displacement of the system (in-line

76

brace-friction damper) at the time t_i is bigger than $|\lambda_o u_d|$, an uniaxial equivalent material labelled MinMax material in OpenSees controls the behaviour by "switching off" the device from t_i until the end of the analysis. This switching condition was imposed in the model by setting up the MinMax material to fail when the strain developed by elements #1, #2 and #3 working in parallel falls below or above a threshold value. The former is able to return zero stress and stiffness from the later, when the strain is bigger than a prescribed value. Thus, the mechanical model for the Pall Friction damper is composed of a set of three elements in parallel: Element #1 to whom a BoucWen material was assigned, Element #2 (gap element in tension) to whom Elastic-Perfectly Plastic material was assigned and Element #3 (gap element in compression) with the same material as Element #2. Finally the MinMax material is assigned to this set in order to limit the strain capacity (Figure 3.16). Since the brace is assumed to respond elastically, the properties of the set of elements are defined considering the action in series of the elastic brace and the friction damper as discussed in section 3.2.

Herein the system brace-friction damper was modelled by using a truss member to whom the set of described elements was assigned. Hence, the final model of the structural system (MRF and in-line brace friction dampers) has the capability of simulating the global behaviour while the failure of the system was defined by considering the sudden failure of devices.
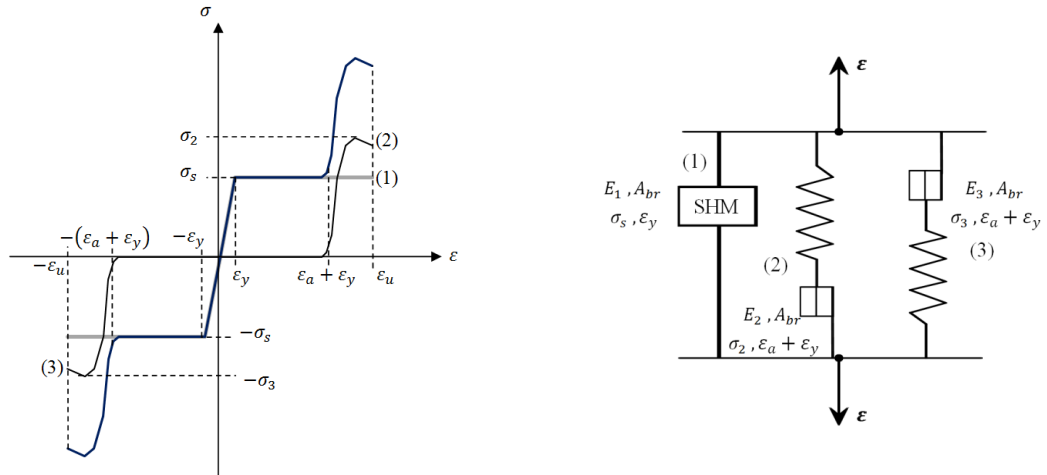
Approximation of the tension-compression strain-stress curve for friction damper device acting in series with brace behaving elastically

Equivalent material used to define the Pall friction damper in series with the elastic brace: #1 Bouc-Wen material; #2 and #3 Elastic-Perfectly Plastic Gap material combined with MinMax material
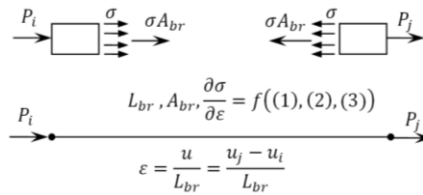
Truss element embodying the equivalent material

Figure 3.16 Modeling in-line brace-friction dampers in Opensees
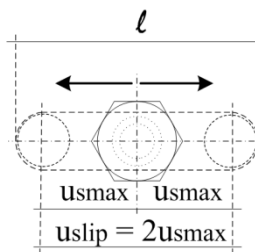
Figure 3.17 Schematic available slip-distance in the device

In this example, the brace element as shown in Figure 3.18 is loaded at joint j along the DOF u, while the applied quasi-static displacement is showed in Figure 3.19, where amplitudes are given in terms of the displacement corresponding to the available

slip distance (u_a) such as: *0.5, 0.75, 1.0, 1.5* and *2u_a*. In this example, brace's cross section corresponds to HSS203x203x9.5 (ASTM A500) class 1 and the brace itself is considered to behave as a truss element loaded in axial tension and compression. By considering an effective brace length of 8.10m and according to the CSA S16-09, the compression strength is C_r = *833kN*. .Thus, the activation load, *Ps*,is selected to be less than C_r/*1.3* as recommended by FEMA 356 (2000) which yilds to *Ps = 600kN*, while the slip limit was set up to u_a=*24mm*. The axial stiffness of the brace computed as $k_{br}=A_{br}E/L$ is equal to 144.2kN/mm (E=200000MPa). Regarding the setting of Bouc-Wen model parameters without degradation, based on the conducted study, their selected values are: *Ao = 1.0, δ_A= δ_v=δ_η= 0, α = 1x10^{-5}, n = 10* (computation is conducted in mm and kN). To complete the setting, the activation displacement point, u_y, and the parameters γ and β shall be defined. By using Equation (3.24) it conducts to u_y = *Ps/k_0* and by equating the stiffness of damper to the stiffness of brace k_o= k_{br} it leads to u_y = *4.2mm*. By employing Equation (3.11), the shape control parameters are computed: γ + β = *5.855x10^{-7}*. Recalling that for simulating the linear unloading branch, γ and β are equal and yields to γ = β = *5.855x10^{-7}/2=2.927x10^{-7}*. On the other hand, for the slip-lock model, the maximum expected force to be developed at bearing, f_{max} such that the brace to behave elastically was set to be f_{max} = *150kN*. Based on setting verification:, f_{max} + *Ps* =*750kN* < C_r = *833kN,* the elastic brace response is preserved. In order to account the drop in the force exerted by the device after the maximum force at bearing has been exceeded, the postyielding ratio, η, was defined as -0.9 for elements 1 and 4. The input data for the slip-lock system is given in Table 3.7 whilst the parameters defining the set of springs depicted in Table 3.8 were calculated as indicated in Table 3.6.

Table 3.7 Slip-Lock Parameters

General Data *			
δ_u [mm]	10	f_b [kN]	100
u_a [mm]	24	f_c [kN]	130
u_b [mm]	31	f_d [kN]	150
u_c [mm]	36		
u_d [mm]	48		

*Assumed data. See Figure 3.12 for the meaning of each component.

These values should be determined from experimental tests.

Table 3.8 Breakdown of the slip-lock components*

Element	u_i [mm]	k_i [kN/mm]	f_i [kN]	η_i
1	20.7	1634.2	45.4	-0.9
2	24	4562.5	55.5	0
3	27.3	12795.4	49.1	0
4	-20.7	1634.2	-45.4	-0.9
5	-24	4562.5	-55.5	0
6	-27.3	12795.4	-49.1	0

*See Table 3.6 and Figure 3.18
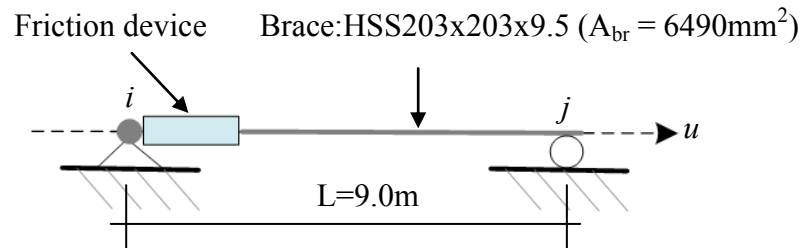
Figure 3.18 Friction device – Brace system. Numerical application

From Figure 3.21 is evident that the model proposed for the system friction device–brace, adjusts well the desired activation force level (*Ps*), which in this case was of 600kN, following an approximate rectangular shape with smooth transitions within stick-slip stages at the specified activation displacement (*u_y*).
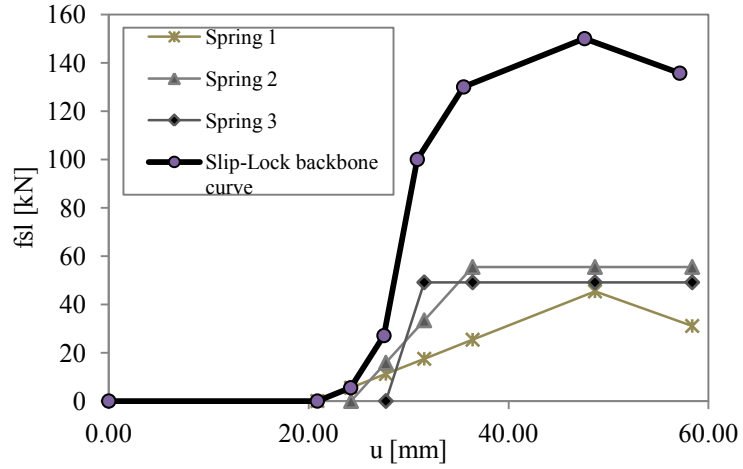
Figure 3.19 Tension side of the slip-lock model. Numerical application
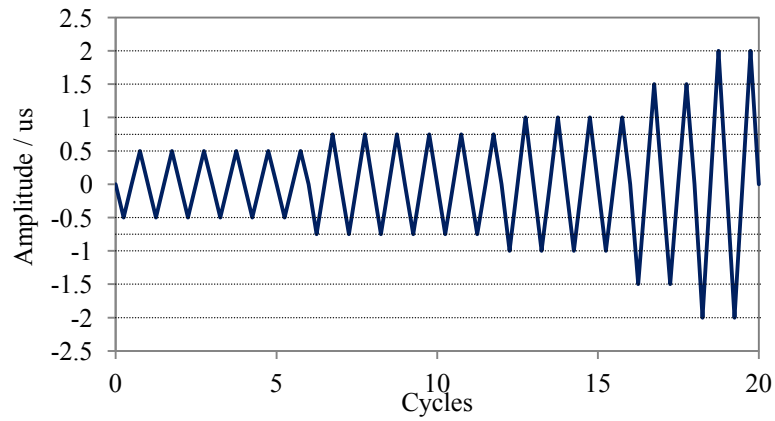
Figure 3.20 Quasi-static displacement loading
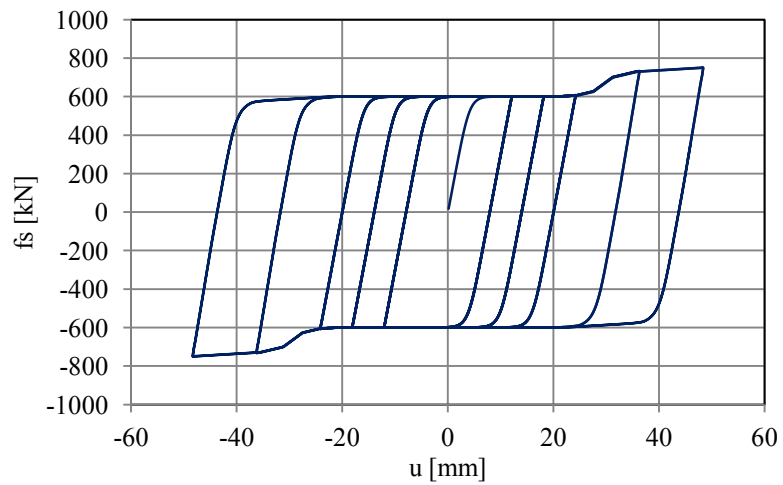
Figure 3.21 Hysteresis model proposed. Numerical application

81

Additionally, the maximum force exerted by the system was always below the threshold value established as: $f_s + Ps = 750$kN. At the neighbouring of the slip limit ($u_a = 24$mm) it can be seen the gradual transition for the bolt impact and near to the threshold value, additionally, a transition representing the inelastic behavior during the bearing stage is shown.

This example showed the capability of the hysteresis model proposed in offering smooth transitions at sharp changes in the behaviour of the system. It also incorporates the option of the slip distance limit in the analysis within a threshold value of the force exerted by the device, avoiding an overshoot in the force. The main limitation is that this model does not include the degradation resulting from the loose of pretension force in bolts due to the bolt impact and bearing phase behaviour as previously discussed. In Chapter 5, this simulation is included in modelling steel braced frame buildings equipped with friction dampers in order to analyse their performance.

CHAPTER 4

Seismic Performance of MRF Buildings

Moment resisting frames are designed to dissipate energy in bending when plastic hinges are formed in the end zones of the beams in vicinity to the beam-to-column connections. However, replacing damaged beam members and the connected slab is a costly process in term of retrofit and building operation function. To overcome this inconvenient, friction dampers are proposed to be incorporated in-line with diagonal braces in new or existing MRFs buildings. Thus, in this study, a new system consisted of steel MRF with friction dampers is introduced. To study the efficiency of the proposed system, friction dampers are incorporated in a moderately-ductile MRF. However, for a retrofitting case, friction dampers may be incorporated (in general) in a conventional MRF structure.

In this study, a 4-, 8- and 12-story moderate-ductility MRF-MD building located on a firm soil (site class C) in Montreal were selected. The rational of selecting a MD frame is that member sizes are reduced in comparison with those designed for conventional MRFs and this system is cost-efficient. Meanwhile, the interstory drift is preserved within the code limit.

The differences between the conventional and MD-MRF system are: larger members' cross-sections and increased design base shear which implies large overturning

moments transferred to the columns. The design of the MD-MRF frame and conventional system is summarized in sections 4.1.1 and 4.1.2, according to the NBCC 2010 and CSA/S16-2009 provisions.

The behaviour of the case studies is investigated through dynamic analysis by employing the linear modal response spectrum method implemented in SAP2000 and the numerical integration nonlinear time-history method implemented in the OpenSees software framework. These buildings were subjected to a set of simulated and historical records (Atkinson 2009) selected and scaled to match the uniform hazard spectrum (UHS) for Montreal, according to the procedure developed by Reyes and Kalkan (2011).

4.1 STUDIED BUILDINGS

4.1.1 General Description

The plan view and elevations of the studied office buildings with normal importance category ($I_E = 1$) are showed in Figure 4.1 and consists of 5 typical bays spaced at 7.6m along each orthogonal direction, with heights of 4.5m at the first level and 3.8m above. There are two MD-MRFs with three equal bays located in the East-West direction, along the external axes 1 and 6 and two similar MD-MRFs located in the North-South direction, along the internal axes B and E (Figure 4.1). None one of these buildings is characterized by in-plan or elevation irregularities. The specified dead load (DL), live load (LL) and snow load (SL) are given in Table 4.1.

Table 4.1 Specified loads (DL, LL and SL) for the 4, 8 and 12-story buildings

Description	Load [kPa]
Roof DL, includes: roofing, insulation, deck, steel beams and misc (flooring, ceiling, fireproof, MEP).	3.00
Typical floor DL, includes: partitions, deck-slabs, steel beams, girders and misc (flooring, ceiling, fireproof, MEP).	4.70
Cladding walls	1.00
Roof LL	1.00
Typical floor LL	2.40
Roof SL	2.48

Plan View

8-Story Elevation A-A

4-Story Elevation A-A

12-Story Elevation A-A
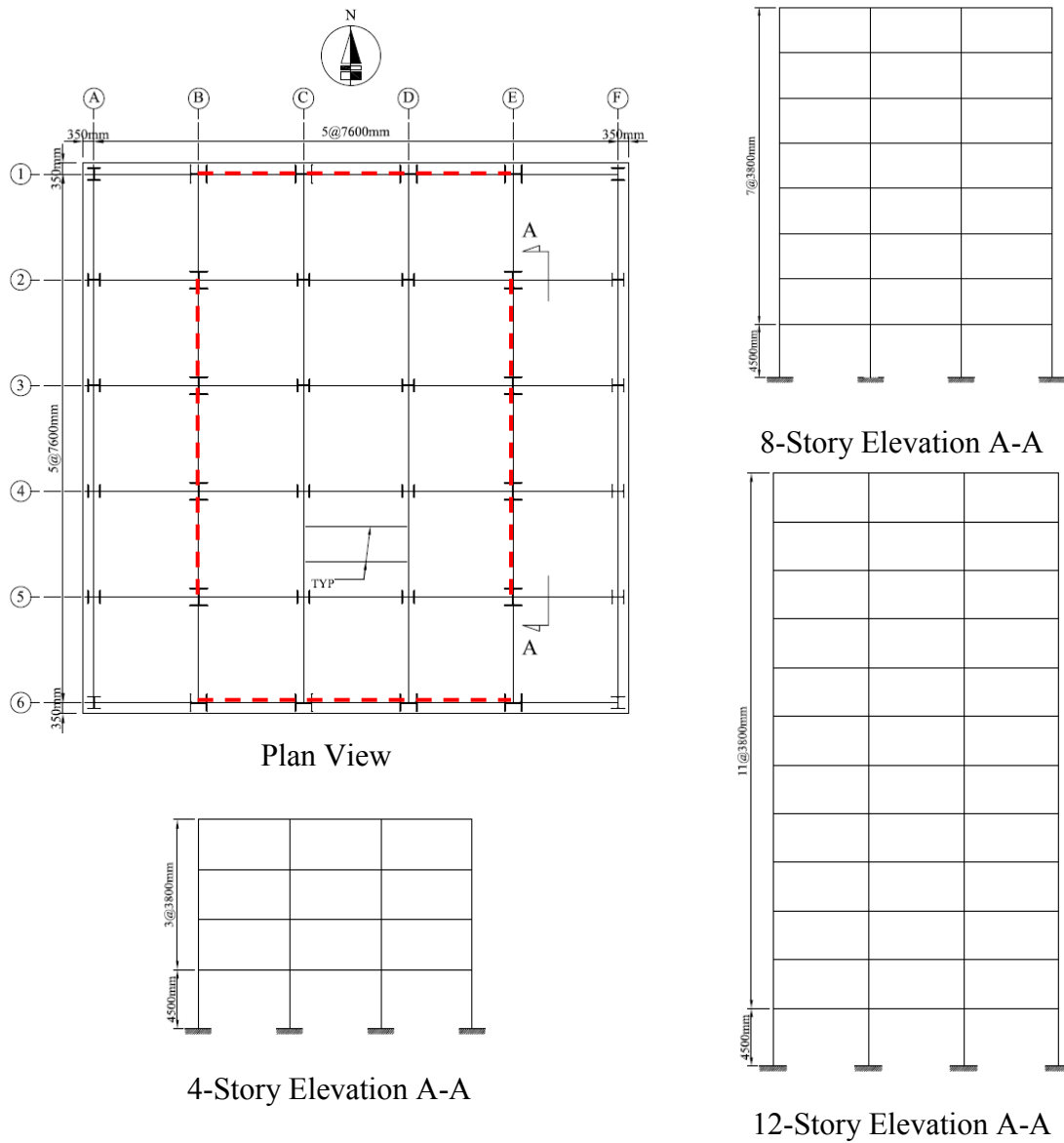
Figure 4.1 Typical plan and elevation views of studied buildings

4.1.2 Buildings Design

4.1.2.1 Seismic Design of MD-MRF Buildings

Since the total height of the taller regular building considered in this study is less than 60m, the NBCC allows to use the equivalent static force procedure for design of MD-MRFs members. This procedure requires that the minimum seismic base shear, V, calculated from Equation (4.1), shall be within the boundaries given by Equation (4.2).

$$V = \frac{S(T_a)M_V I_E W}{R_d R_o} \tag{4.1}$$

$$\frac{S(2.0)M_V I_E W}{R_d R_o} < V < \frac{2}{3}\frac{S(0.2)I_E W}{R_d R_o} \tag{4.2}$$

Herein, the $S(T_a)$ is the design spectral response acceleration corresponding to the fundamental period, M_v is the higher mode factor equal to 1 for buildings with $T \leq 1.0$ s and equal to 1.2 for buildings with $T \geq 2.0$ s if $S(0.2)/S(2.0) \geq 8$, while R_d and R_o are the ductility and overstrength related force modification factors accordingly. Thus, for a MD MRF system, these factors are: $R_d = 3.5$, $R_o = 1.5$. The fundamental building's period computed according to the empirical equation given in NBCC 2010 is showed in Table 4.2 in addition with the total seismic weight (W) of the buildings. The M_v factors computed for the 4-, 8-, and 12-storey buildings are: *1.003, 1.136* and *1.2* respectively.

The uniform hazard spectrum for Montreal (site class C) and the spectral ordinates corresponding to the estimated fundamental period are shown in Figure 4.2.

The total seismic force, V, is distributed along the height of the building, at each level x by an amount Fx determined from Equation (4.3), where Ft is a concentrated force

applied at the roof level and is given in Equation (4.4). For the 4-, 8-, and 12-storey buildings the computed values are: 55kN, 112kN and 121kN.

Table 4.2 Fundamental period and seismic weight, W, of studied buildings

Building	h_n [m]	W [kN]	$T_a = 0.085(h_n)^{3/4}$ [s]	$T = 1.5T_a$ [s]
4-story	15.90	29362.8	0.68	1.02
8-story	31.10	60854.8	1.12	1.68
12-story	46.30	92578.5	1.51	2.26
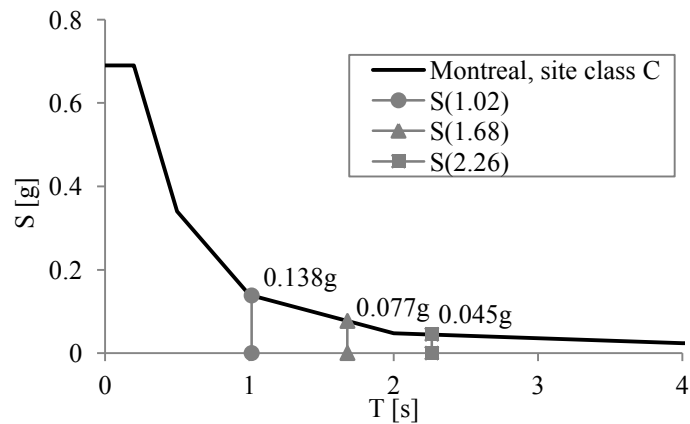
Figure 4.2 UHS for Montreal corresponding to 5% damping and site class C with a probability of exceedance of 2% in 50 years

The seismic weight per floor including the afferent weight of the columns, cladding walls and the 25% of the snow load at the roof level, as well as the distribution of forces along the building height and the base shear are depicted in Table 4.3. To establish the sensitivity to torsion of the studied buildings, the ratio $B = \delta_{max}/\delta_{ave}$ must be computed in agreement with the NBCC 2010 provisions,. Herein, δ_{max} is the maximum storey displacement calculated at the extreme points of the building in the direction of the applied static lateral forces acting at distances of ±0.1Dnx from the centres of mass at each floor, while *Dnx* is the dimension of the building perpendicular to the direction of

87

the applied forces and δ_{ave} is the average storey displacement of these extreme points. Thus, for cases characterised by $B > 1.7$, buildings are considered to be irregular (irregularity type 7 conforming to NBCC 2010). Based on the value of B ratio shown in Table 4.3, it was concluded that the three studied buildings are not torsional sensitive ($B < 1.7$) and the base shear developed in MD-MRF buildings may reduce to $80\%V$ if a dynamic analysis is employed.

$$F_x = (V - F_t)\frac{W_x h_x}{\sum_{i=1}^n W_i h_i} \tag{4.3}$$

$$F_t = \begin{cases} 0.07 T_o V \leq 0.25V & ; T_o > 0.7s \\ 0 & ; T_o \leq 0.7s \end{cases} \tag{4.4}$$

Table 4.3 Seismic weight W, storey forces F and B ratio computed in x- direction according to the static equivalent method

Level	12-Story			8-Story			4-Story		
	W_x [kN]	F_x [kN]	B_x	W_x [kN]	F_x [kN]	B_x	W_x [kN]	F_x [kN]	B_x
12	5824.9	291.50	1.190						
11	7814.3	137.67	1.189						
10	7819.2	125.48	1.188						
9	7824.1	113.28	1.187						
8	7836.3	101.14	1.186	5813.6	307.07	1.197			
7	7848.4	88.96	1.185	7791.6	203.50	1.197			
6	7868.6	76.69	1.184	7797.2	175.36	1.197			
5	7888.8	64.39	1.182	7802.9	147.17	1.196			
4	7912.4	52.08	1.181	7836.3	119.20	1.196	5813.6	322.0	1.200
3	7936.0	39.72	1.179	7869.7	90.87	1.194	7791.6	265.2	1.198
2	7952.8	27.29	1.175	7910.7	62.45	1.191	7827.5	182.4	1.196
1	8052.5	14.97	1.174	8032.9	34.23	1.190	7930.2	99.9	1.193
V=ΣF$_x$	92578.5	1133.2		60854.8	1139.8		29362.8	869.5	

4.1.2.2 Design of Conventional MRF Buildings

In section 4.1.2 the calculation of the base shear force for the MD-MRF buildings was presented. Herein, for the case of conventional MRF buildings, designed to behave

elastically, the ductility factor, R_d is equal to *1.0* and R_o = *1.5*. The lateral distribution of

the seismic forces is given in Table 4.4 and the total base shear is computed in the last

row of the table. The seismic weight is considered the same for both MD and

conventional structures as well as the empirical fundamental period (Table 4.2). The

design methodology for the conventional-MRF is based on the premise that it should

remain elastic; therefore no capacity design procedure nor ductility requirements are

applied. Hence, members are designed for strength and deflection criteria, while their

selected cross sections are shown in Table 4.5 and Table 4.6. Based on the elastic

analysis using SAP2000 software, the computed interstory drifts are given in Table 4.7

and are within code limit.

Table 4.4 Conventional-MRF buildings. Seismic weight W, storey forces F and B ratio
computed in x- direction according to the static equivalent method

Level	12-Story			8-Story			4-Story		
	W_x [kN]	F_x [kN]	B_x	W_x [kN]	F_x [kN]	B_x	W_x [kN]	F_x [kN]	B_x
12	5824.9	1020.9	1.172						
11	7814.3	482.0	1.168						
10	7819.2	439.5	1.165						
9	7824.1	396.9	1.162						
8	7836.3	354.3	1.167	5813.6	1075.9	1.074			
7	7848.4	311.5	1.167	7791.6	712.8	1.096			
6	7868.6	268.5	1.164	7797.2	614.5	1.108			
5	7888.8	225.4	1.163	7802.9	515.9	1.163			
4	7912.4	182.5	1.159	7836.3	417.5	1.161	5813.6	1127.0	1.107
3	7936.0	139.3	1.157	7869.7	316.6	1.158	7791.6	928.1	1.083
2	7952.8	94.2	1.152	7910.7	217.4	1.160	7827.5	639.6	1.109
1	8052.5	51.0	1.150	8032.9	118.5	1.164	7930.2	348.3	1.095
V=ΣF$_x$	92578.5	3966.0		60854.8	3989.1		29362.8	3043	

Table 4.5 6 Members cross sections of the Conventional-MRF Buildings in East-West direction

Level	12-Story			8-Story			4-Story		
	Exterior Columns	Interior Columns	Beams	Exterior Columns	Interior Columns	Beams	Exterior Columns	Interior Columns	Beams
12	W360x110	W360x162	W360x72						
11	W360x110	W360x162	W410x67						
10	W360x162	W360x179	W410x74						
9	W360x162	W360x179	W460x82						
8	W360x179	W360x196	W530x85	W360x79	W360x122	W360x72			
7	W360x179	W360x196	W530x109	W360x79	W360x122	W460x74			
6	W360x196	W360x237	W530x109	W360x101	W360x196	W460x97			
5	W360x196	W360x237	W530x109	W360x101	W360x196	W530x109			
4	W360x287	W360x347	W610x125	W360x122	W360x216	W530x123	W360x91	W360x122	W360x57
3	W360x287	W360x347	W610x140	W360x122	W360x216	W610x113	W360x91	W360x122	W410x85
2	W360x347	W360x421	W610x140	W360x162	W360x314	W610x113	W360x162	W360x287	W460x89
1	W360x347	W360x421	W610x155	W360x162	W360x314	W610x125	W360x162	W360x287	W530x109

Table 4.7 Members cross sections of the Conventional-MRF Buildings in North-South direction

Level	12-Story			8-Story			4-Story		
	Exterior Columns	Interior Columns	Beams	Exterior Columns	Interior Columns	Beams	Exterior Columns	Interior Columns	Beams
12	W360x122	W360x162	W410x67						
11	W360x122	W360x162	W410x67						
10	W360x162	W360x196	W410x85						
9	W360x162	W360x196	W460x89						
8	W360x179	W360x237	W530x92	W360x79	W360x162	W410x85			
7	W360x179	W360x237	W530x109	W360x79	W360x162	W460x97			
6	W360x216	W360x262	W530x109	W360x122	W360x196	W530x101			
5	W360x216	W360x262	W530x123	W360x122	W360x196	W530x123			
4	W360x314	W360x347	W610x125	W360x179	W360x262	W530x138	W360x101	W360x162	W410x74
3	W360x314	W360x347	W610x140	W360x179	W360x262	W610x125	W360x101	W360x162	W460x97
2	W360x382	W360x421	W610x140	W360x196	W360x382	W610x125	W360x216	W360x314	W530x92
1	W360x382	W360x421	W610x155	W360x196	W360x382	W610x153	W360x216	W360x314	W530x138

Table 4.8 Interstory drifts for conventional-MRF Buildings

Level	12-Story		8-Story		4-Story	
	E-W	N-S	E-W	N-S	E-W	N-S
12	0.50%	0.55%				
11	0.71%	0.79%				
10	0.76%	0.85%				
9	0.84%	0.94%				
8	0.82%	0.92%	0.07%	0.07%		
7	0.86%	0.97%	0.37%	0.39%		
6	0.83%	0.92%	0.51%	0.55%		
5	0.84%	0.92%	0.66%	0.66%		
4	0.72%	0.80%	0.63%	0.62%	0.73%	0.60%
3	0.72%	0.80%	0.70%	0.69%	1.06%	0.98%
2	0.67%	0.73%	0.66%	0.63%	0.85%	0.84%
1	0.56%	0.58%	0.66%	0.59%	0.78%	0.75%

4.1.2.3 Design of MD-MRF Buildings

The capacity design procedure used to proportion the MD-MRF members is in agreement with CSA/S16-2009 and is summarized as follows: i) selection of preliminary member sizes; ii) verification to assure the design concept: "strong column – weak beam"; iii) interstorey drift verification; iv) stiffness verification such that the amplification factor, U2, which accounts for the P-delta effect of gravity loads acting on the laterally displaced storey does not exceed 1.4; v) computation of moment connections and column joint panel zone.

The selection of preliminary member sizes was made in order to have beams of Class 1 sections (although the CSA/S16-09 allows to use both Class 1 and 2) and columns of Class 1 and/or 2. Concurrently, the building structure has to meet the interstory drift limitation (NBCC 2010) which is 2.5%h_s for normal importance category buildings. After sizing all beam members, the second step is to design columns to resist

gravity loads together with the forces induced by the plastic hinges developed in beams in conformity with equation (4.5). Herein, according to FEMA 350, the formation of the plastic hinges in beams was considered to occur at a distance equal to half of beam's depth measured from the face of the column.

$$\Sigma M'_{rc} \geq \Sigma \left[1.1 R_y M_{pb} + V_h \left(x + \frac{d_c}{2} \right) \right]$$

(4.5)

Here, M'_{rc} is the sum of the column factored flexural resistance computed at the intersection of the beam and column centerlines, M_{pb} is the nominal plastic moment resistance of the beam (ZF_y), and V_h is the shear developed at the plastic hinge location when $1.1R_y M_{pb}$ is reached at the beam hinge. The capacity design described is deemed to force the beams to yield first than the panel zone and the columns, such that the criteria of strong column-weak beam to govern the design of MRF members. Then, the design of columns was made such that the interaction equation composed of the bending moments developed in columns due to the plastic hinging of beams and the afferent axial forces together with the gravity component resulting from the combination (DL+0.5LL+0.25SL) to be satisfied. The beams and columns sections of the MD- MRFs, as resulted from the static equivalent method are summarized in Table 4.8 and Table 4.9. The computed amplification factor, U2 was smaller than 1.4 at all floors. Finally, for preliminary design, the interstory drifts were evaluated through a linear dynamic analysis as described in the next subsection.

Table 4.9 Members cross-sections of the MD-MRF buildings in East-West direction

Level	12-Story			8-Story			4-Story		
	Exterior Columns	Interior Columns	Beams	Exterior Columns	Interior Columns	Beams	Exterior Columns	Interior Columns	Beams
12	W360x79	W360x91	W360x33						
11	W360x79	W360x91	W360x33						
10	W360x91	W360x101	W360x51						
9	W360x91	W360x101	W360x51						
8	W360x101	W360x122	W360x57	W360x79	W360x91	W360x33			
7	W360x101	W360x122	W360x64	W360x79	W360x91	W360x51			
6	W360x110	W360x179	W360x72	W360x91	W360x110	W360x51			
5	W360x110	W360x179	W410x67	W360x91	W360x110	W360x57			
4	W360x122	W360x196	W410x67	W360x101	W360x162	W360x64	W360x79	W360x122	W360x33
3	W360x122	W360x196	W410x74	W360x101	W360x162	W410x60	W360x79	W360x122	W360x57
2	W360x162	W360x216	W410x74	W360x110	W360x179	W410x60	W360x101	W360x162	W360x57
1	W360x162	W360x216	W530x66	W360x110	W360x179	W410x67	W360x101	W360x162	W460x52

Table 4.10 Members cross sections of the MD-MRF buildings in North-South direction

Level	12-Story			8-Story			4-Story		
	Exterior Columns	Interior Columns	Beams	Exterior Columns	Interior Columns	Beams	Exterior Columns	Interior Columns	Beams
12	W360x79	W360x162	W310x52						
11	W360x79	W360x162	W360x64						
10	W360x91	W360x179	W360x72						
9	W360x91	W360x179	W360x72						
8	W360x162	W360x237	W410x85	W360x79	W360x162	W310x52			
7	W360x162	W360x237	W460x74	W360x79	W360x162	W360x64			
6	W360x179	W360x262	W460x82	W360x110	W360x179	W410x67			
5	W360x179	W360x262	W460x82	W360x110	W360x179	W410x74			
4	W360x196	W360x314	W460x89	W360x162	W360x237	W460x74	W360x91	W360x179	W360x64
3	W360x196	W360x314	W460x89	W360x162	W360x237	W410x85	W360x91	W360x179	W360x72
2	W360x216	W360x347	W530x85	W360x179	W360x262	W410x85	W360x162	W360x216	W460x68
1	W360x216	W360x347	W530x85	W360x179	W360x262	W460x82	W360x162	W360x216	W460x82

4.1.2.3.1 Linear Modal Response Spectrum Analysis

The modal response spectrum analysis (MRS) consists in finding the response of a structural system when subjected to a uniform hazard spectrum (UHS), defined for a given location and site class. The UHS is defined for 5% of the critical damping and a 2% in 50 years probability of exceedance or 2475 years return period. In this analysis, the buildings studied were modeled in SAP2000 and torsion and P-delta effect were considered. The number of vibration modes included in analysis was determined such that the total mass excited to be more than 90% of the seismic mass.

From dynamic analysis, the fundamental period of vibration and the base shear, V_{dyn}, obtained are summarized in Table 4.10. Since the torsional sensitivity factors were less than 1.7 and buildings are considered as regular, the base shear computed from dynamic analysis, V_{dyn} has to equate at least *80%V*. If this requirement is not satisfied, V_{dyn} shall be scaled up until the *0.8V* is reached. If from computation, V_{dyn} is larger than *0.8V*, the V_{dyn} value shall be used in design.

Table 4.11 Dynamic characteristics of buildings from linear MRS analyses

Building	T_1 [s]	0.8V [kN]	E-W Direction			N-S Direction		
			V_{dyn} [kN]	V_d [kN]	V_d/V_{dyn}	V_{dyn} [kN]	V_d [kN]	V_d/V_{dyn}
4-Story	1.69	695.6	390.8	695.6	1.780	377.2	695.6	1.844
8-Story	2.86	911.8	425.3	911.8	2.144	418.9	911.8	2.177
12-Story	4.13	906.6	434.2	906.6	2.088	434.0	906.6	2.089

The distribution of interstory drift along the buildings heights as resulted from dynamic analysis is shown in Table 4.11. It is clear that these values are lower than the 2.5%h_s.

Table 4.12 Interstory drift ratios computed for studied buildings from the MRS analyses

Level	12-Story		8-Story		4-Story	
	E-W	N-S	E-W	N-S	E-W	N-S
12	0.64%	0.46%				
11	0.95%	0.71%				
10	1.08%	0.82%				
9	1.22%	0.92%				
8	1.13%	0.86%	0.37%	0.40%		
7	1.22%	0.93%	0.66%	0.69%		
6	1.17%	0.90%	0.79%	0.83%		
5	1.24%	0.96%	0.94%	0.97%		
4	1.25%	0.96%	0.83%	0.88%	0.70%	0.71%
3	1.33%	1.03%	0.95%	1.00%	1.14%	1.14%
2	1.33%	1.06%	1.02%	1.07%	1.24%	1.26%
1	1.34%	1.03%	1.18%	1.14%	1.27%	1.25%

4.2 ANALYSING THE MRF BUILDINGS USING OPENSEES

4.2.1 OpenSees framework

OpenSess is an open source FE framework for earthquake engineering simulation. Developed at the University of California at Berkeley by Frank McKenna in 1997 (McKenna 1997), it has been enhanced with contributions of other researchers during the last decade and was sponsored by the National Science Foundation (NSF), the Pacific Earthquake Engineering Research Center (PEER) and George E. Brown, Jr. Network for Earthquake Engineering Simulation (NEES). The constant evolution of its capabilities trough contributions made worldwide supported by analytical and experimental studies makes this software a versatile tool for analyzing the nonlinear response of structural systems. Since the amount of information regarding this software might be overwhelming, the web-site (http://opensees.berkeley.edu/wiki/index.php/Main_Page) OpenSeesWiki has been created and all information about members, connections and

material definition, non-linearity, algorithms, links to the support publications and examples are embedded.

Details of this framework are not in the scope of this work. Nevertheless, a summary description of the modeling process is outlined. In general terms, OpenSees is an object-oriented software framework written in C++ with several interpreters reading input information written in the Tcl programming language. The modeling process including nonlinearities at the level of the cross section and members are summarized in Figure 4.3.

Initially, the dimensions and the corresponding DOFs of the problem are specified to construct the space model. Then, all nodes are created base on the required geometry and define constraints and concentrated masses along the DOFs where applicable. After the material is defined and the cross section object is built, it is possible that a cross section aggregator might be assigned if different features than those assigned by the material are required. For example, for a 3D model, this step is necessary in order to assign torsional stiffness at the cross section level. At this point, the element is defined by using the cross section, the geometric transformation and the nodes to be connected with. "Recorders", which are monitoring the results of the analysis process, are specified in accordance with the information required from nodes, cross sections or elements amongst others. The next step is to establish the loading patterns and the type of the analysis tools describing how the solution process is carried out and the value of allowable tolerances, etc. Lastly but not least, the type of analysis is chosen among the static (gravity loading) and transient or variable transient (earthquake loading). It is mentioned that the analysis tools available in OpenSees comprise a variety of algorithms, solvers and other features

that can be used to overcome convergence problems. Further discussion about these tools can be found in the web-site http://opensees.berkeley.edu/wiki/index.php/Main_Page as well as the references supporting their implementation.

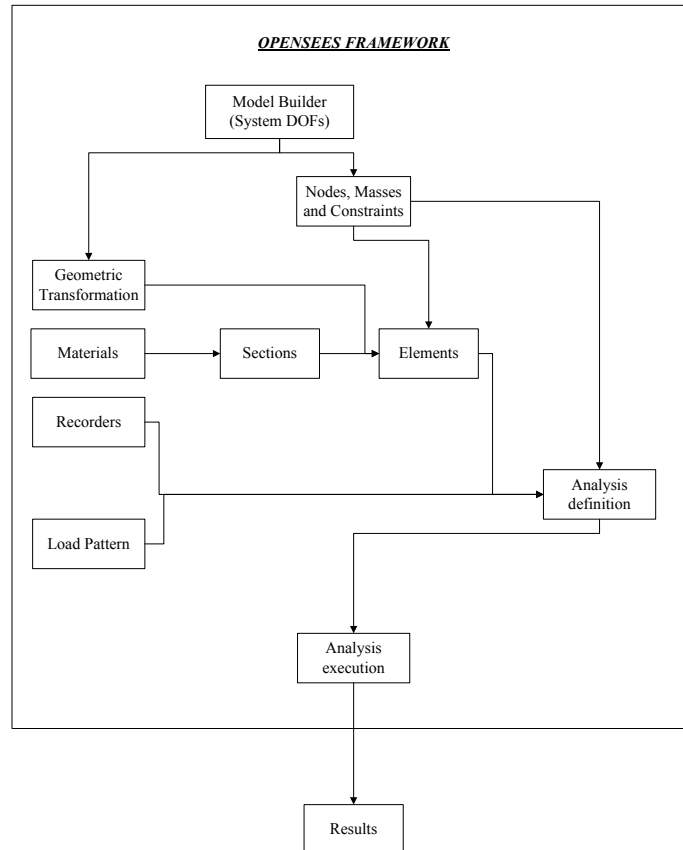Figure 4.3 Modeling process in OpenSees software

4.2.2 Discretization of the models for the studied buildings in OpenSees

4.2.2.1 Model definitions

Due to the symmetry of the buildings, the MD-MRFs located in the N-S direction were modeled as a 2D frame according to Figure 4.4. In this regard, the cross sections shown in Table 4.9 were used and half of the seismic weight per floor level, as depicted

97

in Table 4.3, was lumped at each MRF' node along the horizontal DOF. In order to take into account the rigid diaphragm effect, the horizontal DOF was assigned to develop equal lateral deformation with the master nodes. All the columns of the MRF system were fully restrained at the base. All beams and columns belonging to the SFRS are represented by force-based beam-column elements with distributed plasticity along the plastic hinge's length (beam with hinges). Herein, the two-point Gauss Radau integration method as described by Scott (2006, 2011) is employed and Steel 02 material was assigned for the MRF's members. The model was built considering center line distances, therefore the plastic hinges will form at the column face and the joint panel deformation was neglected in order to reduce the complexity of the model without loss of generality since the main contribution to the interstory drift is due to the beam behavior. Degradation of the hysteretic response was also neglected. The three buildings were subjected to the set of simulated ground motion records discussed in section 4.3. In order to consider the P-Δ effects that might arise during the seismic event due to the lateral deflection of the structure and the actual gravity loads, leaning columns were used. They were pinned connected to the main system by rigid links and vertical forces resulting from the difference within the loads of the half of the building and those corresponding to the MRF's columns according to their afferent area were assigned.

For the rigid links, axially-rigid elastic truss elements were used. Whereas, the leaning columns were modeled with elastic beam-column elements pinned at the base and with shear splices every two storeys.
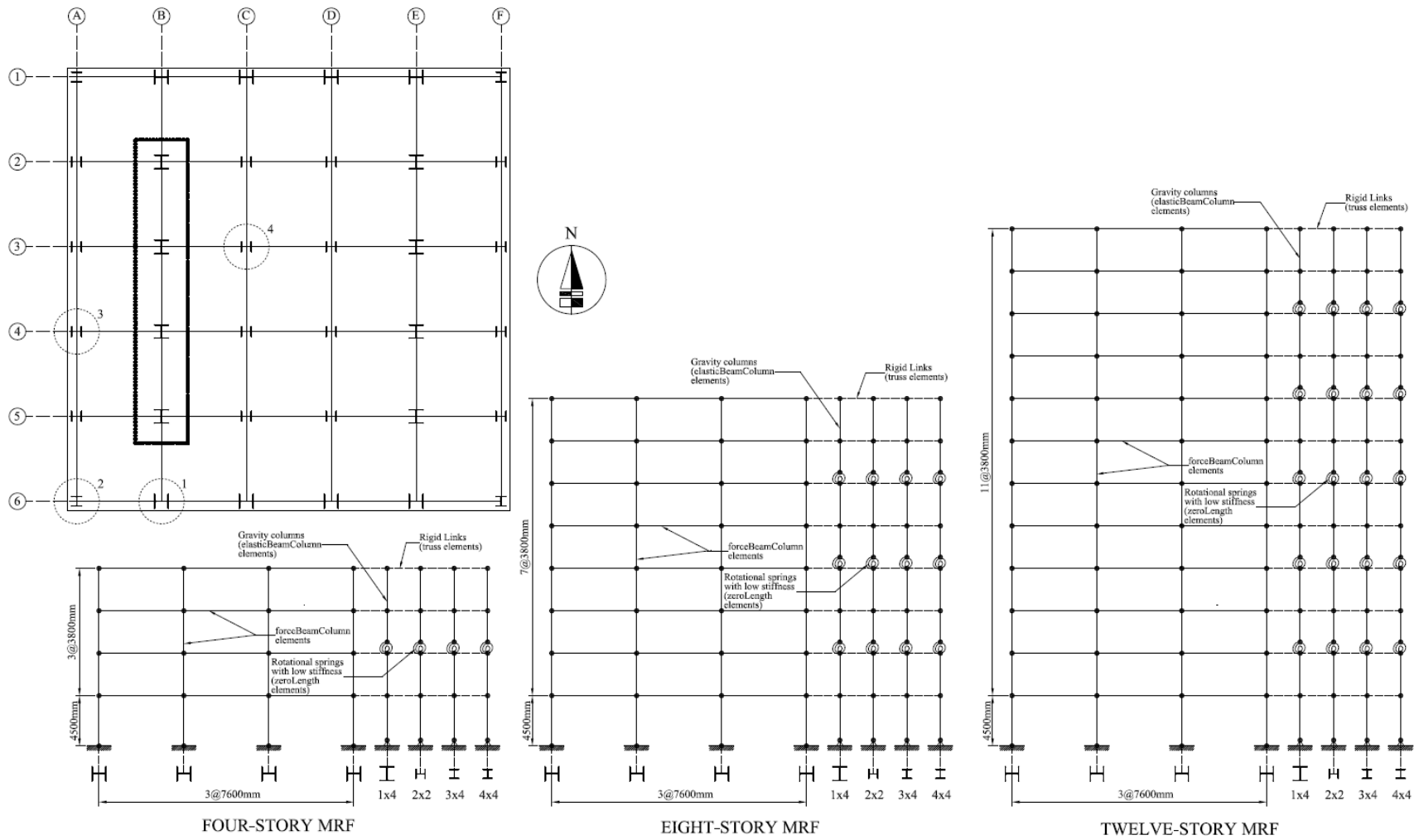
Figure 4.4 Schematic models in Opensees of the studied MRFs

4.2.2.2 Modelling of MRF with distributed plasticity along the plastic hinge's length

There are two types of force-based beam-column elements developed in OpenSees for modeling the nonlinear behaviour of the MRF's members: nonlinear beam-column element with concentrated plasticity (beam with hinges) and nonlinear beam-column element with distributed plasticity. Meanwhile there are two approaches commonly used to simulate the behaviour of MRF as follows: beams are modeled with elastic beam-column elements, while plasticity is concentrated at the ends of the elastic member and simulated by zeroLength rotational spring elements, embodying the rules for the hysteresis response   Regarding the second approach, the MRF's members are simulated with the beam with hinges element which allows the possibility of forming plastic hinges near the ends of the element along the defined plastic hinge's length (beam with hinges). Although, by using the beam with hinges element it seems that computational time is reduced, Lignos and Krawinkler (2008) have demonstrated that both approaches give similar response. In addition Lignos and Krawinkler have developed in OpenSees framework an uniaxial material labelled "Bilin material" which incorporates cyclic loading deterioration as defined in the study conducted by Ibarra and Krawinkler and know as Ibarra-Krawinkler deterioration model. This material was calibrated by using more than 350 experimental tests conducted on beam-column moment connections under cyclic loading (Lignos and Krawinkler 2011). Recently, this material was added to the Opensees library and was posted by Eads (2010) together with two examples of a 2-storey MRF (2D model) built in the light of both aforementioned approches (Figure 4.5 and Figure 4.6). Therefore, in the first example the MRF's members (beams and columns) are represented by elastic beam-column elements

connected with zeroLength rotational springs located at the two ends of each member. These springs have assigned the Bilin material without considering cyclic deterioration.

The second model (Fig. 4.6) considers beam-column elements with plastic hinges (beamWithHinges), i.e. the plasticity is considered distributed along the plastic lengths *Lpi* and *Lpj* defined at the ends i and j of the element, accordingly. The beamWithHinges element localises the integration points within the plastic hinge zone.
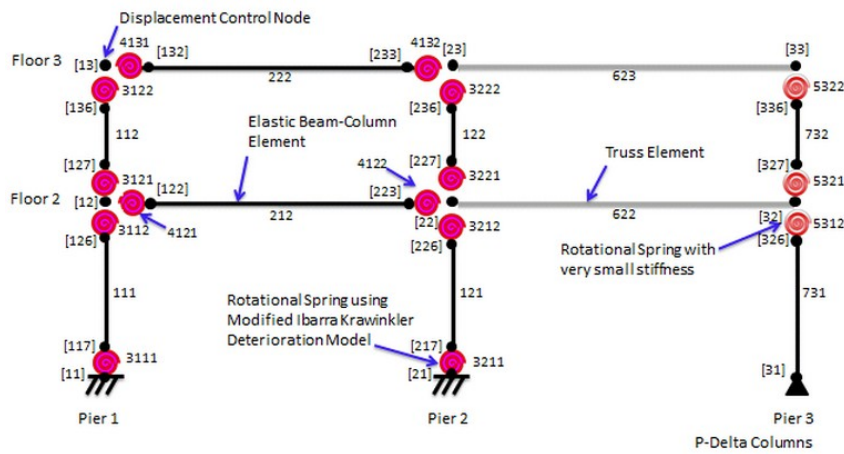

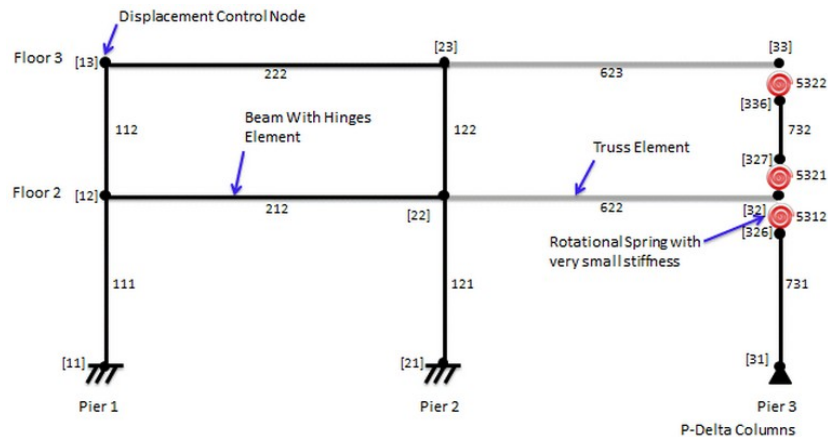Figure 4.5 The MRF model with concentrated plasticity (after Eads 2010)

Figure 4.6 The MRF model with distributed plasticity along the plastic hinge' length
(after Eads 2010)

As is shown in Figure 4.7, under a pushover analysis the model with distributed plasticity along the plastic hinge's length provides a good approximation to the model with concentrated plasticity.
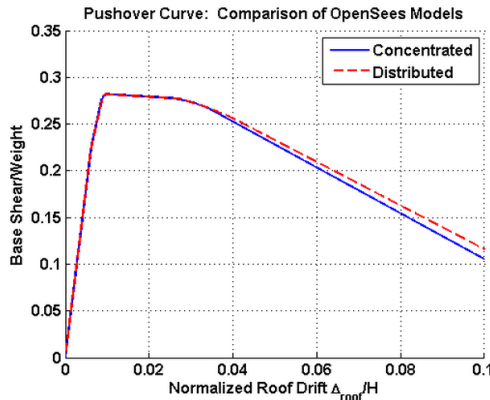

Figure 4.7 Pushover Curve: Comparison of the MRF model with concentrated plasticity versus the MRF model with distributed plasticity in Opensees (after Eads 2010)

The beamWithHinges element object is divided in three parts: one linear-elastic zone in the middle accompanied by two nonlinear regions within the plastic hinge length at each end. Regarding the plastic hinge integration scheme, Scott and Fenves (2006) showed that, when the member is expected to have a postyielding hardening response, the two-points Gauss-Radau integration approaches is recommended. This integration approach, consider other point inside each plastic hinge length beside the one point at each end, leading to a beam-column element with four integration points as shown in Figure 4.8. Moment-rotation curve of a simply supported beam subjected to antisymmetric bending moments and modelled as beamWithHinges with different plastic hinge integration methods such as: midpoint integration, endpoint integration, two-point Gauss-Radau integration and modification of two-point Gauss-Radau integration is shown in Figure 4.9. In this example, the flexural behaviour in the plastic hinge zone is

described by a bilinear moment-curvature relationship and the length of the plastic hinge at each end was considered as 0.15L. Herein, the strain hardening is given by αEI where EI is the elastic stiffness. As is shown in Figure 4.9, the two-point Gauss-Radau integration scheme matches the closed-form solution.
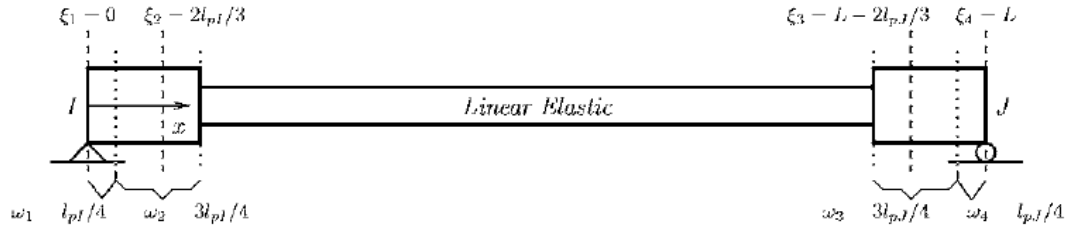

Figure 4.8 Two-point Gauss-Radau integration scheme. ξ_i: location of the i-th integration point, ω_i: weight of the i-th integration point; *lpi* and *lpj*: plastic hinge regions and *l*: length of the member. (after Scott and Fenves 2006)
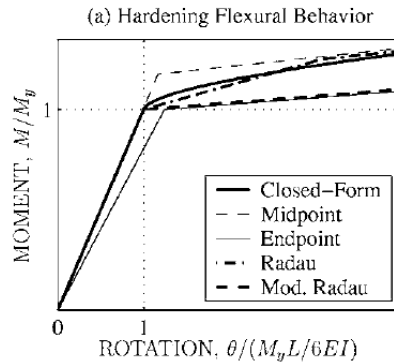

Figure 4.9 Moment-Rotation for a beam with different integration schemes. (after Scott and Fenves 2006)

Thus, the force-base nonlinear beam-column element object (beamWithHinges) with two-point Gauss-Radau integration scheme (see Scott 2011) and Steel02 material is used hereinafter for modeling the beams and columns of MRFs. In this research, the backup MRF system is expected to perform elastically and is no need for assigning Bilin material to plastic hinges in order to simulate cyclic degradation. The cross sections

within the plastic hinge regions were discretized into fibers to account for the interaction between axial forces and bending moments. Thus, the web of W-shape was divided in 32 fibers (16 along the web's depth) and each flange was divided in 64 fibers with 4 fibers along the flange thickness. For such purpose, an isotropic material without degradation and exhibiting strain hardening following the Giuffre-Menegotto-Pinto model and labelled Steel02 was assigned to the fibers.

Due to the large number of elements and information involved in the modeling process, several scripts were made in the Tcl language for input data such as definition of the beams, columns, nodes, connectivity and assignation of properties. In addition, for the post-processing of results, an interaction within Matlab was created for the output files. Thus, among other parameters monitored during the analysis, the strain developed in all fibers of cross section at the location of plastic hinges was recorded.

To show the capability of the model with spread plasticity within the plastic hinge region an example of 4-storey MD-MRF system which is illustrated in Figure 4.4 is conducted, while the members' sizes are those given in Table 4.9 (north-south direction). The leaning columns are modeled with the elastic beam-column elements and are connected to the beam-column joint by ZeroLength rotational springs with almost zero stiffens. Links between leaning columns and MRF's joints are modelled as Truss element object assuming it is axially rigid. Gravity loads are assigned to the beam-column joints as plain load pattern with constant time series. The model consider mass and stiffness proportional Rayleigh damping of 2% assigned to the first and the third vibration mode of the structure according to Equation 4.6, where ω_1 and ω_K are the circular frequencies in

the first and third mode . Herein damping is proportional to initial stiffness matrix and is assigned to the MRF's members. From the OpenSees analysis the 1st, 2nd and 3rd vibration mode are: $T_1 = 1.67s$, $T_2 = 0.54s$ and $T_3 = 0.17s$.

$$\begin{Bmatrix} \alpha \\ \beta \end{Bmatrix} = \frac{2\omega_1\omega_k}{\omega_k{}^2 - \omega_1{}^2}\begin{bmatrix} \omega_1 & -\omega_k \\ -1/\omega_k & 1/\omega_1 \end{bmatrix}\begin{Bmatrix} \xi_1 \\ \xi_k \end{Bmatrix} \tag{4.6}$$

In this analysis, the Newton algorithm was selected and the time step used for integration is 0.002 which is less or equal to the accelerogram time step. The simulated #10,record given in Table 4.12 and illustrated in Figure 4.10a was scaled to match the UHS for Montreal. The seismic response of the 4-storey MD-MRF building is shown in terms of time-history base shear in Figure 4.10b and roof displacement in Figure 4.10c. In particular, the behavior of the beam located at the central bay of the 2nd floor is analysed in terms of strain, stress and moment- curvature distribution. Thus, fibers of cross sections located in the plastic hinge region experienced strain levels ε beyond the elastic onset $\varepsilon_y = 0.002$ and the plastification process progresses,from the extrem fibers towards the interior fibers. As the plastification grows across the cross section's height, the element starts to exhibit hysteretic behaviour during the loading and unloading phases. This behavior is accentuated if the seismic demand increases. Strain and stress distribution across the cross section's height (W460x82) at different time steps is shown in Figure 4.10d and Figure 4.10e respectively, while the moment-curvature hysteresis loop is illustrated in Figure 4.10f.
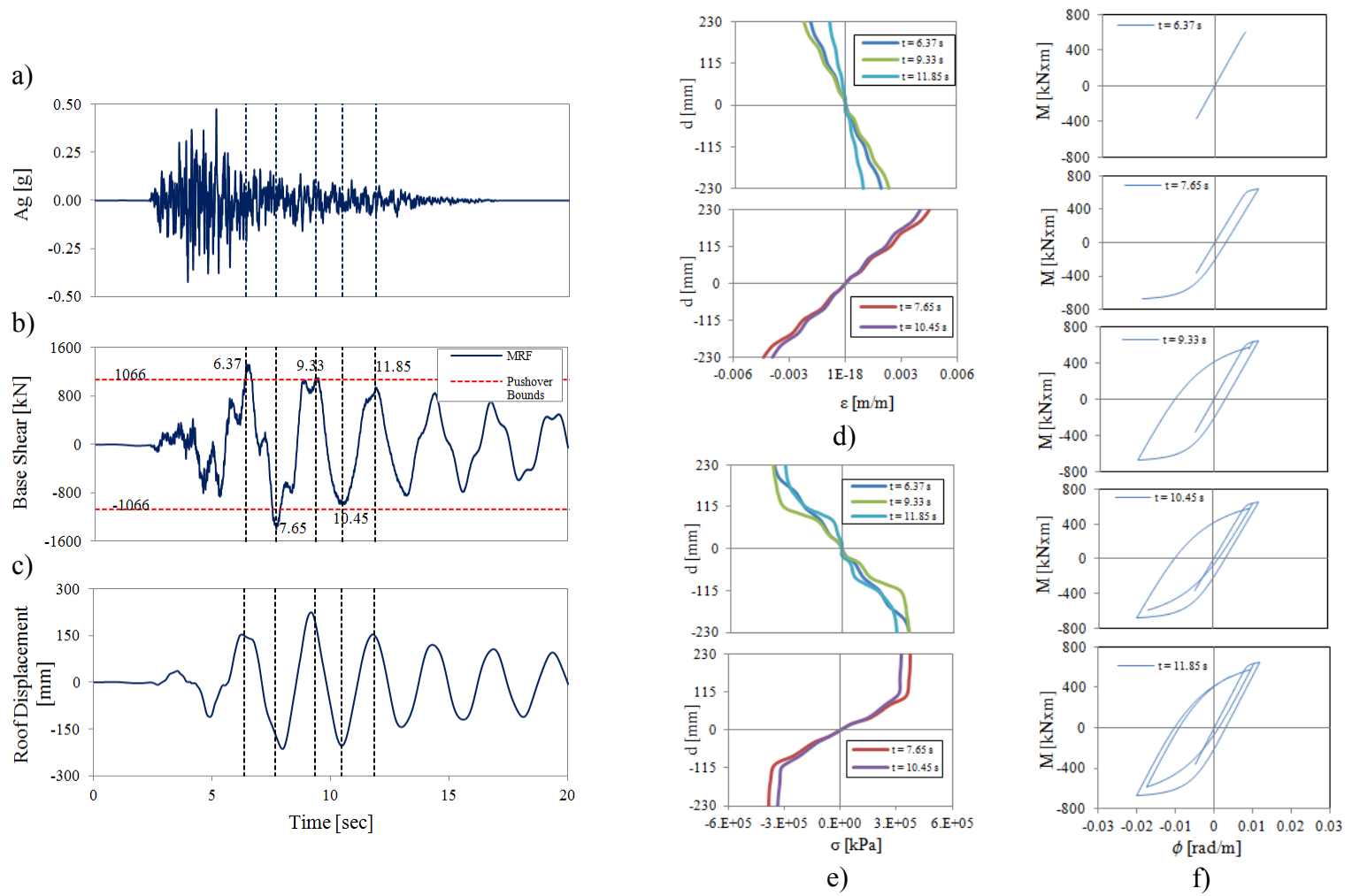
Figure 4.10 Seismic response of the 4-storey MRF: a) #10 simulated record; b) time-history and pushover base shears; c) time-history roof displacement; d) Strain distribution across the beam's cross section(W460x82 beam); e) Stress distribution and f)Hysteresis moment-curvature behaviour.

106

4.3 GROUND MOTIONS SELECTION AND SCALING METHODOLOGY

The NBCC requires the use of ground motions selected for the building location site (Montreal in this case) and scaled to be compatible with the 2% of exceedance in 50 years UHS for Montreal area.

Nevertheless, the Canadian code does not specify precisely the number of ground motions that should be used for analysis. However, in the Commentary J of the User's guide of Part 4 of NBCC 2010 it refers to the NERHP 2000 provisions that requires at least three records or seven or more records to be used in analysis. In this regard, the ASCE/SEI-7 is more precise and specifies: "if at least seven or more ground motions" are used in analysis, the engineering demand parameter (EDP) should be computed as the "*average*" value of the recorded EDP under the suite of ground motions. Otherwise, "if only 3 records are considered", the maximum value of the EDP shall be retained. This "*average*" value is not specified explicitly in the ASCE/SEI-7 as being the arithmetic mean, but has been commonly taken as mentioned (Reyes and Kalkan 2011). Hence, in order to consider the mean of the response parameters, fifteen simulated and historical records have been selected and used in this analysis.

Although the Commentary J of NBCC 2010 requires that the spectral acceleration of the record to equate the UHS ordinate corresponding to the main period of the building and to match or exceed the design spectral values for higher modes than the fundamental, it is clear that by applying this scaling factor, the spectral accelerations corresponding to short period ranges can exceed several times the design spectra. In addition, when specifying the period range of interest, the Commentary J of NBCC Part 4 does not

consider that the structure under seismic actions might enlarge the period of vibration due to inelastic behavior. For the reasons discussed, the scaling procedure in this study follows the requirements mentioned in the ASCE/SEI-7. Therefore, instead of scaling each individual record to be equal or larger than the UHS within the interval $0.2T_1$ to $1.5T_1$, in this study all records are scaled such that the mean of the response spectra of all considered records does not fall below the UHS over the range of interest.

The ASCE/SEI-7 procedure was implemented according to an optimization methodology developed by Reyes and Kalkan (2011) where the goal was twofold:

a) to rank the records from a set of scaled ground motions in function of the magnitude of the required scale factor. Herein, the scale factor is computed by minimizing the difference between the response spectra and the UHS over the period of interest $(0.2T_1 - 1.5T_1)$ ensuring that the mean of the response spectra is bigger or equal to that of the UHS;

b) to select from the selected ground motion assembly the suitable records (characterised by small scale factor) and to re-compute the scale factor based on the above procedure.

As computed in OpenSees, the fundamental period of the building in the N-S direction of the 4-, 8- and 12-storey building is given in Table 4.15 of part 4.4.

To analyse the behaviour of structure located in Montreal area, researchers have to rely mostly in simulated records than in historical ground motions. Upon today there are two seismic events that can be considered in analyses: the 5.9 magnitude Saguenay

earthquake (Quebec, November 1988) and the most recent 5.8 magnitude Virginia earthquake (USA, August 23/ 2011).

Regarding the simulated ground motions, Atkinson (2009) developed more than 180 records compatible with the UHS for eastern and western Canada, by considering different magnitudes and several fault-distances. For eastern Canada, two moment magnitude values M6 and M7 were considered as dominant. Thus, simulated records were generated according to M6 and M7 for different site classes and ranges of fault-distance: 10 to 15 km and 20 to 30 km for M6 and 15 to 25 km, 40 to 100 km for M7. In addition, each simulated record has three components (two horizontal and one vertical) which can be selected from the website: http://www.seismotoolbox.ca/NBCC2005.html.

Among the fifteen ground motions selected in this study for site class "C", fourteen are simulated records corresponding to M6 and M7 earthquake and different fault distances and one record was retained from Saguenay earthquake in the set of M6 as shown in Table 4.12. (From the available Saguenay records, only one matched the UHS, whereas the response of the others required scale factors larger than 10.) The accelerogram of the chosen 15 ground motions are shown in Appendix B.1. The response spectra of the 15 unscaled records is shown in Figure 4.11 against the UHS. The scale factor applied for records employed in the analysis of the 4-, 8- and 12-storey are given in Table 4.13, while the afferent response spectra across the period range of interest of scaled ground motion, the mean value, the mean ± one standard deviation and UHS are shown in Figures 4.12, 4.13 and 4.14.

Table 4.13 Selected records

| GM	M	R [km]	PGA [cm/sec²]	PGV [cm/sec]	PGV/PGA [sec]	Significant Duration* [sec]	Total Duration [sec]
#1	6	10.7	901	25.0	0.028	2.4	8
#2	6	12.8	753	30.4	0.040	1.3	12
#3	6	16.6	429	17.4	0.041	1.9	12
#4	6	21.5	273	8.0	0.029	2.0	12
#5	6	25.6	175	10.2	0.058	3.6	12
#6 (S7)	5.9	91.0	171	6.1	0.036	11.9	53
#7	7	13.8	586	49.7	0.085	7.5	20
#8	7	14.2	1060	67.3	0.063	5.5	20
#9	7	16.4	676	31.8	0.047	7.2	20
#10	7	20.1	467	22.4	0.048	6.8	20
#11	7	25.2	464	27.2	0.059	6.5	20
#12	7	41.6	224	13.5	0.060	8.4	22
#13	7	50.3	120	9.5	0.079	8.9	22
#14	7	69.9	88	9.6	0.109	9.6	22
#15	7	98.6	130	8.8	0.068	8.5	22

*See Appendix B
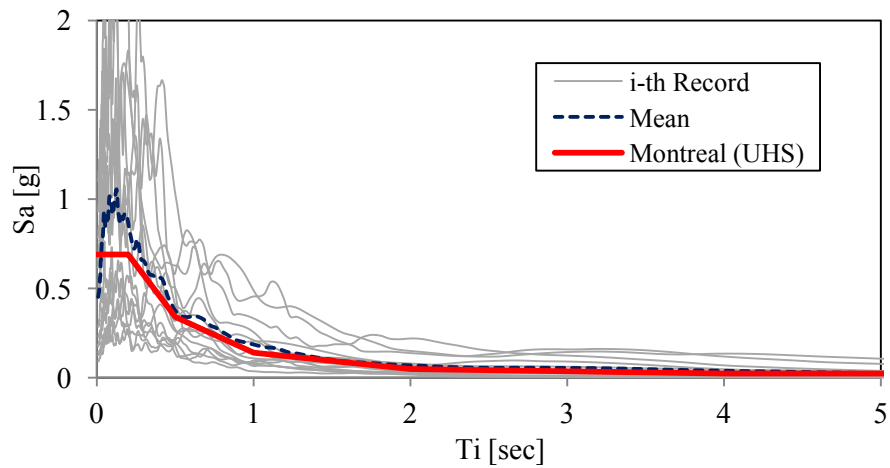
Figure 4.11 Response spectra of the selected records against the UHS defined for Montreal with site class C. The damping ratio for all the response spectra is 5%

110

Table 4.14 Scale factors for the 4-, 8- and 12-story Building
($T_{1(4-st)}$ = 1.67 s; $T_{1(8-st)}$ = 2.81 s; $T_{1(12-st)}$ = 3.95 s)

GM	Scale Factor (SF) for the 4-st building	Scale Factor (SF) for the 8-st building	Scale Factor (SF) for the 12-st building
#1	0.649	0.621	1.395
#2	1.007	1.021	1.452
#3	1.073	1.177	2.364
#4	1.611	1.991	3.863
#5	1.709	1.568	3.634
#6	2.208	3.898	6.807
#7	0.435	0.392	0.559
#8	0.385	0.409	0.592
#9	0.551	0.504	0.741
#10	1.012	0.954	1.354
#11	0.827	0.914	1.556
#12	1.513	1.324	2.099
#13	2.154	1.837	2.632
#14	2.383	2.188	3.221
#15	2.329	2.154	3.206
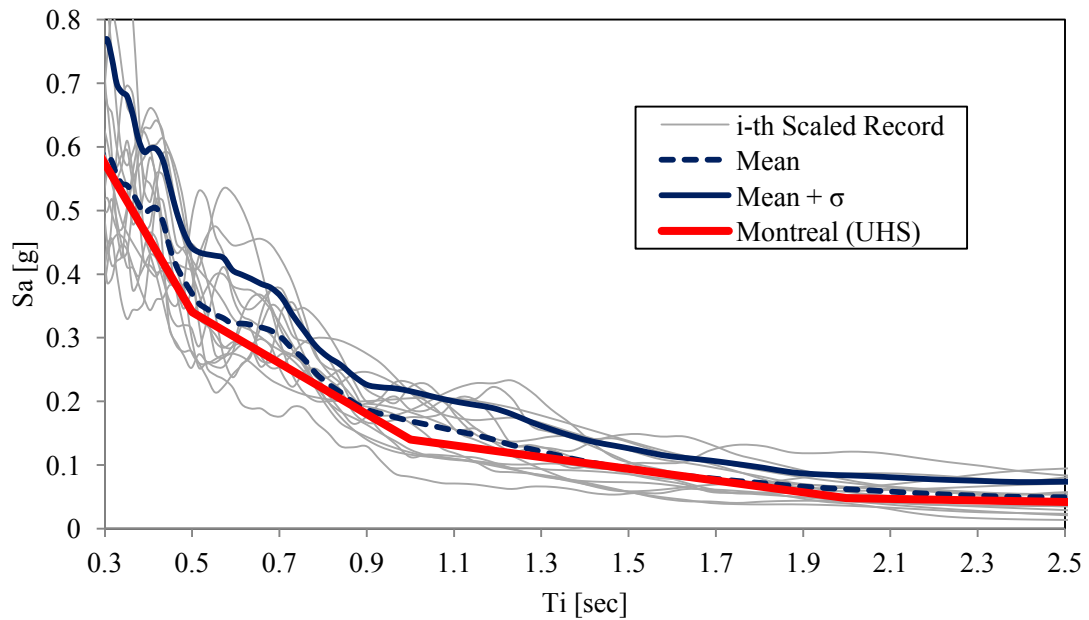
Figure 4.12 Scaled response spectra across the period of interest ($0.2T_1 - 1.5T_1$) for the 4-story building (T_1 = 1.67 s)
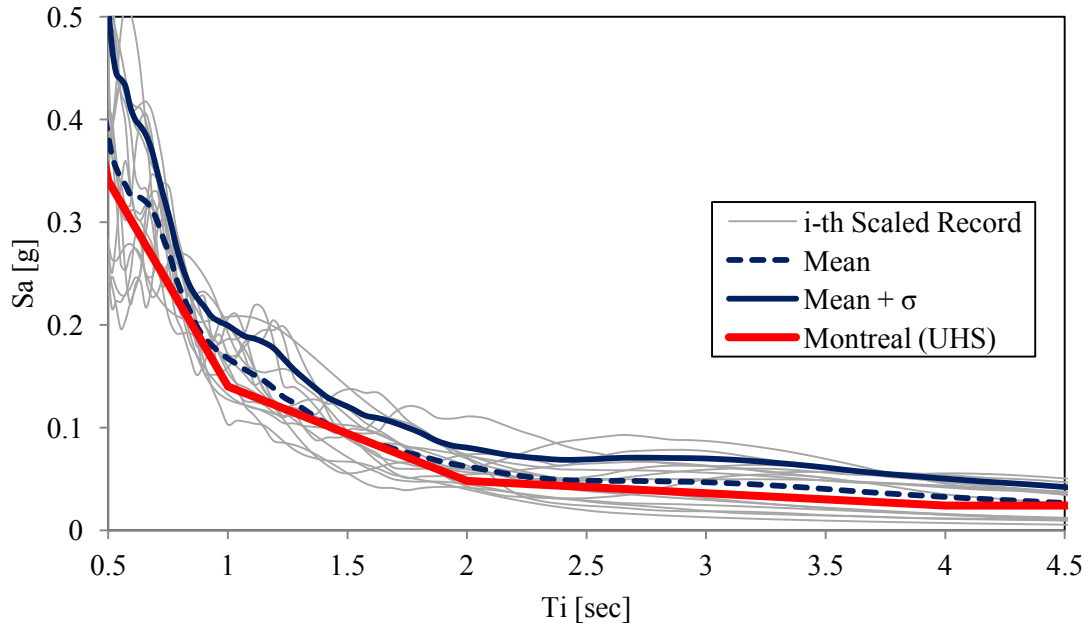
Figure 4.13 Scaled response spectra across the period of interest ($0.2T_1 - 1.5T_1$) for the 8-story building ($T_1 = 2.81$ s)
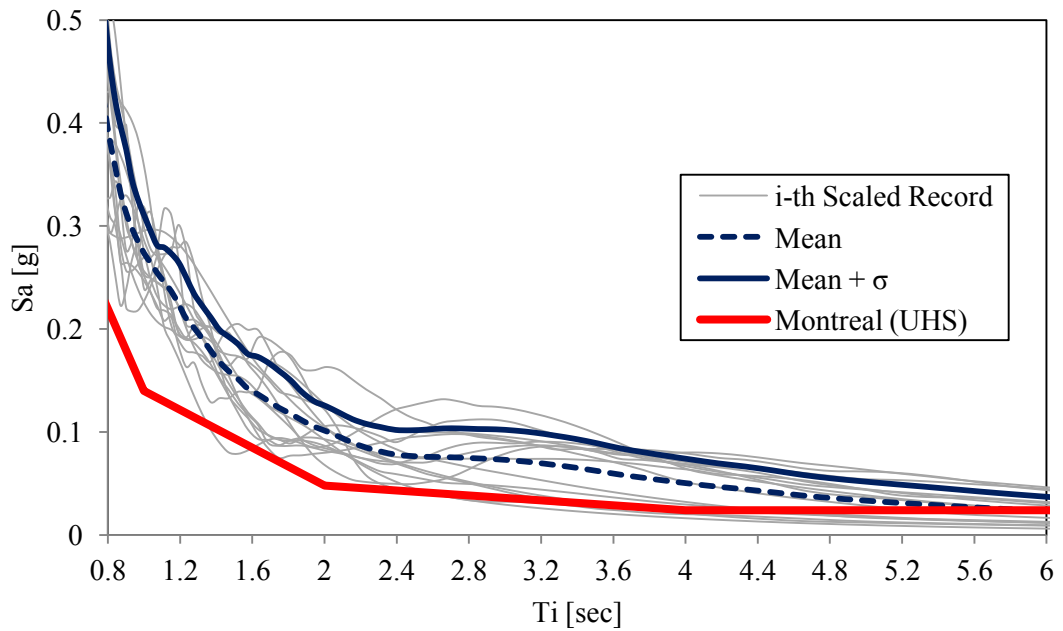

Figure 4.14 Scaled response spectra across the period of interest ($0.2T_1 - 1.5T_1$) for the 12-Story building ($T_1 = 3.95$ s)

4.4 BUILDING RESPONSE

The fundamental period of vibration in the North-South direction of the 4-, 8- and 12-storey building, computed in Sap2000 and OpenSees software are summarized in Table 4.16. It is clearly shown that the difference in building period is below than 5%. Although the analysis conducted in Sap2000 are linear and in OpenSees non-linear, the period of vibration is computed based on elastic stiffness matrix.

Table 4.15 Fundamental period of vibration of the 4-, 8-, and 12-storey building in SAP2000 and OpenSees

	T1 (s)	
Building	SAP2000	OpenSees
4-story	1.69	1.67
8-story	2.86	2.81
12-story	4.13	3.95

The three buildings modelled in the OpenSees software framework were subjected to the selected records which were scaled as described in section 4.3. In this study, recorders were defined in accordance with the EDPs related to the global response of structure such as: the interstorey drift Δs, given in $\%h_s$ and the drift angle *(Dumax/h$_z$)* in radians, as well as local response of structural members as maximum beam's plastic hinge rotation computed at each floor, θ_{max}. Herein the ratio *(Dumax/h$_z$) is* computed as the maximum story displacement *Dumax* divided by the distance from the base to the reference level (h_z) and the maximum beam's plastic hinge rotation per floor, θ_{max}, is calculated as the curvature recorded at the section level multiplied by the length of the plastic hinge which was assumed to be equal to the cross section's depth. In general the drift angle is the most stable parameter, while the interstorey drifts depend on the relative

storey strength and stiffness. For instance, Gupta and Krawinkler (2002), Medina and Krawinkler (2005) and other researchers have considered these EDPs in order to assess the performance of MRFs. The first two demand parameters are related to the deformability damage under lateral loads associated with the P-Δ effect, while the beam's plastic hinge rotation parameter accounts for the integrity of the MRF's connections and the permanent deformations developed at the level of the members across the plastic hinge length. To capture the maximum strain levels of MRF's members under each ground motion, a conventional scale of strain development based on the simplified stress-strain curve of the structural steel is shown in Figure 4.15. In this regard, for steel with *Fy* = *350MPa*, the strain at yielding, ε_y is approximately equal to *0.002* and the strain at which the material starts to experience strain-hardening, ε_{sh}, is considered as being equal to *(10ε_y)*. In addition, the elastic and strain hardening modulus, *E* and *E_{sh}*, are *200000MPa* and E_{sh} = *1/30E $\approx$ 670MPa*, respectively (Bruneau et al. 1998).

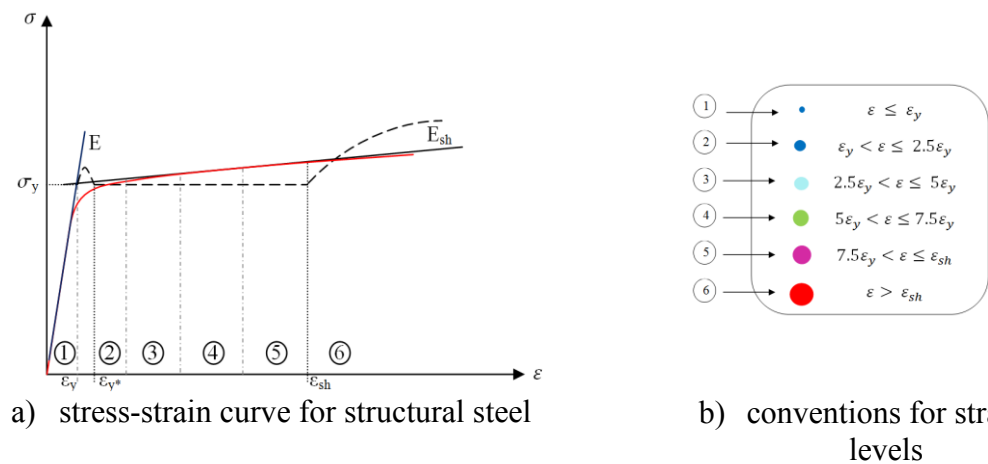a) stress-strain curve for structural steel   b) conventions for strain levels

Figure 4.15 Conventions for different strain levels in the strain-stress curve (dashed line) for structural steel (according to Bruneau et al. 1998). The approximation provided by the material in Opensees is shown by the red line

114

In Figure 4.16 and 4.17 the three aforementioned EDPs are summarized for the studied MRF buildings under the ensemble of scaled records. Thus, for the 8-th and 12-storey buildings the variation of the EDPs is more noticeable and the distribution across the building's height varies with each ground motion. On the other hand, taller buildings are experiencing large interstorey drift and the sections beyond the onset of yielding are appearing at some storeys rather than throughout all beams members for a specified record. Hence, for one record the beams at yielding are located at some storeys, whereas for other records the formation of plastic hinges may appear at others, which shows the dependency of the inelastic response on structure deformation as captured during the seismic excitation. On the other hand, since more than seven records were used, the mean value of the EDPs is computed and shown in the aforentioned figures. In these case studies, the mean value of the maximum interstory drift is larger than 1% h_s and reaches values of 1.24% h_s, 1.28% h_s and 1.87% h_s for the 4, 8 and 12-story buildings respectively. Thus, from computation is showed that the mean interstory at the design level is smaller than $2.5\%h_s$ and larger than $1\%h_s$ which implies damage of non-structural elements such as facades and partition walls. In all cases, the mean drift angle is larger than 0.007 radians which means the demand is in the plastic range. However, the mean beam's plastic hinge rotation is bellow 0.01radians which means a large reserve in the rotation capacity.

To explain the behaviour of studied buildings, a detailed response is shown in Figure 4.18 for the 4- and 8-storey building subjected to records #10 and #11 respectively. Thus, for both structures the maximum strain is below $5\varepsilon_y$ and was developed at the first floor for the 4-storey and the first and 3rd floor for the 8-storey

building, while curvature is in the range of Φy to $2.5\,\Phi y$. The seismic response of the 12-storey building under the record #15 is shown in Figure 4.19. However, in all beams belonging to the 12-storey frame, the strain at the location of plastic hinges was below than $5.0\varepsilon_y$ which means that the plastification of the entire cross-section was not encountered. In this case, the maximum curvature was signalised at the 9th and 10th floor where is close to $5\,\Phi y$. Therefore, reducing the seismic effects by using friction dampers is an appealing strategy.
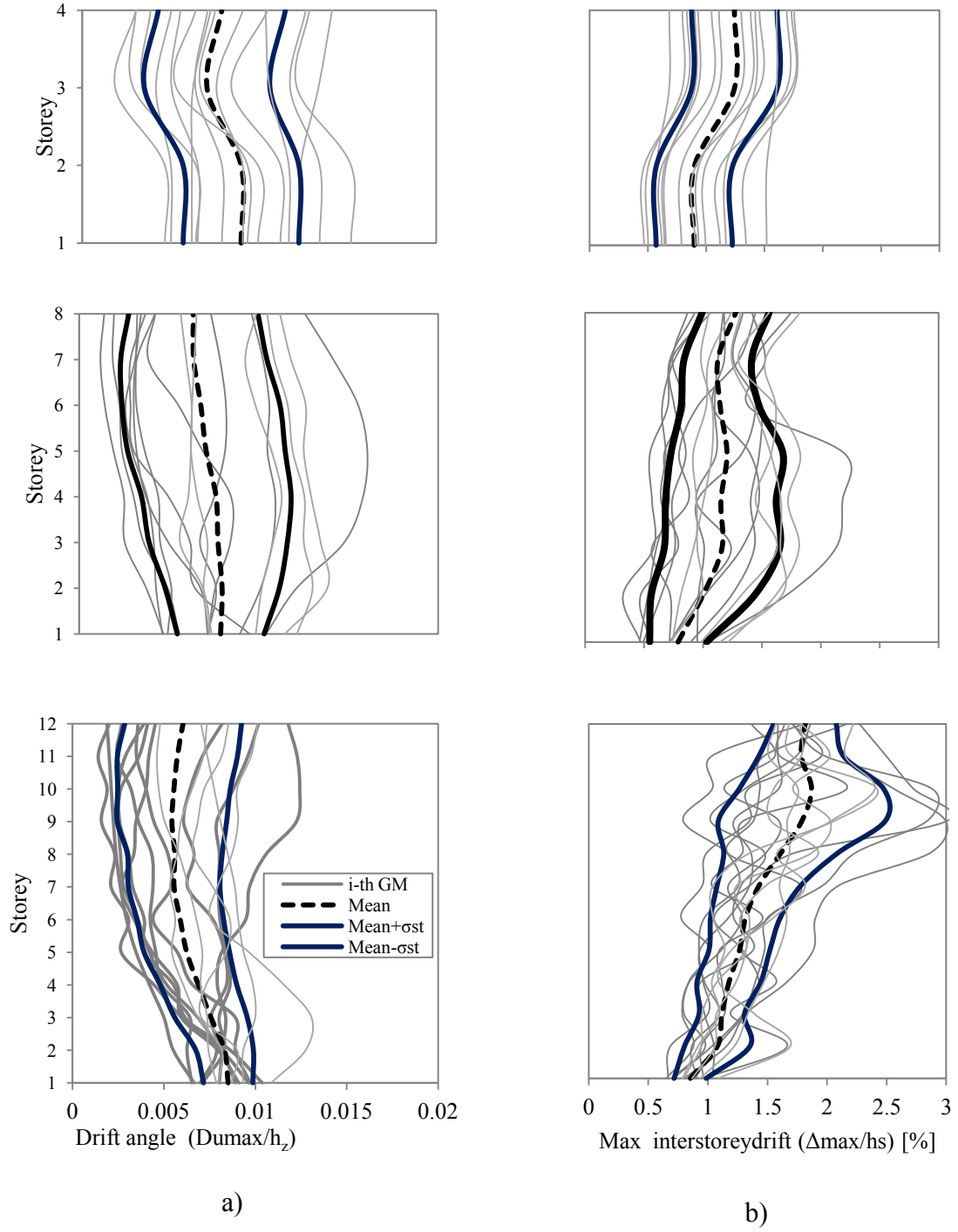
Figure 4.16 Response of 4-, 8-, and 12- storey MRFs building: a) Drift angle; b) Interstorey drift.
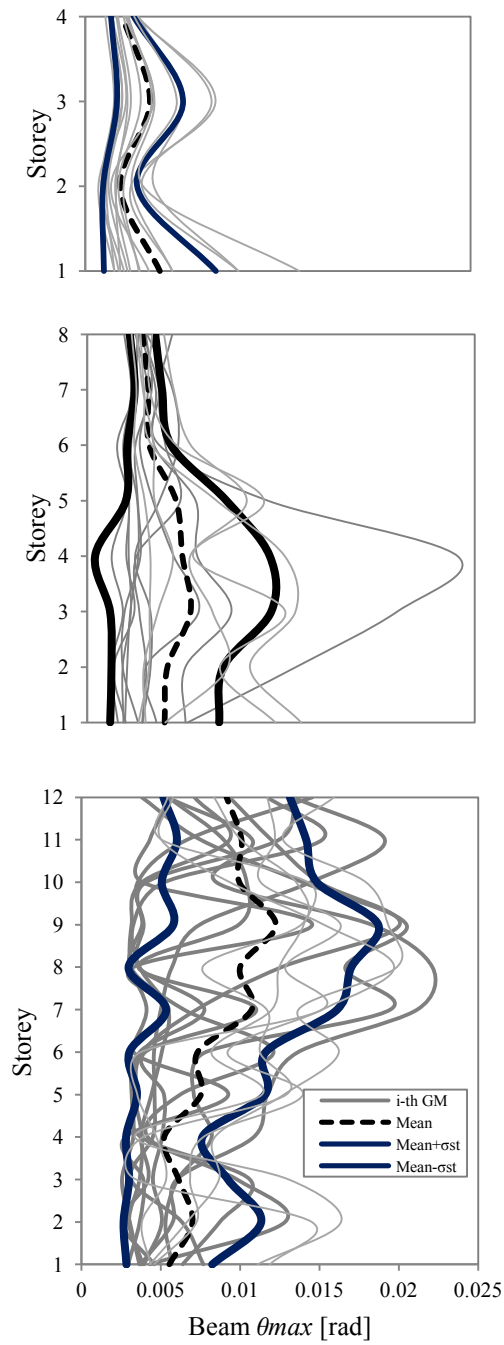
Figure 4.17 Response of 4-, 8- and 12-storey MRFs building: maximum beam's plastic hinge rotation per story, *θmax*.
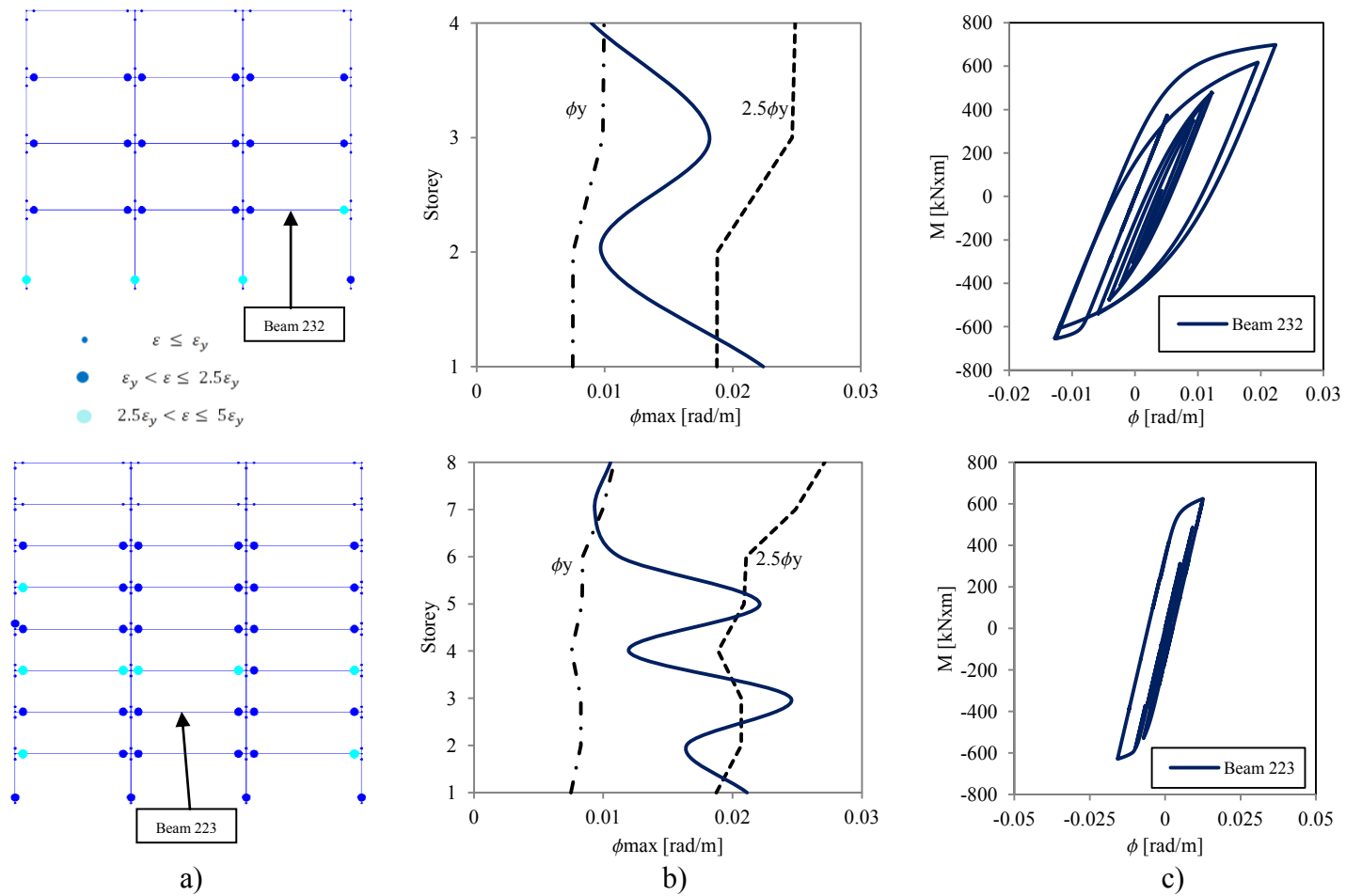
Figure 4.18 Response of the 4- and 8-storey MRF building under the records #10 and #11 respectively: a) strain history across the MRF's height; b) distribution of maximum curvatures computed for MRF's beams and c) beam's hysteresis behaviour
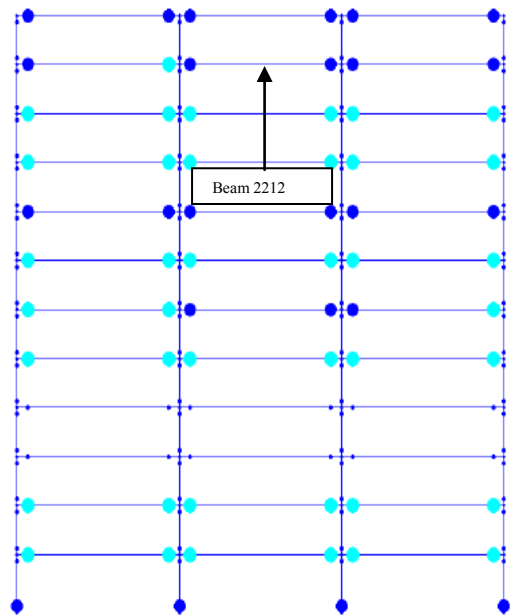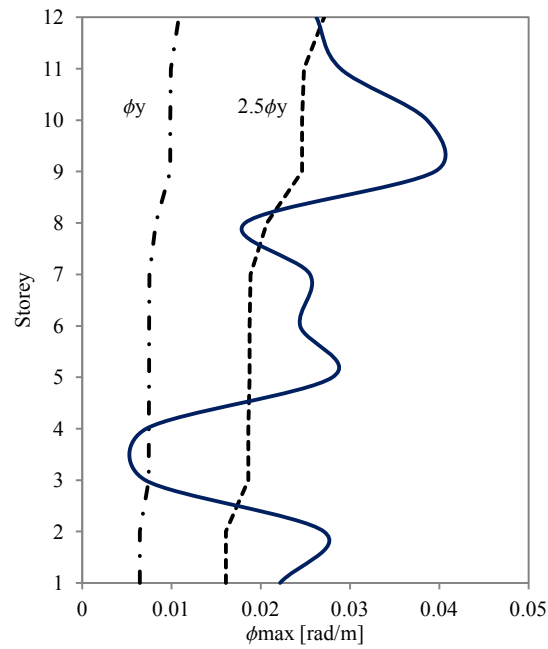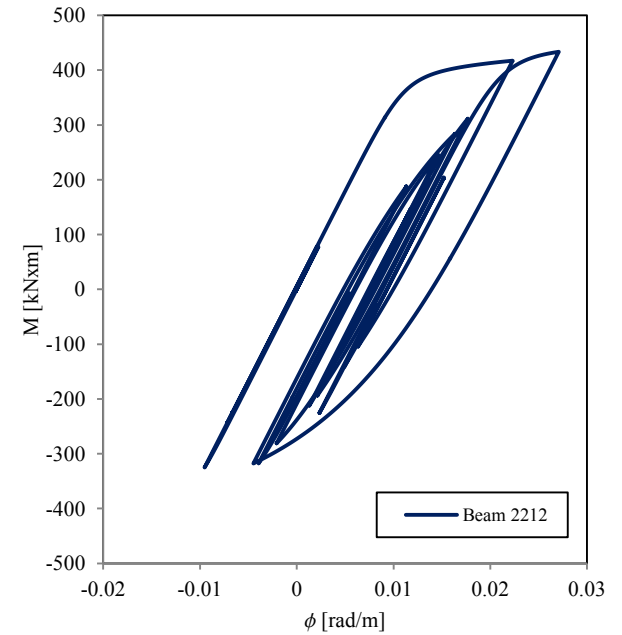
Figure 4.19 Response of the 12-storey MRF under the record #15. a) strain history across the MRF's height; b) distribution of maximum curvatures computed for MRF's beams and c) beam's hysteresis behaviour.

CHAPTER 5

Seismic Performance of 4-, 8-, and 12-Storey MRFs Building Equipped with Friction-Damped Diagonal-Bracing Devices

The performance of the MRFs was studied in the last chapter in term of the EDPs (maximum interstorey drift, maximum drift angle and maximum plastic hinge rotation per floor developed in MRF's beams). It was shown that for the studied 4-, 8- and 12-storey MD-MRF building located in Montreal, the mean interstorey drift is about $1.2\%h_s$ at the upper floors of the 4- and 8-storey building and it falls in the interval $1\%h_s$ to $1.9\%h_s$ for the 12-storey building. However, by adding damping and stiffness to a new or existing MRF building, located in a moderate to high risk seismic zone, the level of expected damage is substantially decreased.

Thus, the need of adding damping to an existing MD-MRF structure is justified in the following two cases: a) allow dampers to dissipate energy by friction, while the inelastic response of all structural MRF's members is reduced and b) decrease the level of expected damage by controlling the interstorey drift to be less than $1\%h_s$, with the aim to prevent the failure of non-structural components (e.g. brick facades, curtain walls, and others).

In this chapter, a study is conducted with the aim to deliver an efficient design for MD-MRF buildings equipped with friction-damped diagonal-bracing devices. From the

preliminary design of conventional MRF conducted in Chapter 4 part 4.1, it was noticed that members sizes are larger than those of the MD-MRF system. Thus, for economical reason and for the expectation of finding an equivalent ductility although the energy is dissipated by friction and the inelastic behaviour of MRF's members is largely decreased, the MD-MRF structure was retained for the bare frame system. In addition, a design procedure of the entire system was developed by minimising the difference between the total energy input and energy dissipated by friction dampers.

The performance of the MD-MRFs equipped with in-line brace-friction damper devices is evaluated numerically in OpenSees software framework by considering three different scenarios of brace location and 15 ground motions. In addition, friction damper in-line with diagonal-bracing device is modelled with and without consideration of slip-distance limitation.

5.1 DESIGN PROCEDURE FOR FRICTION-DAMPED DIAGONAL-BRACING SYSTEMS

In general, the design process of passive devices incorporated in a structural system consists of setting the number of dampers per floor, the value of slip-load and selecting their location (Tirca 2009). Essentially, this design process is made in two steps: i) find the optimum load activation of friction dampers per each floor; and ii) select the optimum location of dampers base on analysing the lateral deformation in order to minimise torsion.

Thus, the first step is related to find the optimum activation load (slip-load) of each damper, $V_{s,j}$ that consists of minimising the difference between the seismic input energy, E_I and the energy dissipated by dampers, E_h. It is mentioned that the energy concept was also employed by Filiatrault and Cherry (1988) in order to compute the parameters involved in structures with passive devices. These parameters depend mainly on the structure properties and frequency content of ground motion. Herein, the purpose of adding dampers to a bare frame system is to protect the MRF's members from seismic damage, while dampers are designed to slip when the shear deflection, $\varDelta_{s,j}$ is reached. By transposing the shear deflection, $\varDelta_{s,1}$, equation as well as the equation of energy dissipated by friction devices, $E_{f,1}$ of one-storey frame (Baktash and Marsh 1986) to a multi-story frame, the expression of the aforementioned parameters defined for the j-storey are given in Equations. (5.1) and (5.2).

$$\Delta_{S,j} = \frac{V_{f\&br,j} - V_{br,j}}{k_{u,j}} \tag{5.1}$$

In light of this, $V_{f\&br,j}$ is the shear force exerted by the frame and added braces at storey j, $V_{br,j}$ is the shear force exerted by the bracing system alone at level j and $k_{u,j}$ is the lateral stiffness of the unbraced frame (bare frame). By considering that the shear deformation of the frame after slipping is equal to the cosine projection of the slip drive distance, the energy dissipated by friction devices at storey-j is:

$$E_{f,j} = \frac{V_{br,j}\Delta_{S,j}}{\cos^2 \theta_j} = \frac{V_{br,j}}{\cos^2 \theta_j}\left(\frac{V_{f\&br,j} - V_{br,j}}{k_{u,j}}\right) \tag{5.2}$$

The seismic input energy developed at storey-j is given as follows:

$$E_{I,j} = V_{f\&br,j}\Delta_{f\&br,j} = (V_{f,j} + V_{br,j})\Delta_{f\&br,j} \tag{5.3}$$

where $\Delta_{f\&br,j}$ is the total shear deflection at floor j that contains the participation of frame and braces and $V_{f,j}$ is the lateral shear force at level j exerted by the unbraced frame alone. The minimised difference between the seismic input energy and the energy dissipated by friction devices is obtained by differentiating Equation (5.4) with respect to $V_{br,j}$ and equating the result to zero as is shown in Equation (5.5).

$$E_{I,j} - E_{f,j} = (V_{f,j} + V_{br,j})\Delta_{f\&br,j} - \frac{V_{br,j}}{\cos^2\theta_j}\left(\frac{V_{f\&br,j} - V_{br,j}}{k_{u,j}}\right) \tag{5.4}$$

$$\frac{\partial E_{I,j}}{\partial V_{br,j}} - \frac{\partial E_{f,j}}{\partial V_{br,j}} = \Delta_{f\&br,j} - \frac{V_{f\&br,j}}{k_{u,j}\cos^2\theta_j} + \frac{2V_{br,j}}{k_{u,j}\cos^2\theta_j} \tag{5.5}$$

By expressing $\Delta_{f\&br,j} = V_{f\&br,j}/k_{f\&br,j}$, the solution of Eq. (5.5) is equal to:

$$V_{br,j} = \frac{V_{f\&br,j}}{2}\left[\sin^2\theta_j + \left(\frac{k_{br,j}}{k_{f\&br,j}}\right)\cos^2\theta_j\right] \tag{5.6}$$

where $k_{br,j}$ is the lateral stiffness of braces alone and $k_{f\&br,j}$ is the lateral stiffness of MRF equipped with braces.

Once the shear force exerted by braces alone at the j-storey $V_{br,j}$ and the stiffness of braces were found, the slip-load calculation became straightforward. Based on FEMA 356 Provisions, diagonal-bracing system is designed to behave elastically in axial tension and compression under a force equal to 130% design slip-load. Thus, the summation of the horizontal component of slip-load per floor is equal to the ratio $V_{br,j}/1.3$. The optimum slip-load distribution over the building height is determined based on numerical analyses and is depended on the lateral shear force distribution.

According to the findings of Levy et al. (2000) the stiffness of the structure is assumed as follows: i) the stiffness of the MR frame with braces and dampers is equal to the stiffness of the braced frame (MRF with braces) as long as the slip-load is not activated in dampers and the velocity of sliding surfaces within the friction damper is equal to zero; ii) the stiffness of the structural system is equal to the MRF stiffness when the slip-load is reached and the velocity of sliding surfaces within the friction dampers is larger than zero and equates the storey velocity at each floor. It is noted that any reverse horizontal movement applied to the structure returns the system to the initial stage. After the total number of dampers is calculated based on Equation (5.6), their optimum location throughout the building may be assigned by controlling the torsional seismic response. In this regard, especially for plan-asymmetric buildings, the optimum location of the friction-damped diagonal-bracing system may be found by employing the Kokil and Shrikhande (2007) objective function $f(x)$ as given in Equation (5.7), where V_u and Δ_u are the maximum base shear and maximum interstorey drift in the MRF structure.

$$f(x) = \frac{V_{f\&br,j}}{V_u} + \frac{\Delta_{f\&br,j}}{\Delta_u} \qquad (5.7)$$

However, by choosing pairs of tension-compression braces incorporated into an existing steel frame building, the processing data for optimal dampers location based on minimising Equation (5.7) is reduced. Generally, there are four dampers located in X-direction and four dampers located in Y-direction. It is assumed that among the four dampers, two of them act in tension and the other two in compression. To minimise the torsional effect it is required that at least two dampers (one in each direction) to be located in one quarter of the building floor area (FEMA 356).

It is known that adding stiffness to an existing building the interstorey drift is reduced while adding damping the magnitude of forces developed in all structural members are also reduced. In contrast with the conventional braced frame system, the added in-line brace –friction damper devices doesn't need to be vertically continuous in order to dissipate the amount of energy as required by design. However, this statement is discussed in part 5.4 of this Chapter. In order to optimise the amount of supplemental damping added to a MRF building, it is mandatory to verify the stiffness distribution over the structure height. Although the storey stiffness calculation is not well defined in the building code, herein the recommendation given by Paulay and Presley (1992) is considered and the calculation of storey stiffness is made by dividing the storey shear to the interstorey drift at each floor level. Storey shear and interstorey drift are the response of the building to an arbitrary horizontal force applied in the centre of masses of the roof level. The normalised value of storey stiffness for the bare frame building in the direction of calculation is shown in Figure 5.1. It can be seen that in general the ground floor of the MRF buildings which is characterised by larger storey height provides smaller stiffness than the floor above which can lead to soft story mechanism formation. However, the mean responses of the maximum interstory drift obtained from nonlinear time integration analysis and shown in Chapter 4 (Fig. 4.16) revels that storey drift is larger than *1%h$_s$* and the maximum value is encountered at the most upper floors.

By applying the aforementioned method, the results are summarised in Table 5.1 for the 4-, 8- and 12-storey building. Thus, the table contains the shear force per floor exerted by the MRF with braces $V_{f,j+br,j}$; the shear force per floor exerted by the bracing system alone $V_{br,j}$ (computed as per Equation (5.6)); the sum of the horizontal projection

126

of the slip load magnitude per floor computed as $V_{br,j}/1.3$; the total number of devices per floor; the optimal slip load $P_{i,j}$ per device and the assigned slip load P to each device, as well as the total slip load per floor P_{storey}. In addition, the same Table shows the stiffness ratio $k_{br,j}/k_{f,j+br,j}$. For the MRF system and for the system of MRF with in-line brace-friction damper devices, the normalised storey stiffness over the structure height is illustrated in Figure 5.1. It is shown that the stiffness of each lowest storey exceeds or equates that of the storey immediately above.
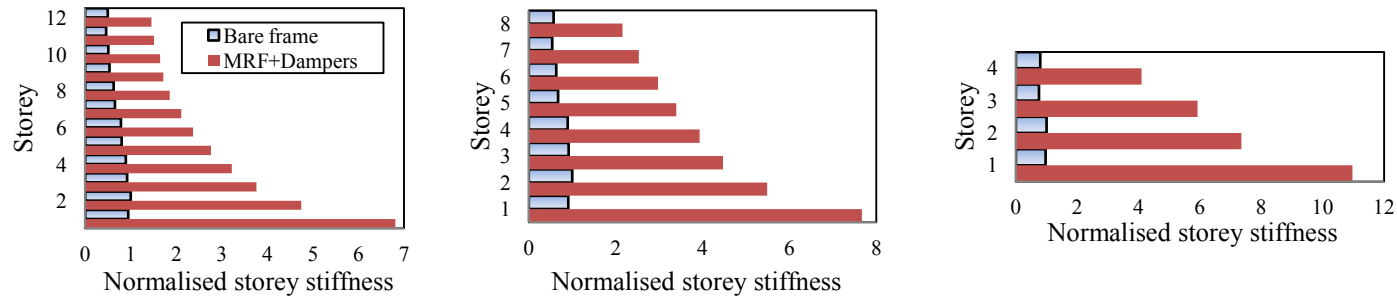
Figure 5.1 Normalised storey stiffness over the structure height: a) 12-storey, b) 8-storey and c) 4-storey buildings with dampers allocated at each floor

Table 5.1 Shear force and the optimum dampers slip-load settings for the studied buildings

St (j)	12-Storey							8-Storey							4-Storey					
	$k_{br,j}/k_{f\&br,j}$	$V_{f\&br,j}$ [kN]	$V_{br,j}$ [kN]	$V_{br,j}/1.3$ [kN]	$P_{i,j}(*)$ [kN]	P [kN]	P_{story} [kN]	$k_{br,j}/k_{f\&br,j}$	$V_{f\&br,j}$ [kN]	$V_{br,j}$ [kN]	$V_{br,j}/1.3$ [kN]	$P_{i,j}(*)$ [kN]	P [kN]	P_{story} [kN]	$k_{br,j}/k_{f\&br,j}$	$V_{f\&br,j}$ [kN]	$V_{br,j}$ [kN]	$V_{br,j}/1.3$ [kN]	$P_{i,j}(*)$ [kN]	P [kN]	P_{story} [kN]
12	0.66	589	214	165	92	300	600														
11	0.70	867	328	252	141	300	600														
10	0.69	1120	421	324	181	300	600														
9	0.69	1349	507	390	218	300	600														
8	0.66	1553	567	436	244	300	600	0.74	620	244	188	105	300	600							
7	0.69	1733	652	501	280	300	600	0.79	1031	428	329	184	300	600							
6	0.67	1887	694	534	298	330	660	0.79	1385	575	442	247	300	600							
5	0.71	2017	775	596	333	330	660	0.80	1682	707	544	304	330	660							
4	0.72	2123	826	635	355	350	700	0.77	1923	786	605	338	350	700	0.81	650	275	211	118	300	600
3	0.76	2203	886	681	381	380	760	0.79	2106	880	677	378	380	760	0.87	1186	533	410	229	300	600
2	0.79	2258	939	722	404	400	800	0.82	2233	954	733	410	420	840	0.86	1554	692	533	298	330	660
1	0.86	2288	1026	790	459	450	900	0.88	2302	1050	807	469	480	960	0.91	1756	821	631	367	380	760

(*): $P_{i,j}=V_{br,j}/(1.3QCos\theta_j)$, where Q is the number of devices per frame at determined storey (as shown in Figure 5.4 and Figure 5.5. Q = 2 for all the analyzed cases) and θ_j is the angle of the brace with in-line friction damper at the j-th storey

5.2 SEISMIC RESPONSE OF THE 4-, 8-, AND 12-STOREY MRF BUILDING EQUIPPED WITH FRICTION-DAMPED DIAGONAL-BRACING DEVICES WITHOUT MODELING THE SLIP-LOCK PHASE

In order to show the enhancement of the response of MD-MRFs equipped with friction dampers three scenarios of devices location were evaluated for each studied building. The first one, scenario A, consists of friction dampers located at each floor, the second scenario, B, corresponds to dampers staggered at alternate open storeys as per Filiatrault and Cherry study (1988) and scenario C considers a number of dampers lesser than case B. It is noted that scenario C with staggered devices is rather a parametric study than a result of an optimisation procedure. The building elevation with dampers' locations for each scenario is shown in Figure 5.2 and 5.3. Each scenario was analyzed under 15 records scaled for Montreal area. The responses of these scenarios without modeling the slip-lock phase are given in Appendix C.

The Bouc-Wen material parameters γ and β are given in Table 5.2 together with the slip force per damper and the elastic deformation, u_y, of the brace projected on the diagonal direction corresponding to the slip force. The parameters defining BoucWen material are computed as per Equations given in Chapter 3 and the slip force per damper is the same as that given in Table 5.2 for the 4-, 8- and 12-storey building. The fundamental period of the studied buildings computed for the three scenarios is shown in Table 5.3.

The history of roof displacement of the 4-storey MFR building is showed in Figure 5.4a against those computed for each MRF with devices installed accordingly to scenarios A, B, and C. This case illustrated in Figure 5.4b emphasises the seismic

response under record #2. Thus, the time at which the first damper is activated is close to the 5% of the Arias intensity (AI) of the ground motion, with the exception of scenarios C. Beyond this point, the differences between responses becomes more evident due to the increment of the input energy. After the ground motion has accumulated 95% of AI, friction dampers are still activated until the end of the shaking and even after during the free vibration phase. Before devices are activated, the response is undamped and the behaviour of bare frame with added braces and that with added braces and friction devices is almost the same. For instance, Figure 5.4a scenario C shows that by adding only one brace at the bottom of the structure the period doesn't change too much in comparison with the MRF. For this regard, the elastic time-history response is almost similar until damper is activated. In general, when the device is activated, the effective stiffness of the brace with in-line friction damper approaches zero and the stiffness of the structure equate the stiffness of the bare frame while dissipating energy through the hysteretic behaviour of devices. However, the general trend doesn't follow exactly the bare frame response since all devices are not activated simultaneously and/or undergo the maximum slip distance at the same time. Thus, for scenario C the total duration between the first and the last activation is 3.18s and the hysteresis loop for the friction-damped diagonal-brace located at the 1st floor is shown in Figure 5.5a. Meanwhile, for scenarios B and A the total duration between the first and the last activation of slipping is 2.65s and 2.09s, respectively. In addition, the hysteresis loop for the 1st floor brace is shown in Figure 5.5b and 5.5c. Therefore by adding more dampers into a structural system, the slipping distance exhibited by each damper is reduced. Thus, without imposing the slip-lock phase in the model, the required slipping distance computed for each damper during

the sliding phase under the input of 15 ground motions is shown in Figure 5.6. For scenario B, record #2 leads to the largest demand of slip distance, such as *usmax = 21mm,* followed by records: # 9; #10, #11, #13 and #14.

On the other hand, Figure 5.7 shows the enhancement of the building response when devices are incorporated to match the three scenarios. Regarding this, the monitored EDPs are: interstorey drift measured in *%h$_s$*, drift angle and maximum beam plastic hinge rotation per floor measured in radians. Therefore, the mean value of the aforementioned EDPs, resulted from the response of MFR with devices subjected to the assembly of 15 ground motions is shown in Figures 5.7a, 5.7b and 5.7c against the EDPs computed for the bare frame. Thus, for the 4-storey building, even in the case of scenario C, the mean value of the interstorey drift drops below *1%h$_s$* and all beams plastic hinge rotations are in the elastic range. The computed 84% percentile (P84) defined as the value exceeding the 84% of the set of maximum EDPs recorder per storey is shown in Figure 5.7d, 5.7e and 5.7f. The reduction in the inelastic response of MRF tends to recenter the system after the occurrence of earthquake. Nevertheless, even when all the MFR members are behaving elastically, there is not a complete recentering because as noted in the hysteresis loops of the friction dampers there will be always small residual displacements in the device. If the bare frame is a CBF, no lateral stiffness is provided when dampers are activated and no frame action can be claimed.

A similar response is obtained for the 8 and 12-storey building and is exemplified under the records #10 and #8. The three scenarios considered for this analysis are shown in Figures 5.2 and 5.3. The roof time-history displacement for the 8-storey building as per scenarios A, B and C are shown in Figure 5.8. Herein, for the 8-storey building with

devices, the response of scenarios B and C is approximately similar. In this example, scenario B contains 8 devices (4 in each direction) and scenario C contains 6 devices. As is shown, in both cases devices are activated near the 5% AI. Especially for scenario C, dampers start to be activated almost at the beginning of ground motion and the last activation of dampers was signalised right after the 95% AI. For scenarios A and B the last activation was recorded before t =14.0s while the total ground motion duration is 20s. Figure 5.8b shows the accelerogram time-history of record #10. The hysteresis loop of the first floor brace with damper belonging to the MRF with devices installed as per scenarios A, B and C is shown in Figure 5.9a, 5.9b and 5.9c. Among the 15 ground motions, the maximum slip distance recorded for the 8-storey building under record #11 was 30mm. A large displacement was recorded under #8 too as shown in Figure 5.10. Similarly, the same EDP computed for the 8-storey building are shown in Figure 5.11a. 5.11b and 5.11c while the 84% percentile (P84) of the aforementioned parameters are shown in Figures 5.11d, 5.11e, and 5.11f. Therefore, by adding a reduced number of devices, the maximum interstorey drift drops below *0.75%h_s* versus *1.25% h_s* for the bare frame, while plastic hinges start to be initiated in MRF's beams.

On the other hand, for the 12-storey building, the time-history roof displacement under the record #8 for the three cases (A, B, C) is shown in Figure 5.12a. In this case, the three scenarios registered the first activation of the dampers practically at the beginning of the record (see Figure 5.12b), before the 5% AI was reached. However, scenarios A and B recorded the last slip phase earlier than in scenario C. The later showed excursions into the slip phase during the free vibration. Herein in case of scenario B, the maximum travel displacement along the diagonal direction is 56mm and occurred

under record #11 (Figure 5.14). By projecting this value on an horizontal line, it exceeds the *1.0%h$_s$*. The EDPs are shown in Figures 5.15a, 5.15b and 5.15c and the envelope of the 84% percentile (P84) of EDPs is shown in Figures 5.15d to 5.15f. For the bare frame, the maximum interstorey drift is almost 2%hs and drops below 1%hs if only 8 dampers are added, while the rotation of beams is less than 0.004 radians for a damped response.

Therefore, in all cases, the mean interstory drift was reduced to lesser than 0.75%h$_s$ for all studied scenarios of the 4- and 8- and 12-storey building without the case of 12-storey scenario C. It was recorded that in average all MRF members have an elastic behaviour. In addition, it was observed that plastic hinges were initiated in MRF members when the drift ratio was larger than *1%h$_s$*. Accordingly, by adding staggered friction dampers to a MD-MRF system designed with an *R$_d$= 3.5* and *R$_0$ = 1.5* (R$_d$R$_0$ = 5.25) the maximum beam rotation was reduced as well as the maximum interstorey drift and floor displacement. In addition, the envelope of the 84% percentile (P84) of EDPs is in general closer to the mean value for the damped MRF buildings as illustrated in Figures 5.7d, e ,f, 5.11d, e, f and 5.15d, e, f. The maximum reduction in building response parameters was reached for scenarios A and B, although the number of dampers in scenario B is half than in scenario A. However, even for a minimum number of dampers as illustrated in scenario C an important improvement in the response recorded in term of interstorey drift was observed. Therefore, placing dampers in all storeys is not necessary. From the above analysis, scenario B with staggered distribution devices is recommended as being the most cost-efficient system able to reduce the interstorey drift below *0.75%h$_s$* even for the 12-storey and in a consequence the building facade is protected from collapse during a seismic event in Montreal.

From the above analysis it was concluded that the demand slip distance is an important parameter. If the demand slip distance is larger than the available slip distance, then the slip-lock phase has to be study. On the other hand, by providing larger slotted hole the positive aspect of elastic MRF action is diminished, but friction damper is prevented from failure. Regarding this, Figure 5.16 shows the maximum slip distance demands, defined as the largest absolute displacement recorded along the diagonal direction, and the mean values for the three buildings analyzed with the configuration of scenario B. For the 4-storey building, the mean of the slip distance demand (u_{smax}) is 15mm (see Figure 5.16a) and the mean plus one standard deviation is 19mm. For the 8-storey building, the mean of the slip distance demand is 18mm (Figure 5.16b) and the mean plus one standard deviation is 24mm. In the case of the 12-storey, the mean of the slip distance demand is 28mm (see Figure 5.16c) and the mean plus one standard deviation is 38mm. From these analyses and in order to avoid the slip-lock phase, the following values for slip distance are recommended for design: 20mm for the 4-storey building; 25mm for the 8-storey building and 35mm for the 12-storey building. In addition it is recommended that MRF with devices to be designed to undergo a mean interstorey drift around $1\%h_s$. If an interstorey drift larger than $1\%h_s$ is recorded, the failure mechanism of the device must be known in order to properly define the slip-lock phase in the computer model. In all case studies, torsion was neglected and P-Δ effect was included.

Specimen 4A   Specimen 4B   Specimen 4C

Specimen 8A   Specimen 8B   Specimen 8C

a)   b)   c)
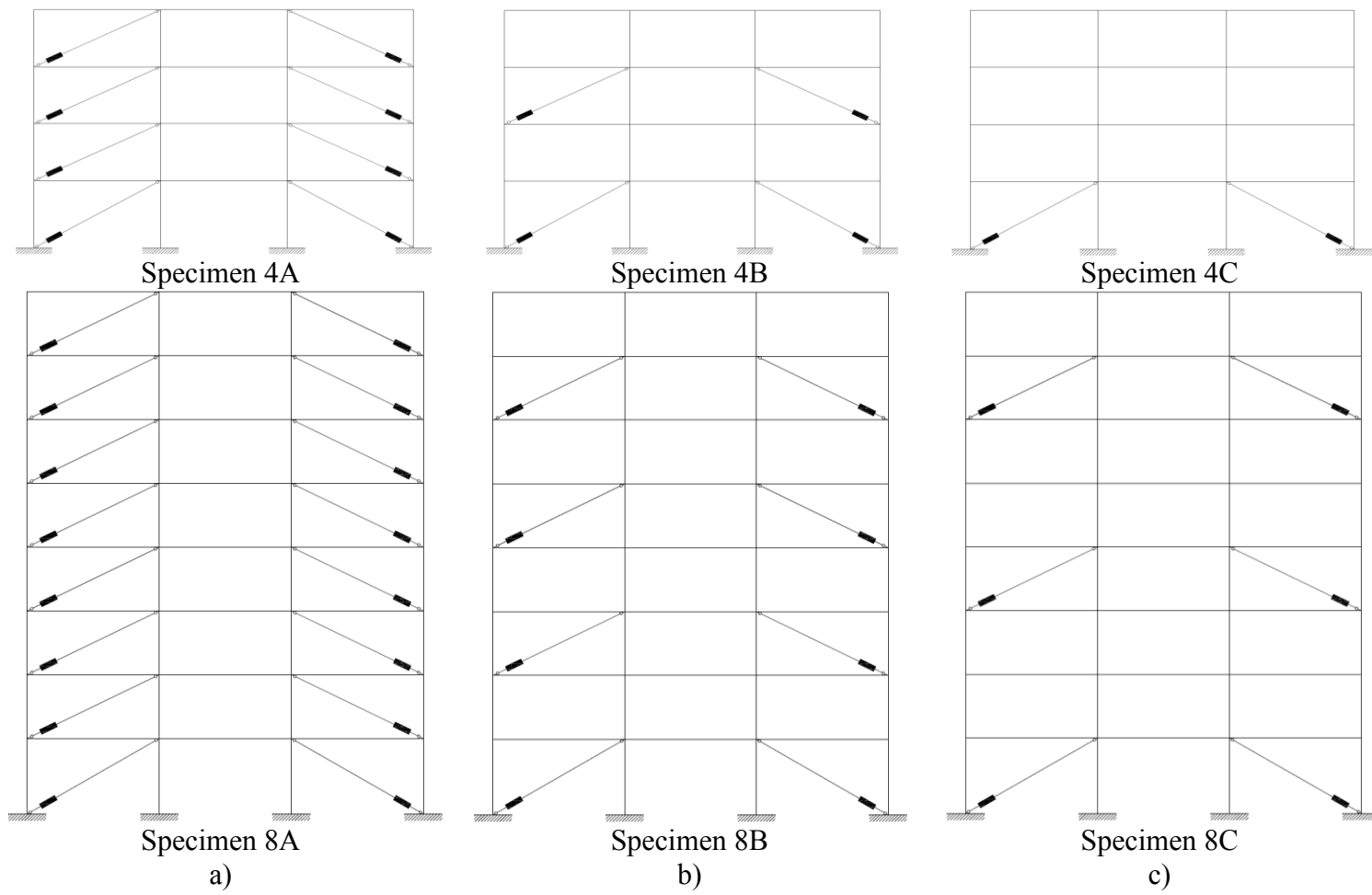
Figure 5.2 Configurations of the 4- and 8-storey MRF with in-line brace friction damper: a) scenario A; b) scenario B; c) scenario C

135
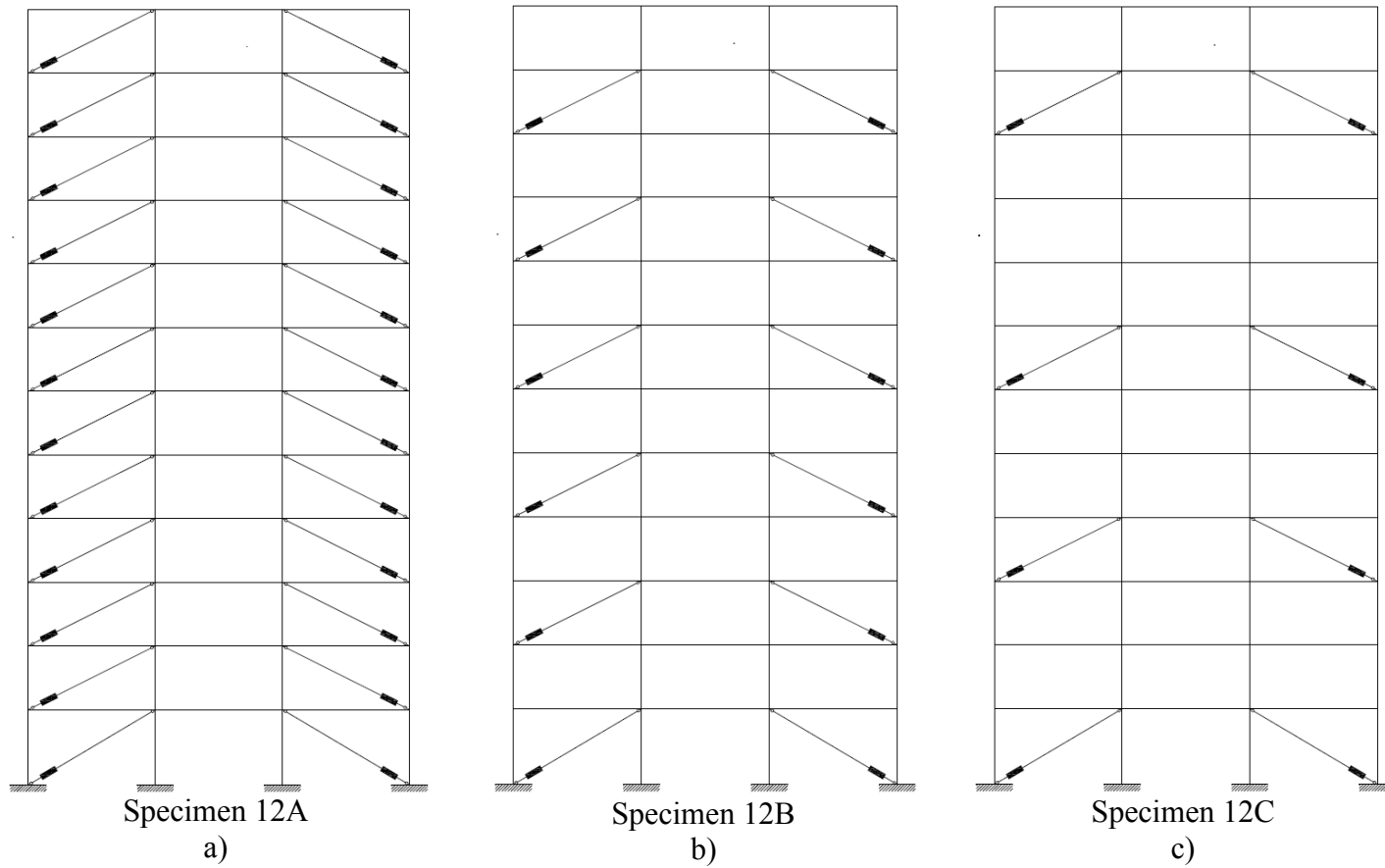
Figure 5.3 Configurations of 12-storey MRF with in-line friction damper: a) scenario A; b) scenario B; c) scenario C.

Table 5.2 Parameters for the SHM in OpenSees (BoucWen material) with no degradation ($\delta_A = \delta_v = \delta_\eta = 0$) considering: $\alpha = 0.00001$, n = 10, A_o =1 and k_o = E

St.	12-Storey				8-Storey				4-Storey			
	Brace Section	P [kN]	u_y [mm]	$\gamma=\beta$	Brace Section	P [kN]	u_y [mm]	$\gamma=\beta$	Brace Section	P [kN]	u_y [mm]	$\gamma=\beta$
12	HS178x8	300	3.4	2.77E-06								
11	HS178x9.5	300	2.8	1.49E-05								
10	HS203x9.5	300	2.5	6.29E-05								
9	HS203x9.5	300	2.5	6.29E-05								
8	HS203x9.5	300	2.5	6.29E-05	HS152x13	300	2.6	3.44E-05				
7	HS203x13	300	1.9	8.60E-04	HS178x13	300	2.2	1.96E-04				
6	HS203x13	330	2.1	3.32E-04	HS178x16	300	1.8	1.35E-03				
5	HS203x16	330	1.7	2.46E-03	HS203x16	330	1.7	2.46E-03				
4	HS203x16	350	1.8	1.37E-03	HS203x16	350	1.8	1.37E-03	HS178x13	300	2.2	1.96E-04
3	HS254x13	380	1.9	9.64E-04	HS254x13	380	1.9	9.64E-04	HS203x13	300	1.9	8.60E-04
2	HS254x13	400	2.0	5.77E-04	HS254x13	420	2.1	3.54E-04	HS203x13	330	2.1	3.32E-04
1	HS254x16	450	2.0	4.14E-04	HS254x16	480	2.2	2.17E-04	HS254x16	380	1.7	2.24E-03

Table 5.3 Fundamental periods of MRF with in-line friction dampers in different configuration according to Figures 5.4 and 5.5

Building	T1 (s)		
	Scenario A	Scenario B	Scenario C
4-storey	0.53	0.90	1.45
8-storey	1.33	1.97	2.22
12-storey	2.14	2.73	3.06
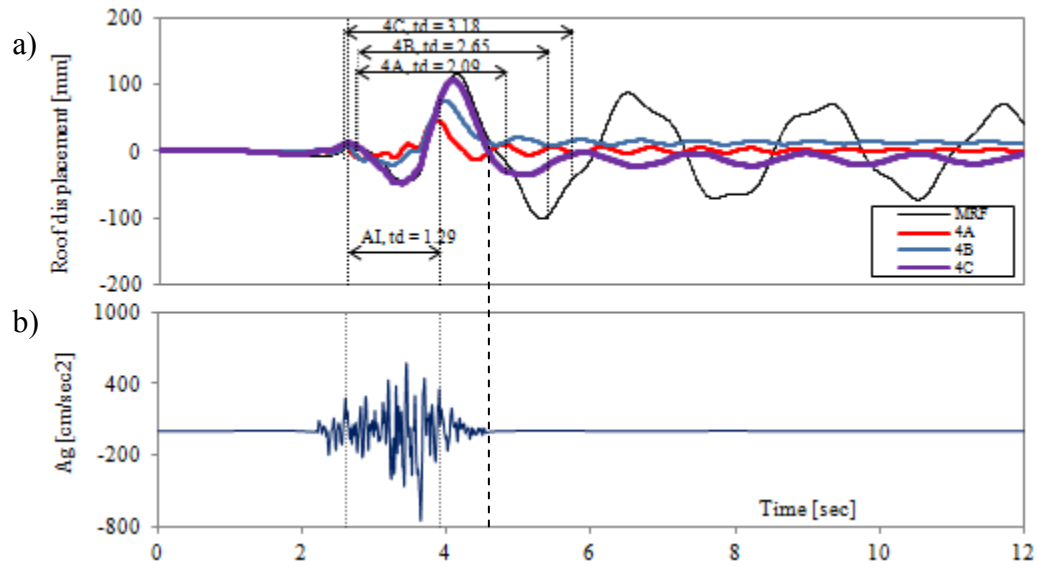
Figure 5.4 Roof displacement history of MRF versus MFR with friction devices (scenarios A, B, C) for the 4-story building: a) roof displacement histories b) record #2
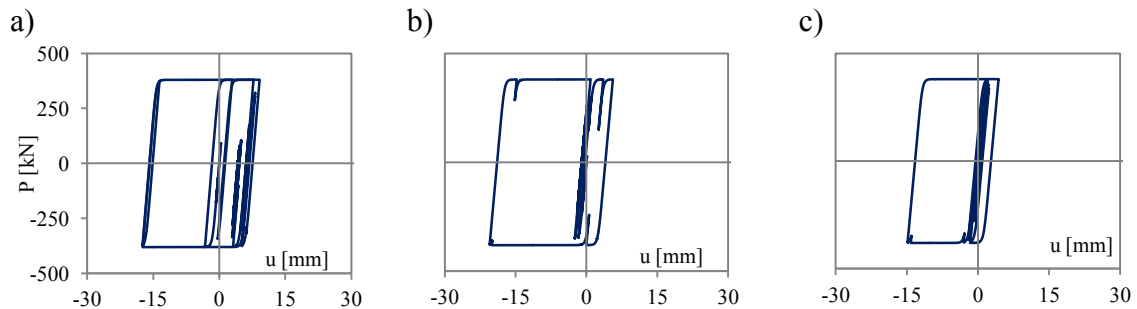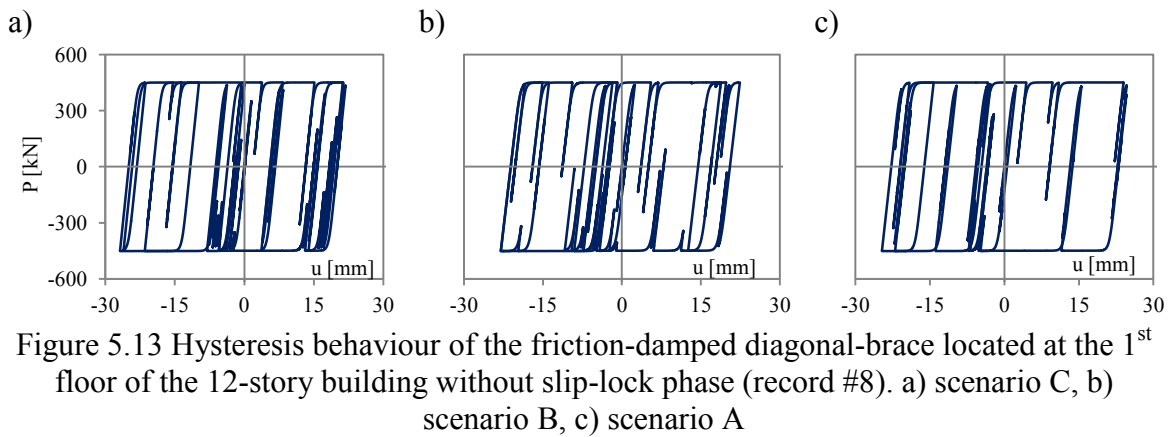

Figure 5.5 Hysteresis behaviour of the friction-damped diagonal-brace located at the 1st floor of the 4-story building without slip-lock phase (record #2). a) scenario C, b) scenario B, c) scenario A
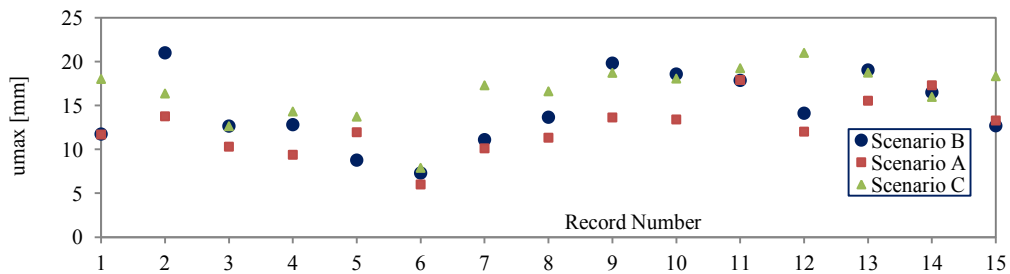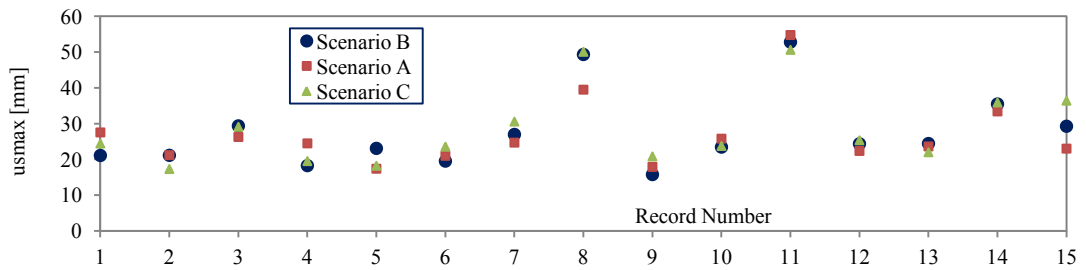

Figure 5.6 Maximum slip distances projected along the diagonal direction, *umax*, in accordance with Figure 3.17 for the 4-story building (scenarios A, B, C) and all records
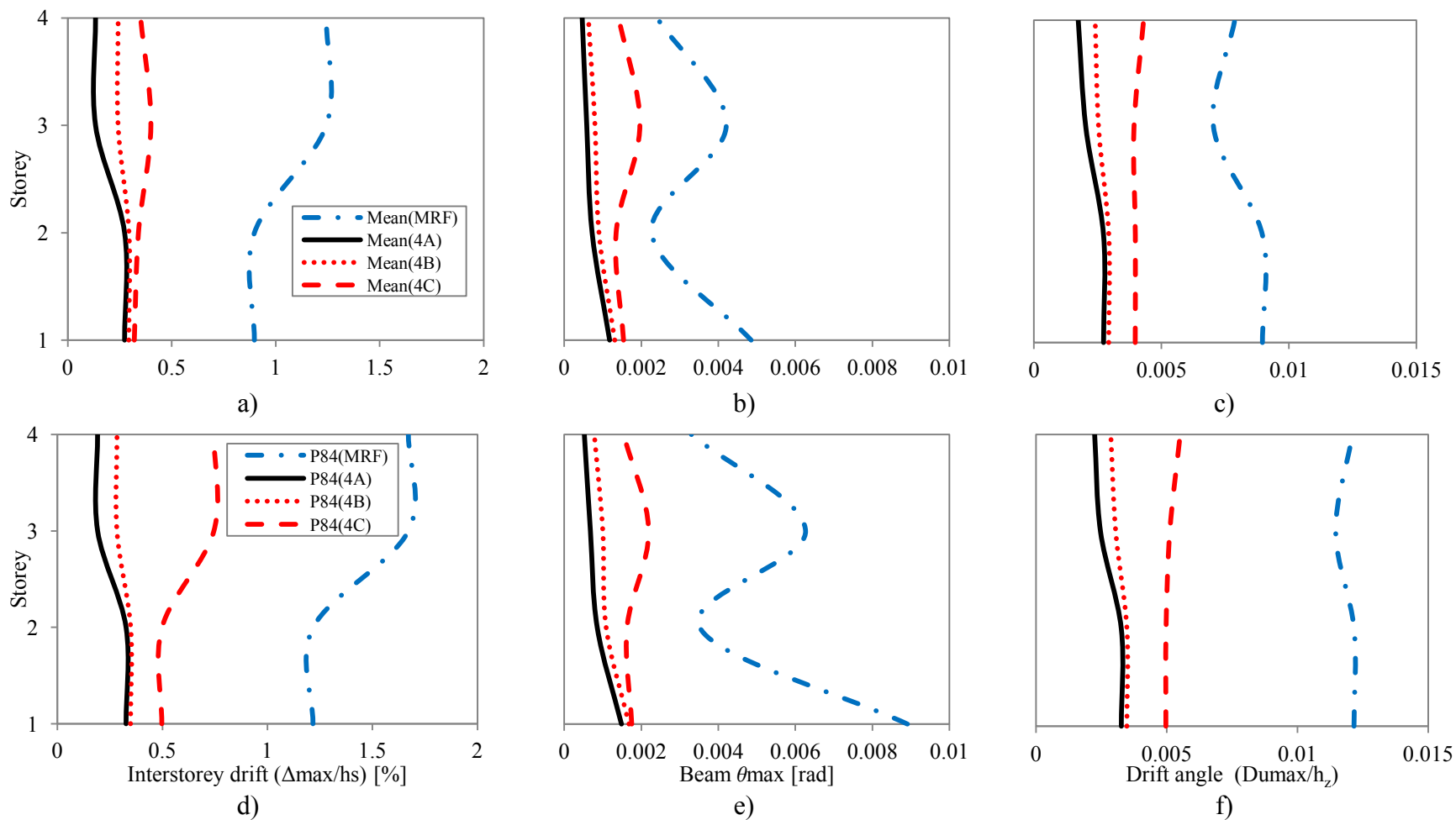
Figure 5.7 EDPs of 4-st building for scenarios A, B, C under 15 records: a) Mean interstorey drift; b) Mean of maximum beam plastic hinge rotation per floor c) Mean drift angle d) P_{84} interstorey drift; e) P_{84} of maximum beam plastic hinge rotation per floor; f) P_{84} drift angle
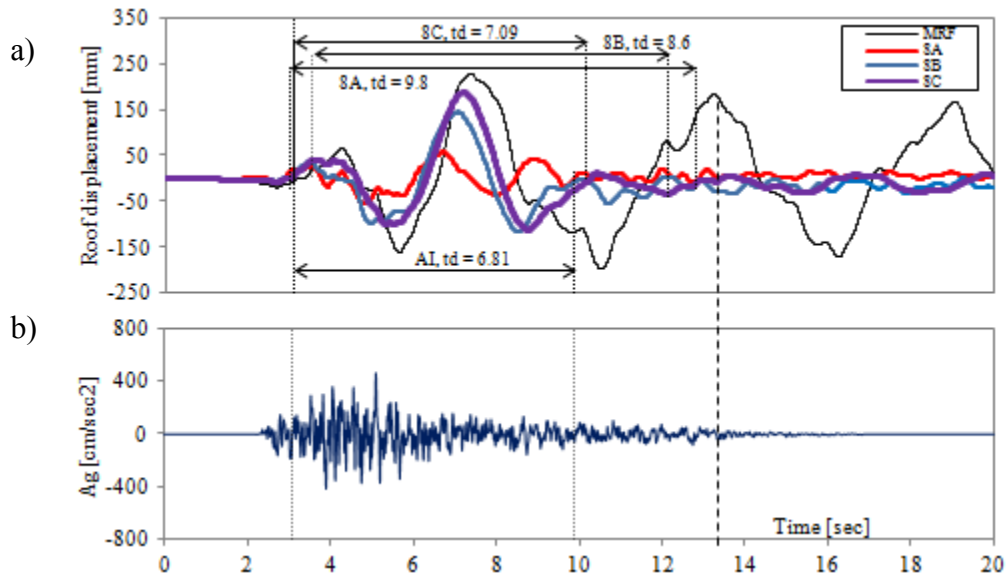
Figure 5.8 Roof displacement history of MRF versus MFR with friction devices
(scenarios A, B, C) for the 8-story building: a) roof displacement histories b) record #10
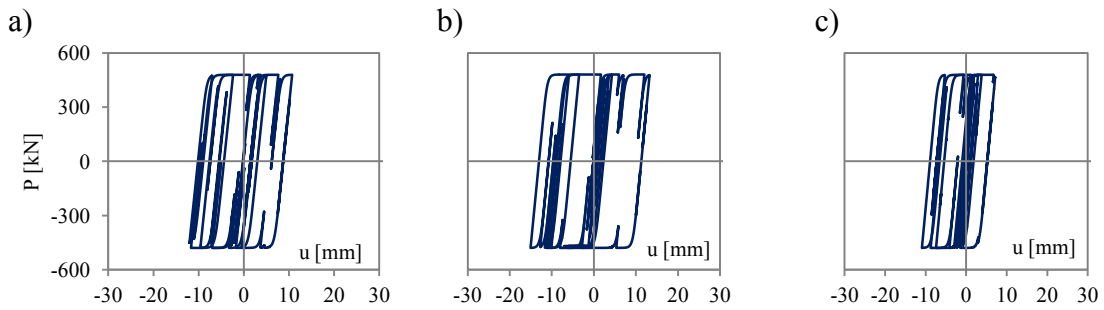
Figure 5.9 Hysteresis behaviour of the friction-damped diagonal-brace located at the 1st
floor of the 8-story building without slip-lock phase (record #10). a) scenario C, b)
scenario B, c) scenario A
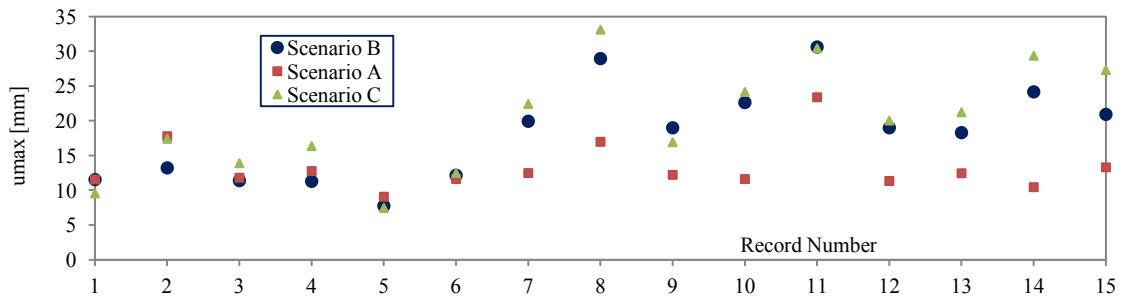
Figure 5.10 Maximum slip distances projected along the diagonal direction, *umax*, in
accordance with Figure 3.17 for the 8-story building (scenarios A, B, C) and all records

140
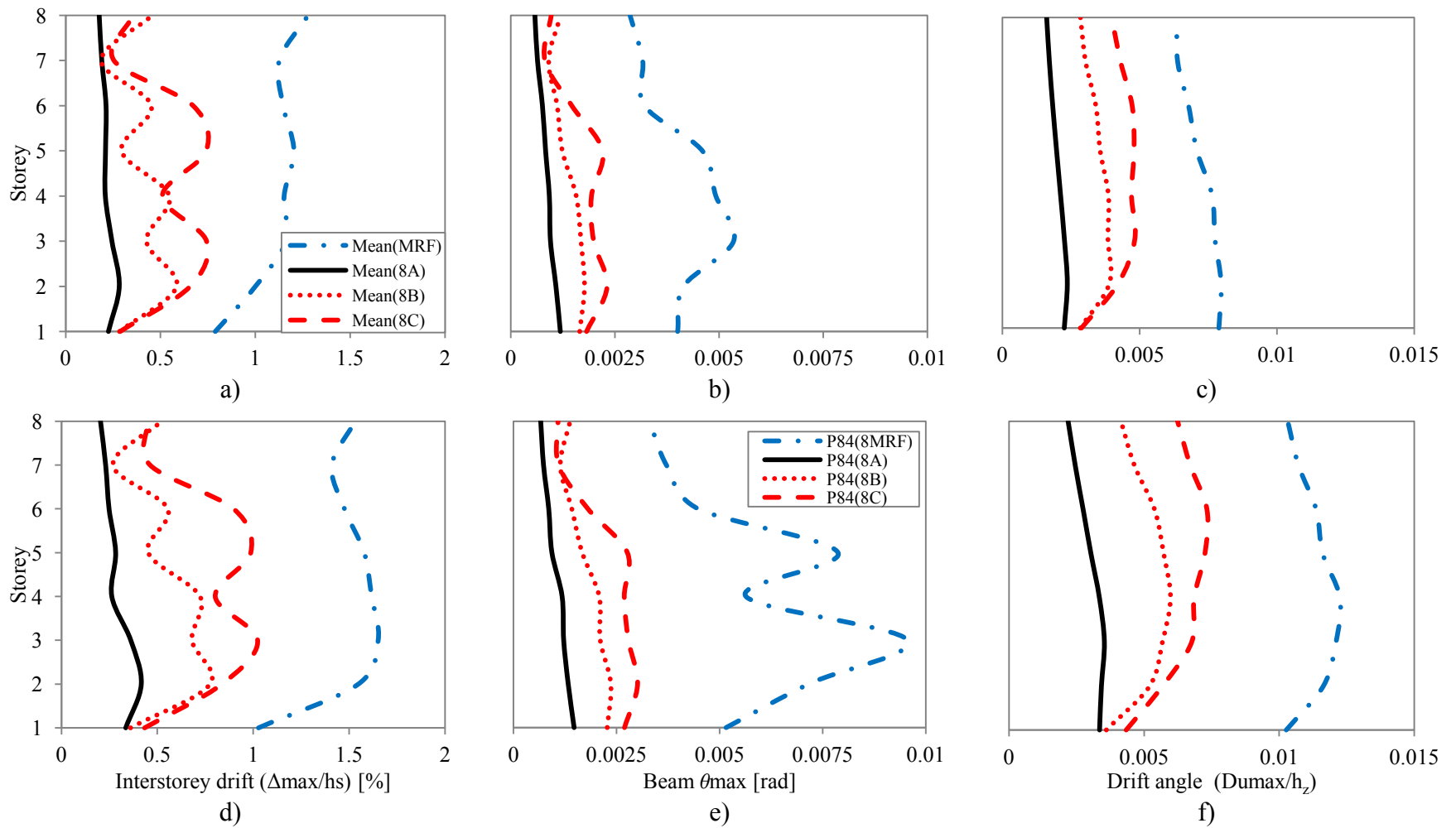
Figure 5.11 EDPs of 8-st building for scenarios A, B, C under 15 records: a) Mean interstorey drift; b) Mean of maximum beam plastic hinge rotation per floor c) Mean drift angle d) P_{84} interstorey drift; e) P_{84} of maximum beam plastic hinge rotation per floor; f) P_{84} drift angle
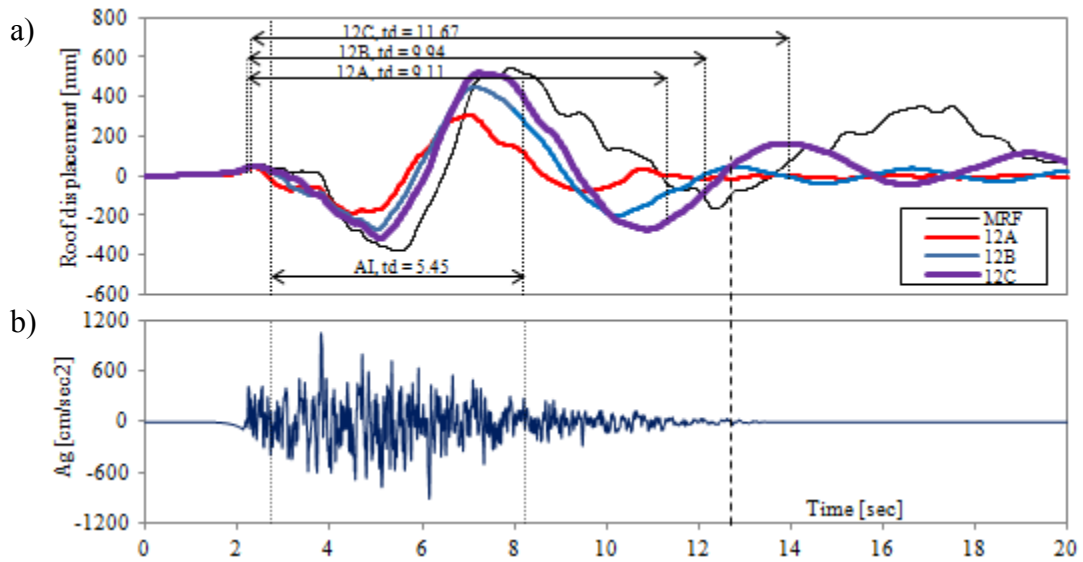
Figure 5.12 Roof displacement history of MRF versus MFR with friction devices (scenarios A, B, C) for the 12-story building: a) roof displacement histories b) record #8

Figure 5.13 Hysteresis behaviour of the friction-damped diagonal-brace located at the 1st floor of the 12-story building without slip-lock phase (record #8). a) scenario C, b) scenario B, c) scenario A

Figure 5.14 Maximum slip distances projected along the diagonal direction, *umax*, in accordance with Figure 3.17 for the 12-story building (scenarios A, B, C) and all records
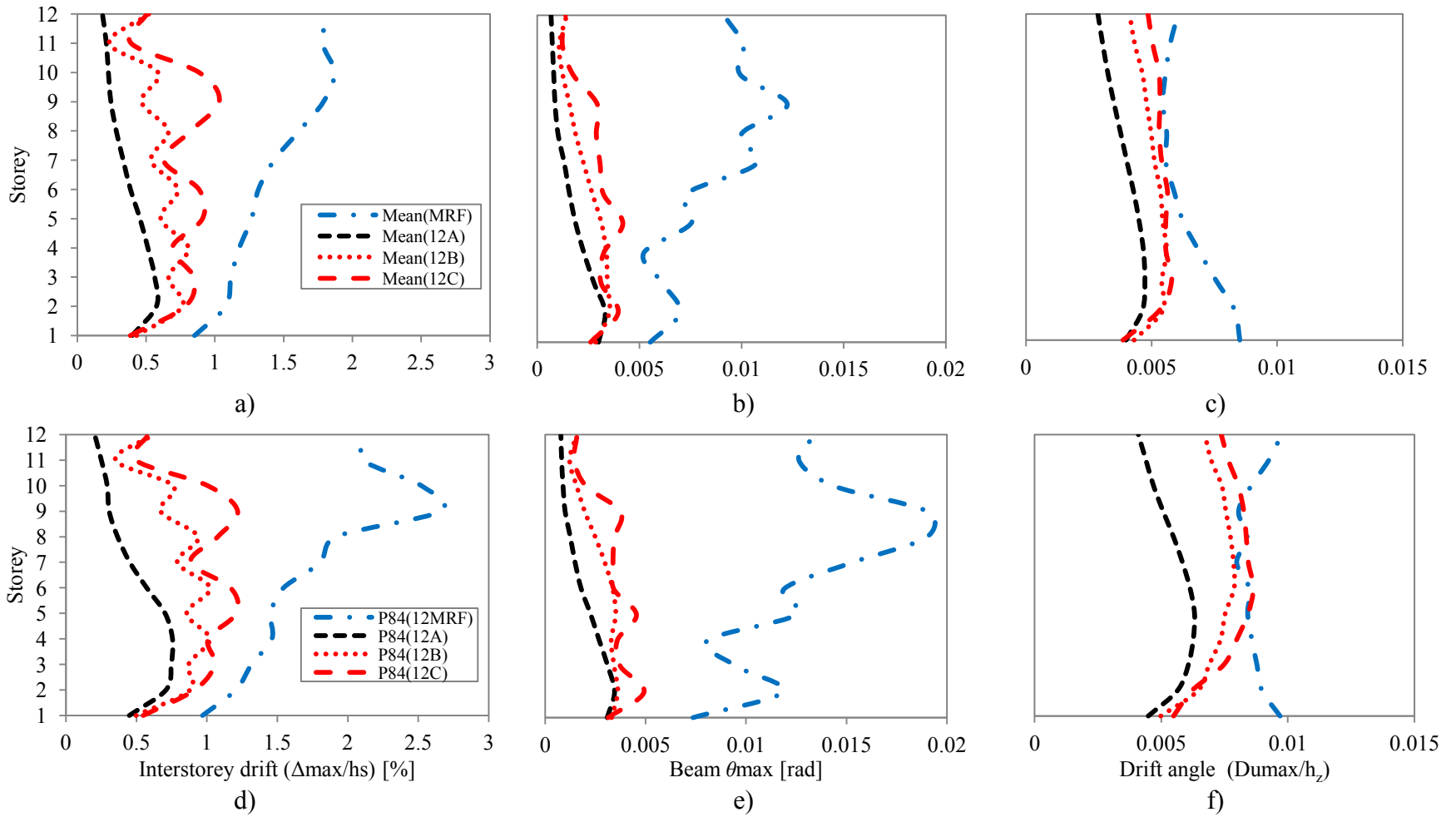
Figure 5.15 EDPs of 12-st building for scenarios A, B, C under 15 records: a) Mean interstorey drift; b) Mean of maximum beam plastic hinge rotation per floor c) Mean drift angle d) P_{84} interstorey drift; e) P_{84} of maximum beam plastic hinge rotation per floor; f) P_{84} drift angle

a)

b)

c)
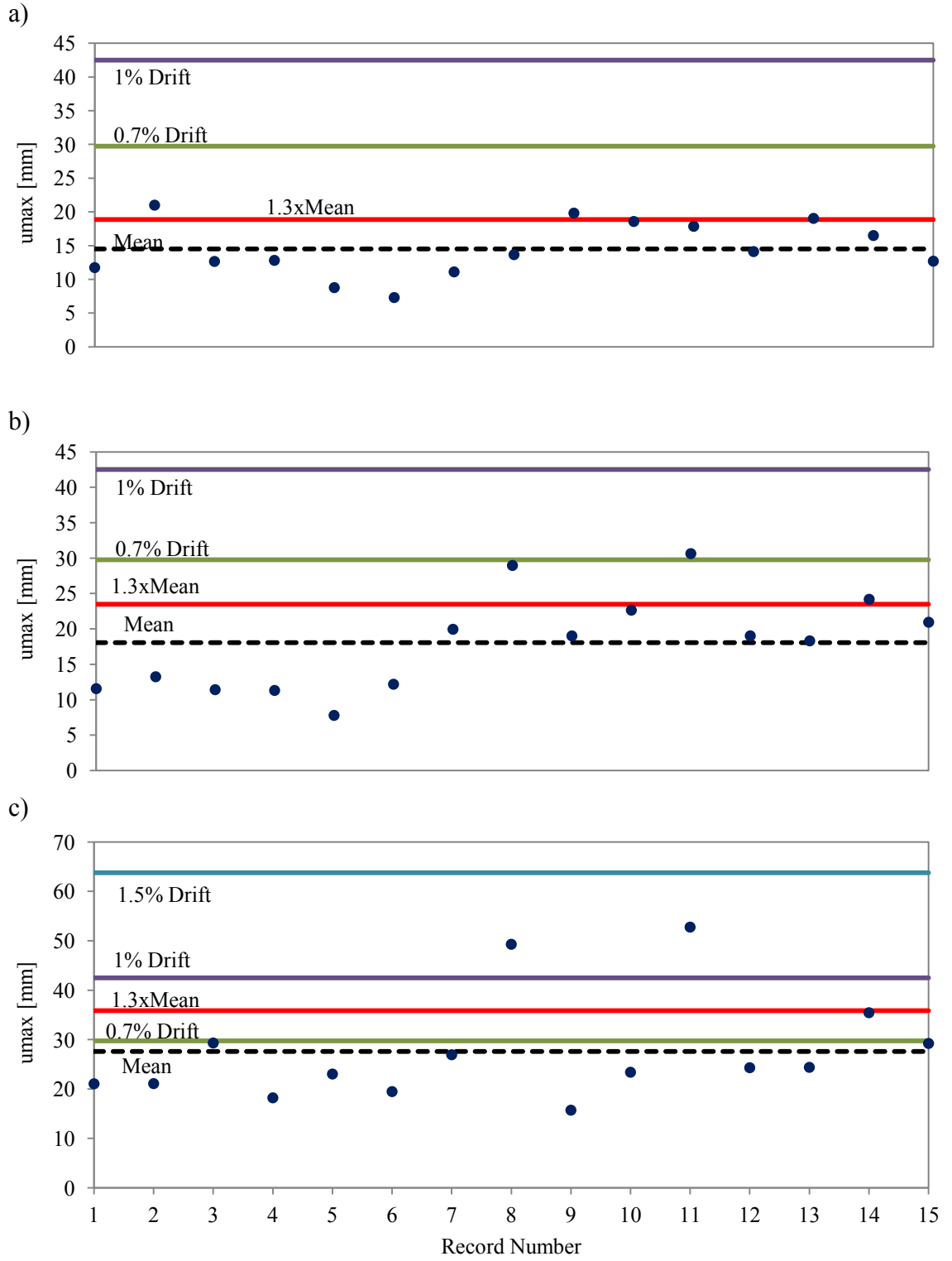
Figure 5.16 Maximum slip distances projected along the diagonal direction for specimens with staggered braces with in-line friction dampers under the 15 ground motions. a) 4B, b) 8B and c) 12B

5.3 THE EFFECT OF IMPLEMENTING THE SLIP-LOCK PHASE IN THE SEISMIC RESPONSE OF BUILDINGS WITH STAGERRED FRICTION-DAMPED DIAGONAL-BRACING DEVICES

The applicability of friction devices is to achieve different performances such as Damage Control and Limited Safety. The performance levels covered in the Damage Control state ranges between Immediate Occupancy and Life Safety, while the Limited Safety state ranges between Life Safety and Collapse Prevention. When friction dampers are used as a mean to reduce the seismic effects, the provisions stipulated in Chapter 9 part 9.3.1 of FEMA 356 (2000) recommend: "If four or more energy dissipation devices are provided in a given story of a building in one principal direction of the building, with a minimum of two devices located on each side of the center of stiffness of the storey in the direction under consideration, all energy dissipation devices shall be capable of sustaining displacements equal to 130% of the maximum calculated displacement in the device in the BSE-2." The earthquake hazard BSE-2 means 2% in 50 years. Thus, the requirement is that these devices shall be designed to withstand 130% more of the maximum slip demand which in this study means *1.3ū̄max* computed from non-linear time-history analysis and illustrated in Figure 5.16 with a red line. This parameter aim to show the demand level when compared with the limitations given by this code. Hence, if the slip distance for each building is defined as *uslip = 2x(1.3ū̄max)* the bolt impact phenomena is expected to occur during the following ground motions: #2, #9, #10 and #13 for the 4-storey building and under the ground motions: #8, #11 and #14 for the 8- and 12-storey building. Herein, we refer to the most cost-efficient versus performance scenario B. To emphasise this effect, the record #2 was chosen for the 4-storey building and # 11 for the 8- and 12- storey building. As consequence, the slip-lock system was

included into the OpenSees models and it was assumed that: i) the available slip distance for each specimen (*ua*) is equal to 2 times the average maximum slip distance increased by 130%, *ua = 2.6ūmax* and ii) the maximum force provided by bearing is lower than the compressive capacity of the brace with in-line friction damper, designed to carry 130% of the required slip force.

The model of the bearing stage, as discussed in section 3.2 assumes failure of the device by decoupling them after the threshold force was reached. The assumed threshold force value is not validated with experimental test results, since there is not information on the existence of these tests regarding failure of Pall friction dampers. In order to show the effect of the bolt impact and what would happen if the demand in device is beyond the slip-length limit, in this study, the following assumptions are made: braces remain elastic and failure of brace in series with friction damper system is recorded when the bearing force reaches the slip-length limit,

As it can be seen in Figure 5.17,the hysteresis loop of dampers belonging to the 1st floor of 4- and 8-storey building and to the 5th floor of the 12-storey building (scenario B) show excursions into the slip-lock phase until failure occurs. Thus, Figure 5.17a shows the behaviour of the friction damper located at the 1st floor of the 4-storey building subjected to the #2 record. Therefore, after the available slip distance is exceeded, the device was driven in the slip-lock phase and a bearing force of 970kN lesser than *Cr* of the brace (Cr = 1979kN) was recorded. In the case of the 8-storey building, the friction damper reached a bearing force of 1400kN (Cr of brace is 1979kN) at the1st floor where an available slip distance of ua=50mm was considered. In the case of the 12-storey

building, under the #11 record the failure of damper located at the 5th floor was attained when the available slip distance of ua = 70mm was provided.

Therefore, the available slip distance parameter is an important criterion in the design of friction devices. In the three aforementioned cases, the slip-lock phase occurred when building was leaded toward a side failure mechanism. In this respect, in Figure 5.18 is showed the behaviour of MRF after a progressive failure of dampers occurred. At floors with larger demand, dampers may reach failure, while forces and deformations are redistributed within the structural system and across the building height. During redistribution, the dynamic characteristics of the system are changed, while the MRF acts as a back-up system and responds to gravity and lateral loads showing growth and changes in the interstory drift pattern when comparing with the case without slip limitations. In addition, during the bolt impact stage, the system undergoes larger displacements while forces in beams and columns increase. Thus, in the case of 12-storey building (scenario B and C), if the slip-lock phase is considered, the #11 record pushes the demand in MRF' members beyond the elastic range until plastic hinges are formed as it can be seen in Figure 5.19c. In contrast, during the slip-lock phase, damping is considerably reduced, the maximum dynamic base shear is increased (Figure 5.20), while the behaviour tends to approach to that of MRF with braces only. Hence, in this phase, due to period consolidation, the building response is moving up on the acceleration spectrum, while the base shear demand is increased. In this regard, Figure 5.21 shows a plot of fundamental periods computed for MRF with braces only and the bare frame (MRF) alone laying on the UHS for Montreal (site class C), from where, the increase in the spectral acceleration for the MRF with braces is evident. Therefore, when using MRF

as a backup system, foundations shall be designed to withstand the case of bolt impact. In any case, if the bearing stage would like to be eliminated, the slip distance demand parameter should be controlled by design. In this regard, the provisions given in FEMA 356 shall be modified indicating that the friction-damped brace system shall be designed in such a way that the brace is able to carried out an axial force of at least the maximum force of the friction damper at the bearing stage and the displacement shall be taken 130% bigger than the maximum of the slip displacements registered for all the assembly of records used in the analysis.

On the other hand, if the MRF is used as a backup system, then the foundation shall be designed considering the increment produced for the bearing stage of the friction dampers in such a way that for larger earthquakes after the system brace with in-line friction dampers are not working any longer the system can have a reserve of strength and stiffness.
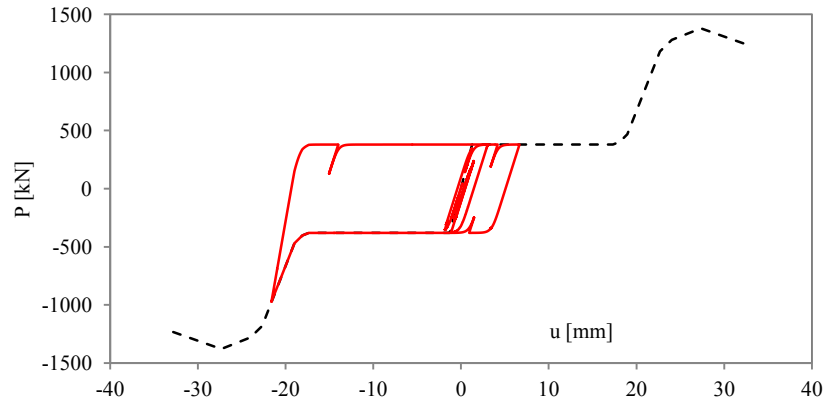
a) Damper allocated at the 1st storey in the specimen 4B under the #2 record
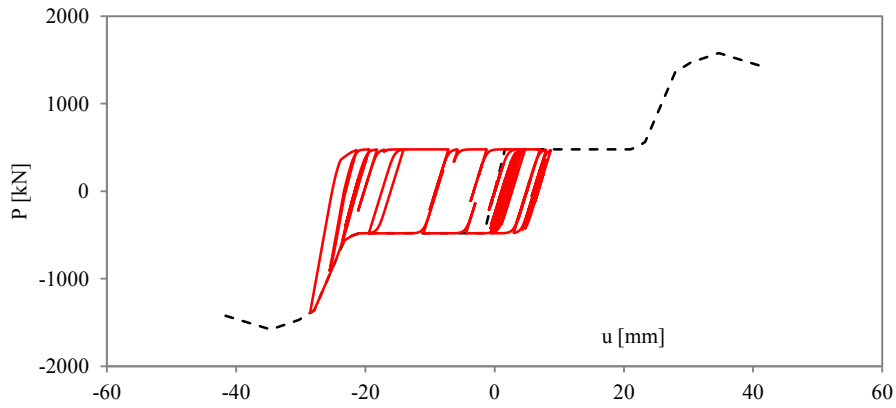
b) Damper allocated at the 1st storey in the specimen 8B under the #11 record
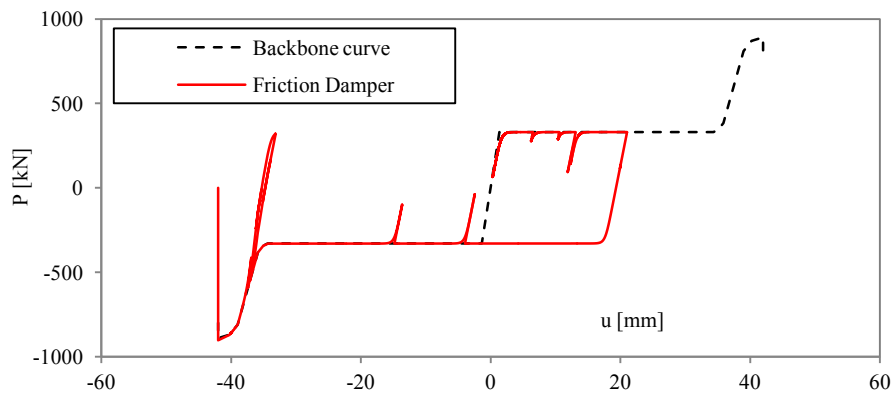
c) Damper allocated at the 5th storey in the specimen 12B under the # 11 record with failure

Figure 5.17 Hysteretic responses of friction dampers when pushed into the bearing stages
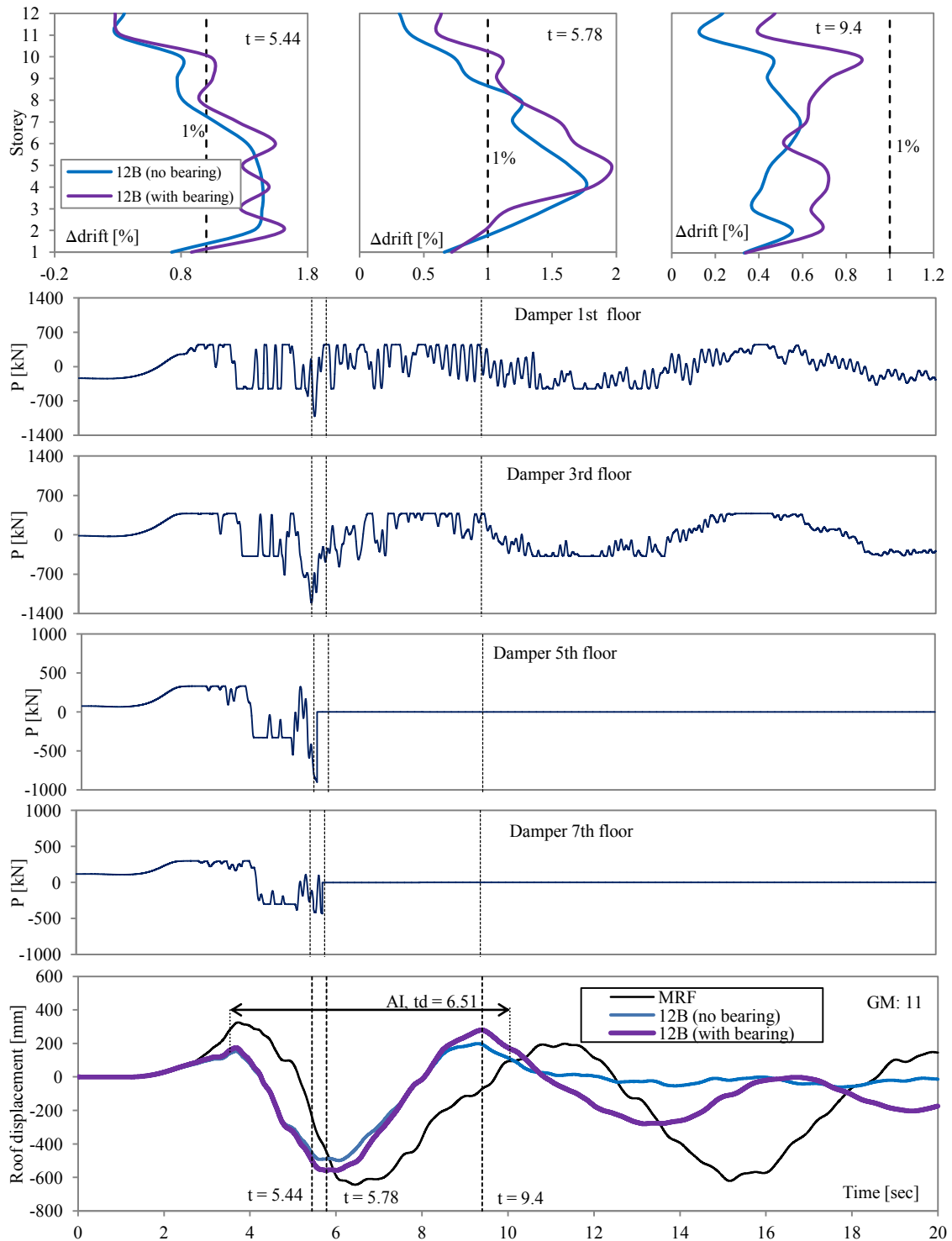
Figure 5.18 Response of the 12-storey scenario B considering friction dampers with bearing (slip-lock phase). a) Interstorey drift; b) time-history of force displacement developed in device; c) roof displacement

150
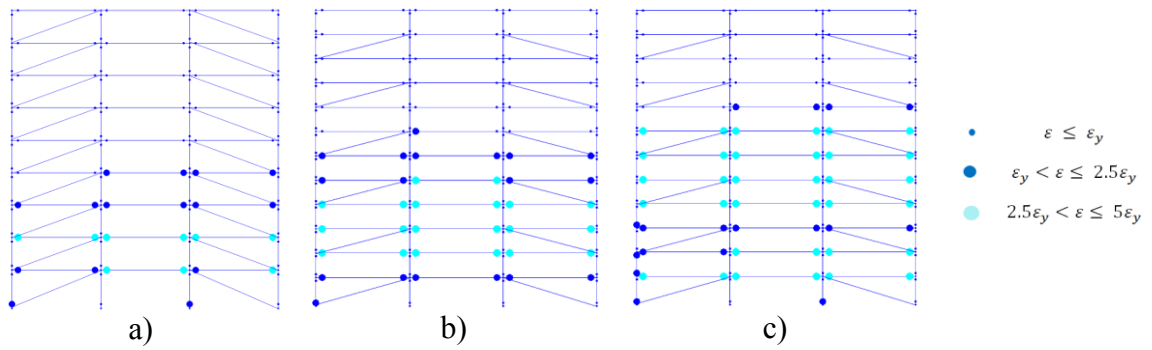
Figure 5.19 Distribution of plastic hinges across the building height under the #11 record.
a) 12-st case A without considering bearing (slip-lock phase), b) 12-st case B without
considering bearing and c) specimen 12-st case B considering bearing
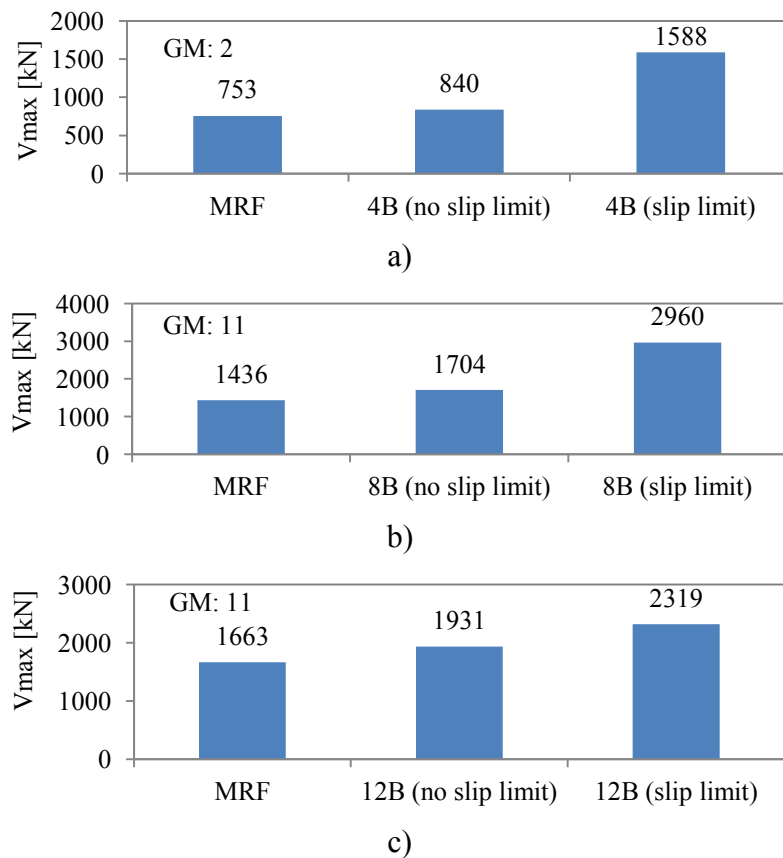
Figure 5.20 Increment of the maximum base shear (Vmax) due to the bolt impact. a) 4-
storey, b) 8-storey and c) 12-storey buildings
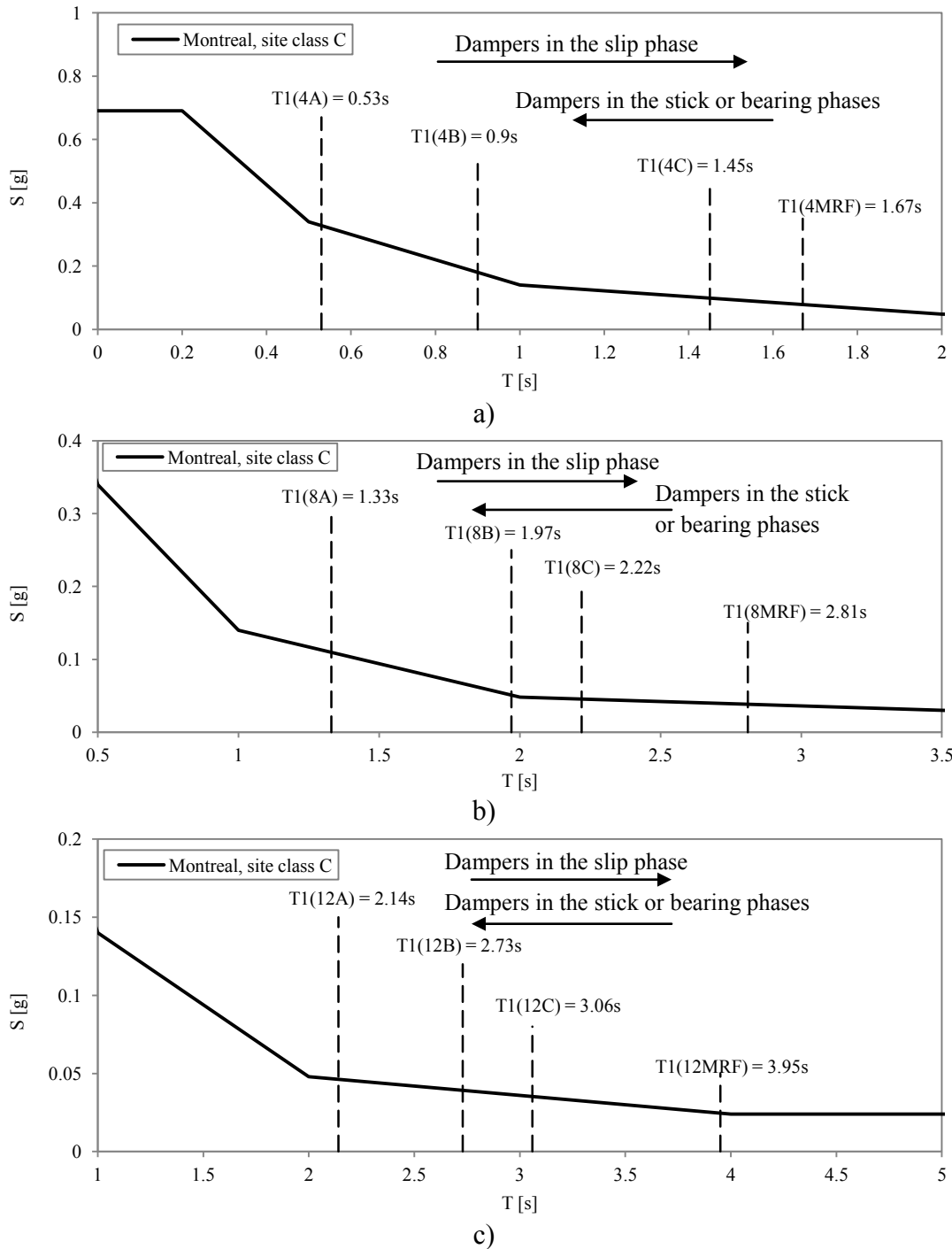
Figure 5.21 UHS and fundamental period laying on the spectrum for the three scenarios
of: a) 4-story building (MRF and Damped MRF scenarios); b) 8-storey building (MRF
and Damped MRF scenarios); c) 12-storey building (MRF and Damped MRF scenarios).

CHAPTER 6

Conclusions and Future Work

6.1 CONCLUSIONS

Among passive energy dissipation devices, friction dampers are used worldwide as means of increasing damping into structural building systems with the aim to reduce the seismic response. These devices, added in-line with diagonal braces and installed in moment frame buildings, are able to reduce the demand of the primary frame system, the interstorey drift, and may control the damage of non-structural components as building envelope. Regarding to their mechanical behavior, friction dampers dissipate energy through the relative sliding of plates clamped with post-tensioned bolts, while slipping occurs along the length of the slotted hole. This device reveals a rigid-plastic behaviour defined by three phases such as: "stick-slip" before sliding occurs, "slipping" during the relative sliding of adjacent plates and the "slip-lock" when the force in the device increases due to the bearing of post-tensioned bolts

This study is the first conducted to numerically simulate the friction-damped diagonal-bracing device in OpenSees software framework. Thus, to define the highly nonlinear behaviour of friction damper, which means to reproduce the smooth transition from elastic to sliding and from sliding to bearing, an equivalent material has been proposed. In this regard the Bouc-Wen material have been selected to define the stick-slip phase before sliding occurred and the slipping phase whereas the slipping force is

recorded versus slipping displacement across the length of the slotted hole. Using the findings of Lukkunaprasit et al. (2004), the failure of device, known as the slip-loak phase was simulated by the Elastic Perfectly Plastic Gap material defined in both oscilation directions (tension and compression) and added in paralel to the Bouc-Wen material. Failure of friction damper occurs when the seismic demand exceedes the availabe slipping distance and the post-tensioned bolts impact the edge of slotted hole driving the post-tensioned bolts to behave either in bearing or in shear. In this computer model, when failure of the friction-damped diagonal-bracing system is recorded, the device is decoupled from the backup frame. To complete the friction-damped diagonal bracing system device model, the equivalent material was assigned to an elastic truss element object.

In this research, the length of slotted hole was identified as being an important parameter which is able to control the seismic response of friction damper. If the length of slotted hole is too small, the slip-lock phase is encountered under 1%hs interstorey drift or 0.005 radians drift angle. However, if the length of slotted hole is too large (correspond to 2.5%hs interstorey drift), important remanent deformations are identified and the re-centering effect is reduced. To emphasise the effect of slotted hole's length, known as slip distance, a MinMax material was assigned to the Elestic-Perfectly Plastic Gap material in order to decouple the device after the maximum bearing or shearing force exhibited by the pretensioned bolts is reached. Thus, in this study, it is clearly underlined the importance of calibrating the length of slotted hole during the design process.

Through numerical analyses, in this study, it was emphasised that changes in behaviour of the MFR system during the stick-slip phase occur and the dynamic

characteristics of the system are modified. Thus, during the stick-slip phase, the stiffenss of the sytem (MRF with devices) is increased, as well as the base shear, while damping due to friction through sliding approches zero. This type of behaviour (transition from MRF with devices to braced frame) with changes in dynamic characteristics should be avoided. In addition, during the bearing stage, the forces in adjacent MRF's members of diagonal-braces are increased and plastic hinges could be expected.

In this study it is proposed that any brace member in-line with friction damper must be proportioned to carry the maximum force computed as: i) 130% of slip load developed in damper and ii) the bearing force able to sustain displacements equal to 130% of the maximum length of slotted hole. If bearing phase is expected, foundations shall be designed to accommodate larger base shear induced by bearing forces developed in friction dampers.

In addition it was observed that during the bearing phase the structure is driven towards the lateral sideway mechanism and its behaviour is transited toward the braced frame behaviour, while as mentioned before the dynamic characteristics of the system change by increasing the forces into the backup frame system.

The proposed MD-MRF system with staggered FDDB devices is recommended to be employed in the following two cases: i) to prevent failure of non-structural components (e.g. brick facades, curtain walls, and others) by controlling the interstorey drift below. $1\%h_s$; ii) to provide a cost efficient system by adding damping and stiffness while reducing the inelastic response of all MRF's members. In addition the MD-MRF

structure is cost-efficient compared to a conventional MRF, while it provides the backup and a re-centering system when devices experience slipping or even failure.

A design methodology was proposed in order to find the optimum activation load (slip-load) of each damper by minimising the difference between the seismic input energy and the energy dissipated by dampers. This slip load magnitude depends mainly on the structure properties and frequency content of ground motion.

6.2 FUTURE WORK

In order to evaluate the performance of the MD-MRF equiped with friction dampers under large earthquakes, degradation of the MRF members shall be included in the structural model. In this research cyclic degradation was not considered in the plastic hinge region of MRF's members.

Since after the device has been pushed into the bearing phase, loss of postension load in the bolts may occur. Thus, degradation in the hysteresis behaviour of the friction device should be considered. This degradation as noted by Lukkunaprasit et al. (2004) shall be exhibited after the bolt impact occurs. However, the rate of degradation, which may not be the same for all the cycles, shall be determined from experimental results.

As showed in this study, the bearing phase tends to shift the MRF behaviour into a braced frame behaviour. Therefore in order to take advantage of friction devices as a dissipative system and to let MD-MRF to respond as a backup system, a decoupled connection between the friction damper and structure should be envisioned when the

developed force in friction damper reaches the brace capacity in compression. Thus, changes of dynamic characteristics of the system are avoided.

Experimental tests conducted on friction-damped bracing system device are strongly required to validate the computer model. In addition, by using the Openfresco technique, extensive test of MD-MRF frame with devices incorporated should be carried out.

REFERENCES

Aiken, I.D. and Kelly, J.M. (1990). Earthquake simulator testing and analytical studies of two energy-absorving systems for multistory structures. Report No. UBC/EERC-90/03, Earthquake Engineering Rresearch Center, Univ. of California, Berkeley, Ca.

Aiken, I.D., Nims, D., Whittaker, A. and Kelly, J.M. (1993). Testing of passive energy dissipation systems. Earthquake Spectra, Earthquake Engineering Research Center,Univ. of California, Berkeley, Ca. August.

Aiken, I.D., Kelly, J.M., and Pall, A.S. (1988) Seismic response of a nine-story steel frame with friction damped cross-bracing. Proc. 9th World Conference on Earthquke Engineering, Tokyo/Kyoto, Japan.

Akiyama, H. (2000). Evaluation of fractural mode of failure in steel structures following Kobe lessons. Journal of Constructional Research, No. 55, 211-227.

American Society of Civil Engineers (ASCE). (2005). Minimum design loads for buildings and other structures. ASCE/SEI 7-05, Reston, Virginia.

Atkinson, G. (2009) Earthquake time histories compatible with the 2005 NBCC uniform hazard spectrum. Canadian Journal of Civil Engineering.

Baber, T. and Noori, M. (1985). Random vibration of degrading, pinching systems. Journal of Enginnering Mechanics, ASCE, Vol. 111, 1010-1025.

Baber, T. and Wen, Y. (1981). Seismic response of hysteretic degrading structures. Journal of Engineering Mechanics, ASCE, Vol. 107, No 6, 1067-1087.

Baktash, P. and Marsh, C. (1986). Seismic behavior of friction damped braced frames. Proc. 3rd U.S. National Conference on Earthquake Engineering. Charleston, SC, 1099-1105.

Bathe, K. J. (2006). Finite element procedures. Prentice Hall.

Bondonet, G. and Filiatrault, A. (1997). Frictional response of PTFE sliding bearings at high frequencies. Journal of Bridge Engineering, ASCE, Vol. 2, No. 4, 139-148.

Bouc, R. (1967). Forced vibration of mechanical systems with hysteresis. Proc. 4th Conference on Nonlinear Oscillation, Prague, Czechoslovakia.

Bruneau, M., Uang, C-M. and Whittaker, A. (1998). Ductile design of steel structures. McGraw-Hill.

Casarotti, C. (2004). Bridge isolation and dissipative devices: state of the art review of seismic response and modelling of modern seismic isolation and dissipation devices. M.Sc. Thesis, University of Pavia and ROSE School, Pavia, Italy.

Christopoullos, C. and Filiatrault, A. (2006). Passive supplemental damping and seismic isolation. Instituto Universitario di Studi Superiori di Pavia, IUSS Press.

Canadian Standard Association. (2009). CAN/CSA-S16-09 Limit states design of steel structures. Canadian Standard Association, Toronto, ON.

Constantineau, M., Mokha, A. and Reinhorn, A. (1990). Teflon bearings in base isolation. II. Journal of Structural Engineering, ASCE, Vol. 116, No. 2, 455-474.

Dobson, S., Noori, M., Hou, Z., Dimentberg, M. and Baber, T. (1997). Modeling and random vibration analysis of SDOF systems with asymmetric hysteresis. Journal of Non-linear Mechanics, Elsevier Science Ltd., Vol. 32, No. 4, 669-680.

Eads, L. (2010). Pushover Analysis of 2-Story Moment Frame. Stanford university. http://opensees.berkeley.edu/wiki/index.php/Pushover_Analysis_of_2-Story_Moment_Frame.

Federal Emergency Management Agency (FEMA). (2000). Recommended seismic design criteria for new steel moment frame buildings. FEMA-350, Washington, D.C.

Federal Emergency Management Agency (FEMA). (2000). Prestandard and Commentary for the Seismic Rehabilitation of Buildings. FEMA-356, Washington, D.C.

Filiatrault, A. (1997). Elements of earthquake engineering and structural dynamics. Presses Internationales Polytechnique.

Filiatrault, A. and Cherry, S. (1988). Comparative performance of friction damped systems and base isolation systems for earthquake retrofit and seismic design. Earthquake Engineering and Structural Dynamics, Jhon Wiley & Sons Ltd., Vol. 16, 389-416.

Foliente, G. (1993). Stochastic dynamic response of wood structural systems. Ph.D. Thesis, Virginia Polytechnic Institute, Blacksburg, Virginia.

Gear, C. W. (1971). Numerical intial value problems in ordinary differential equations. Prentice Hall.

Grigorian, C. and Popov, E. (1992). Slotted bolted connections for energy dissipation. Proc. ATC-17-1 Seminar on Seismic Isolation, Passive Energy Dissipation, and Active Control, San Francisco, Vol. 2, 545-556.

Gupta, A. and Krawinkler, H. (2002). Relating the seismic drift demands of SMRFs to element deformation demands. Engineering Journal, AISC, 100-108.

Haukaas, T. and Der Kiureghian A. (2004). Finite Element Reliability and Sensitivity Methos for Performance-Based Earthquake Engineering. Report No. 2003/14, Pacific Earthquake Engineering Research Center (PEER), Univ. of California, Berkeley, Ca.

Heine, C. (2001). Simulated response of degrading hysteretic joints with slack behavior. PhD Thesis,Virginia Polytechnic Institute, Blacksburg, Virginia.

Ikhouane, F., Mañosa, V. and Rodellar, J. (2007). Dynamic properties of the hysteretic Bouc-Wen model. Systems & Control Letters, Elsevier, No. 56, 197-205.

Ismail, M., Ikhouane, F. and Rodellar, J. (2009). The hysteresis Bouc-Wen model, a survey. Arch. Comput. Methods Eng., International Center for Numerical Methods in Engineering (CIMNE), Universitat Politècnica de Catalunya, Barcelona, No. 16, 161-188. February.

Kokil, A. and Shrikhande, M. (2007). Optimal placement of supplemental dampers in seismic design of structures. JSEE, Vol 9, No. 3, 125-135.

Levy, R., Marianchik, E., Rutenberg, A. and Segal, F (2000). Seismic design methodology for friction damped braced frames. Journal of Earthquake Engineering and Structural Dynamics, No. 29, 1569-1585.

Lignos, D. (2008). Sidesway collapse of deteriorating structural systems under seismic excitations. PhD Thesis, Civil and Environmental Engineering, Stanford University, Palo alto, Ca.

Lignos, D. and Krawinkler, H. (2011). Deterioration modeling of steel components in support of collapse prediction of steel moment frames under earthquake loading. Journal of Structural Engineering, ASCE, article in press: doi:10.1061/(ASCE)ST.1943-541X.0000376).

Lukkunaprasit, P., Wanitkorkul, A. and Filiatrault, A. (2004). Performance deterioration of slotted-bolted connection due to bolt impact and remedy by restrainers. Proc. 13th World Conference on Earthquake Engineering, Vancouver, B.C., No. 1986.

Makkar, C., Dixon, W., Sawyer, W. and Hu, G. (2005). A new continously differentiable friction model for control systems design. Proc. of the 2005 IEEE/ASME International Conference on Advanced Intelligent Mechatronics, Monterrey, California, 600-605.

McKenna, F. (1997). Objetc-oriented finite element programming: frameworks for analysis, algorithms and parallel computing. PhD thesis, Civil Engineering, University of California, Berkley, Ca.

Medina, R. and Krawinkler, H. (2005). Evaluation of drift demands for the seismic performance assessment of frames. Journal of Structural Engineering, ASCE, Vol. 131, No. 7, 1003-1013.

Nims, D., Ritcher R. and Bachman R. (1993). The use of the energy dissipating restraint for seismic hazard mitigation. Earthquake Spectra, Vol. 9, No. 3, 467-489.

Pall, A. and Marsh, C. (1982). Response of friction damped braces. Journal of Strutures Division, ASCE, Vol. 108, No. ST6, 1313-1323.

Pall, A. (1979). Limited slip bolted joints. A device to control the seismic response of large panel structures. PhD Thesis, Building, Civil and Environmental Engineering, Concordia University, Montreal, QC.

Pall, A., Marsh, C. and Fazio, P. (1980). Friction joints for seismic control of large panel structures. Journal of Prestressed Concrete Institue, Vol. 25, No. 6, 38-61.

Pall, A., Verganelakis, V. and Marsh, C. (1987). Friction dampers for seismic control of Concordia University library building. Proc. 5th Canadian Conference on Earthquake Engineering, Ottawa, ON., 191-200.

Pasquin, C., Leboeuf, N. and Pall, T. (2004). Friction dampers for seismic rehabilitation of Eaton building, Montreal. Proc. 4th Structural Specialty Conference of the Canadian Society of Civil Engineering (CSCE), Montreal, QC.

Paulay, T. and Priestly, M.J. (1992). Seismic design of reinforced concrete and masonry buildings. Wieley.

Peternell, L.E. (2009). Seismic interstory drift demands in steel friction damped braced buildings. M.Sc. Thesis, Texas A&M University, Texas.

Popov, E., Grigorian, C. and Yang, T. (1995).Developments in seismic structural analysis and design. Engineering Structures, Elsevier Science, Vol. 17, No. 3, 187-197.

Reyes, J. and Kalkan, E. (2011). How many records should be used in ASCE/SEI-7 ground motion scaling procedure. U.S. Geological Survey (USGS).

Roberts, J. and Spanos, P. (1990). Random vibration and statistical linearization. John Wiley & Sons Ltd.

Roik, K., Dorka, U. and Dechent, P. (1988). Vibration control of structures under earthquake loading by three-stage friction-grip elements. Earthquake Engineering and Structural Dynamics, Jhon Wiley & Sons Ltd., Vol. 16, 501-521.

Sadek, F., Mohraz, B., Taylor, A. and Chung, R. (1996). Passive energy dissipation devices for seismic applications. Report No. NISTIR5923, United States Department of Commerce Technology Administration, National Institute of Standards and Technology (NIST), Gaithersburg, Marlynad.

Scott, M. (2011). Numerical integration options for the force-based beam-column element in Opensees. Civil and Construction Engineering, Oregon State University, Oregon.

Scott, M. and Fenves, G. (2006). Plastic hinge integration methods for force-based bam-column elements. Journal of Structural Engineering ,ASCE, Vol. 132, No. 2, 244-252.

Sextro, W. (2002). Dynamical contact problems with friction. Models, methods, experiments and applications. Edited by Prof.Dr.-Ing. Friederich Pfeiffer, Springer-Verlag, Vol. 3., Berlin.

Sivaselvan, M. and Reinhorn, A. (2000). Hysteresis models for deteriorating inelastic structures. Journal of Engineering Mechanics, ASCE, Vol. 126, No. 6, 633-640.

Soli, B., Baerwald, D., Krebs, P. and Pall, T. (2004). Friction dampers for seismic control of Ambulatory Care Center, Sharp Memorial Hospital, San Diego, CA. Proc. 13th World Conference on Earthquake Engineering, Vancouver, B.C.

Song, J. and Der Kiureghian, A. (2006). Generalized Bouc-Wen model for highly asymmetric hysteresis. Journal of Engineering Mechanics, ASCE, Vol. 132, No. 6, 610-618.

Soong, T. and Dargush, G. (1997). Passive energy dissipation systems in structural engineering. Jhon Wiley & Sons Ltd.

Strang, G. (2007). Computational science and engineering. Wellesley-Cambridge Press.

Tirca, L. (2009). A simple approach for the seismic retrofit of buildings with staggered friction dampers. Proc. Protection of Historical Buildings, Rome, Italy, 761-767.

Tirca, L., Morales, J.D., Guo, G.L. and Chen, L. (2010). Optimal design of friction dampers for multi-storey buildings. Proc. 9th US National and 10th Canadian Conference on Earthquake Engineering: Reaching Beyond Borders, EERI, Toronto, ON.

Tremblay, R. (1993). Seismic behavior and design of friction concentrically braced frames for steel buildings. PhD Thesis, University of British Columbia, Vancouver, B.C.

Vail, C., Hubbbell., O'Connor, B., King, J., Pall, A. (2004). Seismic upgrade of Boeing commercial airplane factory at Everett, WA. Proc. 13th World Conference on Earthquake Engineering, Vancouver, B.C.

Wen, Y-K. (1980). Equivalent linearization for hysteretic systems under random excitation. Journal of Applied Mechanics, ASME, No. 47, 150-154.

Zhou, X. and Peng, L. (2009). A new type of damper with friction. Earthquake Engineering and Engineering Vibration, Vol. 8, No. 4, 507-520.

APPENDIX A

SDOF With SHM

The results of the SDOFs as defined in Table 3.2 are depicted herein. Hysteresis behaviours due the load scenario given in Figure 3.6 and the backbone curve defined by the yielding point and the maximum displacement imposed to each system are shown in this appendix. The relative difference within the bilinear model (backbone curve) and the SHM (BWBN model) was computed as of Eqn. 3.14 at three points: $0.75u_y$, u_y and 1.25 u_y. Where u_y is the yielding point.
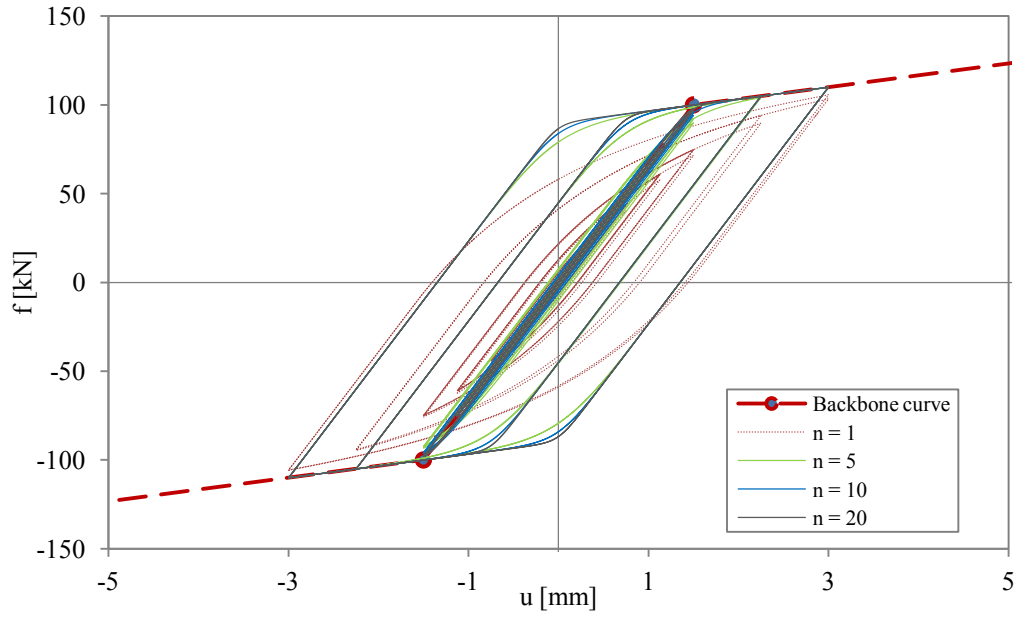
Figure A.1 Response of system 1-A. α=0.1, f_{sy} = 100kN, u_y =1.5mm
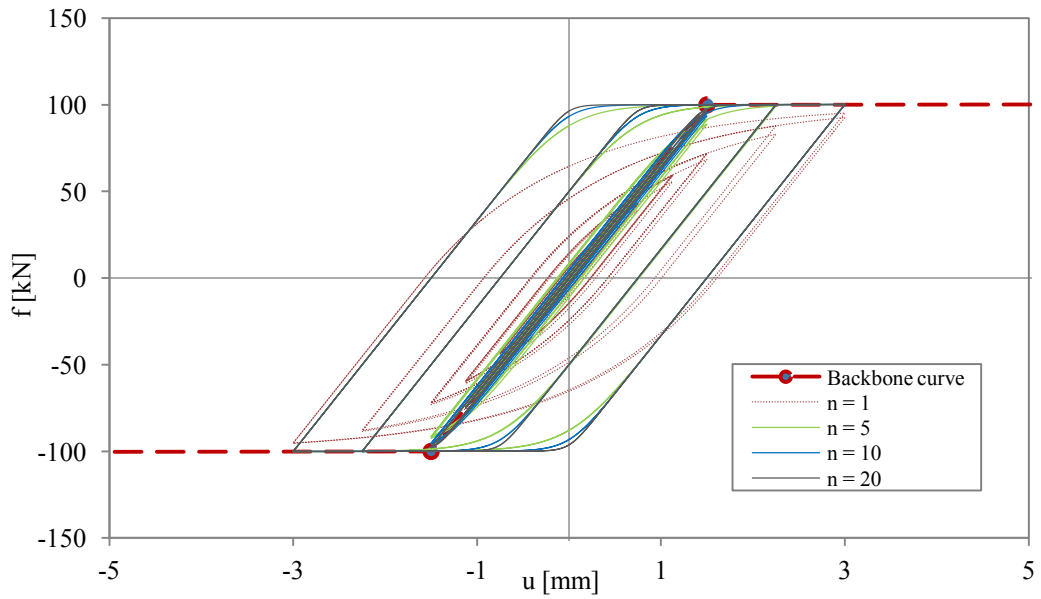
Figure A.2 Response of system 1-B. α=0.001, f_{sy} = 100kN, u_y =1.5mm

168
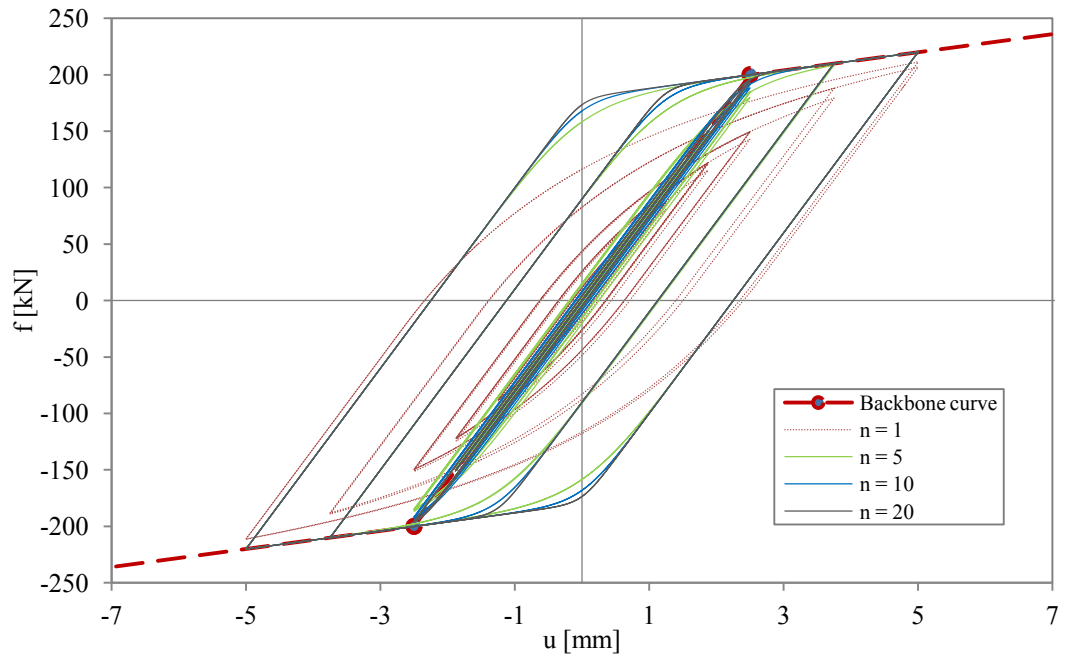
Figure A.3 Response of system 2-A. α=0.1, f_{sy} = 200kN, u_y =2.5mm
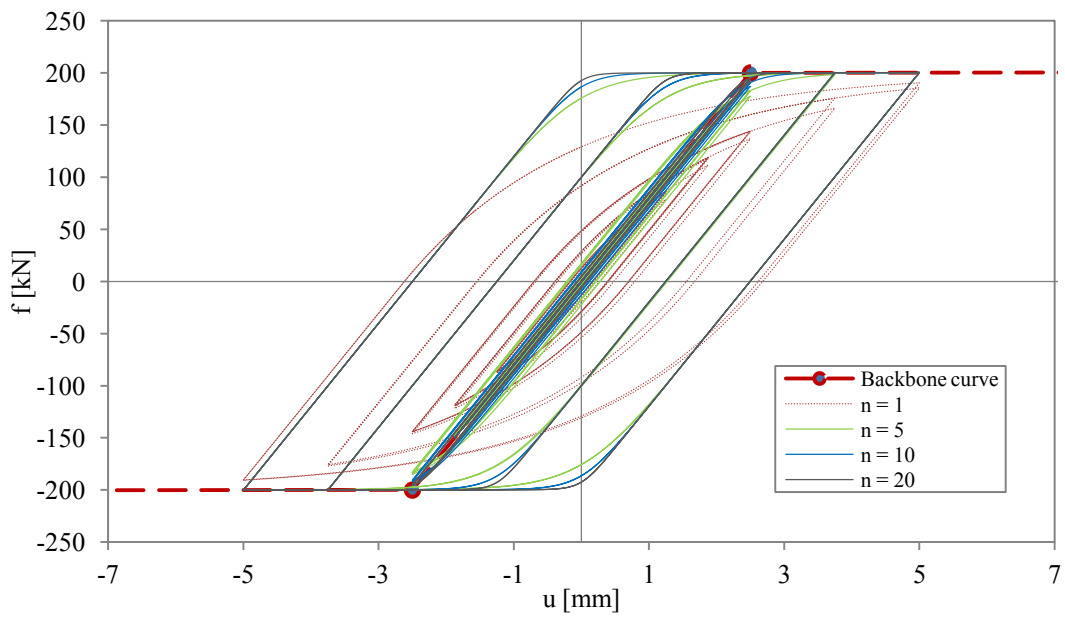
Figure A.2 Response of system 2-B. α=0.001, f_{sy} = 200kN, u_y =2.5mm

	0.75uy	uy	1.25uy
■ n = 1	23.1%	28.9%	19.3%
■ n = 5	3.3%	10.6%	2.6%
■ n = 10	0.5%	6.4%	0.5%
■ n = 20	0.0%	3.7%	0.0%
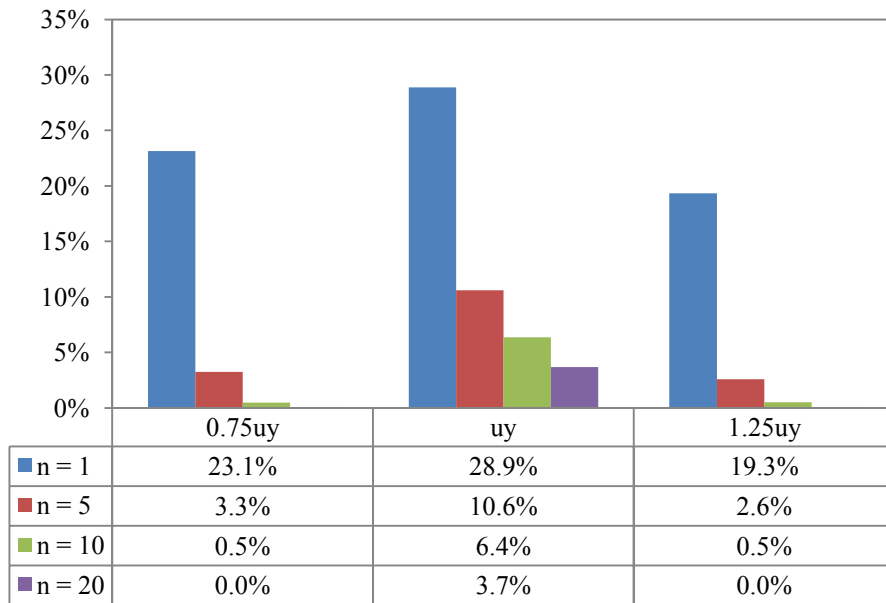
Figure A.5 Relative difference between the backbone curve and the response of 1-A

	0.75uy	uy	1.25uy
■ n = 1	25.7%	31.9%	22.0%
■ n = 5	3.6%	11.7%	2.9%
■ n = 10	0.5%	6.9%	0.6%
■ n = 20	0.02%	4.0%	0.04%
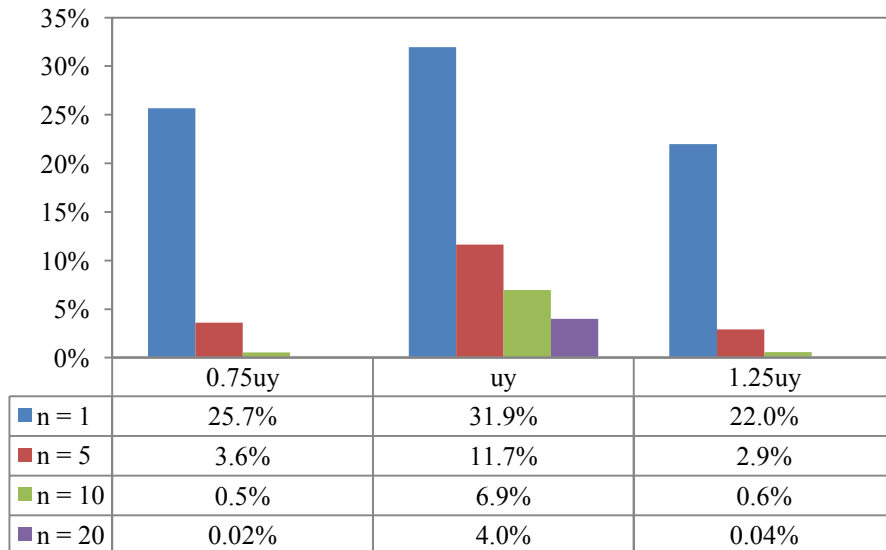
Figure A.6 Relative difference between the backbone curve and the response of 1-B

	0.75uy	uy	1.25uy
n = 1	23.1%	28.9%	19.3%
n = 5	3.3%	10.6%	2.6%
n = 10	0.5%	6.4%	0.5%
n = 20	0.02%	3.7%	0.04%
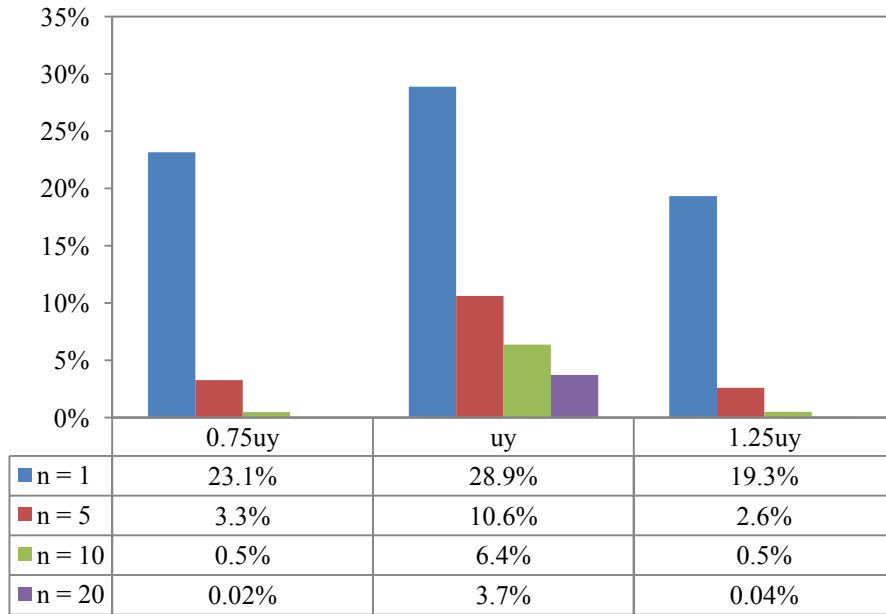
Figure A.7 Relative difference between the backbone curve and the response of 2-A

	0.75uy	uy	1.25uy
n = 1	25.7%	31.9%	22.0%
n = 5	3.6%	11.7%	2.9%
n = 10	0.5%	6.9%	0.6%
n = 20	0.02%	4.0%	0.04%
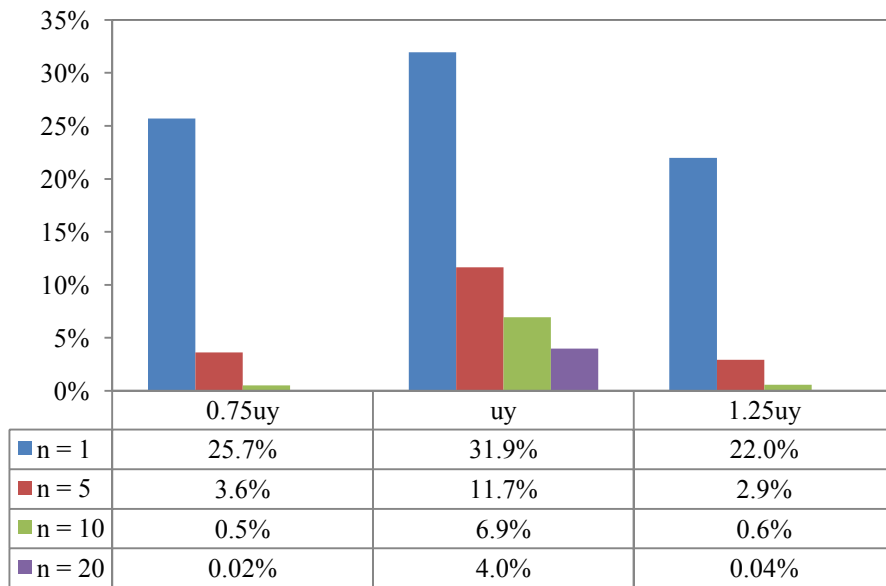
Figure A.8 Relative difference between the backbone curve and the response of 2-B

APPENDIX B

Selected Records

Each record, tagged as of Table 4.12 is depicted herein, including characteristics namely the velocity (v_g), the percentage of arias intensity (AI) and the significant duration (t_d) defined as the time elapsed within the 5% and the 95% of AI. These records were chosen from the data base of simulated records for eastern Canada generated by Atkinson (2009), except the record #6 which corresponds to data recorded during the Saguenay earthquake with M5.9 in November 25, 1988.
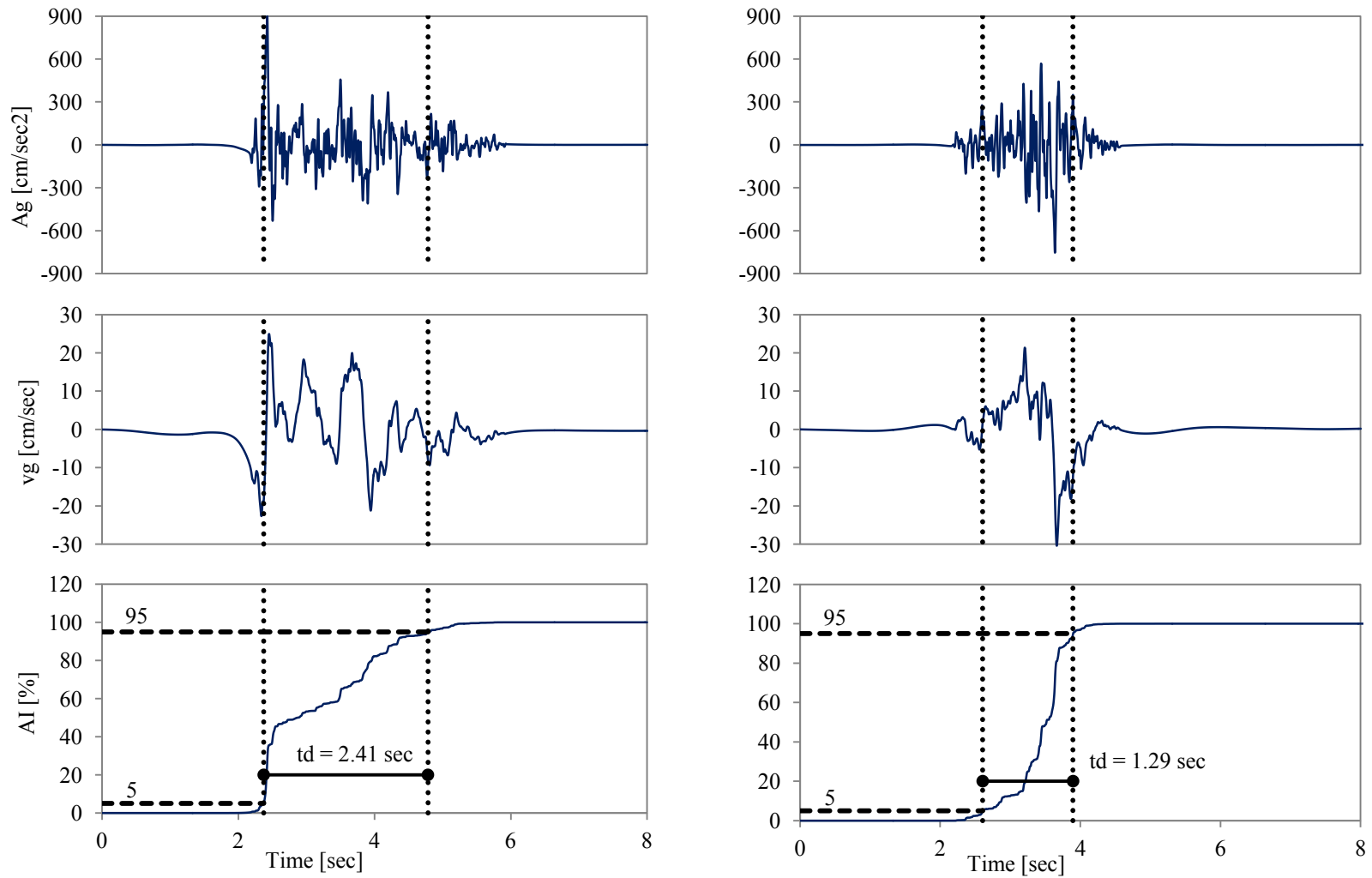
Figure B.1 Characteristics of record #1 (left column) and record #2 (right column)
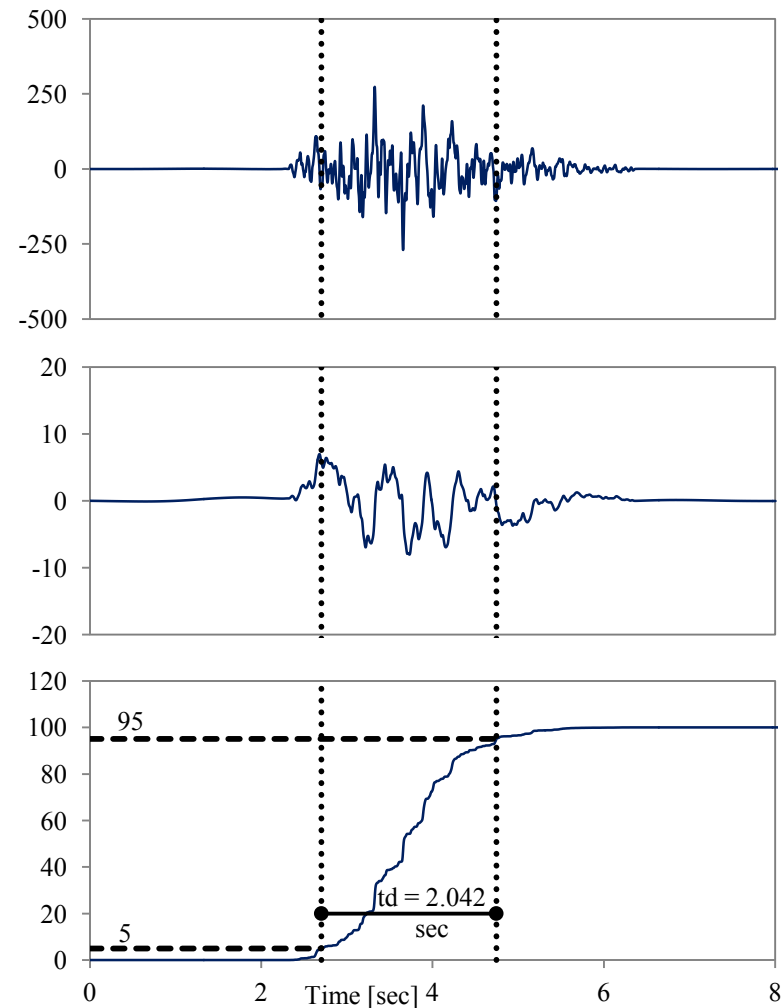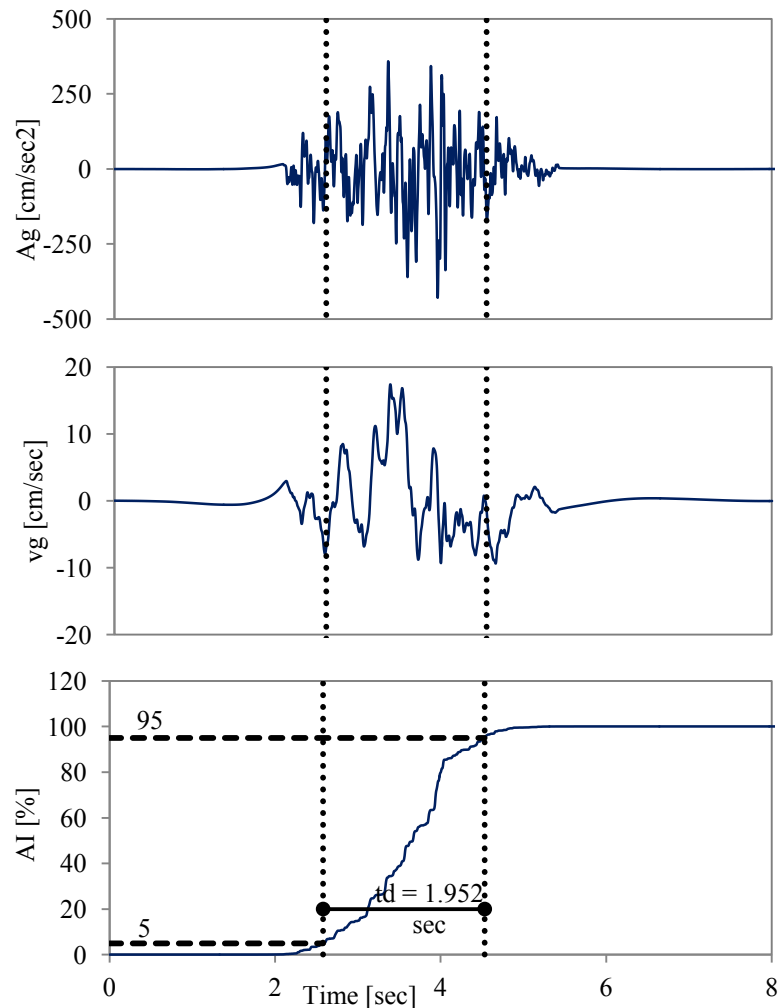
Figure B.2 Characteristics of record #3 (left column) and record #4 (right column)
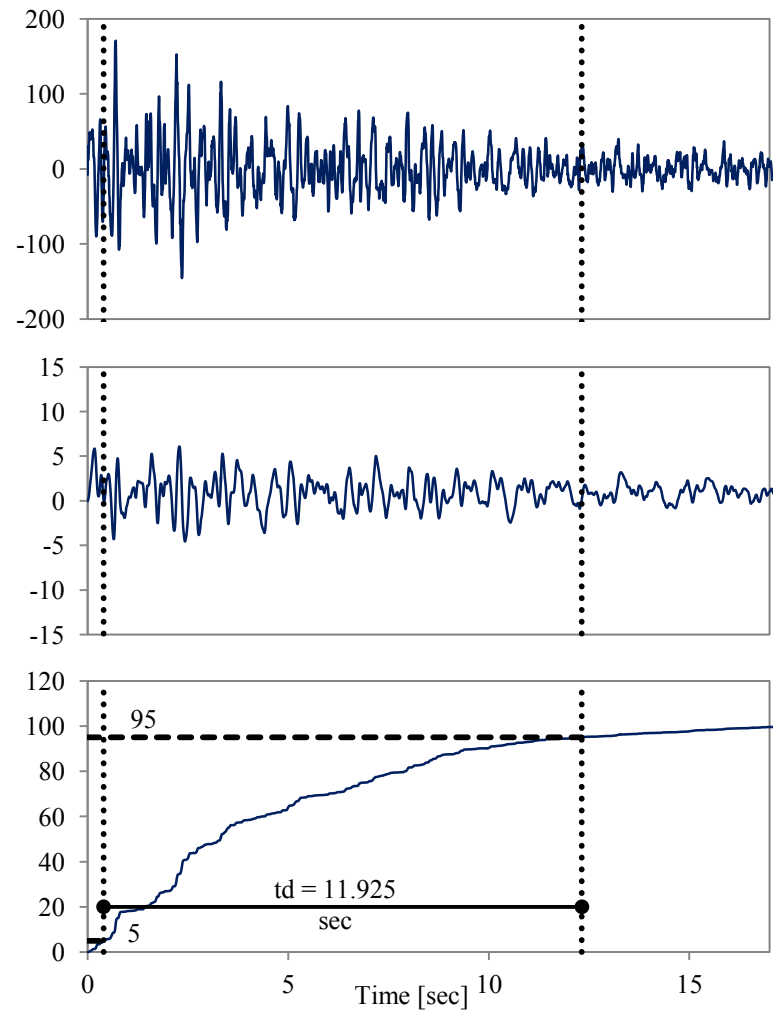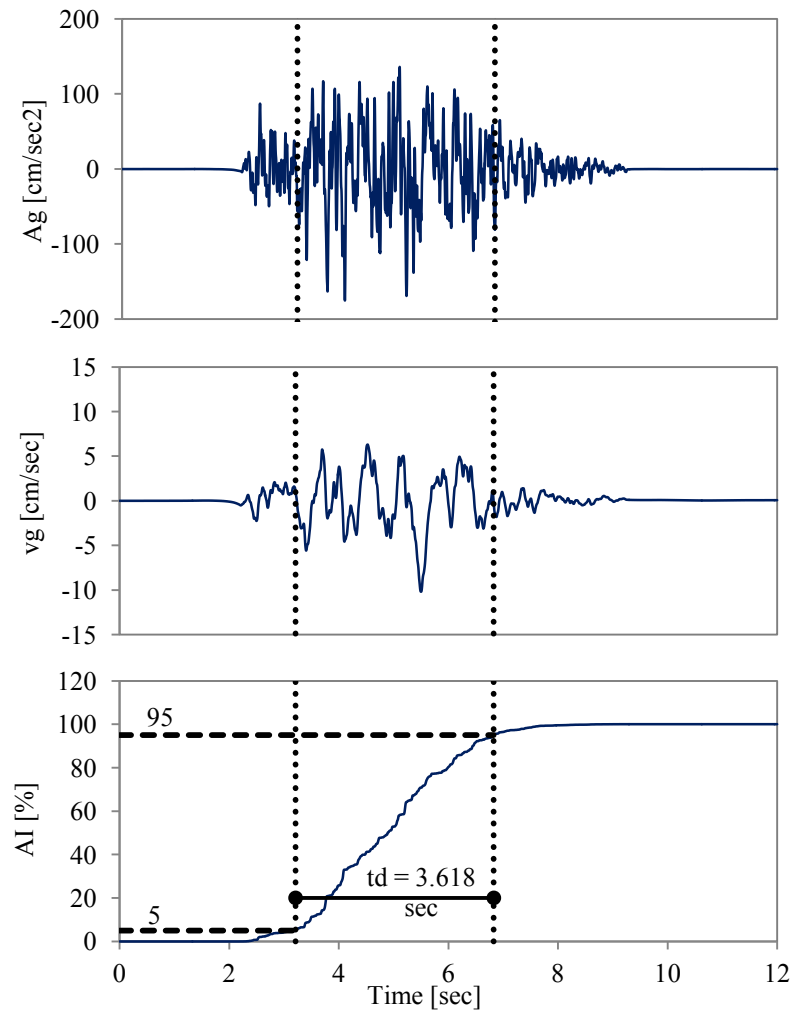
Figure B.3 Characteristics of record #5 (left column) and record #6 (right column)
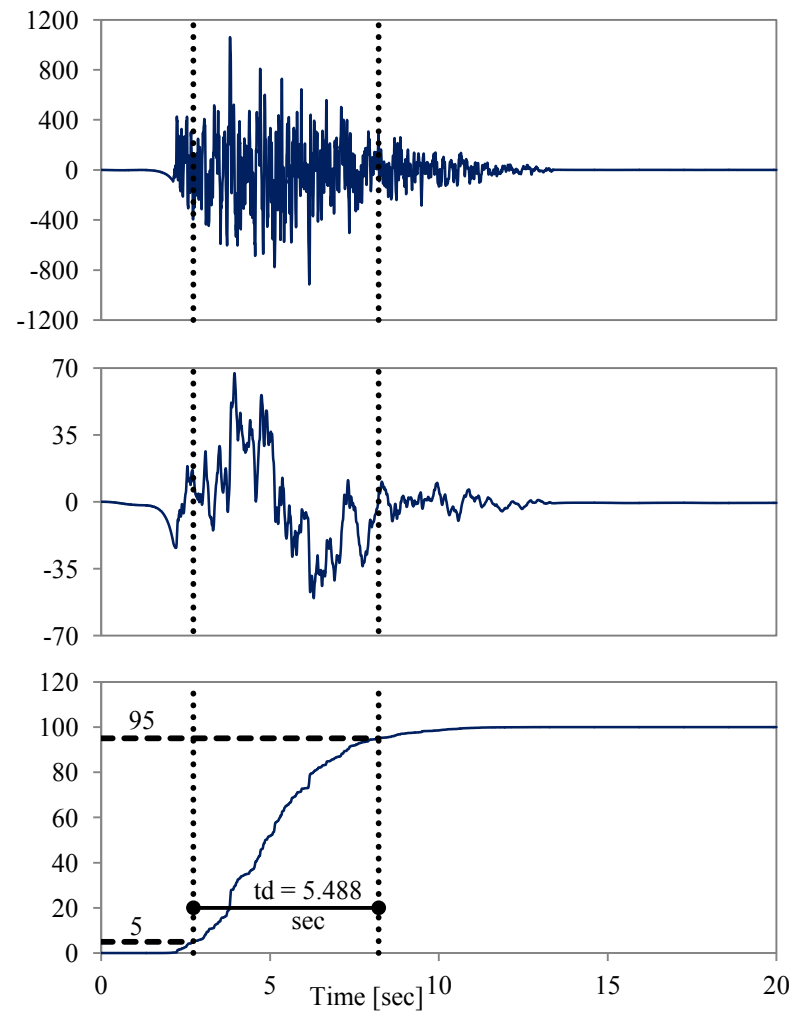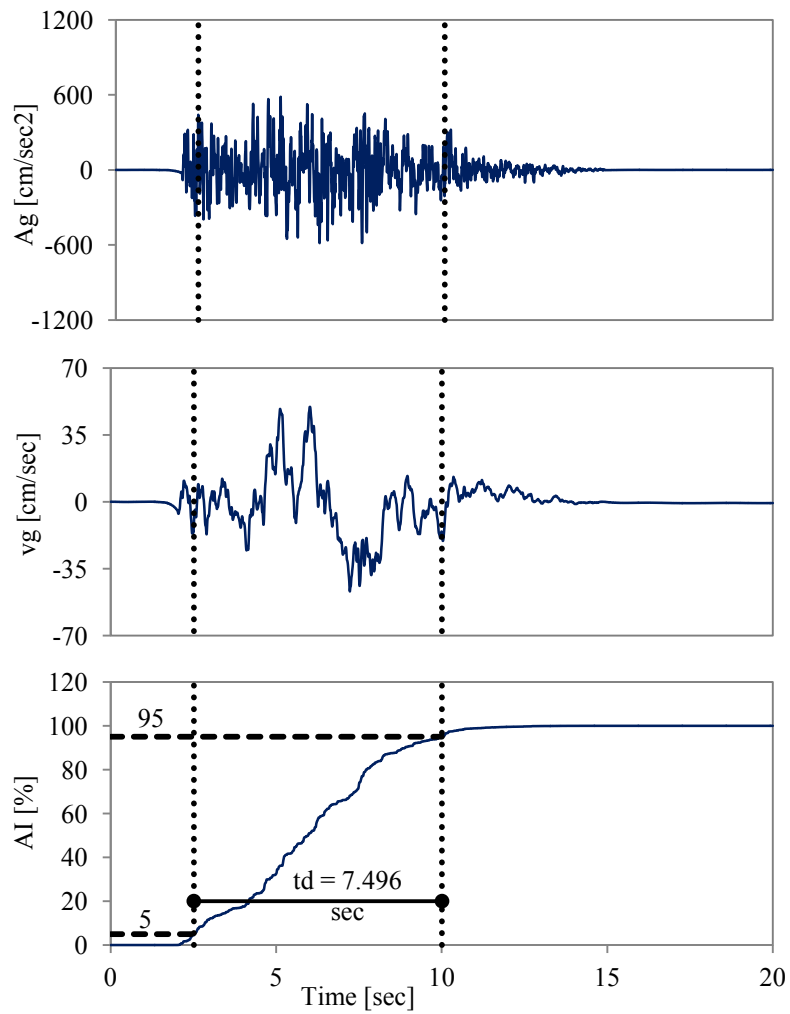
Figure B.4 Characteristics of record #7 (left column) and record #8 (right column)
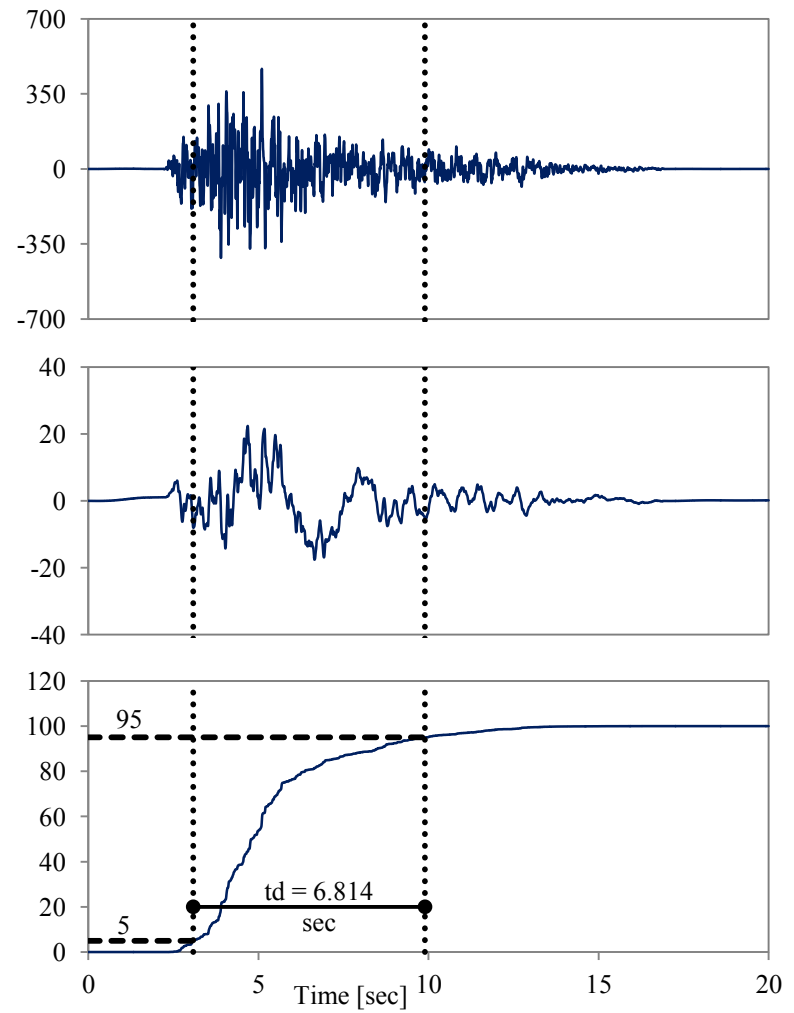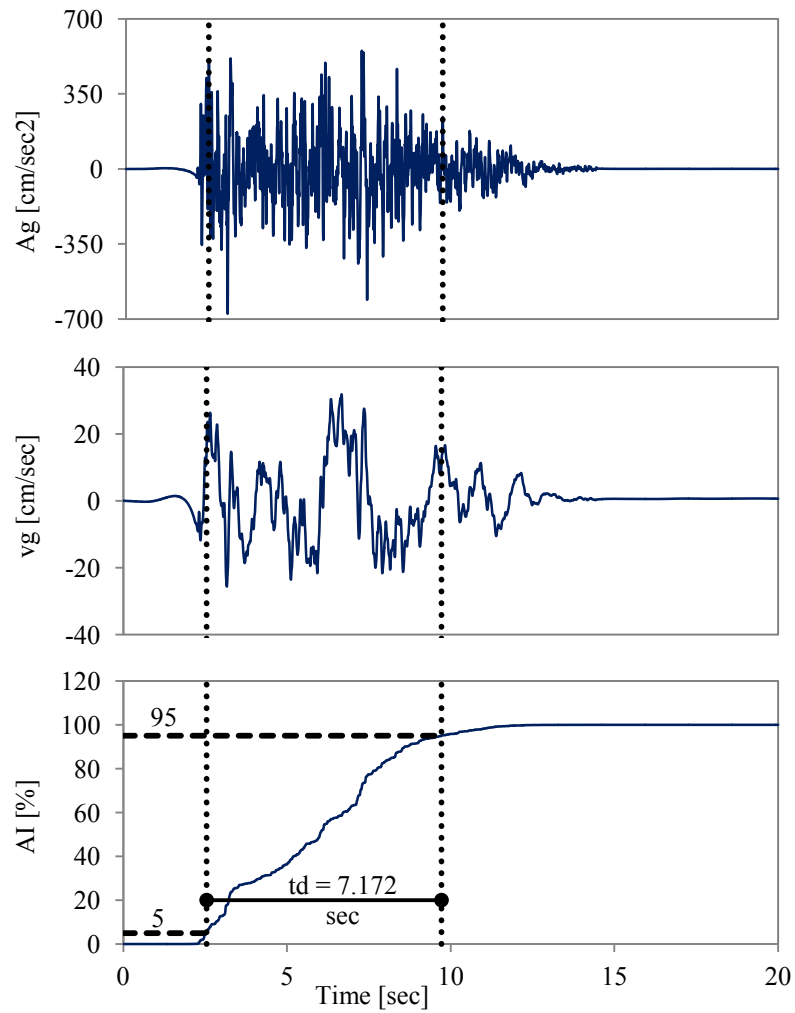
Figure B.5 Characteristics of record #9 (left column) and record #10 (right column)
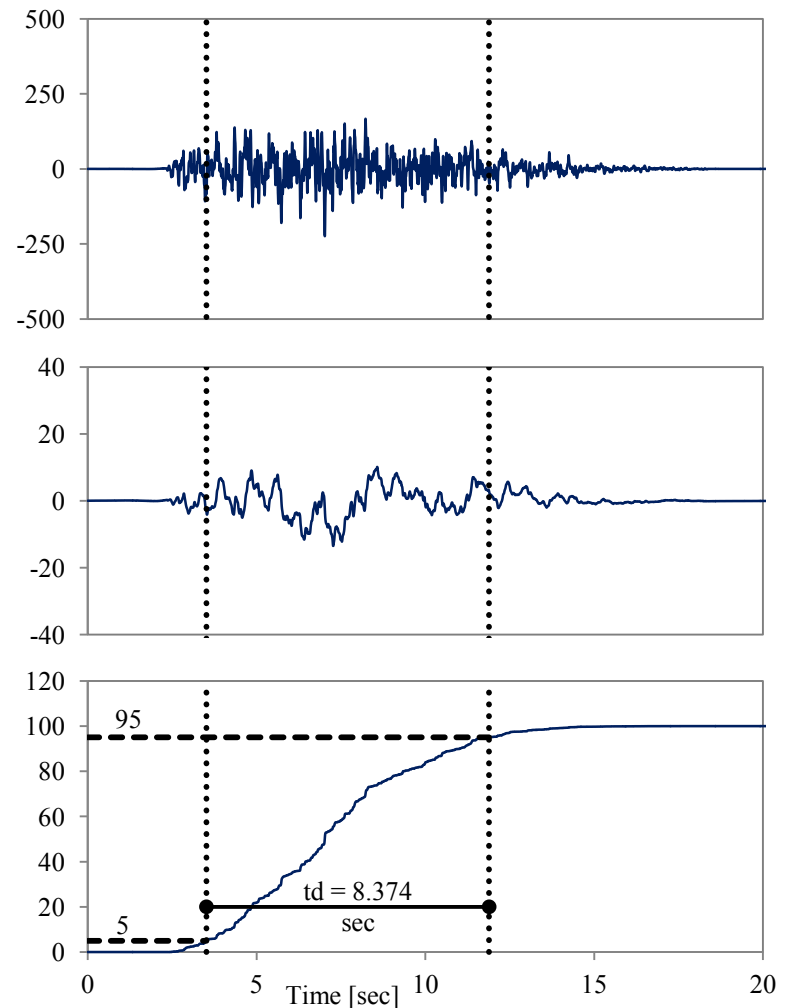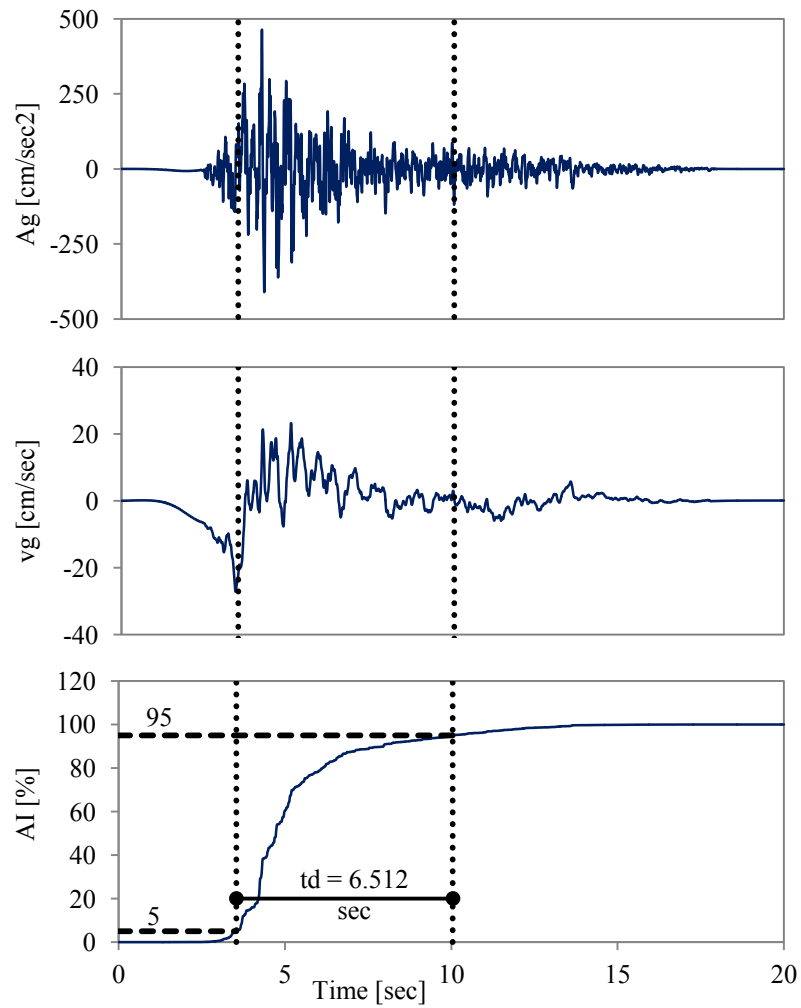
Figure B.6 Characteristics of record #11 (left column) and record #12 (right column)
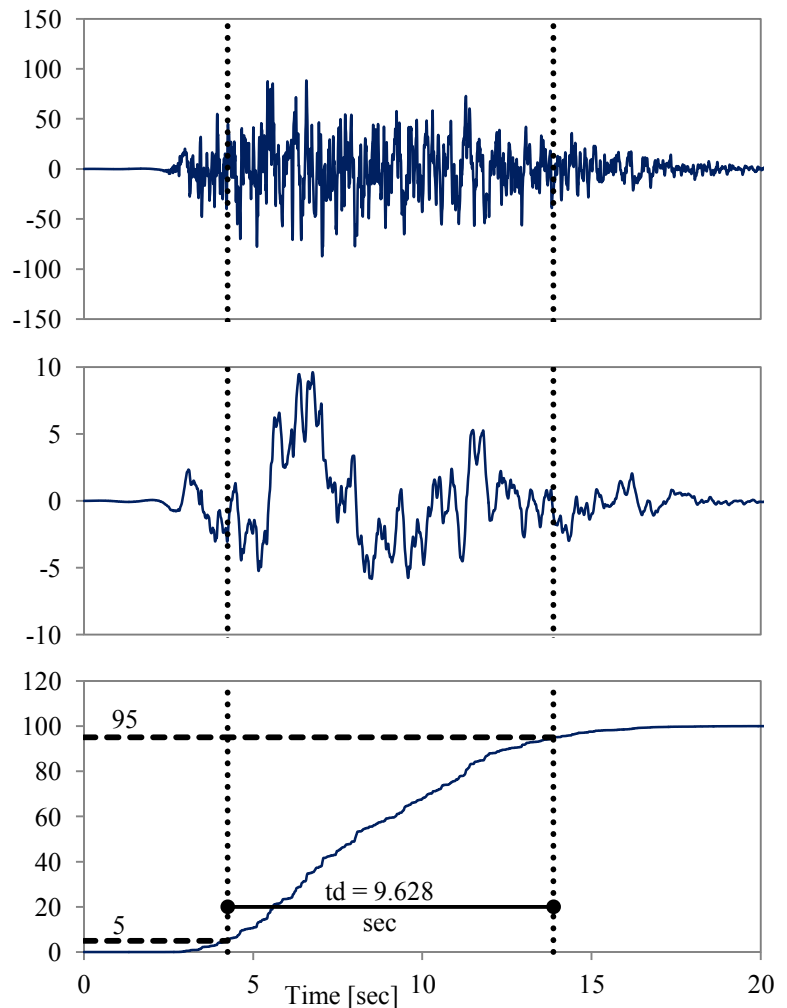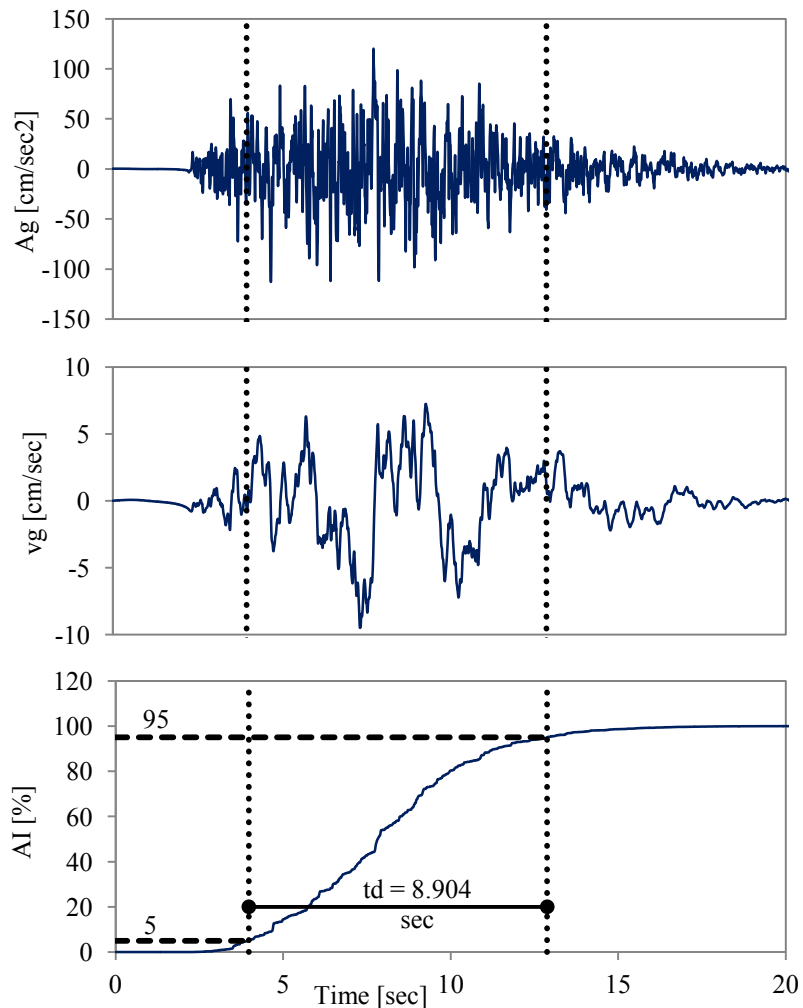
Figure B.7 Characteristics of record #13 (left column) and record #14 (right column)
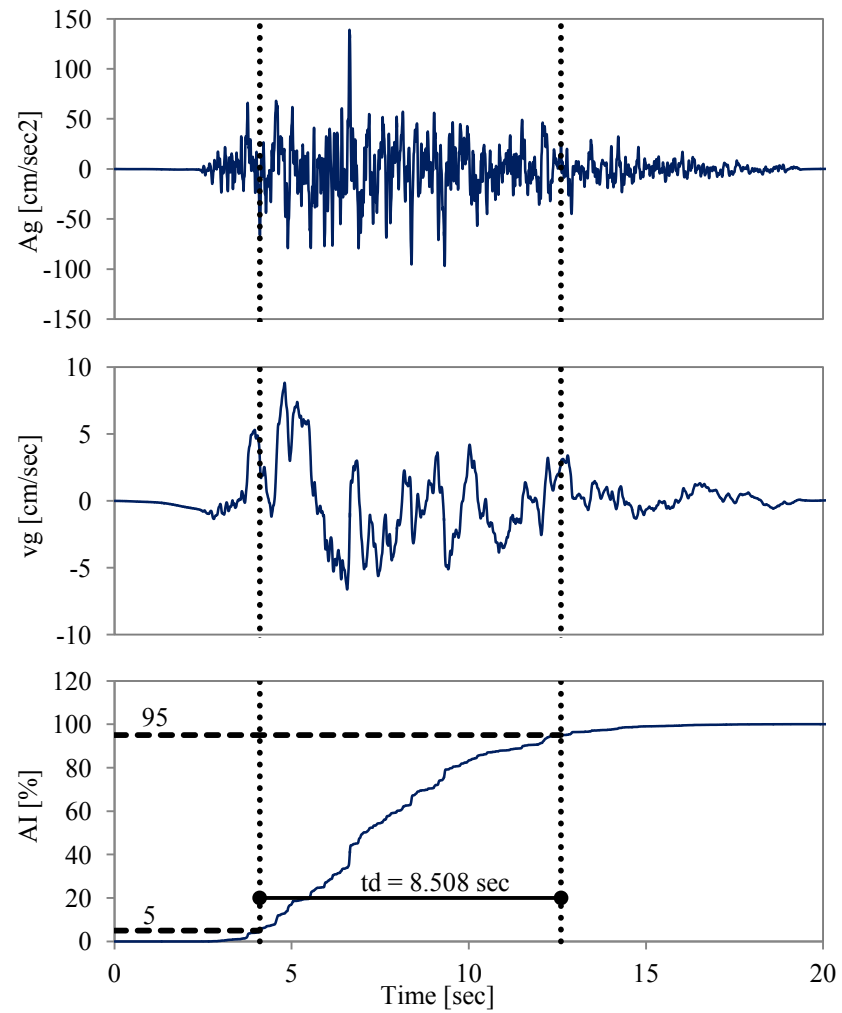
Figure B.8 Characteristics of record #15

APPENDIX C

Response of the Studied MRF Buildings Equipped with Friction-Damped Diagonal-Bracing Devices without Modeling the Slip-Lock Phase. Scenarios A, B and C

In the first part of this appendix the responses of the 4-, 8-, and 12-storey building with the different configurations of dampers (scenarios A, B, C) are depicted. The responses are given in terms of the EDPs: maximum interstory drift ratio, $\Delta max/hs$; maximum drift angle, $Dumax/h_z$ and maximum beam rotation per floor, θmax. Each figure shows the EDP recorded under the set of ground motions shown in Appendix B scaled as discussed in section 4.3. The mean value of the EDP and the mean ± one standard deviation are also shown for each analysis scenario. On the other hand, the second part shows the roof displacement histories of the 4-, 8-, and 12-storey buildings for the scenarios A, B, and C.
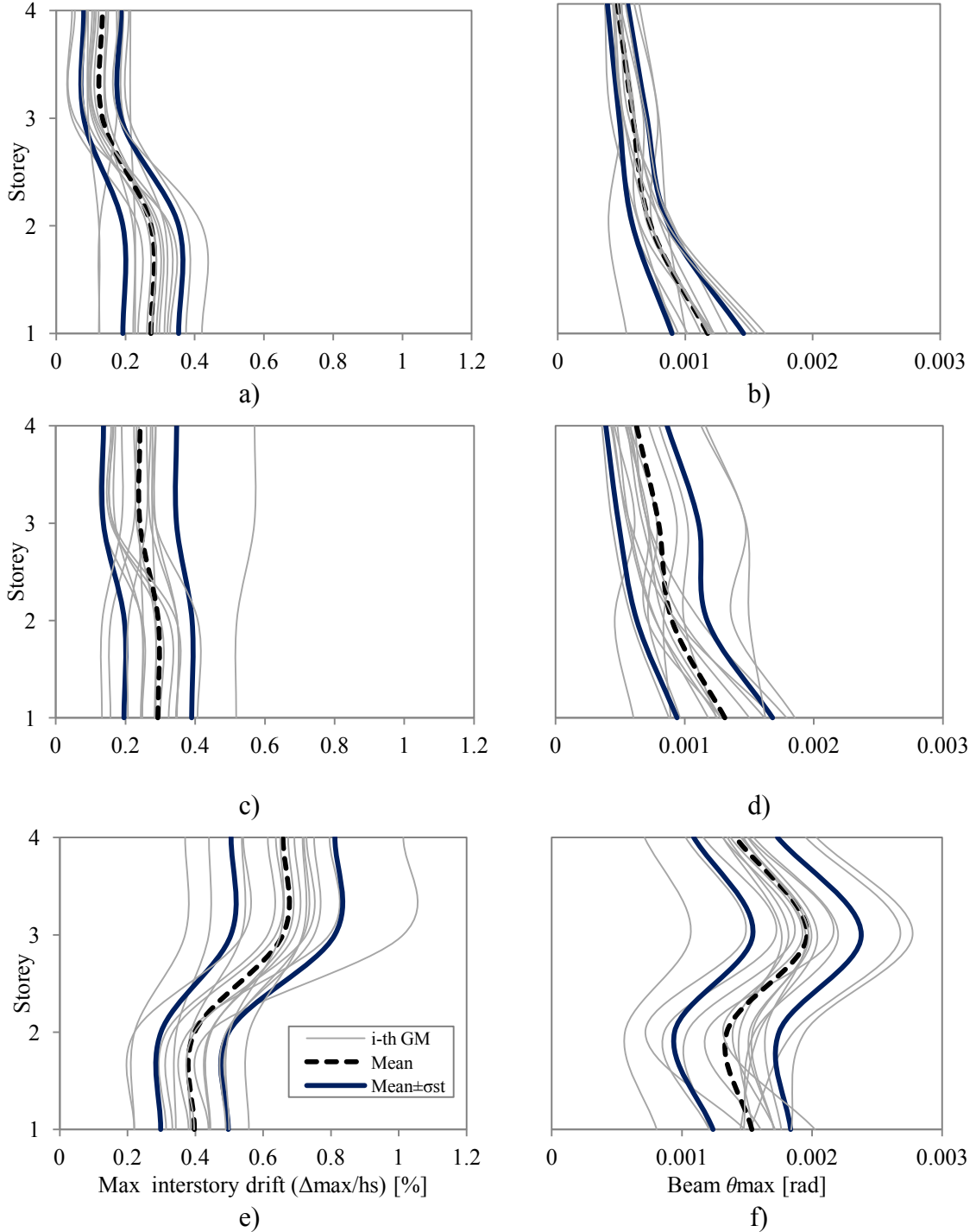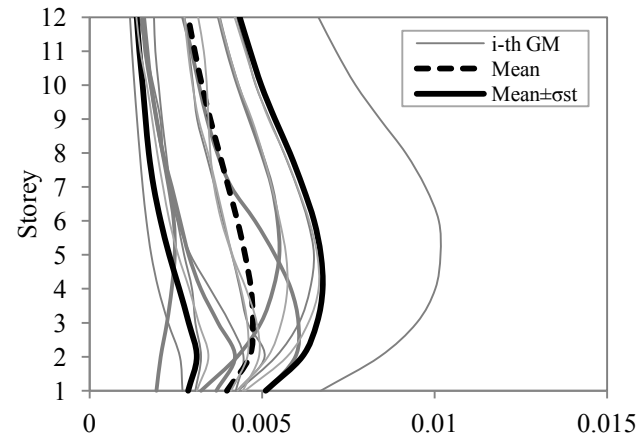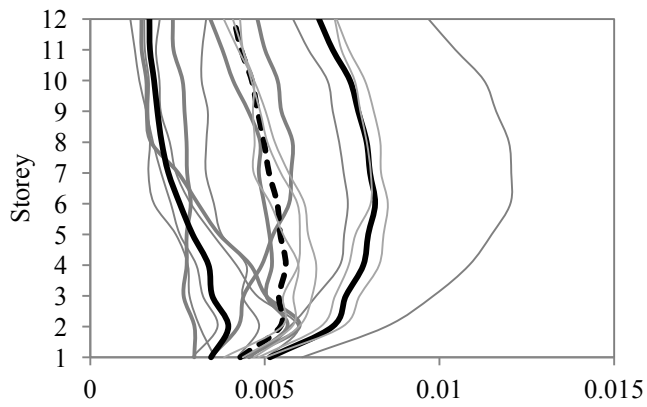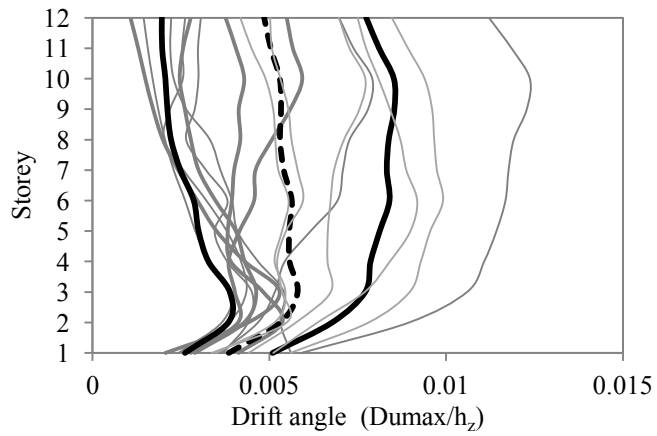
Figure C.1 Response in term of EDPs for scenarios A, B, C of the 4-storey building under 15 records. a) Maximum interstorey drifts-scenario A; b) Maximum beam rotations-scenario A; c) Maximum interstorey drifts-scenario B; d) Maximum beam rotations-scenario B; e) Maximum interstorey drifts-scenario C; f) Maximum beam rotations-scenario C
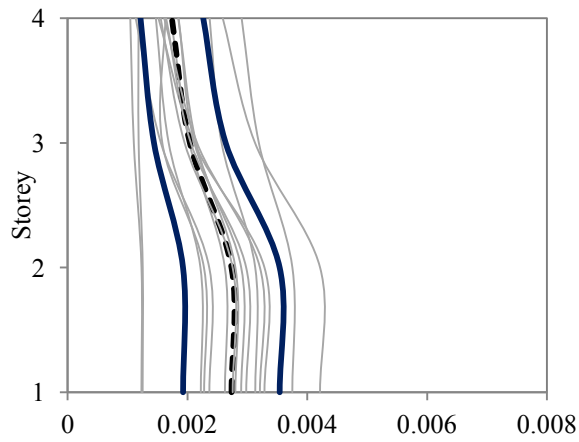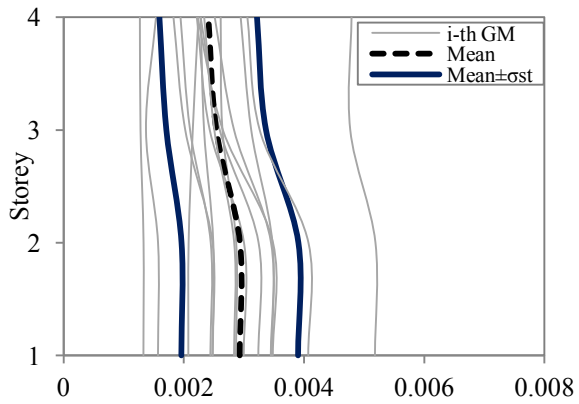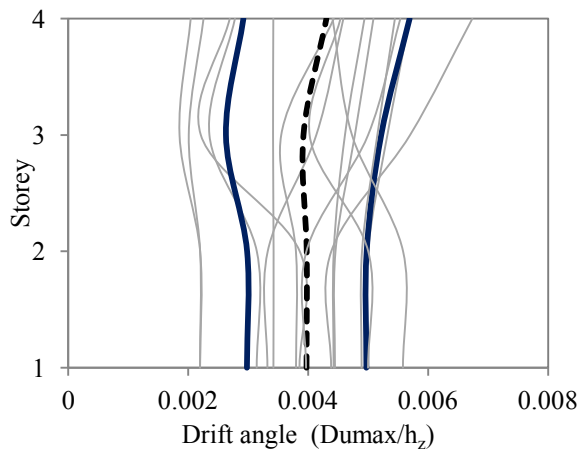
Figure C.2 Response in term of EDPs for scenarios A, B, C of the 4-storey building under 15 records. a) Maximum drift angles-scenario A; b) Maximum drift angles-scenario B; c) Maximum drift angles-scenario C
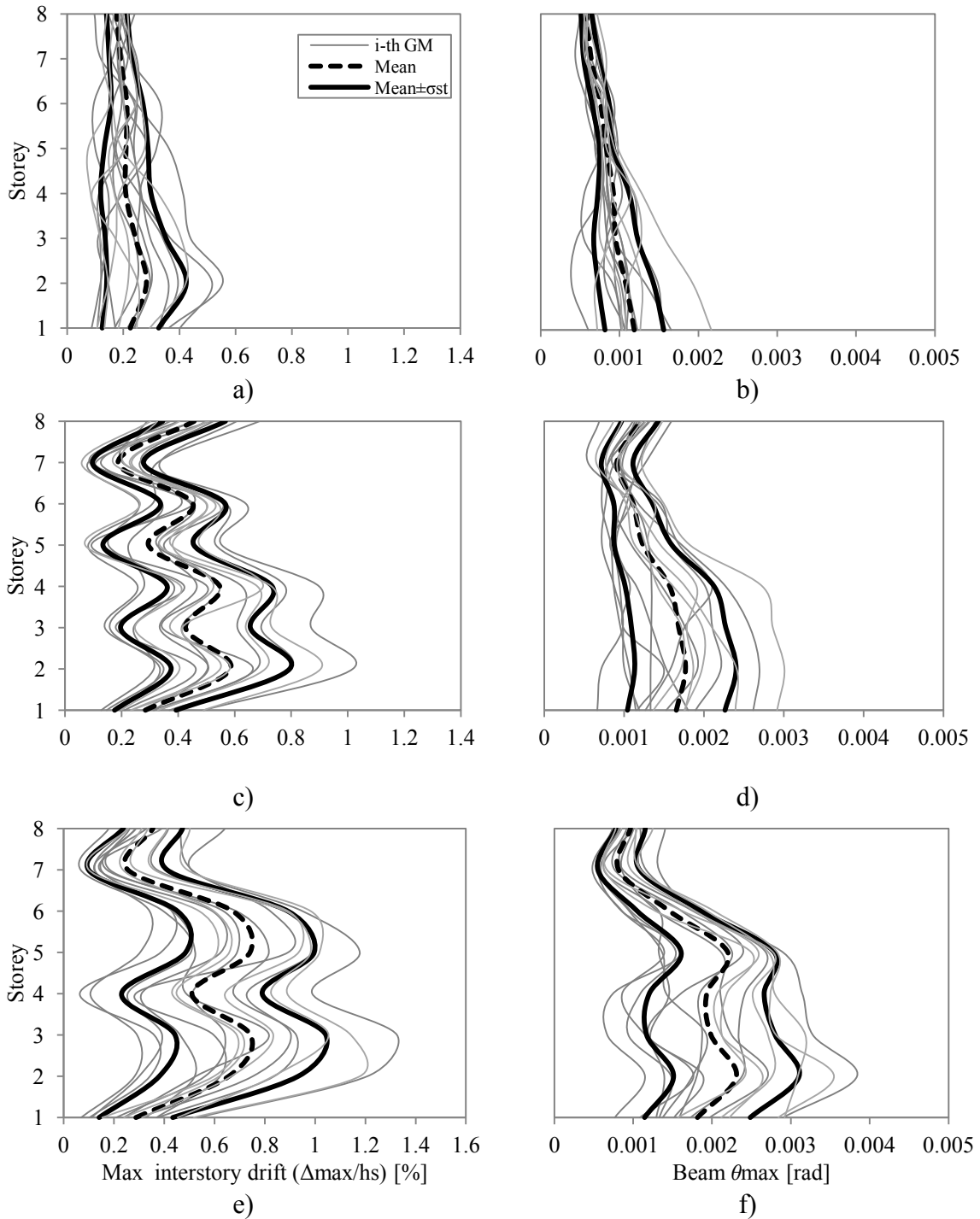
Figure C.3 Response in term of EDPs for scenarios A, B, C of the 8-storey building under 15 records. a) Maximum interstorey drifts-scenario A; b) Maximum beam rotations-scenario A; c) Maximum interstorey drifts-scenario B; d) Maximum beam rotations-scenario B; e) Maximum interstorey drifts-scenario C; f) Maximum beam rotations-scenario C
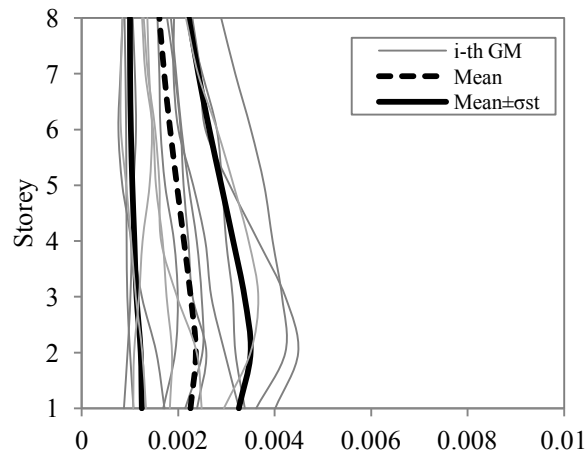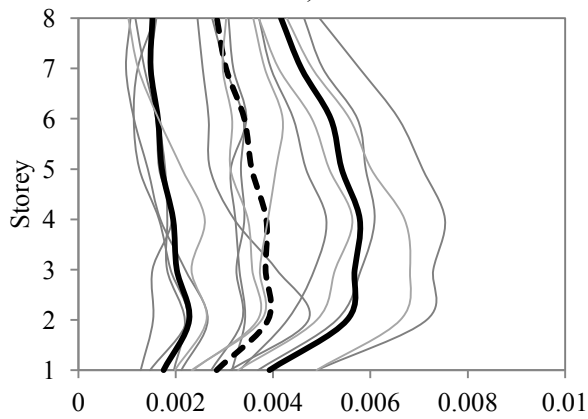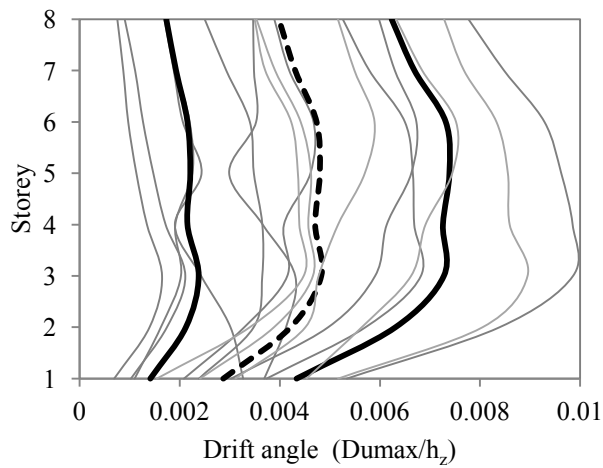
Figure C.4 Response in term of EDPs for scenarios A, B, C of the 8-storey building under 15 records. a) Maximum drift angles-scenario A; b) Maximum drift angles-scenario B; c) Maximum drift angles-scenario C
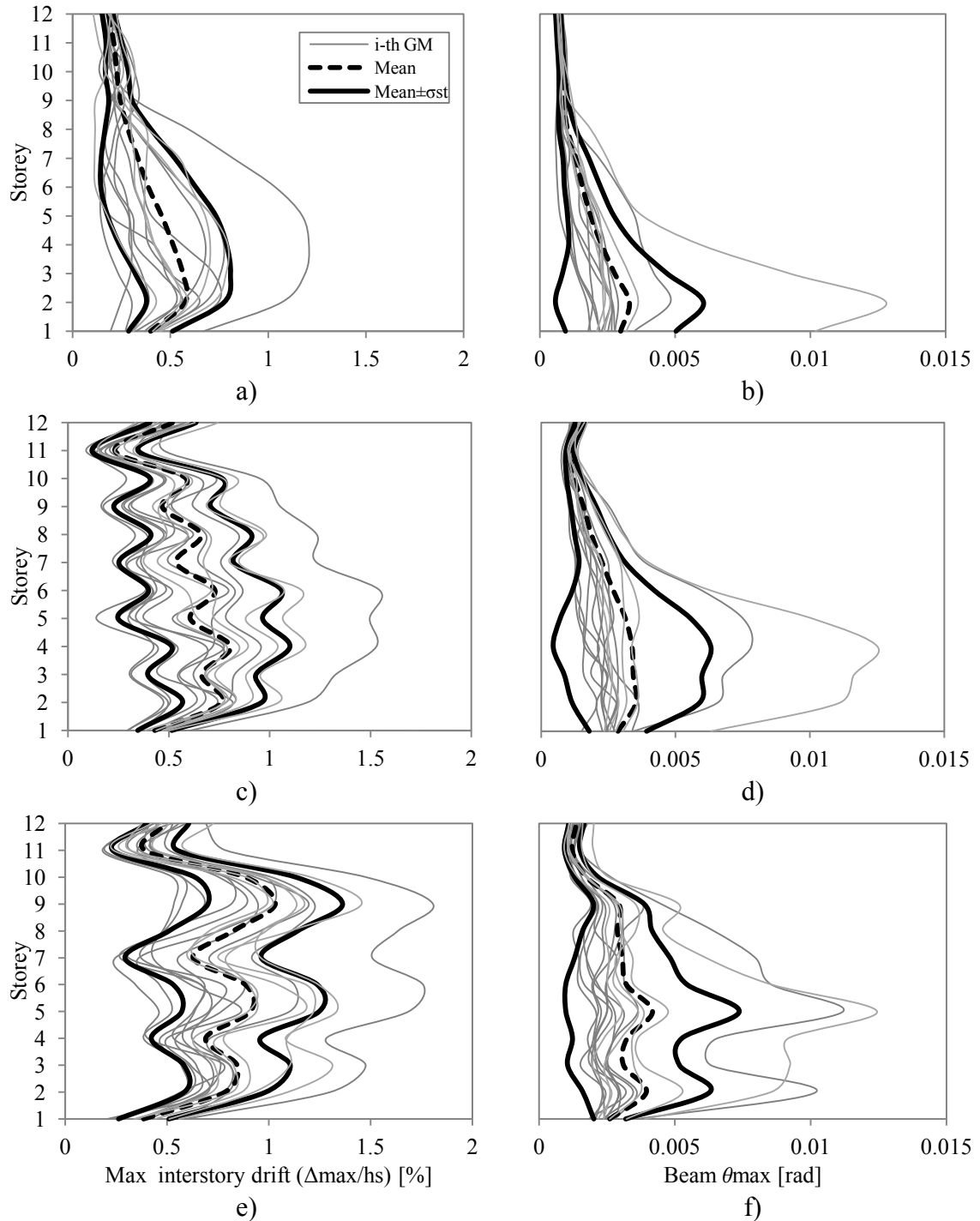
Figure C.5 Response in term of EDPs for scenarios A, B, C of the 12-storey building under 15 records. a) Maximum interstorey drifts-scenario A; b) Maximum beam rotations-scenario A; c) Maximum interstorey drifts-scenario B; d) Maximum beam rotations-scenario B; e) Maximum interstorey drifts-scenario C; f) Maximum beam rotations-scenario C

186

Figure C.6 Response in term of EDPs for scenarios A, B, C of the 12-storey building under 15 records. a) Maximum drift angles-scenario A; b) Maximum drift angles-scenario B; c) Maximum drift angles-scenario C
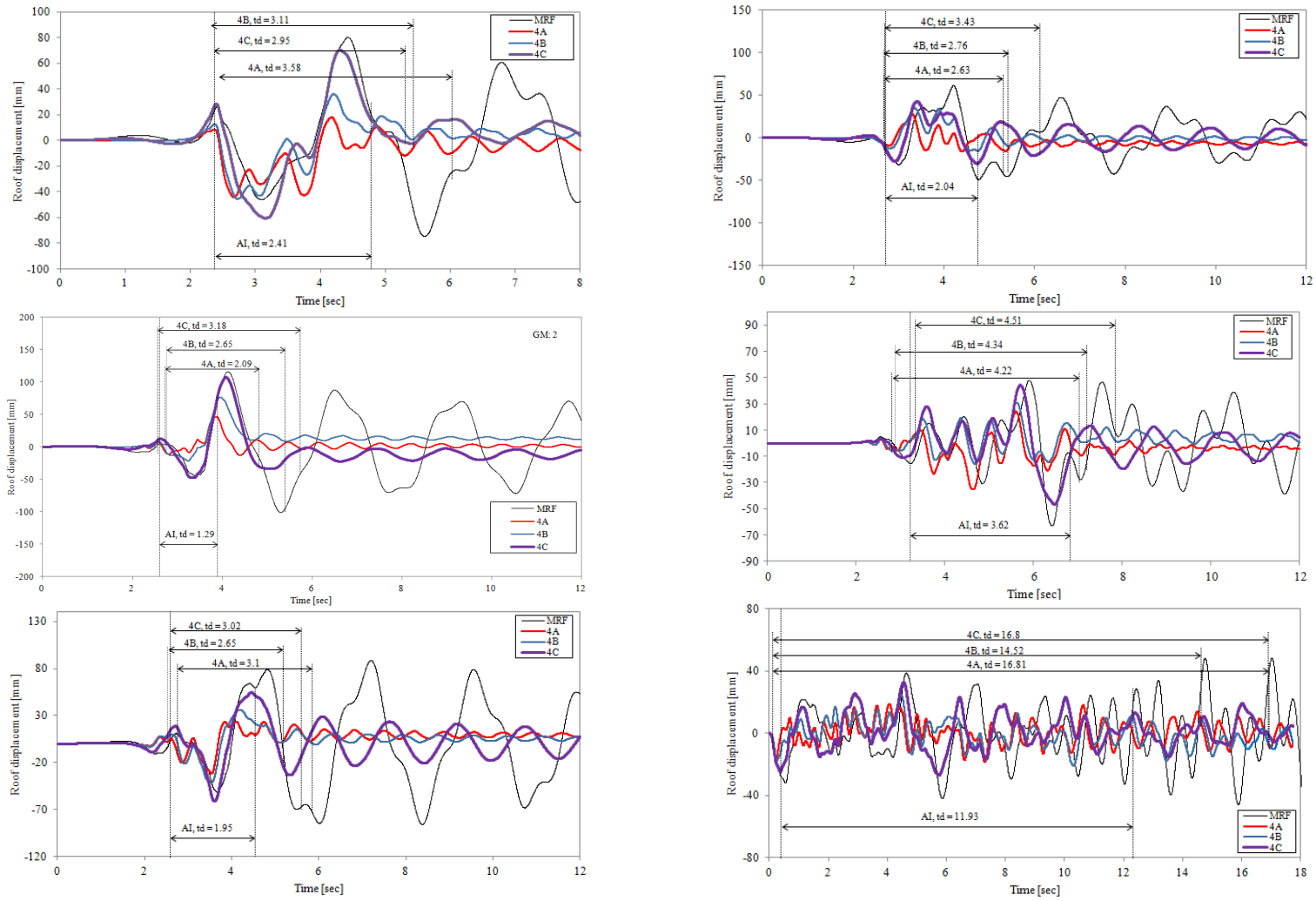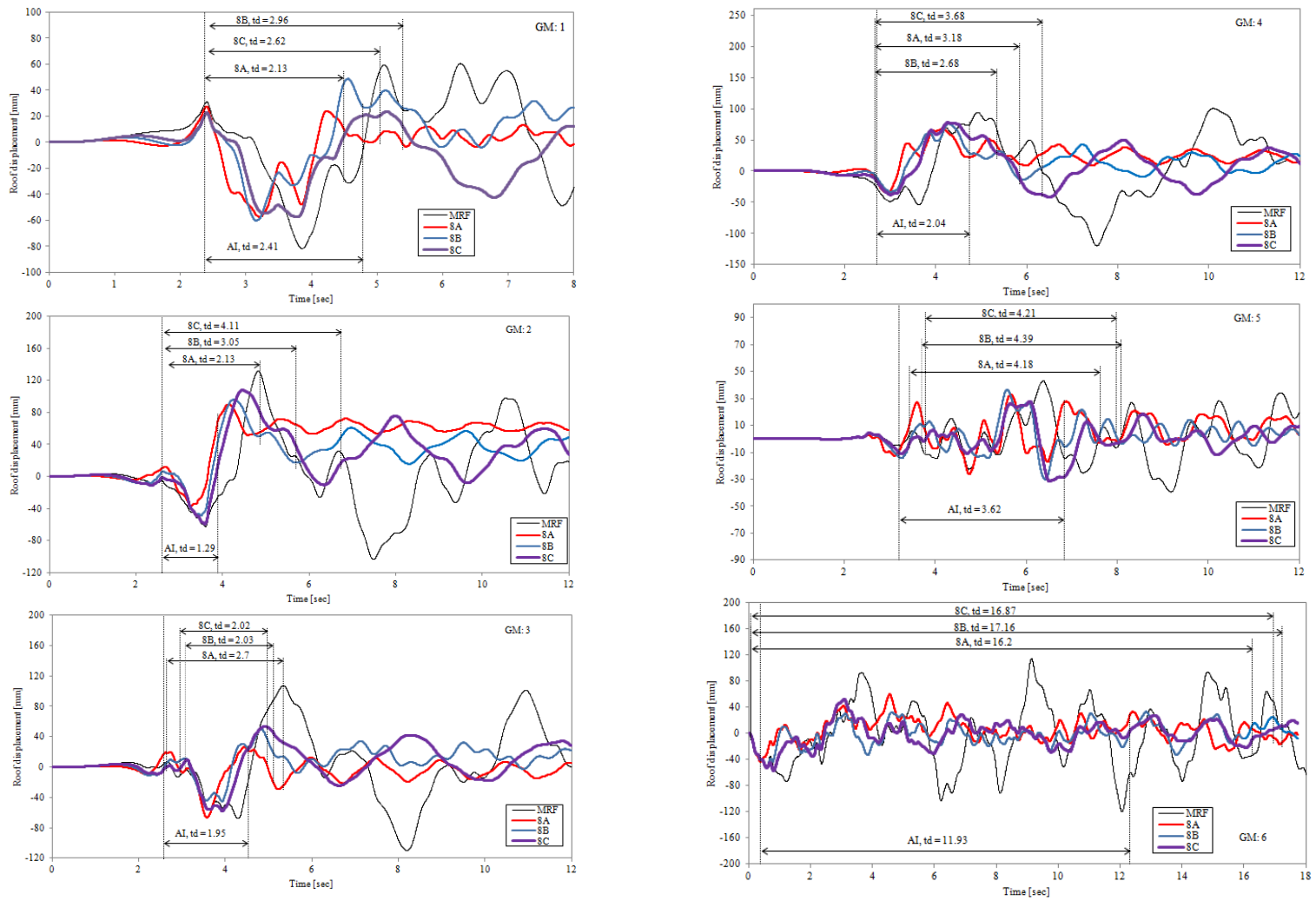
Figure C.7 Roof displacement history of MRF versus MFR with friction devices (scenarios A, B, C) for the 4-story building. Left column: records #1, #2, #3; right column: records #4, #5, #6
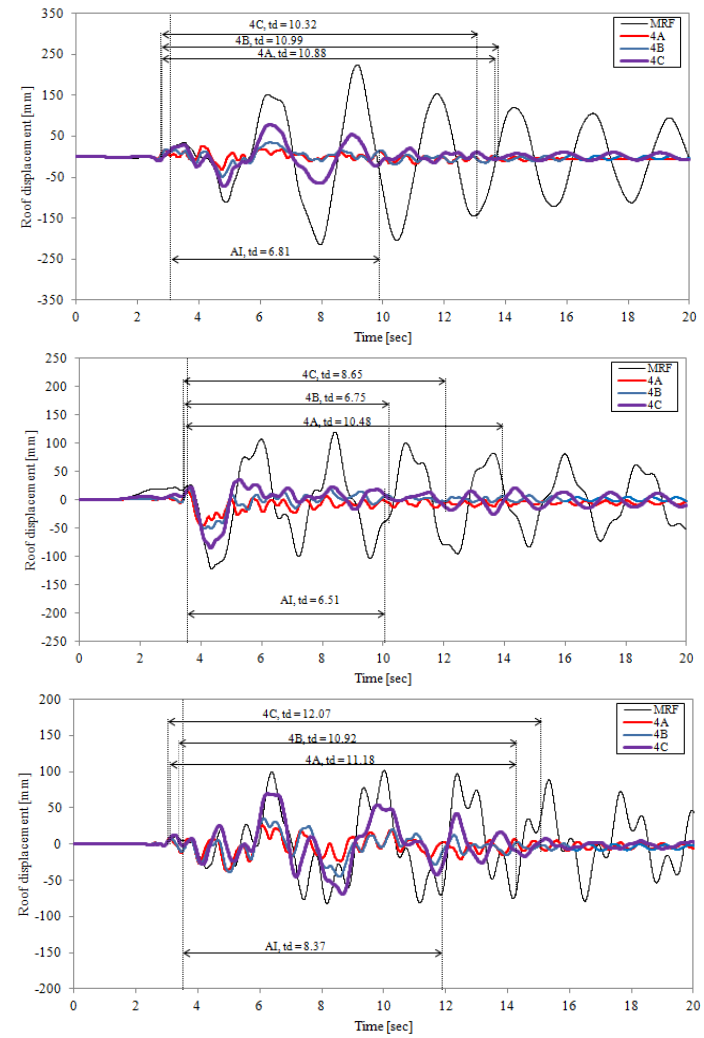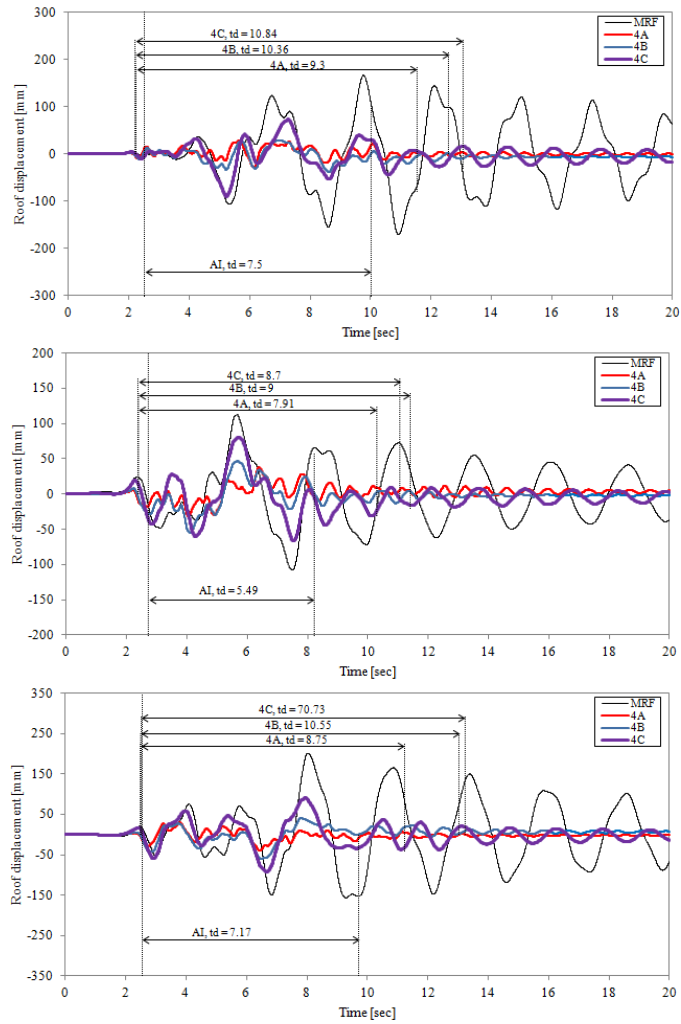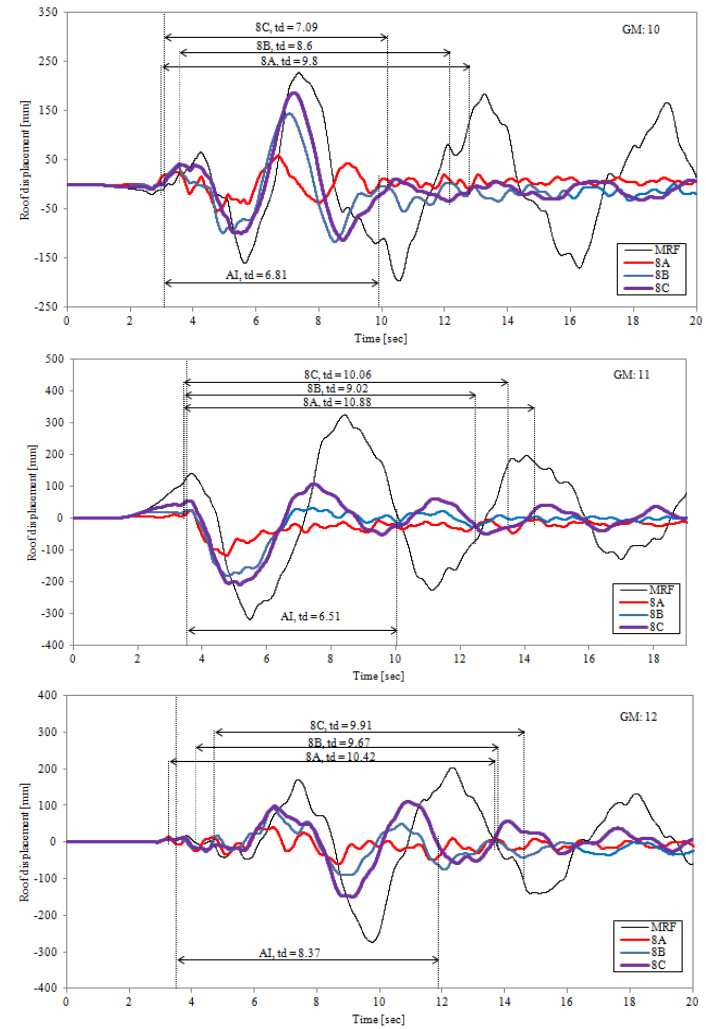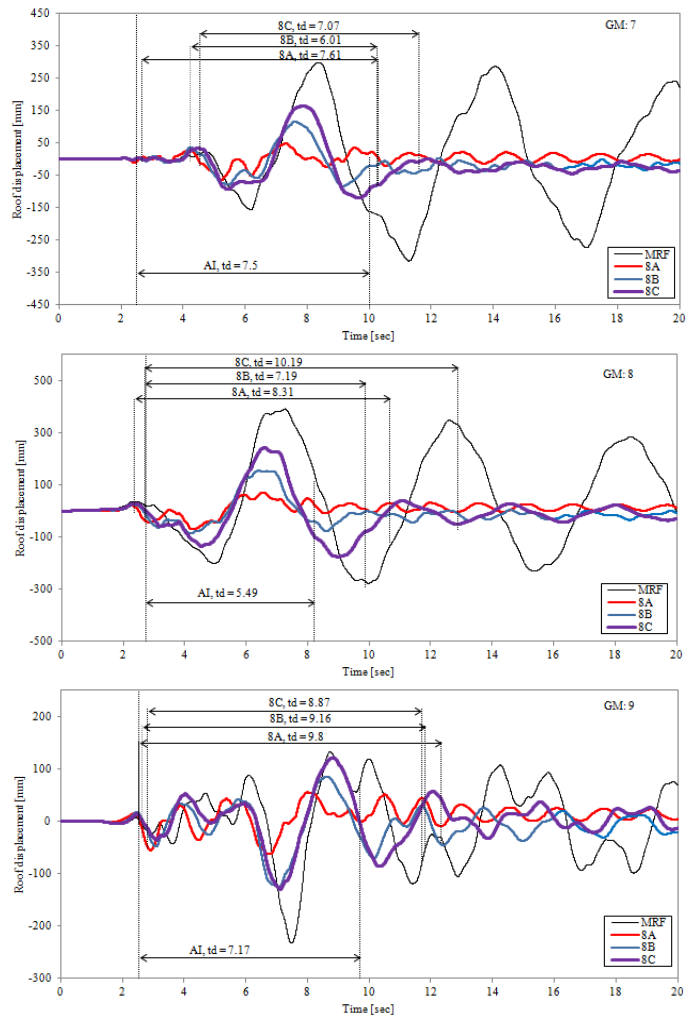
Figure C.8 Roof displacement history of MRF versus MFR with friction devices (scenarios A, B, C) for the 4-story building. Left column: records #7, #8, #9; right column: records #10, #11, #12
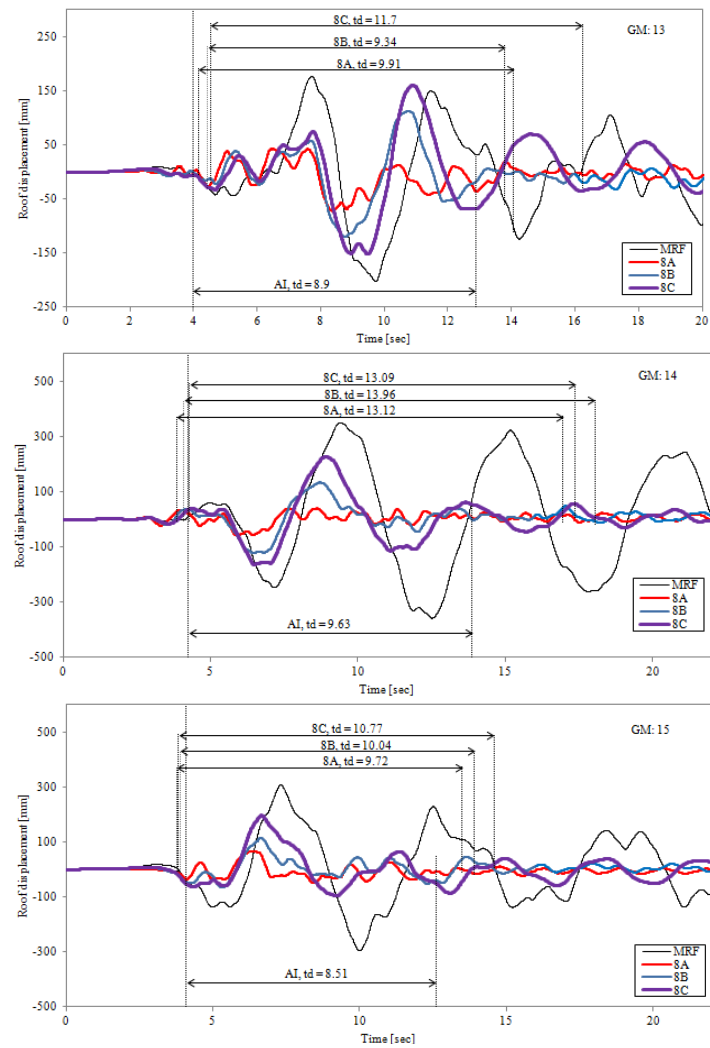
189
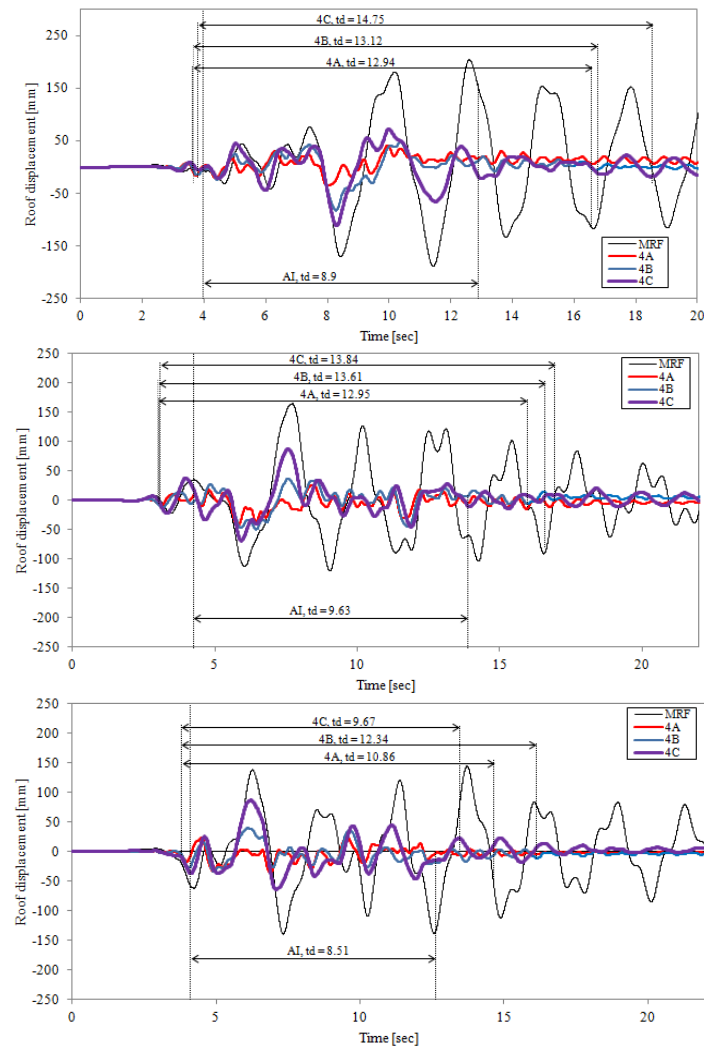
Figure C.9 Roof displacement history of MRF versus MFR with friction devices (scenarios A, B, C) for the 4-story building. Records #13, #14, #15
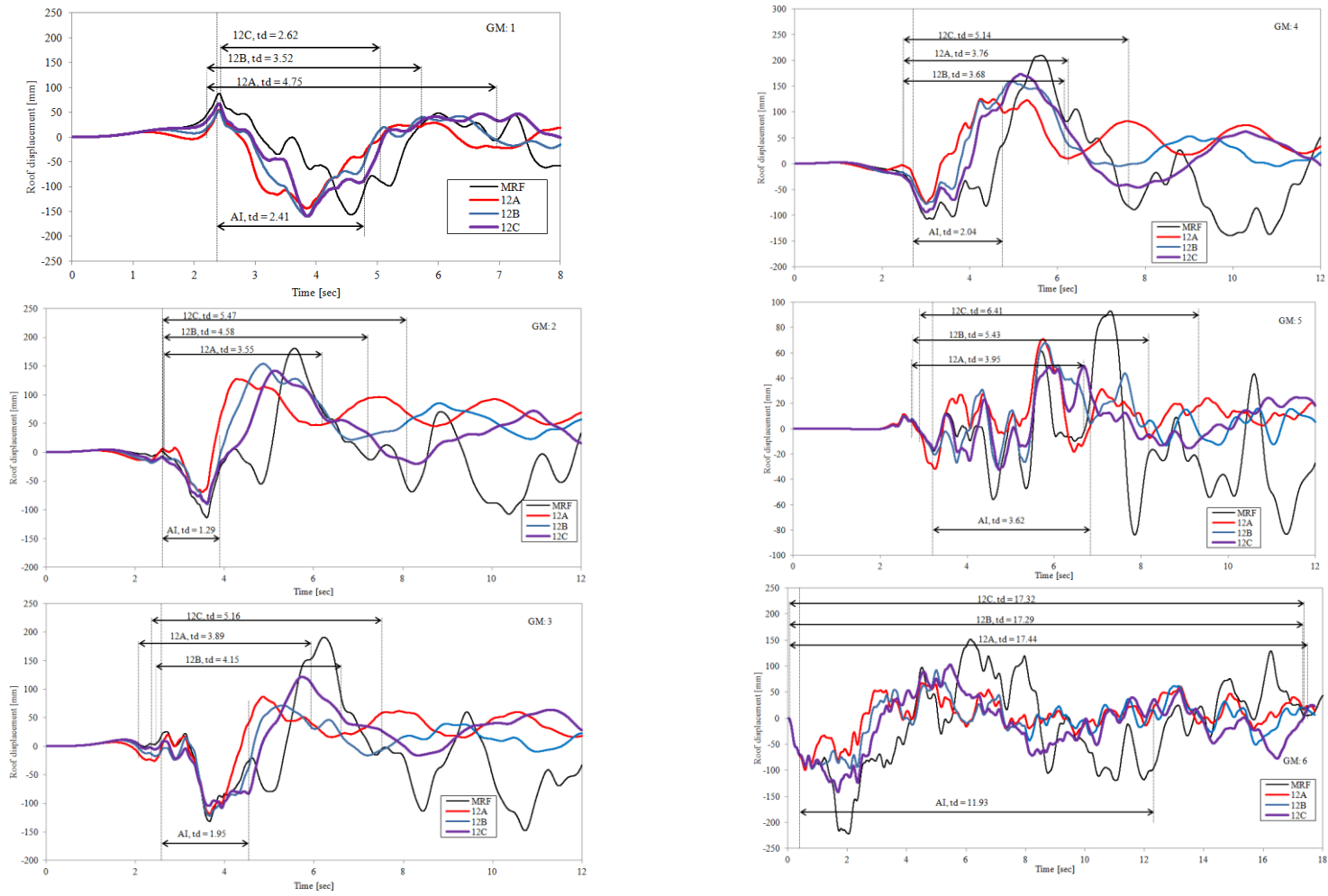
Figure C.10 Roof displacement history of MRF versus MFR with friction devices (scenarios A, B, C) for the 8-story building. Left column: records #1, #2, #3; right column: records #4, #5, #6

Figure C.11 Roof displacement history of MRF versus MFR with friction devices (scenarios A, B, C) for the 8-story building. Left column: records #7, #8, #9; right column: records #10, #11, #12

192

Figure C.12 Roof displacement history of MRF versus MFR with friction devices (scenarios A, B, C) for the 8-story building. Records #13, #14, #15

Figure C.13 Roof displacement history of MRF versus MFR with friction devices (scenarios A, B, C) for the 12-story building. Left column: records #1, #2, #3; right column: records #4, #5, #6
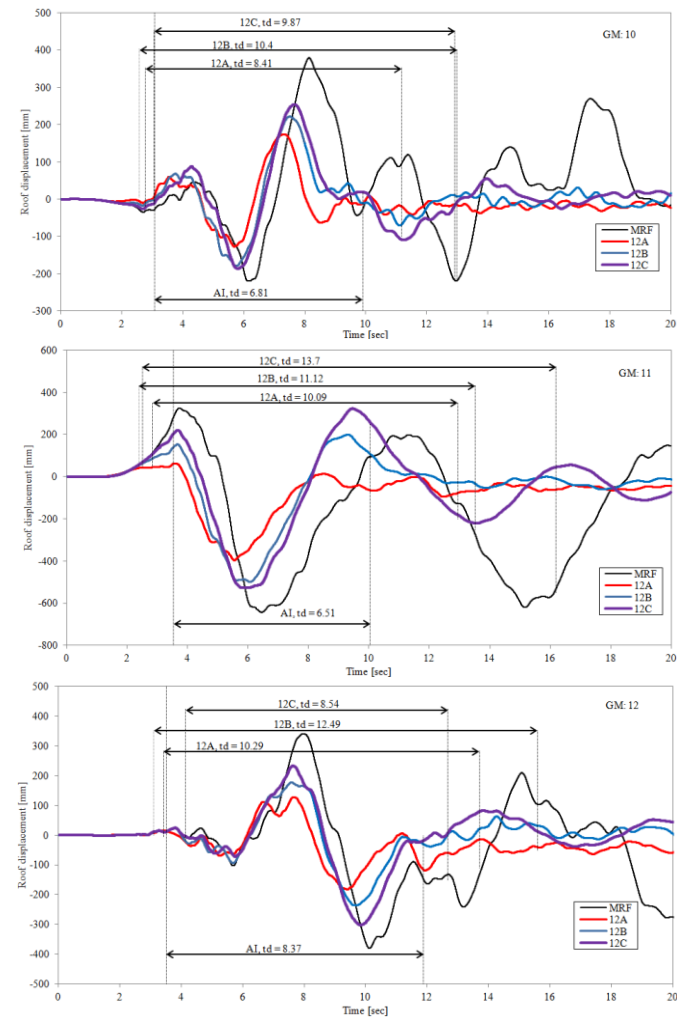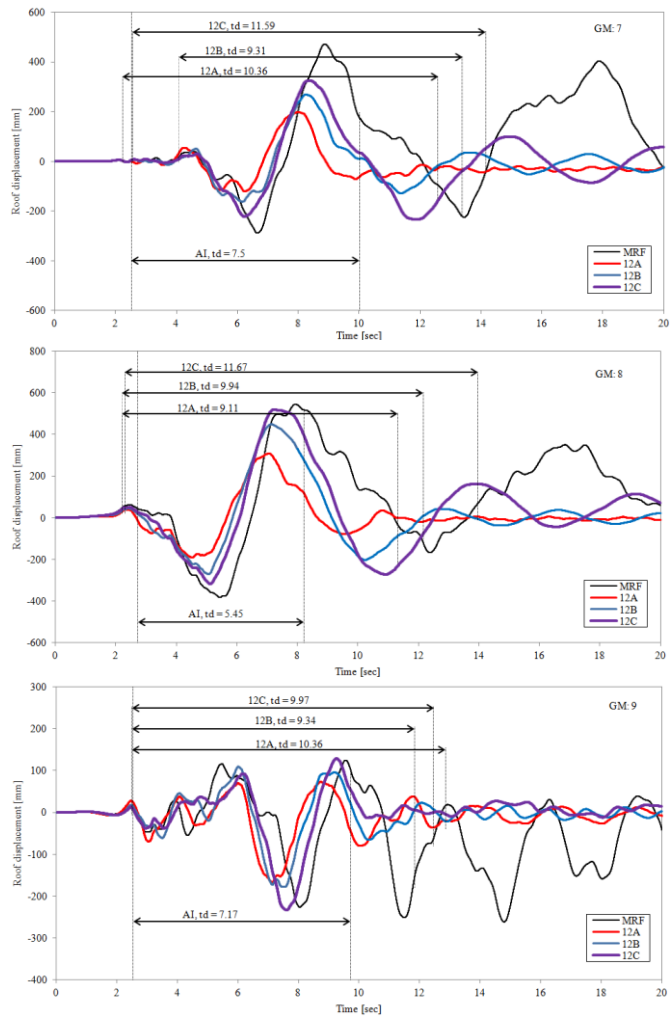
194

Figure C.14 Roof displacement history of MRF versus MFR with friction devices (scenarios A, B, C) for the 12-story building. Left column: records #7, #8, #9; right column: records #10, #11, #12
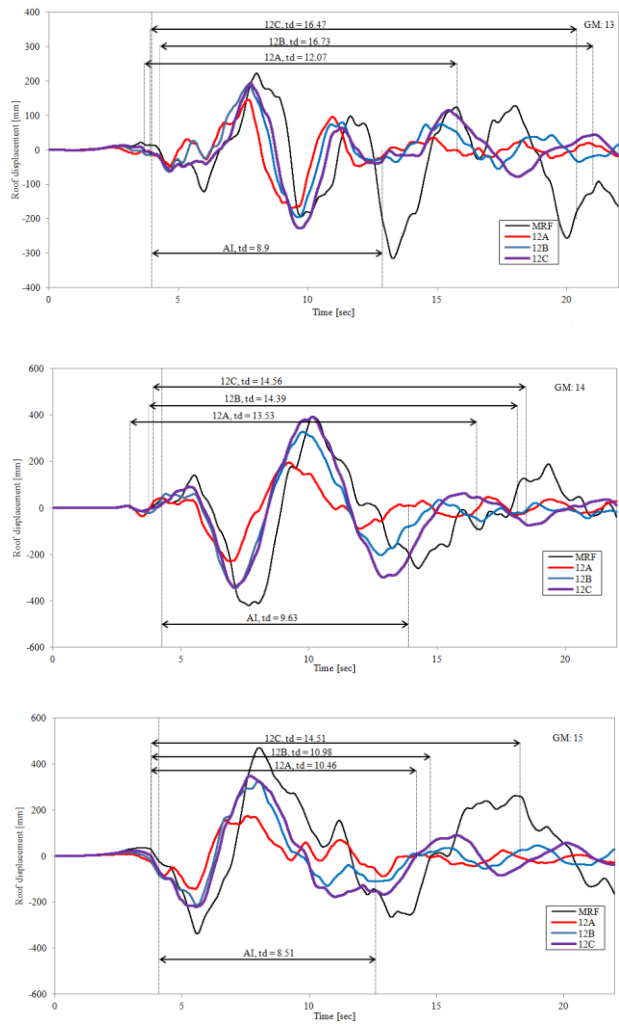
195

Figure C.15 Roof displacement history of MRF versus MFR with friction devices (scenarios A, B, C) for the 12-story building. Records #13, #14, #15